Dynamics of Thin-Walled Aerospace Structures for Fixture Design in Multi-axis Milling

Mouhab Meshreki

Department of Mechanical Engineering
McGill University

Montreal, Quebec
February 2009

A thesis submitted to McGill University in partial fulfilment of the requirements of the degree of Doctor of Philosophy

Abstract

Milling of thin-walled aerospace structures is a critical process due to the high flexibility of the workpiece. Available models for the prediction of the effect of the fixture on the dynamic response of the workpiece are computationally demanding and fail to represent practical cases for milling of thin-walled structures. Based on the analysis of typical structural components encountered in the aerospace industry, a generalized unit-element, with the shape of an asymmetric pocket, was identified to represent the dynamic response of these components. Accordingly, two computationally efficient dynamic models were developed to predict the dynamic response of typical thin-walled aerospace structures. These models were formulated using Rayleigh's energy and the Rayleigh-Ritz methods.

In the first model, the dynamics of multi-pocket thin-walled structures is represented by a plate with torsional and translational springs. A methodology was proposed and implemented for an off-line calibration of the stiffness of the springs using Genetic Algorithms. In the second model, the dynamics of a 3D pocket is represented by an equivalent 2D multi-span plate. Through a careful examination of the milling of thin-walled structures, a new formulation was developed to represent the continuous change of thickness of the workpiece due to the material removal action. Two formulations, based on holonomic constraints and springs with finite stiffness, were also developed and implemented to take into account the effect of perfectly rigid and deformable fixture supports.

All the developed models and formulations were validated numerically and experimentally for different workpiece geometries and various types of loading. These models resulted in one to two orders of magnitude reduction in computation time when compared with FE models, with prediction errors of less than 10%. The experimental validation of the models was performed through the machining of thin-walled components. The predictions of the developed models were found to be in excellent agreement with the measured dynamic responses. The developed models meet the conflicting requirements of prediction accuracy and computational efficiency. In addition, a novel methodology was proposed and validated to compensate for the effect of the dynamics of the force measurement system.

Résumé

Le fraisage des structures aérospatiales à parois minces est un processus critique dû à la flexibilité élevée de la pièce. Les modèles disponibles pour la prévision de l'effet du système de fixation sur la réponse dynamique de la pièce sont basés sur des méthodes numériques très lentes et n'arrivent pas à représenter les cas pratiques du fraisage des structures à parois minces. Basé sur une analyse des composants structurels typiques produits dans l'industrie aérospatiale, un élément généralisé de base avec la forme d'une poche asymétrique, a été identifié pour représenter la réponse dynamique de ces composants. En conséquence, deux modèles dynamiques efficaces ont été développés pour prévoir la réponse dynamique des structures aérospatiales types à parois minces. Ces modèles ont été formulés en utilisant les méthodes de Rayleigh et Rayleigh-Ritz.

Dans le premier modèle, les réponses dynamiques des structures de poches multiples à parois minces sont représentées par des plaques avec des ressorts de torsion et de translation. Une méthodologie a été proposée et mise en application pour calibrer la rigidité des ressorts en utilisant les algorithmes génétiques. Dans le deuxième modèle, la réponse dynamique d'une poche en 3D est représentée par une plaque équivalente de multi-travées en 2D. À travers une étude approfondie du fraisage des structures à parois minces, une nouvelle formulation a été développée pour représenter le changement continu de l'épaisseur de la pièce durant l'usinage. Deux formulations, basées sur des contraintes holonomes et des ressorts avec des rigidités finies, ont été développées et mises en application pour simuler l'effet des supports parfaitement rigides et déformables.

Tous les modèles et les formulations développés ont été validés numériquement et expérimentalement pour des pièces de géométries différentes et divers types d'efforts. Ces modèles ont réduit le temps de calcul de un à deux ordres de grandeur, en comparaison avec des modèles des éléments finis. Les erreurs de prévision étaient moins de 10%. La validation expérimentale des modèles a été effectuée par l'usinage des pièces à parois minces. Les prévisions des modèles développés sont en parfait accord avec les réponses dynamiques mesurées. Les modèles développés répondent aux exigences contradictoires de l'exactitude de prévision et de l'efficacité du calcul. En outre, une méthodologie originale a été proposée et validée pour compenser l'effet de la dynamique du système de mesure des efforts.

Claims of Originality

1. A generalized unit-element with the form of an asymmetric pocket was extracted from typical thin-walled aerospace structures. This unit-element allows the development of simplified models for the analysis of the dynamic response of complex thin-walled structures.

2. A new generalized model was developed and formulated based on an off-line calibration of a plate with torsional and translational springs using Genetic Algorithms, to represent the dynamics of multi-pocket thin-walled structures. This simplified model allows for the reduction of the computational time by at least one order of magnitude when compared to FE models, with prediction errors less than 5%.

3. A model was developed and formulated for the representation of the dynamics of a 3D pocket using a 2D semi-analytical multi-span plate model. For this model, a new set of trial functions were developed for the approximation of the multi-span plate mode shapes. This model allows for the prediction of the dynamic responses of various types of thin-walled aerospace structures with at least one order of magnitude reduction in computation time, compared to FE models, and with prediction errors less than 6%.

4. A new formulation was proposed and implemented to simulate possible cases for the change of the thickness during milling of thin-walled pockets. This formulation was validated through FE models and experimental machining tests. Excellent agreement in the results was achieved with errors less than 10%.

5. An integrated model for the analysis of the effect of the fixture layout on the dynamics of thin-walled structures was developed while taking into account the continuous change of thickness of the workpiece and the effect of rigid and deformable fixture supports. This integrated model was validated numerically through FE models and experimentally through machining tests of thin-walled structures.

6. A novel methodology was developed for the compensation of the effect of the dynamics of the force measurement system, as well as the dynamics of the workpiece.

Acknowledgment

With all gratitude and respect, I would like to thank my supervisors Dr. Helmi Attia and Dr. József Kövecses for their great support and guidance throughout this research. They were always available for me for advice regarding technical and non-technical matters.

In addition, I would like to thank deeply Dr. Helmi Attia who always encourages me, cares for me, and provides me with his experience and his knowledge. In addition, he gave me a great opportunity to perform my PhD experiments at the National Research Council of Canada at the Aerospace Manufacturing Technology Centre and to interact with an amazing team of research officers.

A special thanks goes to all the research officers in the machining group at AMTC, NRC for their support and cooperation, especially Dr. Nejah Tounsi, for his feedback on my PhD work and Nick De Palma for his help in performing the experiments.

I would like to express my gratitude for the National Research Council of Canada for allowing me to use their facilities to perform the experiments. I would like to thank FQRNT (Le Fonds Quebecois de La Recherche sur la Nature et les Technologies) for financially supporting my research.

I would like to tell all my family that they were a great support for me. A very sincere and special thanks goes to my father Adel, my mother Sylvia, and my brother Hakim who have always been there for me throughout my PhD work and my whole life. I wish that one day I could offer them a small portion of what they always give me.

Last but certainly not least, I would like to thank my wife Diana who has always supported me with amazing patience and great love.

Table of Contents

List of Figures

List of Tables

Nomenclature

Capital letter symbols

A_b	Area of a beam (m^2)
A_{ba}	Area of the a^{th} span of a multi-span beam (m^2)
A_f	Maximum amplitude of the response at a given point using the FE model (μm)
A_l	Area of application of the load for a rectangular plate (m^2)
A_{max}	Maximum amplitude of the response at point $\mathrm{P_B}$ using the FE model (μm)
A_p	Maximum amplitude of the response at a given point using the proposed model (μm)
$\boldsymbol{D}$	Matrix for the transformation from $\boldsymbol{q}$ to $\boldsymbol{\phi}$
D_a	Flexural rigidity of the a^{th} span of a plate (N·m)
$D^{(a,b)}$	Flexural rigidity of span (a,b) of the 5× 3 span plate (N·m)
D_E	Flexural rigidity of a plate (N·m)
E	Young's Modulus (Pa)
F_D	Discrete Fourier Transform (DFT) of the force measured by the dynamometer (N)
F_{in}	DFT of the input (applied) force to the dynamometer (N)
F_m	DFT of the measured force during the machining of the side of the pocket (N)
F_o	DFT of the predicted force using the transfer functions T_{sys} (N)
F_s	DFT of the idealized force for the machining of the side of the pocket (N)
$\boldsymbol{F_u}$	Vector of generalized forces for the u^{th} spring (N)
F_{ur}	Generalized force for the u^{th} spring (N)
$\boldsymbol{G}$	Constraints Jacobian matrix
$\boldsymbol{G_m}$	Matrix for the transformation from $\boldsymbol{q_e}$ to $\boldsymbol{q_o}$
I	Second moment of area of a beam (m^4)
I_a	Second moment of area of the a^{th} span of a multi-span beam (m^4)
$\boldsymbol{K}$	Stiffness matrix
$\boldsymbol{K_c}$	Constrained stiffness matrix
K_{xl}	Stiffness per unit length of a translational spring at $x = x_l$ ($\mathrm{N/m^2}$)
K_{xo}	Stiffness per unit length of a translational spring at $x = x_0$ ($\mathrm{N/m^2}$)

K_{yl}	Stiffness per unit length of a translational spring at $y = y_l$ (N/m^2)
K_{yo}	Stiffness per unit length of a translational spring at $y = y_0$ (N/m^2)
$\boldsymbol{M}$	Mass matrix
$\boldsymbol{M_c}$	Constrained mass matrix
P_x	Approximate maximum potential energy of the springs at $x = 0, x_l$ (J)
P_y	Approximate maximum potential energy of the springs at $y = 0, y_l$ (J)
$\overline{P}_{xij}$	Maximum potential energy of the springs at $x = 0, x_l$ for $\overline{W}_{ij}$ (J)
$\overline{P}_{yij}$	Maximum potential energy of the springs at $y = 0, y_l$ for $\overline{W}_{ij}$(J)
$\boldsymbol{Q}$	Vector of generalized forces Q_r
Q_r	Generalized forces of a plate
R	Ratio of the new thickness to the original thickness for the adjacent side (m/m)
R_{xl}	Stiffness per unit length of a rotational spring at $x = x_l$ (N/rad·m)
R_{xo}	Stiffness per unit length of a rotational spring at $x = x_0$ (N/rad·m)
R_{yl}	Stiffness per unit length of a rotational spring at $y = y_l$ (N/rad·m)
R_{yo}	Stiffness per unit length of a rotational spring at $y = y_0$ (N/rad·m)
T	Kinetic energy (J)
T^*	Reference kinetic energy (J·s)
T_{max}	Maximum kinetic energy (J)
T_F	Transfer function between the input force to the dynamometer and the measured force (N/N)
T_{sys}	Transfer function between the applied force on the experimental setup and the measured force (N/N)
T_w	Transfer function for the two degree of freedom system representing the workpiece and the fixture dynamics
T_x	Transfer function between the input force and the output displacement of the dynamometer (m/N)
$\overline{T}_{ij}$	Reference kinetic energy for the trial function $\overline{W}_{ij}$ (J·s)
U	Strain energy of a rectangular plate (J)

$\boldsymbol{U_c}$	Modal matrix for the rigidly constrained system
$\boldsymbol{U_m}$	Modal matrix
U_{max}	Maximum strain energy (J)
$\overline{U}_{ij}$	Maximum strain energy for $\overline{W}_{ij}$ (J)
V	Potential energy (J)
V_{max}	Maximum potential energy (J)
W	Maximum displacement of a rectangular plate (m)
W_r	Exact mode shapes of a rectangular plate
$\overline{\boldsymbol{W}}$	Vector of trial functions $\overline{W}_{ij}$
$\overline{W}_{ij}$	Trial function for a rectangular plate
$\overline{W}_{ij}^{(a)}$	Trial function for the a^{th} span of a plate
$\overline{W}_{ij}^{(a,b)}$	Trial function for span (a, b) of a 5×3 span plate
$\tilde{\boldsymbol{W}}$	Vector of trial functions $\tilde{W}_r$
$\tilde{W}_r$	Approximate mode shape of a rectangular plate (trial function)
$X^{(a)}$	Solution of the BVP [1] for the a^{th} span of a beam in the x-direction
$X_i^{(a)}$	i^{th} mode shape of the a^{th} span of a beam in the x-direction
$\overline{X}_i$	Trial function in the x-direction for a plate
$\overline{X}_i^{(a)}$	Trial function in the x-direction for the a^{th} span of a plate
Y	Solution of the BVP for a single-span clamped-free beam in the y-direction
Y_j	j^{th} mode shape of a clamped-free beam
$Y^{(b)}$	Solution of the BVP for the b^{th} span of a beam in the y-direction
$Y_j^{(b)}$	j^{th} mode shape of the b^{th} span of a beam in the y-direction
$\overline{Y}_j$	Trial function in the y-direction for a rectangular plate
$\overline{Y}_j^{(a)}$	Trial function in the y-direction for the a^{th} span of a plate
$\overline{Y}_j^{(a,b)}$	Trial function in the y-direction for span (a, b) of a 5×3 span plate
Z	Solution of the BVP for a beam
Z_r	r^{th} mode shape of a beam with torsional and translational springs

[1] BVP: Boundary-value problem

Small letter symbols

c_1	First damper for a two degree of freedom system (N·m/s)
c_2	Second damper for a two degree of freedom system (N·m/s)
c_D	Damping factor of the dynamometer (N·m/s)
$\boldsymbol{d}$	Array for the displacement response of the pocket-side (μm)
$\tilde{\boldsymbol{d}}$	Array for the displacement response of the plate (μm)
d_c	Maximum of the calculated displacements at the position of the r^{th} probe (μm)
d_m	Maximum of the measured displacements of the r^{th} probe (μm)
d_p	Tool-path depth or the position of the tool relative to the free edge of the side (mm)
d_r	Maximum amplitude of the displacement of a pocket without fixture layout (μm)
d_y	Axial depth of cut (mm)
d_z	Radial depth of cut (mm)
d_w	Maximum amplitude of the displacement of a pocket with fixture layout (μm)
f	Applied force (N)
f_c	Compensated force (N)
f_p	Force applied on a rectangular plate (N)
f_u	Force of the u^{th} spring (N)
h	Thickness of a rectangular plate (m)
h_a	Thickness of the a^{th} span of a plate (m)
h_n	New thickness of the strip representing the change of thickness (m)
h_o	Original thickness of the plate or the pocket-side (m)
$h_p^{(a,b)}$	Thickness of span (a,b) of a 5× 3 span plate (m)
h_{xa}	Thickness of the a^{th} span of a beam in the x-direction (m)
h_y	Thickness of a clamped-free beam in the y-direction (m)
h_{yb}	Thickness of the b^{th} span of a beam in the y-direction (m)
k	Number of constraints or springs on a rectangular plate
k_1	Stiffness of the first spring for a two degree of freedom system (N/m)

k_2	Stiffness of the second spring for a two degree of freedom system (N/m)
k_D	Stiffness of the spring representing the dynamometer (N/m)
k_l	Stiffness of a translational spring at $u = u_l$ (N/m)
k_o	Stiffness of a translational spring at $u = u_o$ (N/m)
k_u	Stiffness of the u^{th} spring (N/m)
l_x	Length of a rectangular plate in the x-direction (m)
l_y	Length of a rectangular plate in the y-direction (m)
l_u	Length of a beam (m)
m	Mass of a rectangular plate per unit area (kg/m^2)
m_1	First mass for a two degree of freedom system (kg)
m_2	Second mass for a two degree of freedom system (kg)
m_a	Mass of a the a^{th} span of a rectangular plate per unit area (kg/m^2)
m_D	Mass of the dynamometer (kg)
n	Number of included mode shapes
p_{cu}	Location of the u^{th} constrained point
$\boldsymbol{q}$	Vector of generalized coordinates q_r
$\boldsymbol{q_c}$	Eigenvectors for the discretized equations of a plate with internal springs
$\boldsymbol{q_e}$	Vector of dependent coordinates
$\boldsymbol{q_o}$	Vector of independent coordinates
q_r	Generalized coordinates for the approximate mode shapes of a plate
$\bar{\boldsymbol{q}}$	Eigenvectors
r_c	Original stiffness of the calibrated rotational springs (N/rad)
r_l	Stiffness of a rotational spring at $u = u_l$ (N/rad)
r_n	New stiffness of the calibrated rotational springs (N/rad)
r_o	Stiffness of a rotational spring at $u = u_o$ (N/rad)
s_x	Total number of spans of the plate or the beam in the x-direction
s_y	Total number of spans of the plate or the beam in the y-direction
t	Time variable (s)

x	Spatial coordinate for the x-direction
x_a, x_{a-1}	Coordinates of the a^{th} span of a plate
x_u	Location of the u^{th} spring in the x-direction
y	Spatial coordinate for the y-direction
y_u	Location of the u^{th} spring in the y-direction
u	Spatial coordinate of a beam
u_a	Actual displacement of a pocket side (μm)
u_c	Measured displacement by the probe using the calibration curve (μm)
w	Transverse displacement of a rectangular plate (m)
$w^{(a)}$	Transverse displacement of the a^{th} span of a plate (m)
$w^{(a,b)}$	Transverse displacement of span (a,b) for a 5×3 span plate (m)
$\tilde{w}$	Approximate transverse displacement of a rectangular plate (m)
w_c	Calculated displacement using the cutting forces of the machining experiments (μm)
z	Transverse displacement of a beam (m)
z_1	DFT of the displacement for the first mass of a two degree of freedom system (m)
z_2	DFT of the displacement for the second mass of a two degree of freedom system (m)
z_D	DFT of the displacement of the top face of the dynamometer (m)
$z_x^{(a)}$	Transverse displacement of the a^{th} span of the beam in the x-direction (m)

Greek symbols

β	Eigenvalue parameter for a beam (rad·s/m^4)
β_r	r^{th} Eigenvalue parameter for a beam (rad·s/m^4)
β_{xa}	Eigen-value parameter for the a^{th} span of the beam in the x-direction (rad·s/m^4)
β_y	Eigen-value parameter for a clamped-free beam in the y-direction (rad·s/m^4)
β_{yb}	Eigen-value parameter for the b^{th} span of a beam in the y-direction (rad·s/m^4)
β_{yj}	j^{th} eigenvalue parameter for a clamped-free beam in the y-direction (rad·s/m^4)
$\mathbf{\Gamma}$	Vector of generalized forces Γ_r
Γ_r	Generalized forces

$\boldsymbol{\gamma}$	Vector of modal coordinates γ_r
γ_r	Modal coordinates
δ_{rs}	Kronecher delta
ϵ	Percentage error between the proposed model and the FE model
ϵ_c	Percentage error between the measured and predicted displacements for a given probe
ε_1	Measurement error during the impact test due to the inaccuracy of the probe (μm)
ε_2	Measurement error during impact tests due to the inaccuracy of the force sensor (μm)
ε_3	Measurement error during impact tests due to the uncertainty of the location of the load (μm)
ε_f	Total force measurement during machining tests (%)
ε_{f1}	Measurement error during machining tests due to dynamometer inaccuracies (μm)
ε_{f2}	Measurement error during machining tests due to the dynamics of the dynamometer-workpiece setup (μm)
ε_c	Total force measurement error on the calculated response during machining(%)
ε_m	Total probe measurement error on the measured response during machining(μm)
ε_{p1}	Measurement error during machining tests due to probe inaccuracies (μm)
ε_{p2}	Measurement error during machining tests due to probe holder dynamics (μm)
ε_t	Total measurement error during the impact test (μm)
η_r	Generalized modal coordinates for the exact mode shapes
Θ	Time-dependent function for the transverse vibration of a beam
θ	Time-dependent function for the transverse vibration of a beam
λ	Eigen-value parameter
ν	Poisson's ratio
ρ	Density (kg/m^3)
σ_u	Standard deviation for the calibration of the proximity probe sensors (μm)
$\boldsymbol{\Phi_x}^{(a)}$	Transfer matrix between the coefficients of spans $a+1$ and a for the beam in the x-direction

$\boldsymbol{\Phi_y}^{(b)}$	Transfer matrix between the coefficients of spans $b+1$ and b for the beam in the y-direction
$\boldsymbol{\Phi_t}$	Total transfer matrix for the beam in the y-direction
$\boldsymbol{\phi}$	Vector of minimum set of generalized coordinates
Ψ	Deviation parameter for the effect of the fixture layout
ψ	Objective function for the calibration of the stiffness of the springs for the GSSP model
ψ_e	Objective function for the identification of the parameters of the transfer function T_w
Ω	Time-dependent harmonic function
ω	Natural frequency of a rectangular plate (rad/s)
ω_s	Frequency at which the amplitude of the DFT of the measured forces has a peak (rad/s)
ω_u	Natural frequency of a beam (rad/s)
ω_{ur}	r^{th} natural frequency of a beam (rad/s)
ω_x	Natural frequency of a multi-span beam in the x-direction (rad/s)
ω_y	Natural frequency of a beam in the y-direction (rad/s)
$\overline{\omega}_{ij}$	Approximate natural frequency of a plate for the trial function $\overline{W}_{ij}$ (rad/s)
$\tilde{\omega}$	Approximate natural frequencies of a plate (rad/s)
$\tilde{\omega}_r$	Approximate natural frequency of a plate for the trial function $\tilde{W}_r$ (rad/s)

Subscripts

a	Index for the beam or the plate spans in the x-direction
b	Index for the beam or the plate spans in the y-direction
i	Index for the trial functions in the x-direction
j	Index for the trial functions in the y-direction

Abbreviations

CoT	Change of Thickness formulation

CS	Corner Strip for the change of thickness
DFT	Discrete Fourier Transform
FE	Finite Element
FEM	Finite Element Method
FFT	Fast Fourier Transform
FSS	Finite Stiffness Support formulation
GSSP	Generalized Single-Span Plate model
HS	Horizontal Strip for the change of thickness
LS	L-shaped Strip for the change of thickness
MSP	Multi-Span Plate model
PRS	Perfectly Rigid Support formulation
VS	Vertical Strip for the change of thickness

Chapter 1

Introduction

1.1 Introduction

One of the challenging manufacturing processes in the aerospace industry is the machining of the thin-walled structural components that are assembled into the load-carrying members such as the wing and the vertical and horizontal stabilizers. The load-carrying structures are composed of three main components including the skin, the spar and the rib. The wing, for example, has along its length two beams facing each other, which are called the front and rear spars. These spars are connected by ribs and covered by the skin, which gives the aerodynamic shape of the wing while distributing the load on the ribs and the spars. All of these components (rib, spar, and skin) are composed of multiple pockets in order to reduce their weight, while maintaining their stiffness. An illustrative 3D sketch of a spar and a rib is shown in Fig. 1.1. These components are initially rolled or forged and then machined. High-speed multiple-axis milling is a commonly used machining process to produce the final shape of these complex monolithic structural aerospace components. The machining accuracy depends, in general, on the thermal deformations and the cutting temperatures, the selection of the tool-path, the tool material and design, the tool wear, the workpiece material, and the dynamics of the tool, the workpiece and the fixture.

For the machining of thin-walled components, the dynamics of the system is a major factor that greatly affects the accuracy and the efficiency of the milling process. The non-linearity of the system is demonstrated by the coupling between the cutting forces and the dynamics of the system, in which the cutting forces are both affecting and being affected by

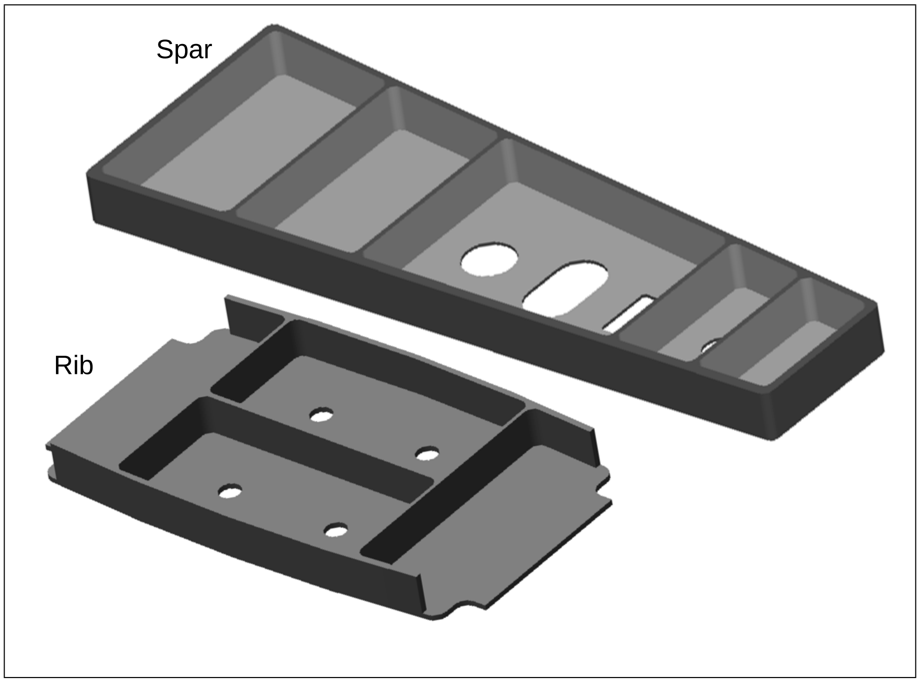

Figure 1.1: Illustrative 3D sketch of an aerospace structural component

the system dynamics. This is compounded by the continuous change in the dynamics of the workpiece-tool system during machining from rigid-flexible to flexible-rigid system.

1.2 Motivation

In the aerospace industry, the machined thin-walled monolithic structural elements has to meet very tight requirements for the tolerances (up to ±125 μm), and the surface quality (0.4-0.8 μm Ra) given that the walls are very thin (1.5 mm to 4 mm) and the parts are considerably large (10 m long and 0.1 m high). Machining is considered as the last major process (before assembly) for these components. Dimensional errors and damaged surfaces lead to the scraping of the whole workpiece thus costing money and time of both the machining process and all the precedent processes. In order to reduce cost and scrap, a "first-time-correct" approach is currently targeted by the aerospace industry. Presently, the designers rely on very conservative guidelines for the selection of the cutting parameters and the design of the fixture, which substantially reduces productivity.

In order to meet the cost, productivity and quality requirements, one needs to control the machining process by determining the effect of the dynamics of the workpiece, the tool, the machine and the fixture on the final part quality (dimensional errors and surface integrity). If the interactions between the machine, the tool, the workpiece and the fixture are predicted accurately, then the final part quality can be determined without the need to perform actual machining tests. This will certainly save a considerable amount of time, money and material and will help reach a "scrap-free" production.

1.3 Scope and Terminal Objective of the Research

To define the scope of the research, one has to identify the essential elements that affect the dynamics of the system. An overview of the different elements of the dynamics of the cutting process is shown in Fig. 1.2. Three main sub-systems have to be considered and they include the fixture-workpiece, the workpiece-tool, and the tool-machine systems.

The dynamics of the fixture-workpiece includes the analysis of the fixture (static and dynamic deformations of its components) and the effect of the fixture on the displacement, deformation and the vibration of the workpiece. This requires the modelling of the effect of the fixture layout (number, location and stiffness of the supports) and the modelling of the contact (linear or non-linear) between the workpiece and the fixture. The workpiece dynamics includes the rigid-body motion and the vibrations of the workpiece as a continuous parameter system. The dynamics of the workpiece-tool system includes, in addition to the dynamics of the workpiece, the study of the static deformation and the dynamic vibrations of the tool. The dynamics of the tool-machine includes the analysis of the dynamic response of the milling machine (the column, the spindle and the tool holder), and the tool.

For the milling of thin-walled structures, the following has to be considered in defining the scope of the research:

1. The vibration of the workpiece, as a continuous parameter system, will be more dominant than the rigid-body motion. Thus, it is more important to focus on the vibration due to the flexibility of the workpiece.

2. The workpiece deformation is mainly affected by the number, location and stiffness

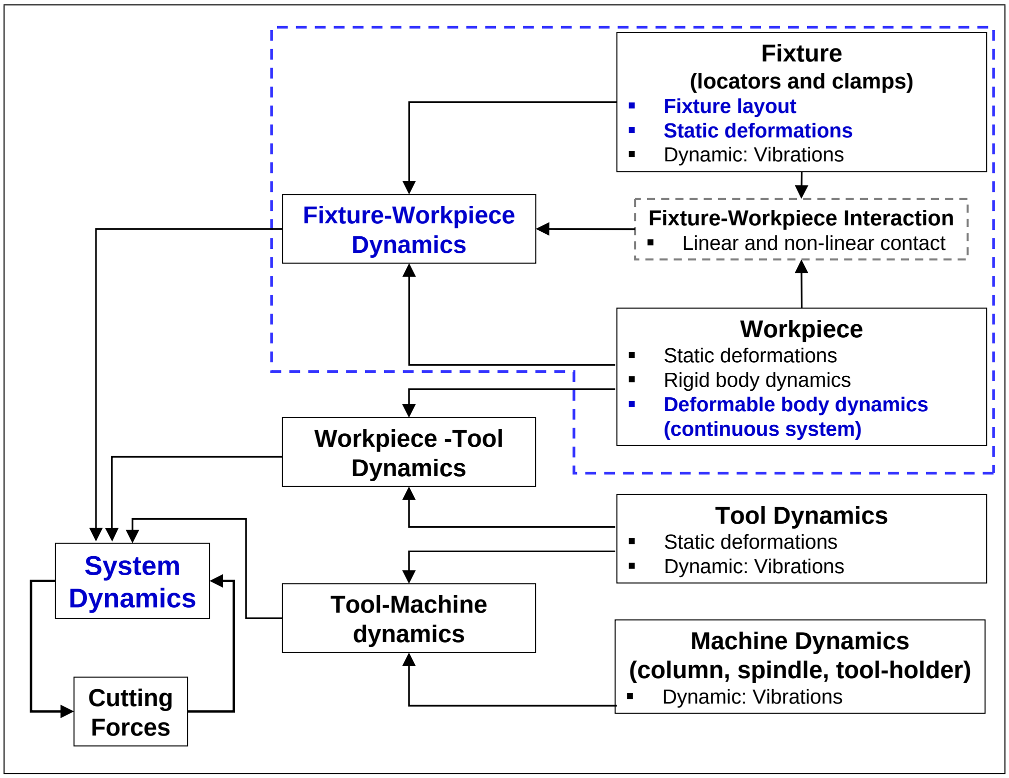

Figure 1.2: Illustration for the elements of the system dynamics in machining

of the fixture supports. The contact between the fixture elements and the workpiece affect mostly the rigid-body motion. The contact has less effect on the deformation of the workpiece away from the contact region. Thus, for the analysis of the deformation of the workpiece, a rigid contact could be assumed between the fixture supports and the workpiece.

3. The machining of thin-walled structures is considered as a finishing process. It is preceded by roughing processes. During the roughing process, the tool dynamics is more dominant since the workpiece can be regarded as rigid. However, in the finishing stage of the thin-walled structures, the dynamics of the workpiece is more dominant and the tool can be considered as a rigid load application element.

4. When comparing the finishing to roughing in machining, the forces in the former are relatively low and will result in very low amplitudes of vibrations for the machine structure. Accordingly, the dynamics of the machine, which is relatively rigid, could be ignored.

Thus, for the analysis of fixtures for the milling off thin-walled structures, the focus is on the fixture-workpiece dynamics. The elements of the fixture-workpiece dynamics that will be considered in this research work are highlighted in blue in Fig. 1.2. The objective is to predict the dynamic response of the flexible workpiece while including the effect of the fixture layout and the effect of the deformation of the fixture locators. With this objective in mind, one has to realize that this should later on help to optimally design the fixture layout. In addition, the prediction of the dynamic response would be integrated to the cutting force models in order to optimize the cutting parameters and the machining tool-path. Both the optimization of the fixture layouts and the integration of the dynamic response in the cutting force models will require the evaluation of a substantially large number of cases (hundreds and thousands) for a given workpiece. One of the main challenges in developing a dynamic model for the workpiece and the fixture is the fact that the shape of the workpiece continuously changes during machining. For such problem, available modelling techniques (e.g. Finite Element Methods) are computationally extensive.

The terminal objective of this research is to develop a computationally efficient dynamic model to predict accurately the dynamic response of thin-walled aerospace structures during milling while taking into account the continuous change in thickness of the workpiece and the effect of the fixture layout in terms of the number, the position and the stiffness of the locators. The detailed objectives of this research program will be presented in Chapter 2, section 2.6.

1.4 Thesis Outline

The thesis outline is as follows:

1. Chapter one briefly introduced the research topic and highlighted the motivation, the scope and the terminal objectives of the research.

2. Chapter two presents a review of the literature related to the fixture design in the machining of rigid and flexible workpieces, the available dynamic and mechanistic force models for the milling of thin-walled structures, and the different model order reduction

techniques for FE models. According to the analysis of the existing methods in the open literature, the detailed objectives of the research will be established.

3. Chapter three describes the main conceptual developments of the research. This includes the introduction of a generalized unit-element and the conceptual development for two models for the representation of the dynamic response of the unit-element. The first and second models are referred to as the Generalized Single-Span Plate (GSSP) and the Multi-Span Plate (MSP) models, respectively. In addition, the change of thickness during milling of thin-walled structure will be analyzed. Finally, a review of plate dynamics will be presented.

4. Chapter four will detail the mathematical formulations for the different models. It will start with a description of Rayleigh's energy and the Rayleigh-Ritz methods. Then the mathematical formulations for the GSSP and the MSP models will be presented. This will be followed by the developed formulation for the change of thickness of the workpiece and the formulations to simulate the effect of the fixture supports.

5. Chapter five will present the validation for the GSSP and the MSP models through FE models of pockets and through experimental impact tests. This will be followed by the validation of the change of thickness formulation and the different formulations for the effect of the fixture supports.

6. Chapter six will present the experimental validation of the developed models through the machining of an actual thin-walled workpiece. This will include the description of the experiment, the analysis and the modelling of the dynamics of the measurement system, the error analysis and the discussion of the obtained results.

7. Chapter seven summarizes the developments and the results of the thesis and highlights the potential areas for future research work.

8. Three appendices are included for additional mathematical formulations related to chapters four and six.

Chapter 2

Literature Review

2.1 Introduction

In the last two decades, the analysis of fixtures for machining applications has gained special attention due to its effects on the productivity, the final part quality, and the cost. To develop new models for the design of fixtures for the milling of thin-walled structures, an analysis of the research available in the literature had to be performed by reviewing three main areas. The first area deals with the existing methods and models for the analysis of the fixtures for machining in general and more specifically, for milling of thin-walled structures. The second area relates to the available models for the dynamics of the milling of flexible structures. In these two areas, the dynamics of thin-walled structures is mainly determined using Finite Element models. These models are computationally prohibitive and do not satisfy the computational requirements for the design and optimization of fixture layouts. Consequently, the third area focuses on available Model-Order Reduction (MOR) techniques of Finite Element Methods (FEM). Based on the review of these areas, the limitations of existing models will be identified, thus putting the objectives of the research in perspective.

2.2 Fixture Design for Machining Applications

Careful examination of the current practice, which included interviewing experienced fixture designers, shows that the fixture design relies on general guidelines and the tool designer's experience, rather than systematic analysis. Although many models exist for the design and the evaluation of the fixtures, they are usually computationally demanding and ignore crucial practical aspects of the machining fixtures. To study the fixture design, one has to analyze the different components of the fixture, their role and the possible sources of errors. A fixturing system consists mainly of a set of locators and clamps. Based on the review of the literature, the following set of design parameters affects the performance of the fixture and they include:

1. The shape and the material of the locators and clamps, which affect the compliance of the fixture components.
2. The number and position of the locators and clamps, which are referred to as the fixture layout.
3. The clamping force, the sequence of part loading, the machining tool path, and the cutting forces.
4. The workpiece material and shape, which affect its dynamic characteristics given that the workpiece shape is continuously changing due to the material removal action.

The fixture role is to properly position and maintain the location of the workpiece relative to some datum points. By analyzing a fixture design, one can determine the errors in the positioning of the workpiece relative to a fixed reference frame. For the sake of this review, the errors are categorized as follows:

1. Static errors for a rigid workpiece: This type of errors is due to violation of the workpiece stability conditions, the positioning errors at the initial setup of the workpiece, and the static deformation of the fixture components.
2. Static errors for a flexible workpiece: They include, in addition to the static errors for a rigid workpiece, the deflection of the workpiece-fixture system.
3. Dynamic errors for a rigid workpiece: They include both the stability and the rigid-body dynamics of the workpiece considering the compliance of the contact between

the workpiece and the fixture and the dynamic vibrations of the compliant fixture components.

4. Dynamic errors for a flexible workpiece: They include the dynamic deformations of the flexible (thin-walled) workpiece, in addition to the dynamic errors for a rigid workpiece.

The different system parameters for the design of fixture and the sources of errors are shown in Fig 2.1. For a given source of error (e.g. workpiece stability), the system parameters that affect it are indicated by a circle. In the following subsections, a review will be presented for the different models developed to predict each category of errors. An additional subsection will be included to present briefly the concept of Computer Aided Fixture Design (CAFD) and the different optimization models for the fixture design.

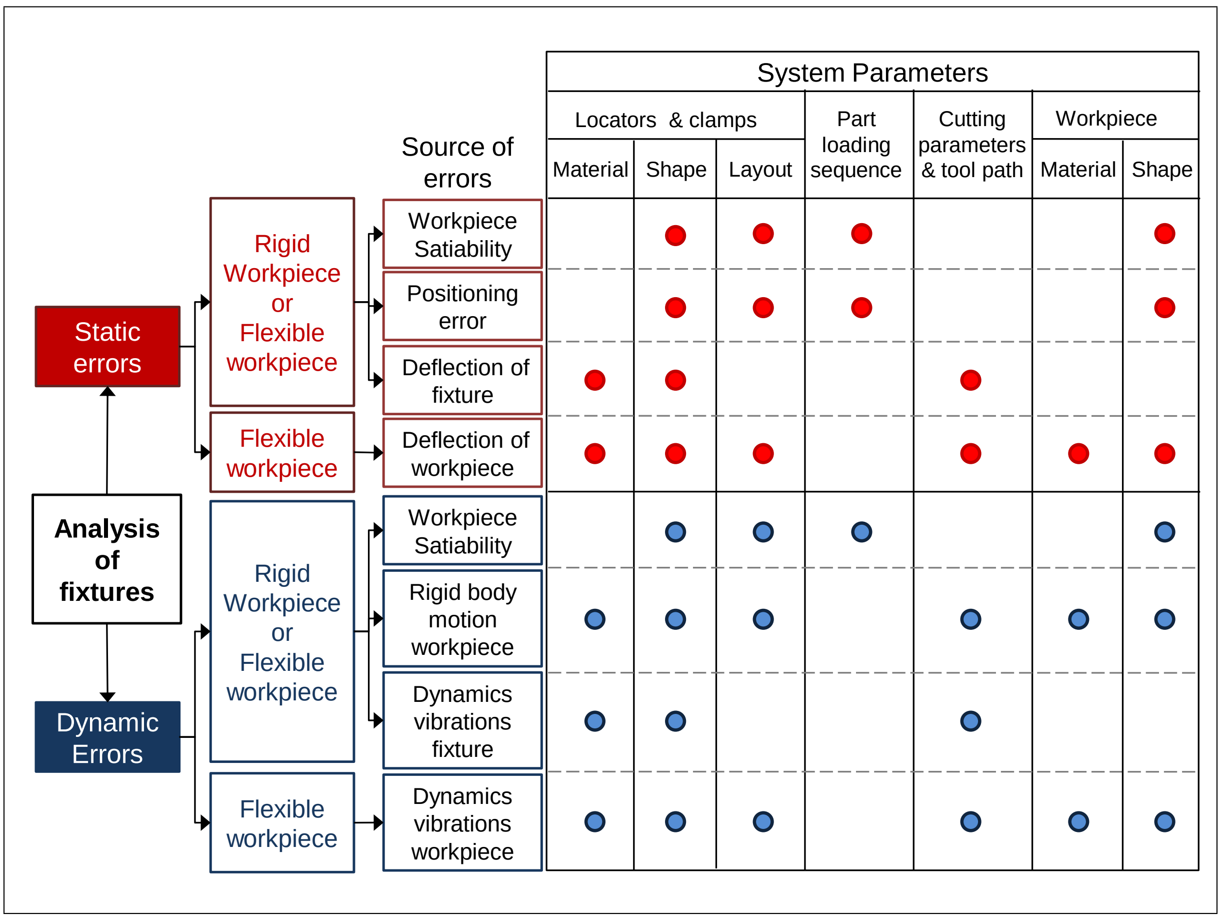

Figure 2.1: Representation of the design parameters of the workpiece-fixture system, the types of analysis and the different criteria for the evaluation of the fixture performance

2.2.1 Static Analysis of Fixtures with a Rigid Workpiece

To properly locate a workpiece, the rule of 3:2:1 is commonly used. In brief, this rule states that on 3 perpendicular surfaces, three, two and one datum points have to be constrained on the workpiece in order to properly locate it. In most of the research work, the fixture layout is applied according to this rule. As mentioned previously, the objective of the static error analysis of a rigid workpiece could be either to determine the positioning errors or the stability of the workpiece-fixture system.

One source of positioning errors is the contact compliance between the workpiece and the fixture. Shawki and Abd-Aal [1] investigated the effect of the contact compliance on the positioning errors by performing an experimental study to characterize the effect of the elastic contact between different types of locators and the workpiece. Li and Melkote [2] developed an analytical model to relate the effect of the contact compliance and the clamping forces on the positioning errors and the stability of the workpiece-fixture system. They used a non-linear optimization scheme to select the optimum positions of the locators and the clamps. They also developed a model to determine the optimum clamping force that reduces the positioning errors, taking into account the non-linear contact between the workpiece and the fixture clamps [3]. A more sophisticated model was developed by Yu and Tong [4] to include the surface properties (curvature and scale factors) to model the contact between the workpiece and the locator and its effect on the positioning errors. In this model, the kinematics of the positioning errors was based on a velocity formulation of the constrained contact.

Another source of positioning errors is the geometrical errors of the locators or the workpiece contact surfaces. Batyrov [5] studied the effect of the dimensional errors of the fixture supports on the positioning errors. He also focused on the effect of the clamping force on the shifting of the workpiece as the major error in positioning it. Bazrov and Sorokin [6] found that the clamping sequence affects the errors in the mounting of the workpiece due to translation, while the position of the supports affected the angular deviations. Mittal *et al.* [7] found that the effect of the clamping sequence is less than the clamping position. Estrems *et al.* [8] proposed a methodology to account for the positioning errors taking into account the tolerances on the dimensions of the fixture and workpiece surfaces. Marin and Ferreira [9] solved the inverse problem of determining the acceptable error in the geometry of the locators and clamps that produces a part within the allowable positional and surface profile tolerances. Qin *et al.* [10] proposed a model and a set of corollaries to check the positioning errors due to manufacturing errors of the locators and the workpiece surfaces and setup errors.

The stability of the workpiece-fixture system is affected by the rigidity of the fixture components and the contact compliance. Shawki and Abd-Aal [11] performed an experimental study to compare the rigidity of different clamping elements during steady loads. It was shown that the rigidity of the workpiece-fixture system diminishes with the increase of the number of contact points. De Sam and King [12] developed a model for the automation of the fixture design of rigid workpieces based on static equilibrium while taking into account different machining operations and the part tolerances.

Screw theory, in which the applied loads are described by a rotation about an axis and a translation along the same axis, has often been used to determine the stability condition of the system. De Meter [13] included the effect of the frictionless and the friction contact in the static analysis of the workpiece-fixture to evaluate the total restraint of the system using screw theory. Sayeed and De Meter [14] developed a software package for the design of fixtures based on the stability of the rigid workpiece using screw theory and kinematic constraint analysis. The analysis included the effect of the friction at the locator-workpiece interface. A tool-path analysis was included to detect collisions with the fixture elements. Li *et al.* [15] looked at the effect of large contact areas on the static equilibrium of the workpiece-fixture system. Wang and Pelinescu [16] used the minimum norm solution to determine a quick estimate of the contact forces between the fixture and the workpiece.

2.2.2 Static Analysis of Fixtures with a Compliant Workpiece

The compliance of the workpiece, in addition to the compliance of the fixture and the fixture-workpiece contact, play an important role in evaluating the performance of the fixture. They can affect the positioning errors, the stability of the workpiece-fixture system and the deflection of the workpiece.

The positioning errors for a compliant workpiece are mainly controlled by the local deformation at the workpiece-fixture contact region. Satyanarayana and Melkote [17] studied the effect of the frictional contact of the spherical-planar and the planar-planar locators' contact geometries. It was shown that for thin-walled structures, when the thickness of the wall is decreased, the contribution of the deflection due to contact compliance is small when compared to the deflection of the workpiece. Thus, for thin-walled structures, the contact between the workpiece and the locators could be assumed rigid, relative to the workpiece flexibility. Melkote and Siebenaler [18] investigated the effect of the fixture compliance on the static deformation of the workpiece using a FE model. In their model, they investigated the effect of the friction on the workpiece local deformation. It was found that 98% of the system deformation could be captured when the workpiece and the fixture tip compliances are included. The results also showed that the change in the friction coefficient had a small effect on the workpiece deformation.

The FEM is commonly used to model the workpiece and sometimes the fixture compliance. The FE model developed in [19, 20], takes into account the fixture geometric errors, the contact geometry and its compliance, the bulk compliance of the workpiece, the compliance of the fixture, as well as the effect of clamping sequence, and the locator reaction forces on the positioning errors. In this model, the contact region on the workpiece was considered flexible, while the rest of the workpiece was assumed rigid. In addition, Qin *et al.* [21, 22] developed a model to check the optimal clamping sequence to minimize the positioning error, taking into account the contact forces, and the compliance of the fixture, the workpiece and the workpiece-fixture contact.

The difference between the stability analysis for a rigid and a compliant workpiece is that the compliance of the workpiece affects the contact and clamping forces. Some researchers looked at determining the clamping force that will result in a stable system. A model was developed to determine the minimum clamping force to prevent slipping of the workpiece [23, 24]. The model was tested for both ramp loads and milling forces. It was shown that the clamp pre-loads are sensitive to the value of the friction coefficient at the contact. Sanchez *et al.* [25] developed a contact model based on evaluating the flexibility of the contact region of the workpiece and the fixture separately. Based on this model, valid clamping regions are identified by satisfying the form closure condition. Sanchez *et al.* [26] combined the studies performed in [8, 25] with a FE model of the static structural deformation in order to determine the total positioning error of the workpiece.

The flexility of the workpiece has a large effect on its machined surface quality and dimensions. Shaogang *et al.* [27] used a FE model of a thin-walled workpiece in order to optimize the location of the locators based on the predicted surface errors of the workpiece. The proposed methodology for selecting the initial layout of the locators was based on the evaluation of the point where the maximum deflection of the workpiece occurred. In this research, the optimization technique and the computational efficiency were not discussed. Ratchev *et al.* [28] proposed a methodology for combining the effect of fixture-contact and the deformation of the workpiece to predict the behaviour of the workpiece using FE models. Another model was developed by Liao and Hu [29, 30] using the FEM to model the effect of the contact, the clamping force, the sequence of part loading and the cutting forces on the deflection of the workpiece system.

Some research work was performed to implement different methods to decrease the computational time of FE models for fixture analysis. Gu *et al.* [31] extracted the flexibility influence coefficients from a FE model in order to determine the static deformations of the workpiece under a given cutting load and its effect on the surface flatness in face milling. The main advantage of using flexibility influence coefficient is the considerable reduction in computational time. Li [32] used FEM to model the workpiece-fixture system and included the contact compliance equation for spherical surfaces. The fixture and the workpiece compliances were formulated using the flexibility influence coefficient. Sayeed and De Meter [33, 34] implemented a mixed-integer programming to optimize the number and position of the locators to minimize the deformation of the workpiece at some candidate points. FEM was used to model the static deformation of the workpiece. In order to reduce the computational time, the output points were chosen at the position of the locators and the cutting tool and the static condensation method was implemented. It was shown that the use of the flexibility influence coefficient lead to considerable reduction in computational time. Similar to the work by Sayeed and De Meter [33, 34], Masset and Debongnie [35] looked at improving the computational efficiency of the FE model by reducing the number of output points to represent only the cutting region and by using flexibility influence coefficients. Their objective was to predict the deflection of the workpiece due to the clamping loads to be able to determine the final form errors on the machined surfaces.

All the previous models did not include the change of thickness due to the material removal action. Only Kaya and Ozturk [36] evaluated the effect of the contact friction between the workpiece and the locator and the effect of the material removal on the bulk deformation of the workpiece. The death element technique was used in order to reduce the computational time of the FE model. It was shown that as the shape of the workpiece changes, the initial configuration of the fixture layout is not optimal. In this model, only the bulk deformation of the workpiece was taken into account.

2.2.3 Dynamic Analysis of Fixtures with a Rigid Workpiece

The rigid body dynamics of the workpiece-fixture assembly plays an important role in evaluating the performance of the fixture especially when the dynamic cutting forces are considered. Most researchers focused on modelling the contact between the workpiece and the fixture in terms of non-linear behaviour, damping and stiffness characteristics.

Mittal *et al.* [7] analyzed the dynamics of the workpiece-fixture system as an assembly of rigid bodies with kinematic constraints and compliant components. All the constraints were holonomic and the contact between the workpiece and the fixture was represented as Hertzian contact of spherical surfaces. A simple model of a cubic workpiece was used for the validation. In this analysis, the effect of the moving cutting force, the position of the locators and clamps, the clamping forces and the sequence of part loading were taken into account. The change of weight and shape of the workpiece were ignored since the computational effort required for this problem was excessively high. It was found that the effect of the clamping sequence on the rigid body dynamics was less than the effect of the position of the clamps.

Hockenberger and De Meter [37, 38] developed a model for quasi-static and dynamic analysis of the workpiece displacement, taking into account the effect of the stick, slip and lift off at the contact regions using polynomial functions for the calculations of the forces at the contact. Yeh and Liou [39] developed a contact model based on Hertz theory while including the surface finish of the workpiece and the locators. This model was applied in a FE model of the workpiece and the frequency response was evaluated and compared to experimental results. Li and Melkote [40] developed a model to calculate the optimum clamping force while taking into account the contact forces between the workpiece and the fixture, and the rigid-body dynamics of the system. Behzadi and Arezoo [41] developed a model for the analysis of the workpiece and the fixture to describe the positioning error and the rigid body dynamics due to the contact compliance. The model investigated the effect of the fixture layout, the stiffness of the supports, and the clamping force. Fang *et al.* [42] included the effect of friction damping in the dynamic analysis of the workpiece-fixture system. A stability analysis was performed to generate the stability lobes while taking into account the effect of the clamping load. Deiab [43] studied the effect of the tribological aspects at the workpiece-fixture contact area on the dynamics of the system. Accordingly, a friction model was incorporated in the FE analysis to predict the dynamics of the workpiece-fixture system during face milling.

Most of the previous studies ignored the change of the workpiece shape due to the material removal action. In a slightly more comprehensive research, Deng [44] developed a model to describe the stability of the workpiece-fixture in terms of the static and the dynamic displacement while taking into account the contact between the fixture locators and the workpiece and the change in the dynamics of the workpiece due to the material removal action. The material removal was modelled using the solid modeller ACIS. The centre of gravity and the principal inertial axis of the workpiece were updated based on the change of the shape of the workpiece according to the planned tool-path. The stiffness matrix was derived in terms of the rigidity of the elements of the fixture. It was shown that the change of geometry and the mass of the workpiece have the largest effect on its dynamic response.

2.2.4 Dynamic Analysis of Fixtures with a Compliant Workpiece

A limited number of research work has focused on the dynamics of the workpiece-fixture system, while taking into account the vibrations due to the flexibility of thin-walled structures. To analyze the effect of fixturing on the dynamics of thin-walled structures, FE models were commonly used to cover various features that cannot be modelled analytically. Although, the FEM is an excellent analysis tool, the computational efficiency for such problems is relatively poor [45]. In some early investigations of this problem, Daimon *et al.* [46] proposed a general guideline for the selection of the supporting points. This guideline was based on the evaluation of the maximum compliance of the workpiece through experiments or FE modelling. Two main features were not treated in this study, namely the effect of the change of the workpiece thickness, and the computational efficiency of the FE model.

Chu *et al.* [47] developed a methodology for updating of the mass and stiffness matrices of the workpiece using experimental measurements and quadratic optimization. The purpose of this study was to develop an accurate FE model of the workpiece-fixture system. De Meter [45] used a FE model to evaluate the deformation of the workpiece due to external load assuming a rigid support and a rigid contact between the workpiece and the fixture. The computational efficiency was improved by selecting candidate points on the FE model and defining the stiffness matrix accordingly. The models did not take into account the material removal effect.

Recently, Rai and Xirouchakis [48] included a comprehensive analysis for the simulation of the milling process while taking into account the deflection of the workpiece and the fixture, the contact compliance, the thermal behaviour of the workpiece and the material removal action. The material removal was simulated by using the death-birth feature of the elements. A simplified model was used to simulate the cutting forces. In this model, the computational efficiency was very low due to the high complexity of the FE model. The validation of the model was presented for relatively thick-parts and thus the vibration was not representative of the vibration encountered in the machining of thin-walled workpieces. The minimum errors between the model and the measurements were greater than 15%. Moreover, during the validation, the dynamics of the measurement system, which substantially distorts the measured forces and displacements, especially during milling with small radial depths of cut, was not taken into account.

2.2.5 Computer-Aided Fixture Design and Fixture Optimization

In the last two decades, some effort has been directed towards the development of Computer-Aided Fixture Design (CAFD) software packages. The main idea here is to combine the different models for the analysis of the fixture performance. As an example, Kang *et al.* [49, 50] developed a framework for computer aided-fixture design that included locator layout optimization, locator tolerance verification and assignment, stability verification, clamping force optimization, and clamping sequence verification. The workpiece was assumed rigid and the material removal action was not considered. These types of software are not adopted by the industry since they lack practicality and are computationally demanding.

It is important to note that CAFD requires the optimization of the design parameters of the fixture. Several researchers proposed different models for the optimization of the fixture layout (number and position of the locators and clamps) or the clamping forces. Meyer and Liou [51] looked at the optimization of the fixture layout to minimize the clamping forces by using linear programming. Only static analysis was performed using an upper bound value for the machining forces. The sequence of the part loading was also taken into consideration. Li and Melkote [2] used a non-linear optimization algorithm to select the optimum fixture layout, which will minimize the clamping forces. In another study, Li and Melkote [40] optimized the clamping forces by using sequential quadratic programming.

To include the static workpiece deformations, some researchers solved the optimization problem using FE models to predict the deflection of a reduced set of candidate points to increase the computational efficiency [45, 52]. Kashyap and DeVries [52] used the penalty function method to optimize the fixture layout while taking into consideration the flexibility of the workpiece. Sayeed and De Meter [33, 34] implemented mixed integer programming with a heuristic approach in order to select a reduced set of machining points for the optimization. Tan *et al.* [53] used the force closure theorem and FEM to determine the optimum clamping and locator layout when the contact friction and the static deformations of the workpiece and the fixture are accounted for.

Global optimization techniques such as Genetic Algorithms (GA) have gained popularity in solving optimization problems since they provide near global optimum solutions when the number of variables is large. Kulankara *et al.* [54] used GA to optimize the fixture layout and the clamping forces with respect to the static deformation of a compliant workpiece. To minimize the computational effort, the Guyan reduction method [55] was implemented. Li [56] used GA to optimize the number of locators and clamps as well as their position in order to minimize the deformation of sheet-metal components. The optimization was performed on two phases: In the first phase, optimal regions for the locators are identified and in the second phase optimum positions are selected within each region.

Some research work was devoted to compare different optimization techniques. Vallapuzha *et al.* [57] used real-coded genetic algorithm with FEM to optimize the fixture layout based on the static deformation of the workpiece. The spatial coordinates of the workpiece were used instead of the FE model nodes. It was shown that the continuous GA offered a faster convergence and better solution than the discrete optimization. The locators and supports were represented by spring elements. The compliance-based formulation was used since it offers some reduction in computation time when compared to the stiffness formulation. A discrete interpolation was used to position the locators in the FE model. In another study, Vallapuzha *et al.* [58] compared the GA and the sequential quadratic programming with discrete and continuous interpolation functions for the placement of the springs representing the locators. It was found that the GA with FE models using continuous interpolation function offered the best results. The method was tested for a simple plate with a coarse FE mesh. As mentioned in this study, the computational time is expected to increase significantly for finer meshes and more complicated structures. Prabhaharan *et al.* [59] compared the GA algorithm to the Ant Colony Optimization (ACO) for the optimization of the fixture layout to minimize the static deformation of the workpiece. It was shown that the ACO converged faster and was consistently nearer to the optimum solution than GA.

As can be seen, most of the optimization problems are focusing on the fixture layout. In addition, in all these optimization problems, the effects of the dynamics of the workpiece and the material removal was not considered due to the complexity and the intensive computational effort required to model the dynamics of the continuously changing workpiece.

2.3 Dynamics of the Milling of Thin-Walled Structures

Milling of thin-walled structures is a critical process due to the high flexibility of the workpiece. Several factors contribute to the complexity of this process, e.g., the closed loop interaction between the cutting forces and the vibration of the tool-workpiece system, the regenerative effect of the previously machined surface and the non-linear contact between the tool and the workpiece. Most of the research in this field was either focused on the suppression of the vibrations of the workpiece during milling through the development of new machining techniques or on the modelling of the process in order to understand the effect of the different cutting parameters on the final surface finish and the dimensional tolerances of the workpiece. The following subsections will present a brief review of the techniques used for the milling of thin-walled structures, the milling force models including either the static deflections or the dynamic vibrations of the workpiece and finally the models for chatter analysis.

2.3.1 Techniques Used for the Milling of Thin-Walled Structures

Currently, the industry is seeking a set of general guidelines and/or techniques for the milling of thin-walled structures. A large number of the thin walls are found in pocket-shaped structures rather than a simple cantilever plate. In a thin-walled pocket, there are two main areas of interest: the rib and the web. The rib is the vertical side wall of a pocket and the web is the bottom floor of the pocket. Different strategies exist for the machining of each of these features.

In an early attempt to control the milling of thin-walled structures, Anjanappa *et al.* [60, 61] developed an online-optimal control to maximize the feed-rate for machining thin-webs while maintaining the dimensional accuracy. The controlling parameters were the measured cutting forces. The thin-rib machining was modelled as a stochastic process. Tlusty *et al.* [62] presented two techniques for the use of long slender cutting tools to avoid chatter. In the first technique, the tool length is adjusted such that the stability lobes coincide with the maximum power and spindle speed of the machine. The second technique is for the machining of thin-walled ribs by using long slender end mills with a relieved shank. It was shown that the relieved shank prevents the over-cutting of the thin-walled ribs when cutting at large depths.

Smith and Dvorak [63] suggested the selection of a certain path for the machining of thin-webs (bottom floor of the pocket), such that the web is supported by the un-machined material of the workpiece. It was shown that tools with zero-corner radii are preferred since they generate smaller forces in the direction normal to the surface of the web. Zhao *et al.* [64] proposed a similar tool-path (stepped spiral-out) for machining of pockets with thin-webs (bottom of the pocket) in which the tool reaches the bottom of the pocket then spirals out such that the web is always supported by a bulk of material. Based on experimental analysis, Wu *et al.* [65] proposed a set of guidelines for the selection of optimum parameters for the milling of thin-walled structures such as low axial depth of cut, large radial depth of cut, high cutting speed and moderate feed per tooth. In a following study, Zhao *et al.* [64] suggested the tilting of the tool for error compensation.

Recently, Herranz *et al.* [66] proposed some guidelines for the machining of thin-walled parts taking into account the static and the dynamic behaviour of the workpiece. These guidelines include the optimization of the tool path to take advantage of the un-machined material as a support for the flexible parts, the use of large tool radii for the machining of ribs and small tool radii for the machining of webs and the use of stability lobes that account for the dynamics of the workpiece to evaluate the stable cutting conditions.

2.3.2 Mechanistic Force Models Including the Static Deflections of Thin-Walled Workpieces

Although the above-mentioned techniques offer general guidelines for the milling of thin-walled structures, more specific force models are required to assess the effect of the various cutting parameters on the machining forces and the final dimensional accuracy and surface quality of the workpiece. Due to the complexity of the milling process, analytical cutting force models are not used. Instead, most researchers use empirical mechanistic force models. In these models, the forces are determined as the product of a specific cutting pressure and the area of the chip. The specific cutting pressure is determined experimentally and the chip area is determined geometrically by the intersection of the workpiece and the cutting tools [67].

Assuming a rigid tool-workpiece system, many mechanistic models were developed for 2.5-axis milling, e.g., [68, 69], and for 4- and 5-axis milling, e.g., [70, 71]. Devor *et al.* [72] were one of the first researchers to develop a mechanistic model that takes into account the deflection of the cutter. Similarly, many other models were developed to include the deflections of the tool, e.g., [73, 74, 75, 76]. Liao and Tsai [77] included also the dynamics of the spindle and the supporting bearings. The milling cutter was simulated by a pre-twisted Timoshenko beam element, which has different moments of inertia about the two axes normal to the tool axis. Recently, Omar *et al.* [78] developed a mechanistic force model for end milling, which incorporated the effects of tool runout, tool deflection, tool tilting, flank face wear and the dynamics of the tool on the surface roughness of the workpiece. The dynamics of the tool was represented by a single degree of freedom model.

As the milling of thin-walled structures gained popularity in the aerospace industry, the developed mechanistic models started taking into account the static and the quasi-static deflections of the workpiece. Kline *et al.* [79] developed a mechanistic model that considers the flexibility of the tool and the workpiece. The cutter was modelled as a cantilever beam, and the static deflection of a simple workpiece geometry in the form of a plate was predicted using 2D FE model. The purpose of the model was to predict the surface accuracy of the machined plate. It was found that, for accurate predictions of the workpiece deflection, the transverse force played the most important role.

Sutherland and Devor [80] developed a methodology to include the relative displacement between the tool and the workpiece due to their flexibility. However, the model was tested for a flexible tool only. Tsai and Liao [81] developed a mechanistic model in which the static deflections of the tool and a flexible stepped plate are accounted for. The stepped plate was modelled using a FE model and 3D 12-node iso-parametric elements. The tool was modelled using a Timoshenko beam element [77]. In this model, the update of the workpiece thickness due to the material removal action was ignored. In addition, the experiment was performed at low rpm (less than 3000) such that the assumption of quasi-static forces is valid.

In a series of research studies, Ratchev *et al.* [82, 83, 84, 85, 86, 87, 88] developed a comprehensive methodology for the compensation of the surface errors during the milling of low rigidity components. The proposed approach included a module for the integration of the force and the workpiece deflection and the integration of the workpiece deflection and the material removal [83, 84]. However, the frequency of the update of the model and the computational efficiency were not discussed and the validation was performed for a simple cantilever plate. A force model was implemented using the perfect plastic layer model developed originally by Merchant [85]. A Voxel-cutting algorithm was presented to simulate the change of thickness of the workpiece during machining and to generate elements, which are compatible with FEM packages [86]. As mentioned in the paper, the frequent update of the workpiece geometry resulted in an extensively high computation time. Another problem was that the Voxel transformation led to the creation of elements of abnormal span-to-thickness ratio, which would result in erroneous results in the FE model. Moreover, for small feed rates, the element size for the update of the workpiece thickness should be accordingly reduced. This further reduces the computational efficiency of the system. Based on the developed models, an off-line single step and multiple step error compensation approach was proposed [87, 88].

Guo *et al.* [89] analyzed the deformations of a thin walled plate during milling using a FE model with special consideration to the effect of the initial residual stresses. Kang *et al.* [90] developed an approach to predict the static form errors in the milling of thin-walled structures. The workpiece was modelled using a 3D FE model to simulate the material removal action. An algorithm was devised using a double iterative approach to predict the maximum surface error.

Recently, Tang *et al.* [91] considered the large deformation of plates during milling by establishing the equations for large deformation of thin-plates and implementing them in a FE model. The effect of the cutting forces, the location of the tool and the thickness of the workpiece on the large deformation of thin-walled structures was studied. Tang and Liu [92] developed an analytical model for the deformation of a cantilever plate using the reciprocal theorem to investigate the effect of the magnitude and location of the cutting forces and the thickness of the plate on its deformation.

As can be seen, for all the developed models, the validation was performed using mainly a simple plate, which does not represent the practical shape of aerospace structural elements. The main problem associated with these models is the low computational efficiency especially when considering the material removal action. In addition, all analysis were static, thus the dynamic interactions between the tool and the workpiece were not captured.

2.3.3 Mechanistic Force Models Including Dynamic Vibrations of Thin-Walled Workpieces

For the development of accurate mechanistic force models, it is crucial to determine the dynamic response of the thin-walls at each location of the tool during milling. The evaluation of the dynamic deflection of the thin wall will affect the intersection of the tool and the workpiece, thus affecting the force predictions, as well as the final part topography. Thus a model describing the dynamics of thin-walled structures is essential to accurately determine the chip load.

Limited research work has been done in this area. Altintas *et al.* [93] developed a mechanistic force model to predict the surface finish of a cantilever stepped plate. The dynamics of the plate was determined using the FEM and modal analysis. The response was determined at the tool-workpiece contact only. The material removal action was not taken into account. Large discrepancies between the measured and the predicted vibrations were found and were attributed mainly to the process damping, which was not included in the model. Davies and Balachandran [94] performed a dynamic analysis of the displacement response obtained during the milling of a cantilever plate. The objective of this study was to investigate the effect of the non-linearities due to the intermittency of the milling process. It was shown that the impact dynamics dominates the vibrations of the thin-walled plate. A simplified cutting model was developed and only one mode of the plate dynamics was included to validate the observations made from the experimental results.

Kanchana *et al.* [95] performed a FE study and found through a frequency response analysis that at high frequency loading, i.e., high spindle speeds, the vibrations of the workpiece are less due to its higher dynamic stiffness. Campomanes and Altintas [96] developed a time domain simulation for the milling process where the dynamics of the tool and the workpiece (cantilever plate) is taken into consideration. The dynamics of the tool-holder-spindle system was modelled using an experimentally measured transfer function. Peigne *et al.* [97, 98] developed a geometrical model to predict generated surfaces during machining. The effect of forced and regenerative vibrations in the milling of a flexible plate on the surface was studied. The workpiece was represented by a single degree of freedom model and the parameters were identified experimentally. It was shown that forced vibrations had a slight effect on the roughness when compared to the effect of the regenerative vibrations.

All the previous studies did not take into account the change of thickness of the workpiece during machining. Only two studies focused on this issue. Sagherian and Elbestawi [99] developed a mechanistic force model that took into account the flexibility of the thin-walled structures as well as the deflection of the tool. The tool was modelled as a cantilever beam and two modes were identified based on impact tests. The workpiece was represented by a beam and modelled using the FEM. Abrari [100] developed a mechanistic force model including the dynamics of the tool and the workpiece. Boundary representation (B-rep) of the workpiece and the tool swept volume were used to determine the intersection between the tool and the workpiece. ACIS solid modeler was used to generate the mesh of the updated workpiece for the FE model. The model was validated using a cantilever plate. The main problem of using FEM is the low computational efficiency since one has to frequently update the model to simulate the continuous change of thickness. For this reason, only simple workpiece geometries (beams and plates) are used for the validation.

One can conclude that most of the studies that were performed to analyze the dynamics of the workpiece during milling did not include the change of the workpiece thickness during machining. The models are usually validated against simple beam and plate workpieces, which do not represent typical thin-walled structures. In addition, most of the research work does not present a validation of the models through the measurement of the dynamic vibrations of the workpiece. This is mainly due to the challenges encountered in measuring the forces and the displacement during low-immersion milling of flexible structures. Finally, none of these studies took into account of the effect of the fixture layout and the compliance of the supports on the dynamics of the workpiece during milling.

2.3.4 Models for Chatter Analysis of the Workpiece-Tool System

Another way to study the dynamics of the cutting process is to evaluate the stability of the process through chatter analysis. The theory of the regenerative chatter was established by Tobias [101]. Other models for chatter analysis were developed later by Hanna and Tobias [102], Tlusty and Ismail [103, 104], and Ruxu *et al.* [105]. Altintas and Budak [106] presented a new model for the prediction of the chatter based on the identification of the transfer function of the cutting tool in the frequency domain. Further models were developed for the prediction of the onset of chatter during milling. Ismail and Soliman [107] developed a new method for the identification of the stability lobes by increasing the spindle speed while monitoring a statistical chatter indicator which is function of the cutting forces. Merdol and Altintas [108] developed a model for chatter analysis while taking into account the coupling between the spindle speed and the process dynamics for low immersion cutting operations.

Most of these models are based on the analytical representation of the tool dynamics. A limited number of models exists for the chatter due to the flexibility of the workpiece. This is mainly due to the difficulty of developing analytical expressions for the workpiece dynamics. Ismail and Ziaei [109] combined an off-line feed scheduling and an online chatter control using the statistical chatter indicator to reduce chatter during the milling of flexible turbine blades. De Lacalle *et al.* [110] performed a chatter analysis while taking into account the relative transfer function between the tool and the workpiece. The workpiece was a cantilever plate and the dynamic characteristics were determined experimentally. A 3D stability lobe chart was developed with the following three parameters: Spindle speed, axial depth of cut and the different steps for the machining of the workpiece. It was shown that the stability lobes, determined using this method, are more accurate than considering the workpiece or the tool individually. The change of thickness during machining was not taken into account. This model was extended for ball endmill cutters while assuming a single degree of freedom workpiece [111, 112]. Thevenot *et al.* [113] generated 3D stability lobes for a thin cantilever plate. A FE model of the plate was developed and updated 10 times to track the change of the thickness of the plate along the tool path. Based on the FE model, the first five natural frequencies and the apparent stiffness of the plate at the force application point were determined and used to generate the stability lobes. Recently, this model was extended by Seguy *et al.* [114] to take into account the effect of ploughing on the prediction of the 3D stability lobes and the surface roughness of the finished part. Mane *et al.* [115] developed 3D stability lobes for a thin-walled cantilever plate by modelling the workpiece, the tool and the spindle using a FE model. In this model, the effect of the change of the spindle dynamics at different rotational speeds was accounted for; however, the change of thickness of the workpiece during machining was not taken into account.

2.4 Model-Order Reduction Techniques

As mentioned previously, FE based models, which are used to evaluate the dynamics of the fixture during the milling of thin-walled structures, are computationally extensive. Therefore, it was necessary to review the different model-order reduction (MOR) techniques in order to assess whether they can be efficiently used for this specific problem where the workpiece dynamics is continuously changing. Different model-order reduction techniques are available in the literature and will be briefly discussed in the coming sections. They include methods for the reduction of the number of physical coordinates, modal superposition, load dependent Ritz vectors, and Component Mode Synthesis. Frequency domain identification methods can also be implemented to FE models to reduce the order of the models [116]; however, they require optimization for the system parameter identification. Although most of these methods can substantially reduce the computational effort, they can be sensitive to the selection of the reduced-order model parameters. Moreover, these techniques will still require the update of the full FE model each time the structural dynamic characteristics change, which is the case when machining thin-walled structures.

2.4.1 Reduction of the Physical Coordinates of the Model

One of the oldest MOR techniques that has been implemented in most commercial FEM packages is the Static Reduction (Guyan) [55]. It assumes that the inertia terms have negligible effects on the dynamic response of the structure. For static problems, this method offers accurate results and very good computational efficiency. For medium and high frequency loading, this method introduces large errors for the dynamic analysis [117]. Other techniques have been used in order to improve this method such as the Improved Reduced System (IRS), which includes a first-order estimate of the inertia terms [118]. However, this method is sensitive to the selection of the included coordinates of the system and thus its use is very limited [119]. An iterative IRS (IIRS) could be implemented by repeating the same transformations using the reduced mass and stiffness matrices [120]. Although this approach offers better approximation of the full-order system, the computational efficiency is reduced due to the iterative nature of the solution.

Dynamic Condensation is another technique to improve the Guyan Reduction. This method explicitly includes a dynamic approximation of the inertial effects by using the steady state harmonic response of the full-order system [121]. Other modifications to this approach were developed to improve its accuracy including the First-Order Dynamic Condensation [122], the Second-Order Dynamic Condensation [123] and an iterative approach [120] similar to the IIRS. One of the main drawbacks of the dynamic condensation approach is its intensive computational requirements [119]

The major advantage of the physical coordinate reduction techniques over other reduction techniques is that they do not require the solution of the eigenvalue problem of the full model. However, these methods might have significant accuracy limitation depending on the selection of the reduced physical coordinates [119]. In addition, for milling applications, the mass and stiffness matrices are continuously changing. The computational efficiency of these methods is substantially reduced as the number of updates of the system parameters increase.

2.4.2 Modal Superposition Methods

The modal superposition method is one of the widely used techniques for the reduction of the order of large complex structures. It is based on the transformation of the physical coordinates to a set of reduced generalized coordinates [124]. It requires the solution of the eigenvalue problem of the system. In general, the modal superposition methods are advantageous when the number of contributing modes is small.

One of the modal superposition methods is the Mode-Displacement method, in which high frequency modes are simply truncated. For better accuracy, modes up to three times the loading frequency have to be included in the model [119]. The mode displacement method does not account for the truncated modes and thus could introduce large errors in the calculated response. For low frequency loading, this method can provide accurate results. One of the limitation of this method is that it requires a model with large number of physical coordinates to avoid numerical problems in the inversion of the transfer matrices [117].

Another modal superposition method is the Mode-Acceleration technique. In this method, the effect of the truncated frequencies and modes is approximated by including the complete set of the system modes in the static term and the reduced set of modes for the dynamic term. However, when the truncated modes have lower frequency than the loading frequency, the errors are larger than those for the Mode-Displacement method [119]. Both the Mode-Displacement and the Mode-Acceleration techniques are suited for low frequency problems. For medium and high frequency loading, the number of included modes increases, and thus the computational efficiency is reduced.

For high frequency problems, quasi-static compensation techniques were developed to take into account a band of frequencies [125]. These techniques are based on representing the dynamic response of the system as the sum of the mode-displacement solution in the desired frequency range and an unknown residual error. Similarly, the forces are represented as a force vector satisfying the mode-displacement equation and a residual force term [119]. By solving the dynamic equilibrium equation of the residual force, an approximate expression for the residual error could be determined. It was shown that the quasi-static method offers better results compared to the Mode-Acceleration method even for the cases when only the high frequency modes are truncated [125].

The main advantage of the mode-superposition technique is that, for a given system, once the eigenvalue problem is solved, a small number of modes is used to represent the response of the system. The main limitation of the mode-superposition technique is that the solution of the eigenvalue problem is often computationally intensive. For fixture design during milling of thin-walled structures, the dynamic characteristics of the system are continuously changing due to the material removal action. Thus, each time the mass and the stiffness matrices are updated, the full eigenvalue problem has to be solved. Consequently, the computational advantage of these methods is lost, especially for high-order problems.

2.4.3 Load-Dependent Ritz Vector Methods

In the Ritz Vector methods, instead of using the exact modes, orthogonal approximate modes are used, which can reduce the computational effort required to solve the eigenvalue problem and sometimes could improve the accuracy. For the Load-Dependent Ritz Vector (LDRV), the modes are generated based on the load applied on the structure. One of the available LDRV techniques is the Wilson-Yuan-Dickens (WYD) algorithm [126] where a static recurrence procedure is used to generate the vectors. The first mode corresponds to the static response of the structure for a given load. This method was extended by other researchers by using different vectors such as the Lanczos vector [127]. These methods are suited for problems with loading at low frequency. For medium and high frequency problems, the generation of the Ritz vectors requires large number of recurrences, thus reducing the computational efficiency and introducing large numerical errors. Gu [119] proposed a quasi-static Ritz Vector method. The approach was based on using a quasi-static recurrence procedure. The solution convergence is controlled by a centring frequency parameter within the desired band of frequencies. It was shown that this method offers better accuracy. As previously mentioned, for dynamically time-varying structures, the computational advantage of the Ritz method is lost unless the number of degrees of freedom of the system is small.

2.4.4 Component Mode Synthesis

The Component Mode Synthesis (CMS) is one of the widely used methods for the analysis of large complex dynamic problems [128]. It is based on partitioning the system into assemblies and components and using a set of approximate functions for the representation of the modes of each component. The CMS aims at replacing the large number of the physical coordinates of each component with a reduced set of basis coordinates. The transformation matrix between the full and the reduced set of coordinates includes pre-selected normal modes of each component and other Ritz-basis vectors (computational mode) [119]. The most popular computational modes are the constrained modes developed by Craig-Brampton [129]. A constraint mode is defined as the static deflection of a component when a unit displacement is applied at one coordinate of its active degree of freedom set while restraining the remaining coordinates. Other types of computational modes can be developed; however, they are beyond the scope of the review. Although the CMS is mainly intended for the solution of low frequency problems, some attempts were made for mid and high frequency problems based on quasi-static modes. These modes depend on the value of a centring frequency, which is employed to capture the effect of truncated modes [130]. Similar to other MOR reduction techniques, the CMS method loses its computational advantage in the case of structures that are continuously changing in terms of their dynamic characteristics.

2.5 Gap Analysis and Limitations of Existing Methods

Based on the review of the literature, the following can be concluded:

- No accurate representation of the dynamic response of typical aerospace structures is presented while including the continuous change of thickness during machining. The available models are mainly based on FE models, which require extremely large computational time when considering an interactive design of fixture layout.

- Although MOR techniques can offer substantial reduction in the computation time, they lose their computational advantage for models where the structural dynamics is continuously changing.

- Generally, the effect of the fixture layout on the dynamics of thin-walled structures has not been extensively investigated.

- Most of the available mechanistic force models do not take into account the effect of the fixture layout on the dynamic response of thin-walled structures.

- The validations of the models are always performed for very simple workpieces such as beams and plates. Thus, a practical solution for the computational efficiency of the models has never been investigated.

- The validation experiments never included a comparison between the models' predictions and the dynamic response of the real structure. Moreover, rough cutting paths were mostly used; consequently, the initial thicknesses of the workpiece were considerably large. This was intended to avoid dealing with the effect of the dynamics of the measurement system on the measured forces and displacements. As a consequence, most of the designed experiments do not represent practical cases encountered in industry.

One can conclude that a computationally efficient integrated model is required to describe the effect of the fixture layout on the flexible workpiece dynamics during milling of thin-walled structures. The model has to take into account the following:

- The dynamics of typical thin-walled structures encountered in the aerospace applications.

- The continuous change of thickness of the walls of the structure during machining.

- The effect of the number, location and stiffness of the fixture locators/supports on the response of the workpiece.

2.6 Detailed Objectives and Approach of the Research

The main objective of this thesis is to develop a semi-analytical approximate model to predict the dynamic response of typical thin-walled structures with an error less than 10%, while minimizing the computational time by at least one order of magnitude compared to FE models. The model will include the change in the workpiece thickness during milling, the effect of the fixture layout and the interaction between the dynamics of the workpiece and the machining forces. The approach to achieve this objective is as follows:

1. Review the current practices in the aerospace industry in order to determine typical thin-walled components.

2. Develop a novel model to describe the dynamics of these thin-walled structures. The computational time for this model has to be minimized without compromising the accuracy in such a way that it can be usable by fixture designers in industrial setups. When comparing the developed model with Finite Element (FE) models, the error in predictions of the responses relative to the maximum amplitude of vibration has to be $< 10\%$ and the computational time has to be reduced by at least one order of magnitude.

3. Develop an extended model to represent the continuous change of thickness of the workpiece during machining. This model should simulate typical machining tool-paths and practical ranges for the reduction in thickness.

4. Represent the effect of the fixture supports, in terms of the location, the number and the stiffness, on the dynamic behaviour of the workpiece.

5. Validate the developed models against FE models and impact tests experiments.

6. Demonstrate the applicability of the model through real machining experiments of a thin-walled workpiece. Due to the flexibility of the workpiece and the nature of the cutting forces encountered in finishing operation, the dynamics of the measurement system has to be analyzed and a new methodology has to be developed to compensate for the dynamics of the measurement system.

CHAPTER 3

Conceptual Development of Dynamic Models for Thin-Walled Aerospace Structures

3.1 Introduction

Based on the literature review presented in Chapter 2, one can conclude that it is necessary to develop models which describe accurately the dynamics of thin-walled aerospace workpieces within a practical computational time frame. This chapter will include a description of the conceptual developments for the proposed models. The analysis of different aerospace structural components will be presented first and a generalized unit-element will be identified to represent the dynamics of these structures. Then, two different models will be proposed to predict the dynamic response of the unit-element. This will be followed by an analysis of the change of thickness of thin-walled structures during milling. Finally, since the formulation of the models is based on the dynamics of plates, a review of this topic will be presented.

3.2 Development of a Generalized Unit-Element

To develop a computationally efficient dynamic model of practical relevance, it is necessary to analyze the different thin-walled aerospace structural components. These components include the skin, the spar and the rib; they are composed of multiple pockets in order to reduce their weight, while maintaining their stiffness. To efficiently study the dynamics of these structural components, they are broken into a series of unit elements with the shape of a pocket with different aspect ratios, and different features (orthogonal vs. slanted walls). A generalized unit-element (pocket) is depicted in Fig. 3.1. Ranges of values for the dimensions representing the generalized pocket encountered in aerospace structural elements are shown in Table 3.1.

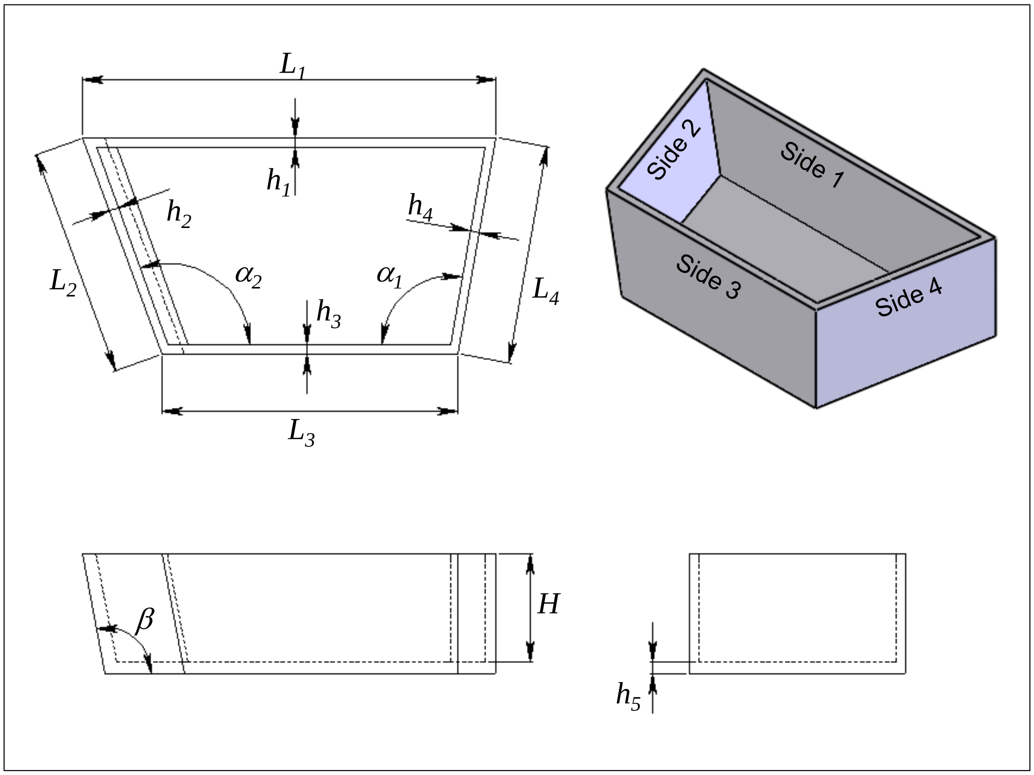

Figure 3.1: Generalized unit-element (pocket) shape

Table 3.1: Dimensions of typical aerospace structural components

Dimensions, angles	Rib	Spar
Height (H)	25 mm - 50 mm	35 mm - 100 mm
Thickness (h_1 - h_5)	1.5 mm - 4.0 mm	2.0 mm - 5.0 mm
Length (L_1 - L_4)	Up to 400 mm	Up to 500 mm
Angle (α_1, α_2)	90° - 135°	90°-135°
Angle (β)	90° - 95°	90°-100°

According to the performed analysis, it was found that the unit element could be found in three main general cases which are illustrated in Fig. 3.2. These cases are:

1. **Single pocket**: This represents the simplest case where the structural component is

a pocket which does not have any adjacent sides to it. This is typically encountered in small ribs.

2. **Single pocket with internal rib-wall**: In this case, the pocket length and width are large and thus the pocket has internal rib-walls to support its outer walls. This case is encountered in structures such as large ribs and small spars. The internal rib-walls are usually thinner than the walls of the pocket and their heights are usually smaller than the height of the pocket. The dimensional tolerances for the thickness of these rib-walls are usually large since they do not fit into other components.

3. **Multiple pockets**: This is the general case where the structure has pockets adjacent to each other. This is mainly encountered in typical spars and some ribs. As seen in Fig. 3.2, the pockets are usually adjacent to each other along a single direction. For a given pocket, depending on the dimensions of the adjacent pockets, one can decide to ignore or include their effect on the vibration of the pocket under consideration.

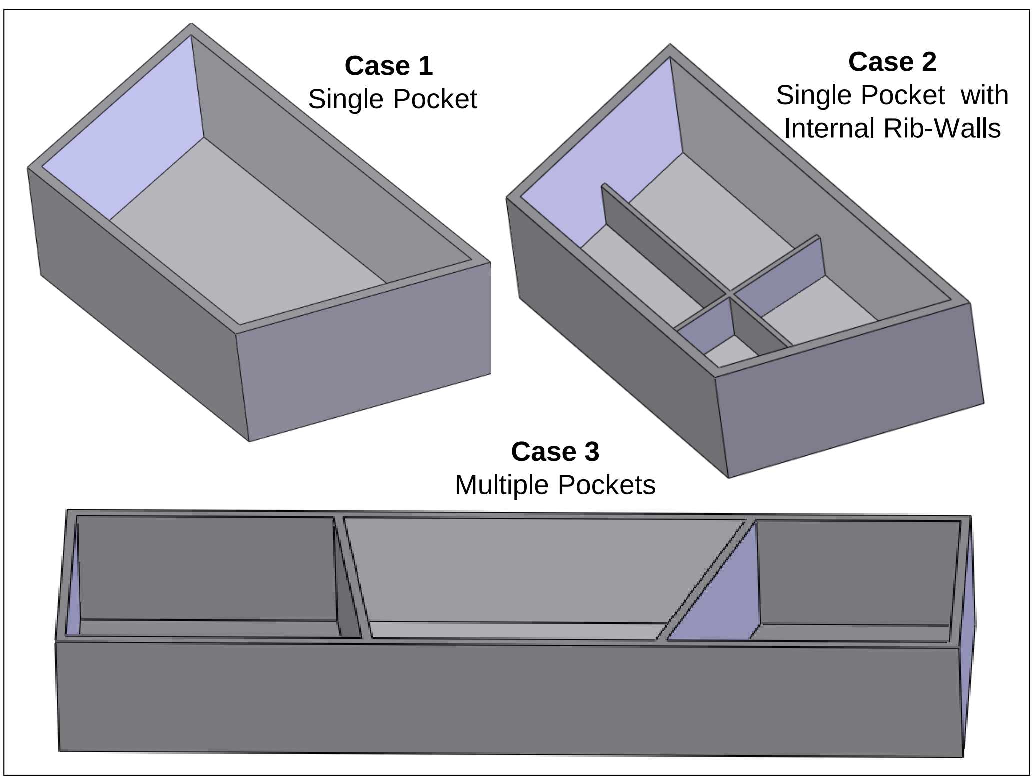

Figure 3.2: Different cases for the unit element (pocket) in aerospace structural components

In the analysis of these cases, the following expressions will be used:

- Load-application pocket: This is the pocket that has the load applied on one of its sides.
- Adjacent pocket: This is the pocket adjacent to the load-application pocket.
- Load-application side: This is the side on which the load is applied and for which it is necessary to predict the dynamic response.
- Adjacent side: This is the side which is directly connected to the load-application side.
- Non-adjacent side: This is the side which is either opposite to the load-application side within the same pocket or any side in an adjacent pocket which is not directly connected to the load-application side.

For example, if the load-application side is side 1 in Fig. 3.1, then the adjacent sides are 2 and 4 and the non-adjacent side is 3.

For the three general cases in Fig. 3.2, two different models are proposed for the prediction of the dynamic response of the unit-element (pocket). These models will be presented in sections 3.3 and 3.4 and their formulations will be described in Chapter 4, sections 4.3 and 5.3. In sections 4.5 and 4.6, these models will be further extended to include the effect of the change of thickness and the fixture layout, respectively. The development of efficient dynamic models to represent the cases in Fig. 3.2, require some simplifying assumptions including:

1. The base of the pocket is rigid and could be simulated by clamped boundary conditions. During machining, the workpiece is usually clamped on the fixture base using vacuum plates, for instance. Therefore, the bottom of the pocket is relatively rigid compared to the side walls of the pocket.
2. The geometric and material non-linearities of the contact between the supports and the workpiece do not affect the displacement away from the support. As mentioned previously, for the analysis of the vibration of thin-walled workpieces, the contact between the supports and the workpiece could be assumed rigid [17].

3. Only the forces normal to the side of the pocket are considered. Using FE models, the effect of the in-plane forces on the transverse vibration of the workpiece was found to be negligible when compared to that of the normal forces. Different comparison cases will be shown in section 3.2.1.

4. The effect of non-adjacent sides on the vibration of the load-application side is negligible. FE models of pockets with different aspect ratios were constructed to validate this assumption and they will be discussed in section 3.2.2.

5. For the case of structures with multiple pockets, the effect of adjacent pockets on the vibration of the load-application pocket depends on the aspect ratio of the wall thicknesses of the pockets. This will be described in details in section 3.2.3.

6. For the prediction of the dynamic response of the load-application side, the effect of the fixture supports applied on adjacent and non-adjacent sides is negligible. This assumption will be verified in section 3.2.4

For the verifications of assumptions 3 to 6, all the FE models are developed on ABAQUS (version 6.4), using 2D quadrilateral linear shell elements and general aluminum material properties: $E = 69\times10^9$ GPa, $\nu = 0.3$ and ρ =2700 kg/m^3.

3.2.1 Effect of In-Plane Forces on the Transverse Vibration of Thin-Walls

To determine the effect of the in-plane forces on the transverse vibration of thin-walls, FE models for nine plates were developed. Each plate has three clamped edges and one free edge. An illustration of the different plates and their dimensions is shown in Fig. 3.3. The in-plane forces are designated as F_x and F_y and the transverse force is F_z. As shown in Fig. 3.3, the forces are applied at the centre of the free edge of the plate. The total number of elements in the FE models of plates 1 to 3, 4 to 6, and 7 to 9 is 1200, 1650 and 2500, respectively.

For each plate, two cases were evaluated. In the first case, the in-plane forces (F_x and F_y) and the transverse force had an amplitude of 30 N each and a frequency of 600 rad/s. In the second case, only the transverse force F_z was applied with the same amplitude (30 N) and frequency (600 rad/s) as in the first case. The responses were calculated at the position of the load application point since it represents the location of maximum deflection. The error between the responses for the two cases was calculated in terms of the maximum amplitude of vibration. It was found that for the nine plates the errors were less than 0.1%. Thus, the effect of the in-plane forces on the transverse vibration of thin-walled structures can be ignored.

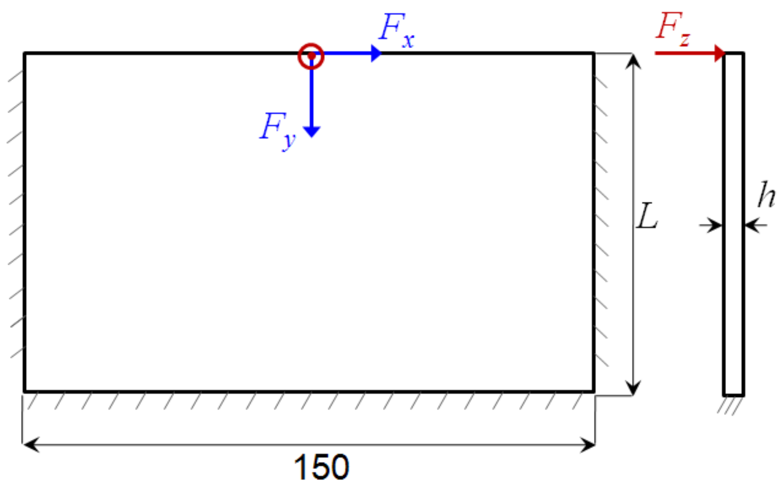

	Dimensions (mm)	
Plate	L	h
1	50	2
2		3
3		4
4	100	2
5		3
6		4
7	150	2
8		3
9		4

Figure 3.3: Illustration of the dimensions (in mm) of the plates used to evaluate the effect of the in-plane forces on the transverse vibration of a plate

3.2.2 Effect of Non-Adjacent Sides on the Response of the Load-Application Side

The effect of non-adjacent sides on the response of the load-application side was examined by developing FE models of rectangular pockets and comparing the response of the load-application side for different thicknesses of the non-adjacent side. The dimensions of the pockets used for this analysis are shown in Fig. 3.4. All pockets have a width of 100 mm, height of 75 mm, and wall thicknesses of 3 mm, 2 mm and 2 mm for sides 1, 2 and 3, respectively. The load-application side is side 1 and the non-adjacent side is side 3. According to the table in Fig. 3.4, there are nine pockets such that each three have the same length.

Pockets 1 to 3, 4 to 6 and 7 to 9 have a length L equals to 50 mm, 100 mm and 150 mm, respectively. For a given length L, the thickness h is either 2 mm, 3 mm or 4 mm. A load of 60 N and 600 rad/s was applied at the middle of the free edge of side 1, as shown in Fig. 3.4. The displacement response was calculated at the same location of the force application. In the FE models, the bottom base of each pocket was clamped. A total of 2600, 3400 and 4300 elements were used for pockets 1 to 3, 4 to 6, and 7 to 9, respectively.

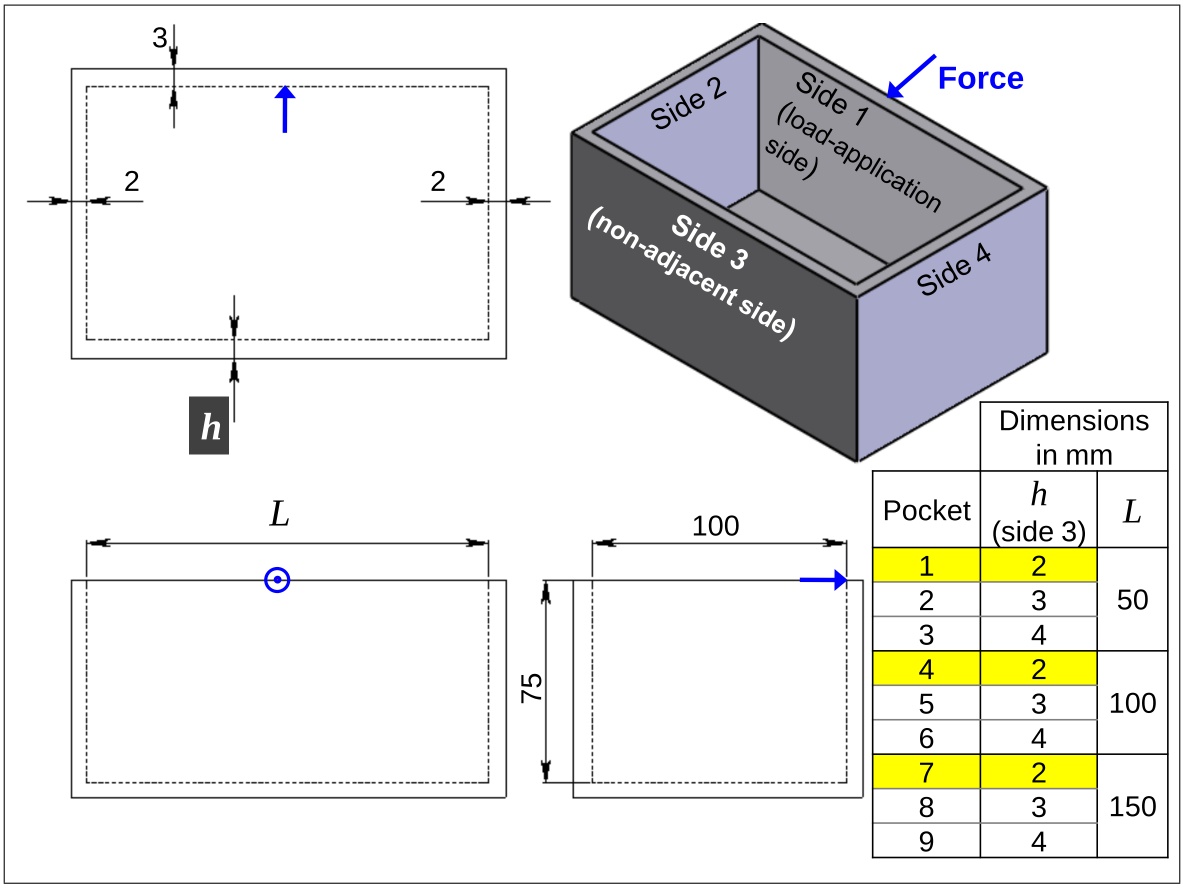

Pocket	Dimensions in mm: h (side 3)	L
1	2	50
2	3	
3	4	
4	2	100
5	3	
6	4	
7	2	150
8	3	
9	4	

Figure 3.4: Illustration of the dimensions (in mm) of the pockets used to evaluate the effect of non-adjacent sides

For a given length L, the responses of the pockets with a thickness h equals to 3 mm and 4 mm were compared to the response of the pocket with a thickness h equal to 2 mm. The errors were calculated in terms of the maximum amplitude of vibration. In Fig. 3.5, for each length L, the responses of the different pockets are shown and the maximum amplitude of vibration and the errors are reported in the adjacent tables. As can be seen, varying the thickness h has a small effect on the response. The errors for L equals to 50 mm, 100 mm, and 150 mm are less than 3.5%, 4%, and 1.5%, respectively. Thus, one can assume that the effect of non-adjacent sides on the response of the load-application side is negligible.

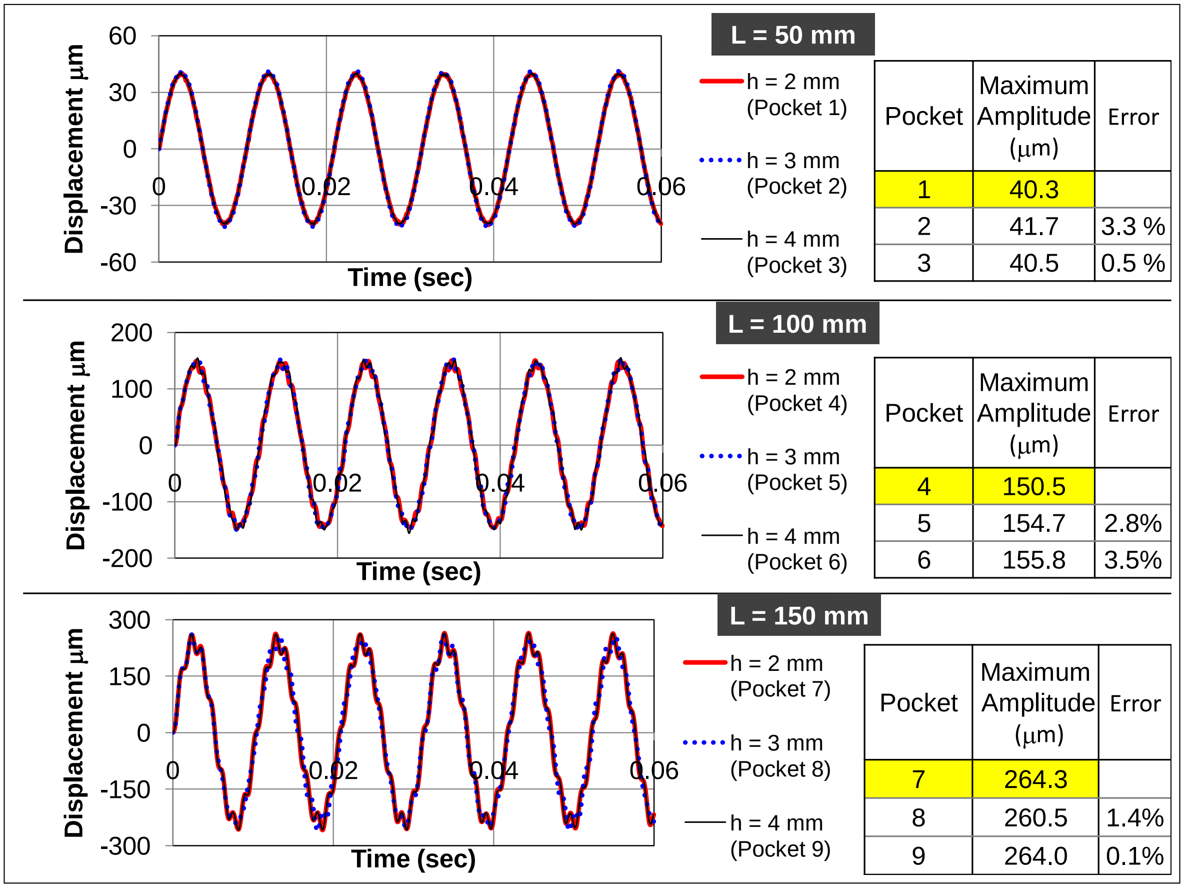

Pocket	Maximum Amplitude (µm)	Error
1	40.3	
2	41.7	3.3 %
3	40.5	0.5 %

Pocket	Maximum Amplitude (µm)	Error
4	150.5	
5	154.7	2.8%
6	155.8	3.5%

Pocket	Maximum Amplitude (µm)	Error
7	264.3	
8	260.5	1.4%
9	264.0	0.1%

Figure 3.5: Summary of the results for the effect of non-adjacent sides on the vibration of the load application side

3.2.3 Effect of the Adjacent Pockets on the Vibration of the Load-Application Side

For structures with multiple adjacent pockets, it is necessary to identify the cases when the effect of the adjacent pocket on the vibration of the load-application side can be neglected. Thus, one has to compare the response of a pocket with and without adjacent pockets. The pocket without adjacent units will be referred to as a single pocket. The dimensions of a three-pocket structure are shown in Fig. 3.6. According to the tables in Fig. 3.6, there are three sets of results, which are set K, set M, and set N. For all sets, the dimensions of the load-application pocket are the same except the thickness h_b. The value of h_b is equal to 2 mm, 3 mm and 4 mm for sets K, M, and N, respectively. For each set, the dimensions of the single pocket (pocket without adjacent units) are the same as the dimensions of the load-application pocket. The main objective is to compare the response of the load application side to the response of the corresponding single pocket, for different aspect ratios of the adjacent pockets. Thus, for each set, two main dimensions are varied, which are the thickness h_a and the length L of the adjacent pockets. The length L is either 100 mm, 150 mm or 200 mm and the thickness h_a was either 2 mm, 3 mm or 4 mm. For all the cases, the width and the height of the structure are equal to 100 mm, and the length of the load-application side is equal to 150 mm.

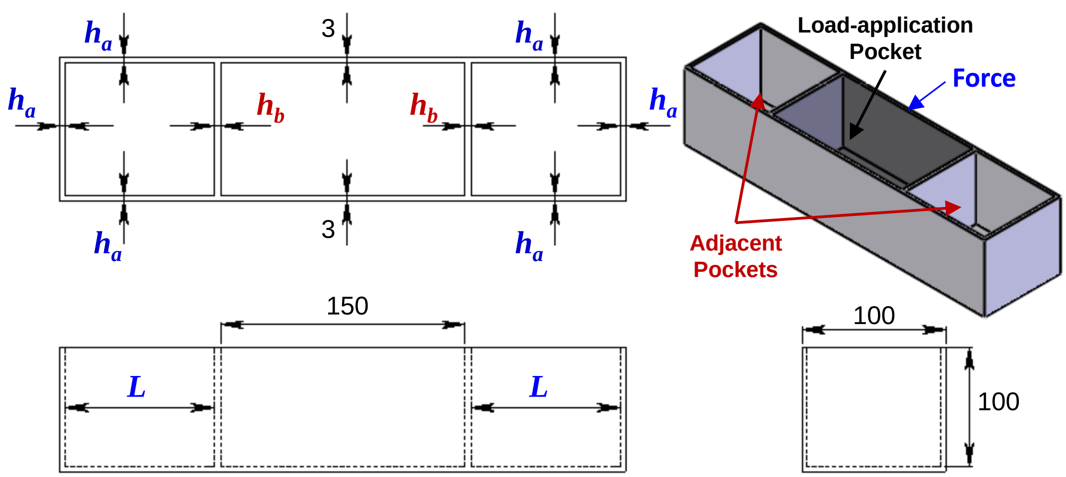

Set K: h_b= 2 mm	h_a	h_a/h_b	L
K1	2	1	
K2	3	1.5	100
K3	4	2	
K4	2	1	
K5	3	1.5	150
K6	4	2	
K7	2	1	
K8	3	1.5	200
K9	4	2	

Set M: h_b= 3 mm	h_a	h_a/h_b	L
M1	2	0.67	
M2	3	1	100
M3	4	1.33	
M4	2	0.67	
M5	3	1	150
M6	4	1.33	
M7	2	0.67	
M8	3	1	200
M9	4	1.33	

Set N: h_b= 4 mm	h_a	h_a/h_b	L
N1	2	0.5	
N2	3	0.75	100
N3	4	1	
N4	2	0.5	
N5	3	0.75	150
N6	4	1	
N7	2	0.5	
N8	3	0.75	200
N9	4	1	

Figure 3.6: Illustration of the dimensions (in mm) of the pockets used to evaluate the effect of adjacent pockets

FE models were developed to calculate the response for the different cases. Clamped boundary conditions were applied at the base of the pockets. The total number of elements for the FE models of the pockets with L equals to 100 mm, 150 mm and 200 mm are 4400, 5200, and 6000, respectively. A load of 50 N amplitude and 1256 rad/s frequency was applied on the middle of the free edge of the load-application side as shown in Fig. 3.6. The displacement was calculated at the same location of the force application. The response of the single pocket for each set is the reference to which the different cases are compared. For a given case in a set, the percentage error between the maximum amplitude of vibration of the response of the load-application side of the three-pocket structure and the response of the corresponding single pocket (reference pocket) is calculated.

The results for the different cases are shown in Fig. 3.7. On the left side, three plots are shown representing the percentage error versus the thickness ratio of h_a/h_b for sets K ($h_b =$ 2mm), M ($h_b = 3$mm) and N ($h_b = 4$mm), respectively. On the right side, the responses for cases K1, M1, and N1 are shown, each with the response of the corresponding single pocket. For each set, as the ratio h_a/h_b increases, the percentage error increases. This is expected since as the thickness ratio h_a/h_b increases, the rigidity of the adjacent pockets increases, and the response of the load-application side is more constrained. These additional constraints are not reflected in the case of a single pocket. For the results of set K ($h_b = 2$mm), the minimum ratio of h_a/h_b is equal to 1.00. For this ratio, the error is greater than 15%. For the results of set M ($h_b = 3$mm), when the ratio of h_a/h_b is equal to 0.67, the error was less than 11%. For the results of set N ($h_b = 4$mm), the maximum ratio of h_a/h_b is 1.0. For this ratio, the error was less than 15%. For the ratios 0.75 and 0.5, the error was less than 11% and 10%, respectively. When comparing the three sets (M, N, and K) at a thickness ratio h_a/h_b of 1.00, one can notice that the errors are almost the same. Thus, the aspect ratio h_a/h_b is a good indicator to identify the cases where the effect of adjacent pockets can be ignored. According to the results shown in Fig. 3.7, when the thickness ratio h_a/h_b is less than 0.75 for both adjacent pockets, one can neglect the effect of the adjacent pockets on the vibration of the load-application side. In addition, it can be seen that the effect of the length L of the adjacent pockets is negligible compared to the effect of the thickness ratio h_a/h_b.

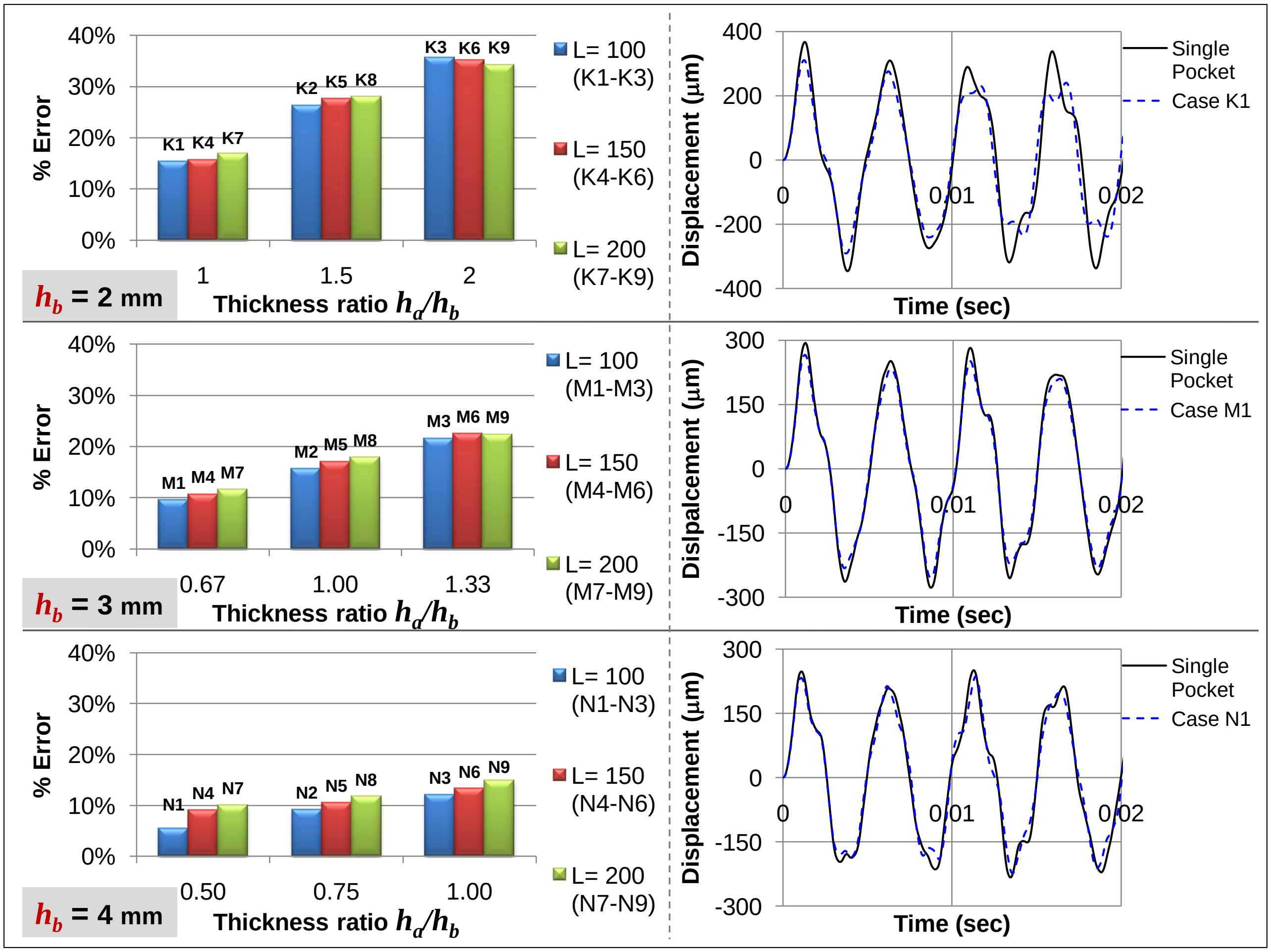

Figure 3.7: Results for the effect of adjacent pockets on the dynamic response of the load application side

3.2.4 Effect of the Fixture Layout on the Response of the Load-Application Side

It is assumed that for the prediction of the dynamic response of the load-application side of a pocket, the effect of the fixture supports applied on the opposite and adjacent sides is negligible. To verify this assumption, the response of the load-application side was compared for different fixture layouts on the opposite and adjacent sides. Four different FE models of rectangular pockets were constructed. All the pockets have a width W, height H and wall thickness of 100 mm, 100 mm and 3 mm, respectively. The lengths of pockets 1, 2, 3 and 4 are 100 mm, 200 mm, 300 mm and 400 mm, respectively. These pockets represent practical dimensions with length-to-width aspect ratios varying from 1:1 to 1:4. The side along the length of the pocket will be referred to as the L-side (Long side). The sides along the width will be referred to as S-side (Short side). A load of 50 N amplitude and 200 Hz frequency was applied first on the S-side and then on the L-side. The location of the load application was always on the top free edge of the side. The displacement was calculated at the same location where the force is applied. The total number of elements for the FE models of pockets 1, 2, 3, and 4 were 2900, 3950, 5300, and 6500, respectively.

For each model, three cases of fixture layouts with 3, 6 and 9 locators were applied on the adjacent and opposite sides. The different fixture layout cases are represented schematically in Fig. 3.8 for the load applied either on the S-side or the L-side. The reference case for a given pocket and load-application side is the pocket without any locators. For a given pocket, force location and fixture layout, the relative difference between the maximum amplitude of vibration of the response for this case and for the pocket without locators (reference pocket) is calculated and referred to as the deviation parameter (Ψ). This can be expressed as:

$$\Psi = \frac{d_w - d_r}{d_r} \times 100 \tag{3.1}$$

where d_w is the maximum amplitude of the calculated displacement of the pocket with locators and d_r is the maximum amplitudes for the reference pocket (no locators).

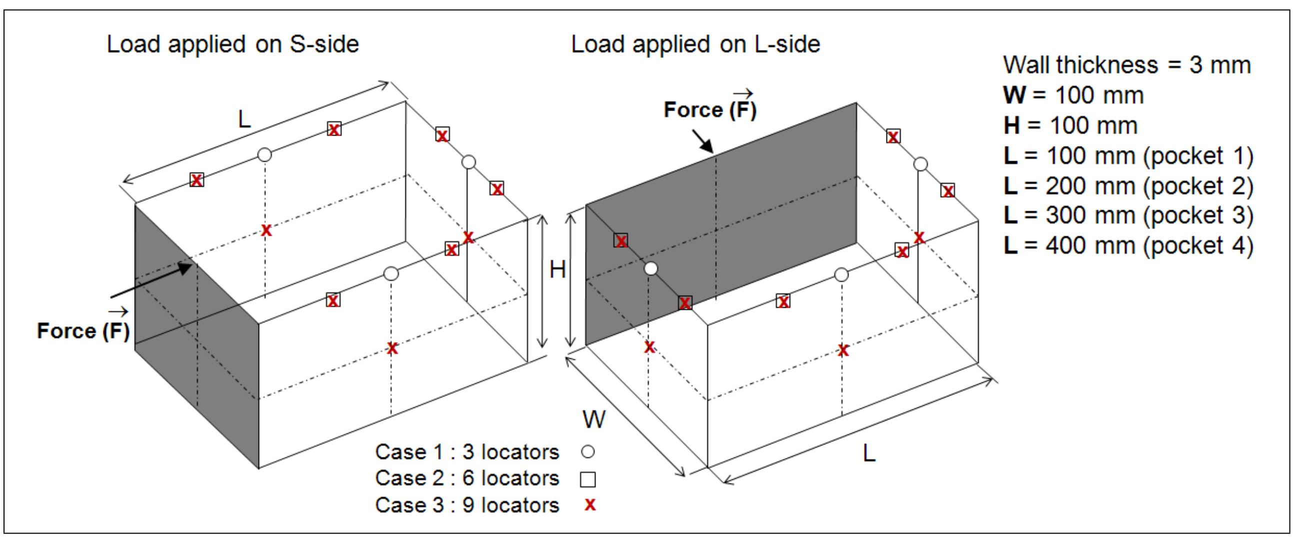

Figure 3.8: Different cases for the fixture layout for the load applied either on the short side (S-side) or the long side (L-side)

The percentage deviation for each case of fixture layout is shown in Table 3.2. It can be concluded that the percentage deviations for all pockets are less than 9%, except for the short side of pocket 2, where the deviations are 11.6%. The responses of pocket 2, with the load applied on the S-side and the L-side are shown in Fig. 3.9 for the different cases of the fixture layout. From this analysis, one can conclude that at the initial stage of the design of the fixture, the response of the load-application side can be approximately predicted without considering the effect of the locators on opposite and adjacent sides. Since the effect of the fixture layout on the sides within the same pocket can be neglected, then for large structures with multiple pockets, the response of the load-application side is negligibly affected by the number of supports applied on adjacent pockets.

Table 3.2: Percentage deviation of the pocket response for different fixture layout

Case	No. of Locators	Pocket 1	Pocket 2		Pocket 3		Pocket 4	
			S-side	L-side	S-side	L-side	S-side	L-side
1	3	3.5 %	0.5%	4.4%	1.5%	3.7%	6.0 %	0.5%
2	6	4.2 %	11.5%	6.2%	8.7%	6.0%	0.2 %	1.4%
3	9	4.5 %	11.6%	7.0%	7.7%	6.4%	0.2 %	1.8%

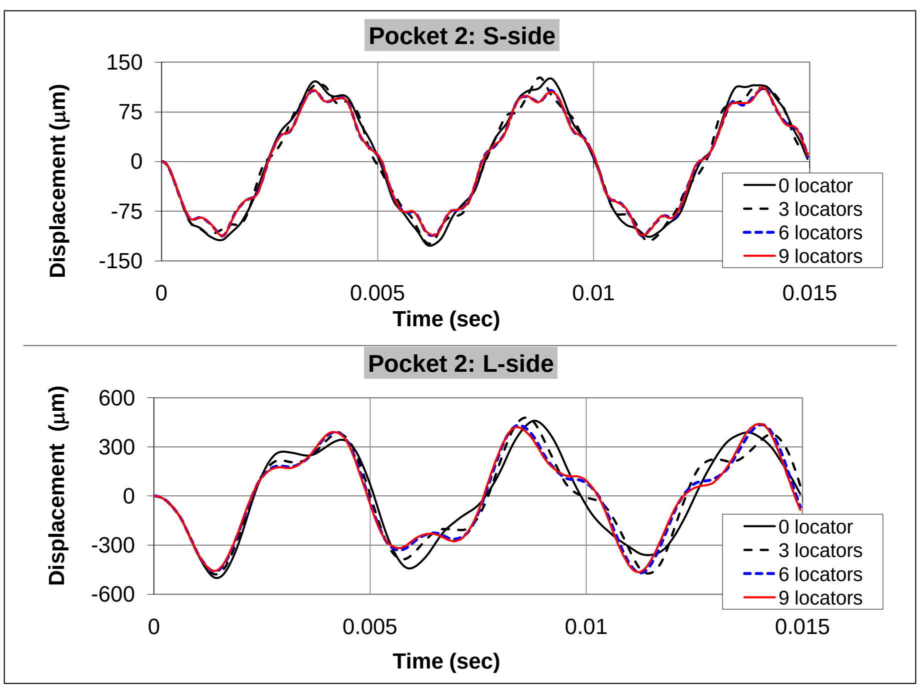

Figure 3.9: Dynamic response of S-side and L-side of pocket 2

3.3 Conceptual Development for the Generalized Single-Span Plate (GSSP) Model

To evaluate a fixture design for milling of thin-walled workpieces, the main target is to predict the dynamic response of the load-application side, especially at the area where the load is applied. It is required to develop a computationally efficient approximate model, which gives an accurate representation for the dynamic behaviour of typical aerospace structures. The proposed model in this section will be referred to as the Generalized Single-Span Plate (GSSP) model.

3.3.1 Description of the Proposed Concept for the GSSP Model

The proposed model is based on discretizing the unit-element to four sides and a clamped floor. The boundary conditions for each side have to represent the effect of adjacent walls, which can be considered by torsional and translational springs. Accordingly, the dynamic response of each pocket-side can be represented by the transverse vibration of a rectangular plate model having torsional and translational springs at the boundaries as shown in Fig. 3.10. The translational springs are in the transverse direction (normal to the plate). The rotational springs act around the axis that coincides with the corresponding edge.

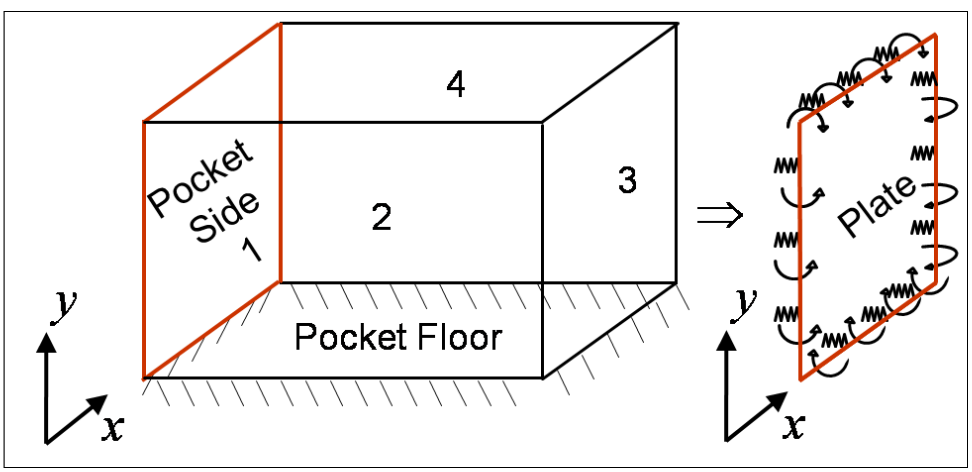

Figure 3.10: Plate representing a side wall of a pocket

The stiffness of the springs is function of the dimensions of the adjacent sides. By properly tuning the values of the springs' stiffness at the edge of the plate, the behaviour of each side of the pocket can be represented. The springs can also take into account the effect of adjacent pockets. In order to tune the values of the stiffness of the springs, virtual experiments, using detailed FE models of the actual workpiece, are performed to determine the dynamic response at representative points on each side of the pocket. By minimizing the error between the response of these points obtained from the FE and the plate models, the optimum values for the boundary springs using global optimization techniques can be determined. The developed model can then be used to predict the response at any point on the sides of the pocket under any time- and position-dependent loads. This model allows the predictions of the dynamic response of the sides of the pocket independently of the other sides of the structure. This, in turn, reduces the computation time.

The integration of this dynamic model in the analysis of the machining and fixture design is shown in the flow chart in Fig. 3.11 and can be described as:

1. The design procedure starts by calibrating the plate model for each pocket-side. The formulation of the thin plate model will be presented in Chapter 4, section 4.3.

2. After calibrating the plate, an optimization process is performed to determine the optimum fixture layout applied on the load-application side while no supports are applied on the adjacent sides nor on the opposite side. In reality, the calibrated stiffness of the plate has to take into account the stiffening effect of the supports applied on the adjacent and opposite sides. As was shown in section 3.2.4, this effect can be neglected at this step of the analysis.

3. Once an optimum layout is determined for all the sides, the values of the stiffness of the springs for a given side are re-calibrated in order to take into account the effect of the fixture layout applied on the opposite and adjacent sides, if necessary.

4. The dynamic response is then integrated with the mechanistic model to predict the final part tolerances and the cutting forces for the suggested fixture layout. This requires the update of the thickness of the load-application side and the adjacent sides. The change of thickness of the load-application side will be simulated by changing the thickness

of the corresponding calibrated plate. The change of thickness of the adjacent sides will be applied by changing the values of the stiffness of the springs according to a relationship that will be established in section 4.3.3.

5. If the final part tolerances, displacements and forces are not within the desired range, the fixture layout is optimized again and steps 2 to 5 are repeated until the displacement, forces and dimensions are within tolerances.

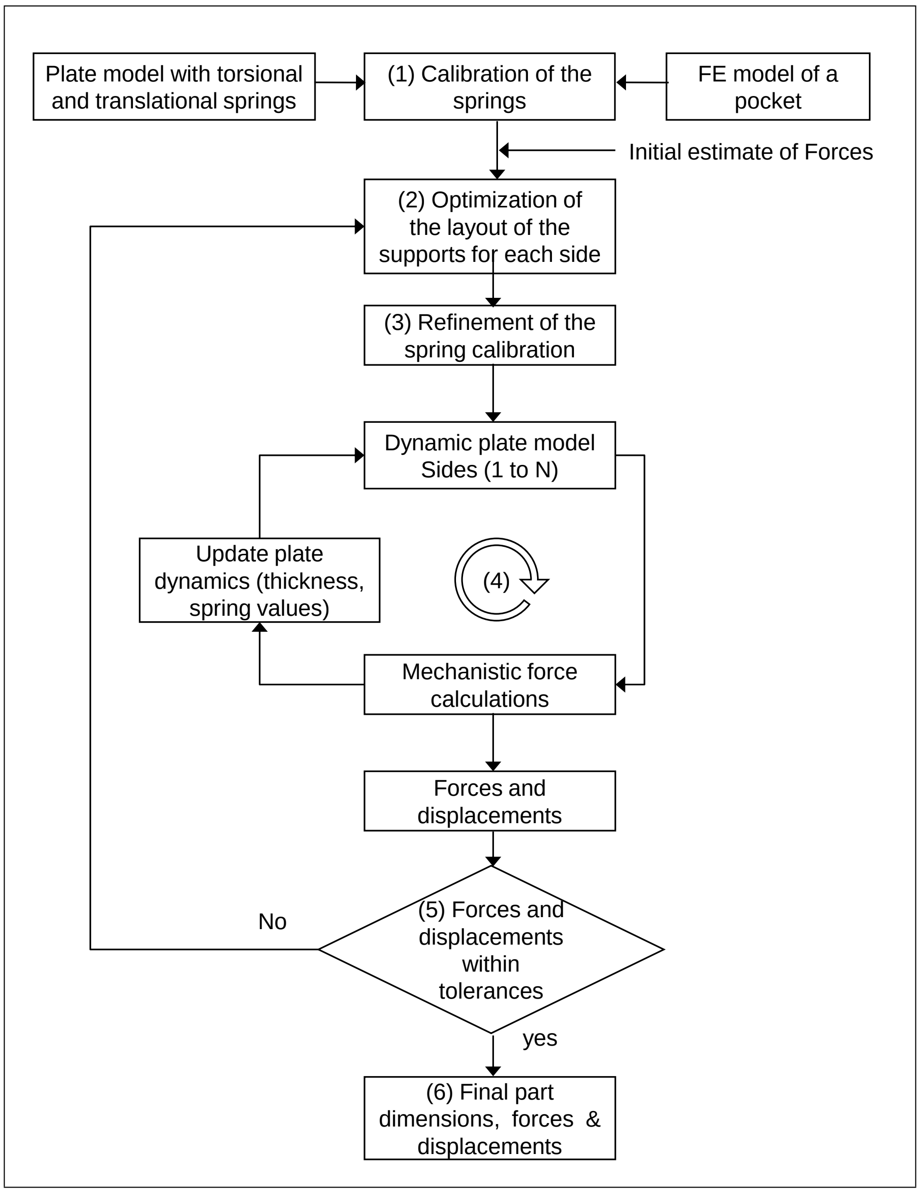

Figure 3.11: Flow chart for the integration of the GSSP model in the analysis of fixtures

3.3.2 Advantages and Limitations of the GSSP Model

There are several advantages for the GSSP model. Unlike a model-order reduction method, when using the GSSP model, the change of thickness of the load-application side or the adjacent and opposite sides does not require the re-evaluation of the dynamics of the whole structure. Instead, the plate parameters will be modified according to established relationships as will be seen in Chapter 4, section 4.3.3. In addition, the computation time is reduced by at least one to two orders of magnitude, as will be shown in Chapter 5. This is due to the fact that only the response of the load-application side is calculated instead of evaluating the response of the whole structure. There is also a limitation to this concept, which is the need to calibrate the stiffness of the springs against FE models. This will slightly reduce the computational efficiency. The additional time associated with the calibration is negligible compared to the reduction of the computation of the model during the optimization of the fixture layout and integration with the mechanistic force models, which require the evaluation of thousands of cases.

3.4 Conceptual Development for the Multi-Span Plate (MSP) Model

As seen from the literature review presented in Chapter 2, using FEM for the calculation of the dynamic response of complex aerospace structural components is computationally extensive. While the GSSP model can offer a new generalized approach to efficiently predict the dynamics of these structures, a calibration of the model parameters is required. To develop a model for complex thin-walled structures without the need for calibration, it is proposed to evaluate the dynamics of each unit-element (pocket) of the structure, without including the stiffening effect from the adjacent pockets.

Although the pocket has a simple geometry as depicted in Fig. 3.1, no exact analytical solution is available to accurately predict its dynamic response within the small computational time frame required in fixture layout optimization schemes and mechanistic force model calculations. Some models were developed in the literature to predict the vibration of box-type structures using approximate techniques. A series solution was developed for symmetrical box-type structures in [131]. For this solution, it was assumed that all edges are simply supported, the corners do not deflect and all corners are at a right angle. Another approximate solution was developed using the Rayleigh-Ritz method and polynomial functions in [132]. The convergence of the solution was based on prior knowledge of the stiffness of the corners of the box. The computational efficiency of this model is relatively poor for interactive applications and is conditional on the presence of simplifying assumptions such as symmetry and uniform thicknesses. Other approximate solutions, which were developed using FEM [133, 134], require the discretization of the structure to a large number of elements, hence the computational efficiency is poor.

3.4.1 Description of the Proposed Concept for the MSP Model

The proposed approach is based on considering the 3D pocket shape as a 2D multi-span plate as shown in Fig. 3.12. The vertical edges of the pocket and the corresponding edges of the multi-span plate are designated by e_0, e_1, e_2, e_3 and e_4. As can be seen, the two edges of the multi-span plate e_0 and e_4 are represented by a single edge $e_{0,4}$ in the pocket. Each side of the pocket and the corresponding span of the plate has four edges: a bottom, a top and two side edges. To accurately represent the dynamics of the pocket, the boundary conditions at each span of the plate have to be equivalent to the boundary conditions at the edges of the pocket. This can be established by analyzing the boundary conditions at the edges of a given side of the pocket and applying similar conditions on the corresponding span of the plate. For example, the boundary conditions at side 2 are:

1. At the bottom edge, clamped boundary conditions are applied (zero displacement and zero rotation about the edge). This is true since the base of the pocket is assumed to be rigidly clamped.

2. At the top edge, free boundary conditions are applied (zero forces and zero moments).

3. For edge e_1, the rotations and bending moments of side 2 and side 1 about e_1 are equal. Similarly, the rotations of side 2 and side 3 about e_2 are also equal.

4. At the edge e_1, the transverse displacement of side 2 is equal to the in-plane displacement of side 1 at the same edge. This would also apply to the transverse displacement of side 2 and the in-plane displacement of side 3 at e_2. The in-plane displacements of side 1 and 3 at e_1 and e_2, respectively, can be assumed to be zero. This is true since the axial (in-plane) stiffness of these sides is relatively high. Thus the transverse displacement of side 2 at e_1 and at e_2 can be neglected and assumed equal to zero.

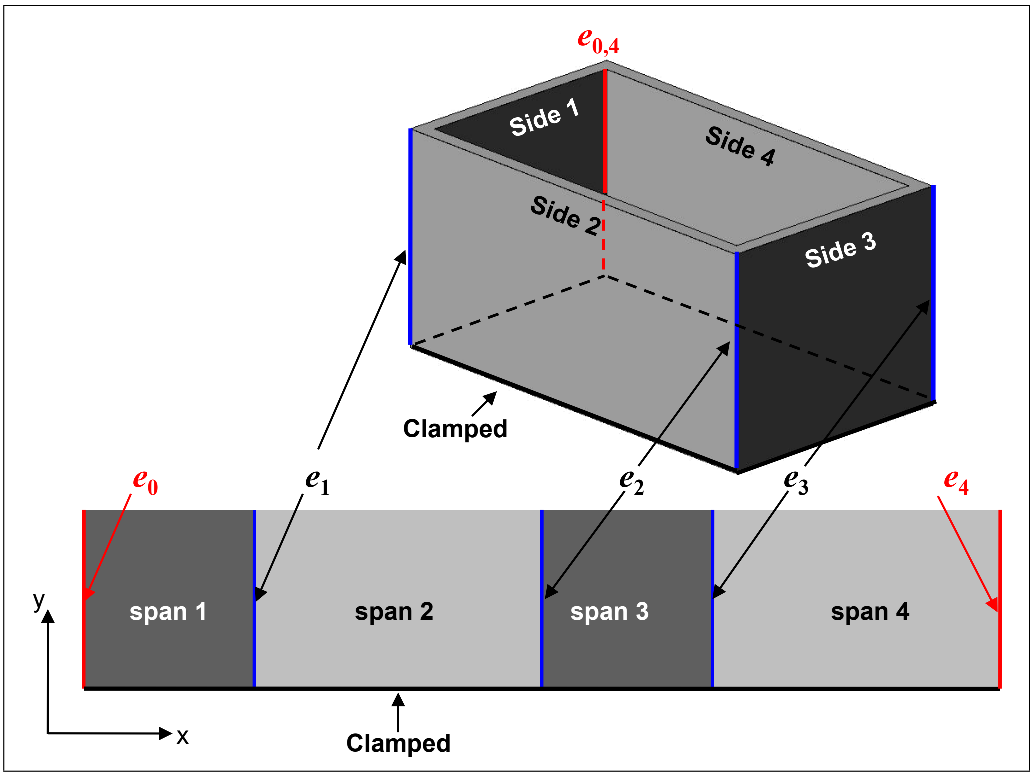

Figure 3.12: Illustration for the representation of a pocket with a multi-span plate

To represent the dynamics of the pocket, the multi-span plate has to have specific boundary conditions for the inner spans (i.e spans 2 and 3) and the outer ones (i.e. spans 1 and 4). For the inner spans, clamped boundary conditions at the bottom edge, free boundary conditions at the top edge, and simply supported boundary conditions at the side (vertical) edges have to be applied. For outer spans, the same boundary conditions are applied except for the outer edges e_0 and e_4. If simply supported boundary conditions are applied at e_0 and e_4 (outer edges), then the multi-span plate will not represent the pocket since the continuity of the rotations and bending moments about edges e_0, e_4 of the pocket will not be satisfied.

Thus, in order to have a close approximation of the pocket response, the displacement at edges e_0 and e_4 have to be equal to zero and the rotations and moments of side 1 about edge e_0 are equal to the rotations and moments of side 4 about edge e_4.

To validate this concept, the frequencies, mode shapes and the responses of various pockets with different aspect ratios and shapes and the corresponding multi-span plates were compared using FE models. Excellent matching of the results was found with errors less than 5% in terms of frequency and response. This analysis will be presented in detail in Chapter 5, section 5.3. Based on this new concept, a mathematical model, which will be referred to as the Multi-Span Plate (MSP) model, will be developed to represent the dynamics of a thin-walled pocket.

3.4.2 Advantages and Limitations of the MSP Model

The main advantage of this model when compared to a FE model is that the computational effort is substantially reduced without loss of accuracy. Reducing the problem from a 3D pocket to a 2D multi-span plate permits the use of an approximate analytical model to predict the response. In addition, with minimal computational efforts, the proposed model can be updated to take into account the effect of the change of thickness of the sides of the pocket.

According to Fig. 3.2, there are three cases for aerospace structural components including single pocket, single pocket with internal rib-walls and multiple pockets. A comparison of the GSSP and the MSP models is shown in Table 3.3 to illustrate the applicability of the proposed models for these cases. Since the GSSP model is more generalized, it can deal with all the cases. The MSP model can deal with the cases of a single pocket and a single pocket with internal rib-walls. In addition, the MSP model can also be used for the case of multiple pockets when the effect of adjacent pockets is negligible. Although the MSP model cannot deal with all the cases, it offers further reduction in the computation time when compared to the GSSP model, since there is no need to calibrate the model.

Table 3.3: Comparison of the GSSP and the MSP models

Case	GSSP model	MSP model
Single pocket	yes	yes
Single pocket with internal rib-walls	yes	yes
Multiple pockets (without the effect of adjacent pockets)	yes	yes
Multiple pockets (with the effect of adjacent pockets)	yes	no

3.5 Special Considerations for the Modelling of the Change of Thickness During Milling of Thin-Walled Pockets

Until this point, the thickness of the sides of the pocket has been assumed to be uniform. However, it is necessary to account for the change of thickness during the milling of thin-walled pockets. One of the features in milling is the gradual change of thickness from the un-machined to the machined area. This change of thickness is shown in Fig. 3.13 for roughing and finishing operations. For roughing operations, the tool diameter and the radial depths of cut are large; consequently, the gradual change of thickness occurs over a large region. For finishing operation, the tool diameter and the radial depths of cut are small. Thus the region for the gradual change of thickness could be represented by a stepped change of thickness between the machined and the un-machined areas.

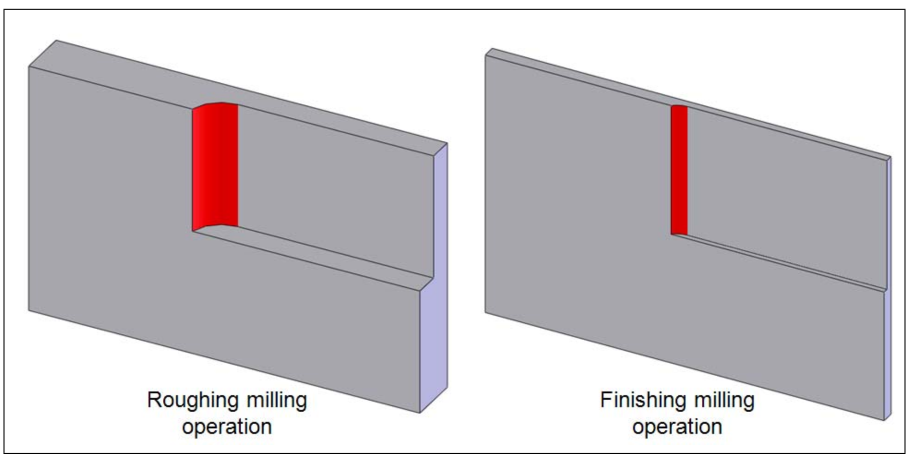

Figure 3.13: Difference between the change of thickness for roughing and finishing operations

The proposed GSSP and MSP models will be based on the theory of plate dynamics. Since plate models are two dimensional, the plate is assumed to be symmetric with respect to its neutral plane. Thus, the thickness from each side of the neutral plane has to be the same. However, in machining applications, the change of thickness occurs from one side only. The difference between these two cases is illustrated in Fig. 3.14. Since the change of thickness in the finishing operations of thin-walled structures is relatively small compared to the thickness of the wall, it is assumed that the symmetric change of thickness with respect to the neutral plane is sufficient to capture the changes in the dynamic behaviour of the workpiece during machining.

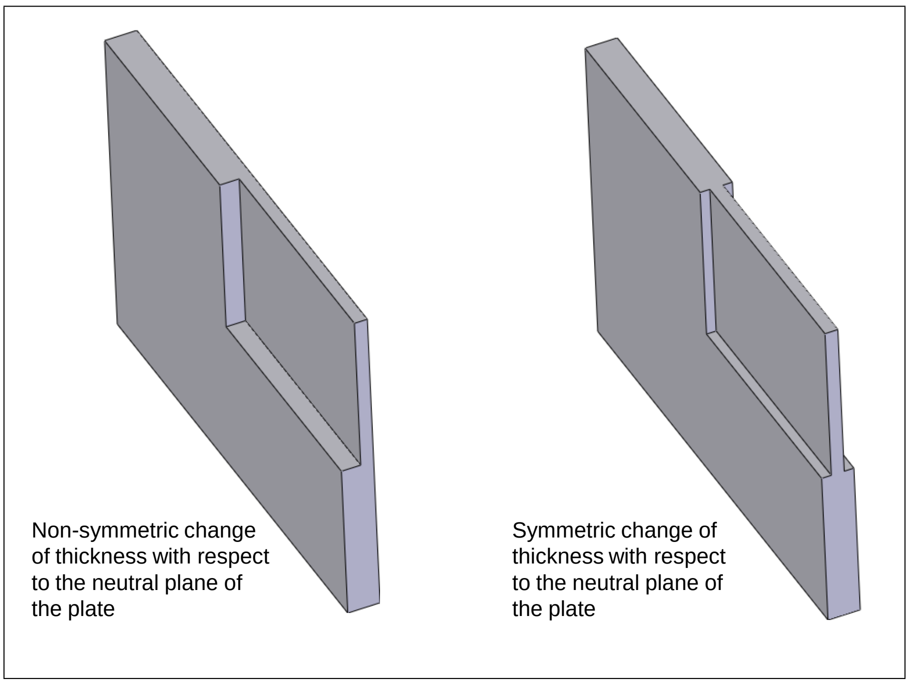

Figure 3.14: Representation of the non-symmetric and the symmetric change of thickness with respect to the neutral plane of a plate

To validate this assumption, a 3D FE model was constructed for two plates with symmetric and non-symmetric changes of thickness with respect to their neutral plane. The dimensions of the two plates are shown in Fig. 3.15(a), and Fig. 3.15(b). The two side edges and the bottom edge of the plates are clamped and the top edge is free. A load of 50 N amplitude and 1256 rad/s frequency was applied at the middle of the top free edge as indicated by the arrows and the circles. The displacement was calculated at the point of load application since it represents the location of maximum deflection. The 3D FE model was developed using 4-node brick elements and Aluminum material properties (refer to section 3.2). The responses for the two cases are shown in Fig. 3.15(c). As can be seen, an excellent matching in response is achieved with errors less than 1.5% in terms of the maximum amplitude of vibration even when the change of thickness was as large as 25% (4 mm to 3 mm). In addition, as will be shown in Chapter 6, the developed models, which are based on this assumption, produced excellent matching between the model and the experimental results.

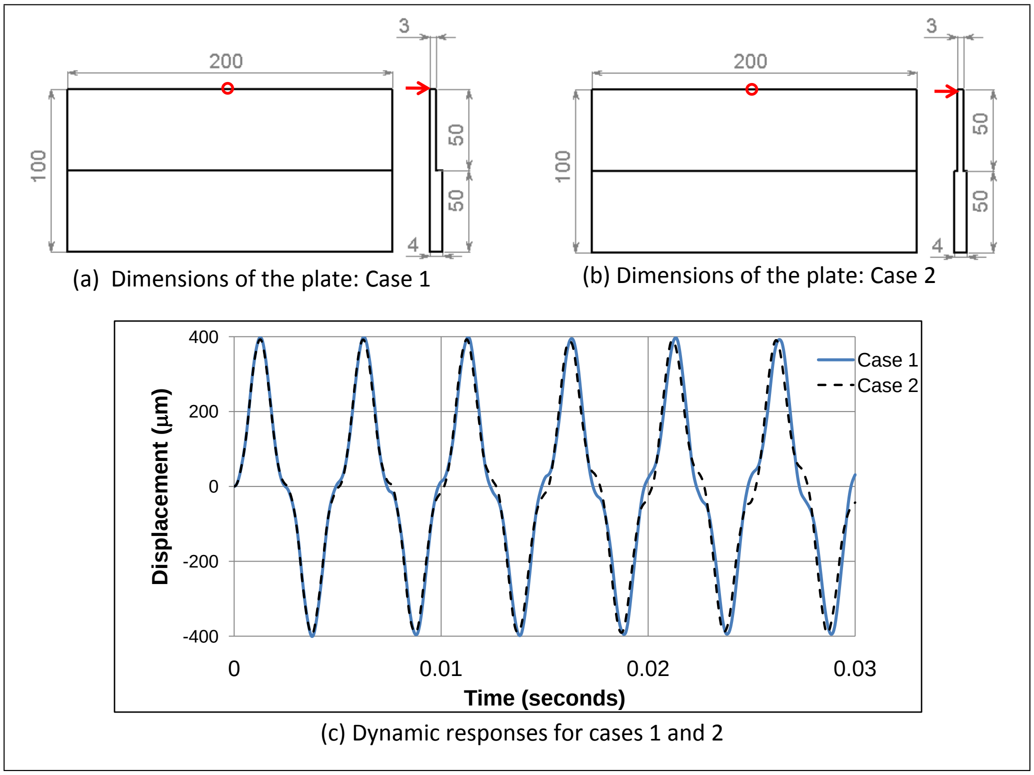

Figure 3.15: Effect of non-symmetric and symmetric change of thickness on the response of a rectangular plate

In order to track the change of thickness during machining, one has to investigate the common tool-paths used for machining thin-walled structures. Figure 3.16 presents an illustration of possible cases for the change of thickness corresponding to different tool-paths during machining of a pocket-side. Although these cases do not represent all conceivable tool-paths, they cover the main ones encountered in practice for finishing of pockets. Case A represents a machining tool-path where the tool moves vertically, thus removing a uniform Vertical strip (VS) or when it moves horizontally with a depth of cut equal to the full depth of the pocket. For Case B, at a given depth, the tool follows a horizontal path, thus removing a Horizontal strip (HS) along the whole width of the side. Cases A and B represent the situations when the change of thickness during milling is small relative to the original thickness of the pocket-side, and thus it is only required to track the change of the workpiece dynamics at the end of each tool path. Cases C and D represent the machining of a side of a pocket by removing either a Corner strip (CS) or an L-shaped strip (LS). These two cases can represent the change of thickness as the tool moves between two points within the tool-path. To represent these four cases, it is necessary to divide the pocket-side into two spans in the x-direction and three spans in the y-direction, as shown by the dashed lines in Fig. 3.16. The spans do not have to be equal to each other.

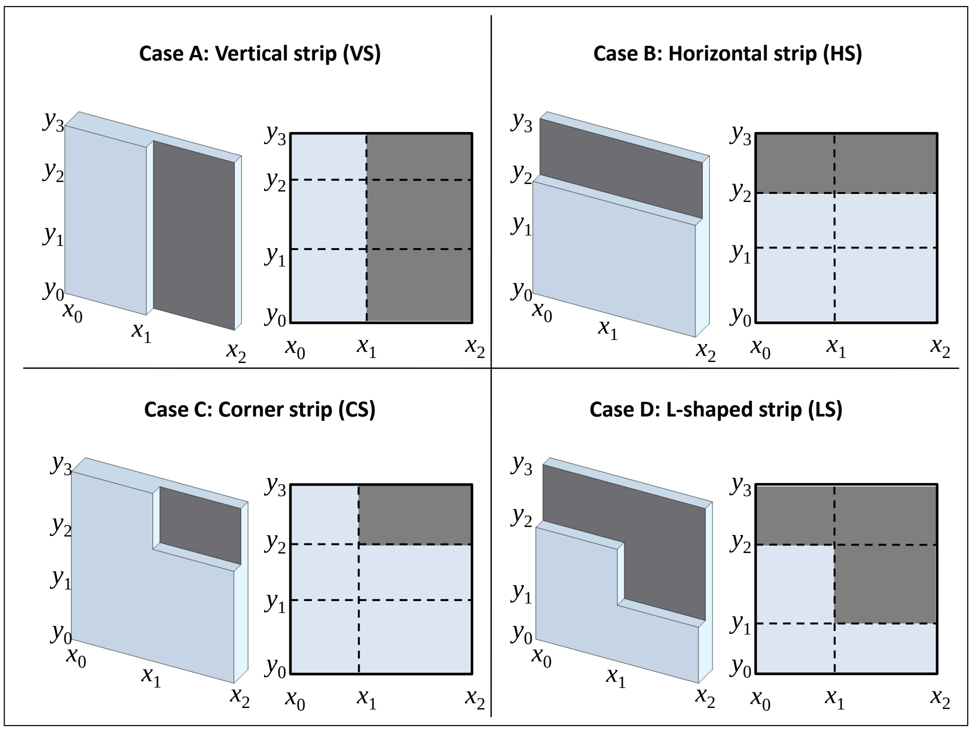

Figure 3.16: Representation of the different cases for the change of thickness

3.6 Review of Methods and Approximation Techniques for Modelling the Dynamics of Plates

The proposed concepts for the GSSP and the MSP models are based on the dynamics of plates. Consequently, a review of the available models in the literature for rectangular plates and multi-span plates is performed to identify the most suitable modelling technique for each model.

3.6.1 Models for Plates with Torsional and Translation Springs

The GSSP model is based on representing the dynamics of a plate with uniformly distributed translational and rotational springs along the four boundaries. An analytical solution for this problem can be obtained by using the superposition method [135]. To apply this method, the problem has to be broken down to several other plate problems with standard boundary conditions. For each of these plates, it is required to solve an eigenvalue problem. Consequently, the computation time is relatively high compared to other approximation techniques.

Some of the common approximation techniques are Rayleigh's energy and the Rayleigh-Ritz methods. Both these methods require the approximation of the mode shapes of the structure. A solution for the frequencies of plates with standard boundary conditions (free, simply supported, clamped) was developed using Rayleigh's energy method and beam mode shapes in [136, 137, 138]. It was shown that beam mode shapes provided good approximation for the plate modes for standard boundary conditions. Better approximations can be obtained by using the Rayleigh-Ritz method; however the computation time is slightly increased [136].

Many models are available for elastically restrained plates using the Rayleigh-Ritz method. Several types of functions can be used to approximate the plate mode shapes including polynomial functions and beam mode shapes. By using polynomial functions, models have been developed for plates with either uniform thickness [139, 140, 141], stepped thickness [142, 143], or uniformly varying thickness [144]. In addition, models have been developed for plates with concentrated masses or springs [140, 145, 146] and for plates with uniformly distributed springs [147, 148]. A commonly used beam mode shape to approximate the mode shapes of elastically restrained plates is the one of the free-free beam model [132]. To obtain better approximation of the mode shapes of the plate, beam mode shapes for a beam model with rotational springs at the boundaries can also be used [149].

Based on this review, one can conclude that the Rayleigh-Ritz method is commonly used to approximate the frequencies and the dynamic response of plates. However, the computational efficiency of Rayleigh's energy method was found attractive for the formulation of the GSSP model, given the requirement for an off-line calibration of the model parameters. The main drawback of Rayleigh's energy method is its sensitivity to the choice of trial functions. Thus, it is necessary to select trial functions that closely resemble the actual mode shapes of the structure in order to obtain accurate results. Both Rayleigh's energy and the Rayleigh-Ritz methods will be used for the development of the GSSP model.

3.6.2 Models for Multi-Span (Continuous) Plates

For the MSP model, it is necessary to identify exact or approximate techniques to represent a multi-span plate with the previously described boundary conditions. It is helpful to specify the designation for the different edges of a multi-span plate. As shown in Fig. 3.12, a four-span plate has two horizontal edges (bottom and top edges) and five vertical edges.

An exact solution exists for multi-span plates that are simply supported at all edges [150, 151]. Elishakoff and Sternberg [152] developed an approximate solution for multi-span plates, clamped at the bottom and top edges, and simply supported at the inner vertical edges, using the modified Boltin' method. Various boundary conditions were applied on the outer vertical edges. Gorman and Garibaldi [153] proposed a model based on the superposition method for multi-span plates with simply supported conditions for the vertical edges and free boundary conditions for the bottom and top edges.

Some researchers used the Rayleigh-Ritz method to approximate the frequencies and the response of multi-span plates. Ercoli and Laura [154, 155] developed a model to approximate a multi-span plate with simply-supported bottom and top edges and elastically restrained vertical edges using the Rayleigh-Ritz method. Marchesiello *et al.* [156] used the Rayleigh-Ritz method to predict the response of multi-span plates with a moving load. Different studies were performed to compare these solutions with FEM results. It was found that the Rayleigh-Ritz method can offer good results for simply supported plates; however, the errors were large when the outer vertical edges are clamped [157, 158].

One of the available techniques, similar to the FEM, to predict the dynamics of multi-span plates, is the Finite Strip method (FSM) [159]. This method is mainly intended for structures which are uniform in one direction. In the other direction, the structure is discretized into small vertical strips. The solution is developed by assembling all the elements and solving for the displacement at the nodes of each strip. The FSM was used by several researchers to develop solutions for multi-span plates with various boundary conditions [160, 161, 162, 163]. This method is not suitable for predicting the dynamics of thin-walled structures during milling since, due to the change of thickness, the structure is not uniform in any direction.

According to this review, one can see that exact solutions are available for a limited number of cases of multi-span plates. For the other cases, approximate techniques, such as the FEM or the FSM, are used. These methods have low computational efficiency. Several models were developed using the Rayleigh-Ritz method. These models used local polynomial functions defined for each span separately to approximate the mode shapes of the multi-span plate. These models seem to provide accurate solutions with reduced computational effort. Consequently, it was decided to use the Rayleigh-Ritz method to model multi-span plates. However, a new set of trial functions, based on multi-span beam models, are used to approximate the mode shape of a multi-span plate. Using these trial functions, fewer modes are needed to approximate the frequencies and the response of the multi-span plate. Consequently, the computational efficiency of the model is further improved. For the same trial functions, the solution will also be developed using Rayleigh's energy method since it provides additional reductions in computation time. A comparison between Rayleigh's energy method and the Rayleigh-Ritz method will be performed.

3.7 Concluding Remarks

In this chapter, different aerospace structural components were analyzed. These components were broken down to unit-elements with the shape of a pocket. Two concepts were proposed for the representation of the dynamics of the unit-element. The first concept is based on discretizing the pocket into four sides, which are represented by a plate with torsional and translational springs. These springs take into account the effect of the adjacent sides. The second concept is based on representing the unit-element by a multi-span plate. The boundary conditions for the pocket are studied and accordingly corresponding boundary conditions are applied to the multi-span plate. In addition, the change of thickness of thin-walled workpieces was analyzed and some simplifying assumptions for the problem were made. Finally, a review of plate models is performed; Rayleigh'Energy method and the Rayleigh-Ritz method are chosen for the development of the mathematical models.

Chapter 4

Mathematical Formulations of the Proposed Dynamic Models

4.1 Introduction

In the previous chapter, different concepts were introduced for the representation of the dynamics of thin-walled structures and the change of thickness during milling. These concepts are essentially based on plate dynamics. In this chapter, the mathematical formulation for the different models will be detailed. The equations for a general plate model will be presented first, followed by a description of the approximation techniques used to predict the response. Based on these approximation techniques, the Generalized Single-Span Plate (GSSP) and the Multi-Span Plate (MSP) models will be developed. This will be followed by the modelling of the change of thickness of a pocket-side and the mathematical formulations for rigid and flexible supports.

4.2 Mathematical Formulation of a Rectangular Plate Model

Based on the Euler-Bernoulli assumptions, the transverse vibration of a thin-plate is given by the following fourth-order, partial differential equation [128]:

$$D_E(\frac{\partial^4 w}{\partial x^4} + \frac{\partial^4 w}{\partial x^2 \partial y^2} + \frac{\partial^4 w}{\partial y^4}) + f_p(x, y, t) = m\frac{\partial^2 w}{\partial t^2} \tag{4.1}$$

where x and y are the spatial coordinates, t is the time, m is the mass per unit area of the plate, $w(x, y, t)$ is the transverse displacement, $f_p(x, y, t)$ is the distributed applied force, and D_E is the plate flexural rigidity expressed as:

$$D_E = \frac{Eh^3}{12(1 - \nu^2)} \tag{4.2}$$

where E is the Young modulus, ν is the Poisson ratio, h is the plate thickness and l_x and l_y are the dimensions of the plate in the x- and y-directions, respectively. The response of the transverse vibration of the plate is given by:

$$w(x, y, t) = \sum_{r=1}^{\infty} W_r(x, y)\eta_r(t) \tag{4.3}$$

where W_r are the exact orthogonal plate mode shapes and η_r represents the generalized modal coordinates, which are functions of time. The exact plate mode shapes are defined by satisfying the boundary conditions of the plate. In many instances, the development of exact mode shapes is not possible. Instead, approximate shape functions which satisfy the geometric boundary conditions are used together with approximation techniques in order to determine the frequencies and the response of the system.

4.2.1 Rayleigh's Energy Method

Rayleigh's energy method is based on Rayleigh's principle which is stated as follows: "The frequency of vibration of a conservative system vibrating about an equilibrium position has a stationary value in the neighbourhood of a natural mode" [124]. Rayleigh's energy method is mainly used for the approximation of the first natural frequency of a system. The method relies on the assumption that natural modes exhibit a harmonic motion. Thus, the transverse free vibration response of a rectangular plate can be expressed as:

$$w(x, y, t) = W(x, y)\Omega(t) \tag{4.4}$$

where W represents the maximum displacement at point (x,y) and Ω is a time-dependent harmonic function. The kinetic energy of the system can be written as

$$T(t) = \frac{1}{2}m\int_0^{l_x}\int_0^{l_y} w^2 dydx = \frac{1}{2}m\dot{\Omega}^2(t)\int_0^{l_x}\int_0^{l_y} W^2 dydx \tag{4.5}$$

If the harmonic function has a frequency ω, then the maximum kinetic energy can be written as:

$$T_{max} = T^*\omega^2 \tag{4.6}$$

where T^* is the reference kinetic energy expressed as:

$$T^* = \frac{1}{2}m\int_0^{l_x}\int_0^{l_y} W^2 dydx \tag{4.7}$$

The strain energy of the plate is written as:

$$U(t) = \frac{1}{2}\int_0^{l_x}\int_0^{l_y} D_E\left[\left(\frac{\partial^2 w}{\partial x^2}\right)^2 + \left(\frac{\partial^2 w}{\partial y^2}\right)^2 + 2\nu\frac{\partial^2 w}{\partial x^2}\frac{\partial^2 w}{\partial y^2} + 2(1-\nu)\left(\frac{\partial^2 w}{\partial x\partial y}\right)^2\right] dydx \tag{4.8}$$

The maximum strain energy is given by:

$$U_{max} = \frac{1}{2}\int_0^{l_x}\int_0^{l_y} D_E\left[\left(\frac{\partial^2 W}{\partial x^2}\right)^2 + \left(\frac{\partial^2 W}{\partial y^2}\right)^2 + 2\nu\frac{\partial^2 W}{\partial x^2}\frac{\partial^2 W}{\partial y^2} + 2(1-\nu)\left(\frac{\partial^2 W}{\partial x\partial y}\right)^2\right] dydx \tag{4.9}$$

Based on the principle of conservation of energy:

$$T_{max} = V_{max} \tag{4.10}$$

where V_{max} is the maximum potential energy due to the strain energy of the plate and the work of conservative forces.

In the absence of conservative forces (e.g. spring forces), the potential energy is equal to the strain energy. By introducing Eqs. (4.6) in (4.10), and assuming the potential energy is equal to the strain energy, the following equation is obtained:

$$\omega^2 = \frac{V_{max}}{T^*} = \frac{U_{max}}{T^*} \tag{4.11}$$

This equation can be recognized as Rayleigh's quotient. To approximate the first natural frequency of the plate, an approximate shape function, satisfying the geometrical boundary conditions of the first mode, has to be substituted for W. It was shown that the frequencies of higher modes could also be predicted by assuming shape functions which closely approximate the corresponding mode shapes of the system and substituting them in Rayleigh's quotient [136]. In this case, the approximate r^{th} natural frequency $\tilde{\omega}_r$ of the system can be determined by substituting W in Eqs. (4.6) and (4.9) by a trial function $\tilde{W}_r$ and substituting these equations in Eq. (4.11). The trial function $\tilde{W}_r$ approximates the corresponding exact mode shape W_r.

By using a series of the space dependent trial functions multiplied by time-dependent generalized coordinates, the transverse vibration response of the plate could be approximated as:

$$\tilde{w}(x,y,t) = \sum_{r=1}^{n} \tilde{W}_r(x,y) q_r(t) \tag{4.12}$$

where n is the total number of included mode shapes and q_r represents the generalized coordinates, which are function of time. Since the trial function $\tilde{W}_r$ closely approximates the corresponding exact mode shape of the plate, one can assume the following orthogonality properties:

$$\int_0^{l_x} \int_0^{l_y} \tilde{W}_r m \tilde{W}_s dydx = \delta_{rs} \qquad r,s = 1,2,... \tag{4.13a}$$

$$\int_0^{l_x} \int_0^{l_y} \tilde{W}_r D_E \left(\frac{\partial^4 \tilde{W}_s}{\partial x^4} + \frac{\partial^4 \tilde{W}_s}{\partial x^2 \partial y^2} + \frac{\partial^4 \tilde{W}_s}{\partial y^4} \right) dydx = \tilde{\omega}_r \delta_{rs} \qquad r,s = 1,2,... \tag{4.13b}$$

where δ_{rs} is the Kronecher delta. By using these orthogonality properties, inserting Eq. (4.12) in (4.1), multiplying by $\tilde{W}_r$ and integrating over the entire domain of the plate (x- and y-directions), the following set of decoupled equations is obtained:

$$\ddot{q}_r + \tilde{\omega}_r^2 q_r(t) = Q_r(t) \tag{4.14}$$

The generalized forces Q_r can be expressed as:

$$Q_r = \int_{A_l} f_p \tilde{W}_r dA_l \tag{4.15}$$

where A_l is the surface of application of the load.

4.2.2 Rayleigh-Ritz Method

In the Rayleigh-Ritz method, the transverse vibration of the plate with standard boundary conditions can be expressed using Eq. (4.12) similar to Rayleigh's energy method. However, in the Rayleigh-Ritz method, one does not assume that the trial functions have the same orthogonality properties as in Eq. (4.13). The equations of motion of the discretized system can be derived using Lagrange's equations, which are expressed as:

$$\frac{d}{dt}\left(\frac{\partial T}{\partial \dot{q}_r}\right) - \left(\frac{\partial T}{\partial q_r}\right) + \left(\frac{\partial V}{\partial q_r}\right) = Q_r \tag{4.16}$$

where T is the kinetic energy of the plate, V is the total potential energy including the work of conservative forces and the strain energy of the plate and Q_r represents the non-conservative generalized forces. The kinetic and potential energy of the system are determined by substituting w in Eqs (4.5) and (4.8) by $\tilde{w}$ from Eq. (4.12). By inserting the expressions for the kinetic and the potential energy of the plate in Eq. (4.16), the following equations of motions of the system are obtained:

$$\boldsymbol{M}\ddot{\boldsymbol{q}} + \boldsymbol{K}\boldsymbol{q} = \boldsymbol{Q} \tag{4.17}$$

where $\boldsymbol{M}$ and $\boldsymbol{K}$ are the mass and stiffness matrices of the system, $\boldsymbol{q} = [q_1, q_2, ..., q_n]^T$ is the vector of generalized coordinates and $\boldsymbol{Q} = [Q_1, Q_2, ..., Q_n]^T$ is the vector of generalized forces, which can be expressed as:

$$\boldsymbol{Q} = \int_{A_l} f_p(x, y, t)\tilde{\boldsymbol{W}} dA_l \tag{4.18}$$

where $\tilde{\boldsymbol{W}}$ is the vector of trial functions $[\tilde{W}_1, \tilde{W}_2, ..., \tilde{W}_r]^T$.

For a harmonic motion, the solution of $\boldsymbol{q}$ has the following form:

$$\boldsymbol{q} = \bar{\boldsymbol{q}} e^{i\tilde{\omega}t} \tag{4.19}$$

where $\bar{\boldsymbol{q}}$ is a constant vector and $\tilde{\omega}$ is the approximate frequency of the vibration of the plate. The eigenvalue problem can be expressed as:

$$\boldsymbol{K}\bar{\boldsymbol{q}} = \lambda \boldsymbol{M}\bar{\boldsymbol{q}} \tag{4.20}$$

where

$$\lambda = \tilde{\omega}^2 \tag{4.21}$$

By solving the eigenvalue problem, the natural frequencies of the system can be determined. To calculate the time response of the system, one has to solve for $\boldsymbol{q}$ in Eq. (4.17). If the non-diagonal terms in the mass and stiffness matrices are neglected, then the equations become decoupled and we obtain a model that is equivalent to the one which results from the application of Rayleigh'Energy method. When the non-diagonal term are small compared to the diagonal terms, Rayleigh's energy and the Rayleigh-Ritz methods yield similar results.

4.3 Mathematical Formulation of the Generalized Single-Span Plate (GSSP) Model

The GSSP model requires the modelling of a rectangular plate with flexible supports along its boundaries as shown in Fig. 4.1(a). The symbols K_{xo}, R_{xo}, K_{xl}, and R_{xl} refer to the torsional and translation springs per unit length at $x = 0$ and $x = l_x$, respectively. Similarly, K_{yo}, R_{yo}, K_{yl}, and R_{yl} are the torsional and translation springs per unit length at $y = 0$ and $y = l_y$, respectively. Two natural boundary conditions for the balance of the shear forces and the bending moments have to be specified at each edge. These are presented in detail in Appendix A, section A.1.

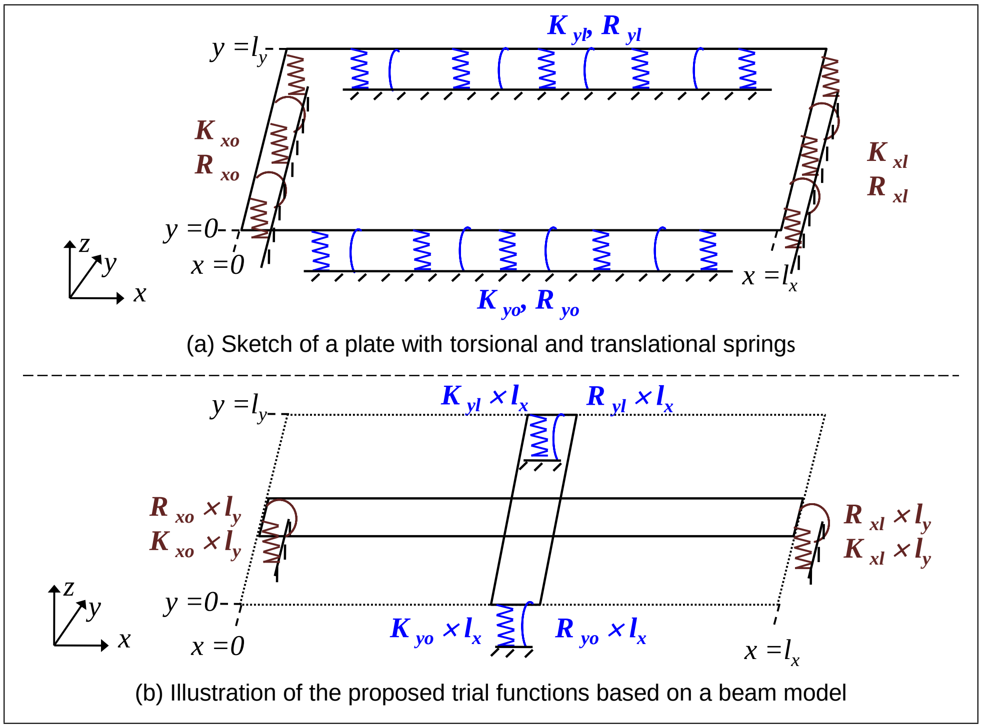

Figure 4.1: Illustration of a rectangular plate with torsional and translational springs and the proposed beam models

4.3.1 Generation of the Trial Functions for the GSSP Model

As mentioned previously, both Rayleigh's energy and the Rayleigh-Ritz methods require trial functions to approximate the mode shapes of the plate. Using separation of variables, a trial function can be expressed as:

$$\overline{W}_{ij} = \overline{X}_i(x)\overline{Y}_j(y) \tag{4.22}$$

where $\overline{X}_i$ and $\overline{Y}_j$ are trial functions in the x- and y-directions, respectively. The functions $\overline{X}_i$ and $\overline{Y}_j$ are generated using the i^{th} and j^{th} mode shapes of a beam model. Instead of using the traditional trial mode shapes based on a free-free beam model [132], the trial functions in the x- and y-directions are generated based on an Euler-Bernoulli beam model with torsional and translational springs at the boundaries, as shown in Fig. 4.1(b). These trial functions allow a good approximation of the plate mode shapes since they closely represent the natural boundary conditions at the edges of the plate.

The transverse motion of an Euler-Bernoulli beam model with a uniform cross section is described by the following equation [128]:

$$\rho A_b \frac{\partial^2 z}{\partial t^2} + EI \frac{\partial^4 z}{\partial u^4} = f(u,t) \tag{4.23}$$

where u represents the spatial coordinate along the neutral axis of the beam with length l_u, $z(u,t)$ is the transverse displacement, $f(u,t)$ is a distributed applied force, ρ is the density, A_b is the cross sectional area of the beam, and I is the second moment of area. The dynamic boundary conditions for the force and moment balances of the beam with torsional and translational springs at $u = 0$, respectively, can be written as:

$$EI \left. \frac{\partial^3 z}{\partial u^3} \right|_{u=0} + k_o \left. z \right|_{u=0} = 0, \tag{4.24a}$$

$$EI \left. \frac{\partial^2 z}{\partial u^2} \right|_{u=0} - r_o \left. \frac{\partial z}{\partial u} \right|_{u=0} = 0 \tag{4.24b}$$

where k_o and r_o are the translational and rotational springs at $u = 0$, respectively. Similarly, the force and moment balances at $u = l_u$ result in the following boundary conditions:

$$EI \left. \frac{\partial^3 z}{\partial u^3} \right|_{u=l_u} - k_l \left. z \right|_{u=l_u} = 0 \tag{4.25a}$$

$$EI \left. \frac{\partial^2 z}{\partial u^2} \right|_{u=l_u} + r_l \left. \frac{\partial z}{\partial u} \right|_{u=l_u} = 0 \tag{4.25b}$$

where k_l and r_l are the translational and rotational spring coefficients at $u = l_u$, respectively. To determine the solution of this problem, the method of separation of variables is used such that:

$$z(u,t) = Z(u)\theta(t) \tag{4.26}$$

where $Z(u)$ represents the spatial dependence and θ gives the time dependence. By inserting Eq. (4.26) into Eq. (4.23) and rearranging the terms, the following equations can be obtained:

$$\frac{EIZ''''(u)}{\rho A_b Z(u)} = -\frac{\ddot{\theta}}{\theta} = \omega_u^2 \tag{4.27}$$

where ω_u is the unknown natural frequency. The prime refers to the derivative with respect to the spatial coordinate u. Eq. (4.27) leads to an initial value problem and a spatial boundary-value problem which can be expressed as:

$$\frac{d^4 Z}{du^4} - \beta^4 Z(u) = 0 \tag{4.28}$$

where

$$\beta^4 = \frac{\rho A_b \omega_u^2}{EI} \tag{4.29}$$

By inserting Eq. (4.26) in Eqs. (4.24)-(4.25), the boundary conditions for the spatial boundary-value problem are obtained:

At $u = 0$:

$$EI \left.\frac{d^3 Z}{du^3}\right|_{u=0} + k_o \left. Z\right|_{u=0} = 0, \tag{4.30a}$$

$$EI \left.\frac{d^2 Z}{du^2}\right|_{u=0} - r_o \left.\frac{dZ}{du}\right|_{u=0} = 0 \tag{4.30b}$$

At $u = l_u$

$$EI \left.\frac{d^3 Z}{du^3}\right|_{u=l_u} - k_l \left. Z\right|_{u=l_u} = 0 \tag{4.31a}$$

$$EI \left.\frac{d^2 Z}{du^2}\right|_{u=l_u} + r_l \left.\frac{dZ}{du}\right|_{u=l_u} = 0 \tag{4.31b}$$

The solution for the boundary-value problem has the following form:

$$Z(u) = A\sin(\beta u) + B\cos(\beta u) + C\sinh(\beta u) + D\cosh(\beta u) \tag{4.32}$$

By inserting Eq. (4.32) in Eqs. (4.30) and (4.31), the characteristic equation of the boundary value problem is determined. The solution of this equation gives an infinite set of eigenfunctions (mode shapes) and natural frequencies. The mode shapes are expressed as:

$$Z_r(u) = A_r\sin(\beta_r u) + B_r\cos(\beta_r u) + C_r\sinh(\beta_r u) + D_r\cosh(\beta_r u) \tag{4.33}$$

where

$$\beta_r^4 = \frac{\rho A_b \omega_{ur}^2}{EI} \tag{4.34}$$

in which ω_{ur} is the r^{th} natural frequency of the beam. The expressions for the characteristic equations and for the coefficients B_r, C_r and D_r are detailed in Appendix A, section A.2. The coefficients A_r are determined through normalization.

The beam mode shapes are substituted in the trial functions $\overline{X}_i$ and $\overline{Y}_j$ in Eq. (4.22) by replacing the variables in Eqs. (4.24)-(4.33) according to Table 4.1. This represents the parameter mapping between the plate trial functions and the calculated modes based on the beam models.

Table 4.1: Parameter mapping for the beam mode shapes

$Z_r(u)$	r	l_u	I	k_o	k_l	r_o	r_l
$\overline{X}_i(x)$	i	l_x	$\frac{1}{12}l_y h^3$	$K_{xo}l_y$	$K_{xl}l_y$	$R_{xo}l_y$	$R_{xl}l_y$
$\overline{Y}_j(y)$	j	l_y	$\frac{1}{12}l_x h^3$	$K_{yo}l_x$	$K_{yl}l_x$	$R_{yo}l_x$	$R_{yl}l_x$

To apply Rayleigh's energy method, Eq. (4.22) is substituted in Eqs. (4.6) and (4.9) to calculate the reference kinetic energy and the maximum strain energy, respectively. The expression for the reference kinetic energy of the approximate mode shape $\overline{W}_{ij}$ is:

$$\overline{T}_{ij} = \frac{1}{2}\int_0^{l_x}\int_0^{l_y} m\overline{W}_{ij}^2 dydx \tag{4.35}$$

Similarly, the maximum strain energy of the approximate mode shape $\overline{W}_{ij}$ is:

$$\overline{U}_{ij} = \frac{1}{2}\int_0^{l_x}\int_0^{l_y} D_E\left[\left(\frac{\partial^2\overline{W}_{ij}}{\partial x^2}\right)^2 + \left(\frac{\partial^2\overline{W}_{ij}}{\partial y^2}\right)^2 + 2\nu\frac{\partial^2\overline{W}_{ij}}{\partial x^2}\frac{\partial^2\overline{W}_{ij}}{\partial y^2} + 2(1-\nu)\left(\frac{\partial^2\overline{W}_{ij}}{\partial x\partial y}\right)^2\right] dydx \tag{4.36}$$

It is also necessary to account for the potential energy due to the stiffness of the springs at the boundaries of the plate. The maximum potential energy due to the springs at $x = 0,\ l_x$ can be expressed as:

$$\overline{P}_{xij} = \frac{1}{2}\int_0^{l_y}\left[K_{xo}\overline{W}_{ij}(0,y)^2 + R_{xo}\left(\frac{\partial\overline{W}_{ij}(0,y)}{\partial x}\right)^2 + K_{xl}\overline{W}_{ij}(l_x,y)^2 + R_{xl}\left(\frac{\partial\overline{W}_{ij}(l_x,y)}{\partial x}\right)^2\right] dy \tag{4.37}$$

Similarly, the maximum potential energy due to the springs at $y = 0$, l_y can be expressed as:

$$\overline{P}_{yij} = \frac{1}{2}\int_0^{l_x} \left[K_{yo}\overline{W}_{ij}(x,0)^2 + R_{yo}\left(\frac{\partial \overline{W}_{ij}(x,0)}{\partial y}\right)^2 + K_{yl}\overline{W}_{ij}(x,l_y)^2 + R_{yl}\left(\frac{\partial \overline{W}_{ij}(x,l_y)}{\partial y}\right)^2 \right] dx \tag{4.38}$$

According to Rayleigh's energy method (refer to Eq. (4.11)), the natural frequency of the plate can be approximated as:

$$\overline{\omega}_{ij}^2 = \frac{\overline{U}_{ij} + \overline{P}_{xij} + \overline{P}_{yij}}{\overline{T}_{ij}} \tag{4.39}$$

A vector $\overline{\boldsymbol{W}}$ of the trial functions $\overline{W}_{ij}$ is defined such that the trial functions are listed in ascending order of their corresponding approximate natural frequencies. For m and l trial functions in the x- and y-directions, respectively, the dimensions of $\overline{\boldsymbol{W}}$ are $(ml \times 1)$. To generate a model with n degrees of freedom, the first n trial functions of the vector $\overline{\boldsymbol{W}}$ are selected and are referred to as $\tilde{W}_r$, for $r = 1, 2, ..., n$. The response of the plate can be approximated using Eq. (4.12). It has to be noted that n has to be less or equal to $m \times l$. The first n approximate frequencies are designated by $\tilde{\omega}_r$, for $r = 1, 2, ..., n$.

To implement the Rayleigh-Ritz method, the kinetic and the strain energies of the plate are calculated by substituting Eq. (4.12) in Eqs. (4.5) and (4.8), respectively. The total potential energy of the plate can be expressed as:

$$V = U + P_x + P_y \tag{4.40}$$

where P_x and P_y are the potential energy terms of the springs at the edges $x = 0$, $x = x_l$ and $y = 0$, $y = y_l$, respectively and they can be calculated as follows :

$$P_x = \frac{1}{2}\int_0^{l_y} \left[K_{xo}\tilde{w}(0,y)^2 + R_{xo}\left(\frac{\partial \tilde{w}(0,y)}{\partial x}\right)^2 + K_{xl}\tilde{w}(l_x,y)^2 + R_{xl}\left(\frac{\partial \tilde{w}(l_x,y)}{\partial x}\right)^2 \right] dy \tag{4.41}$$

and

$$P_y = \frac{1}{2}\int_0^{l_x} \left[K_{yo}\tilde{w}(x,0)^2 + R_{yo}\left(\frac{\partial \tilde{w}(x,0)}{\partial y}\right)^2 + K_{yl}\tilde{w}(x,l_y)^2 + R_{yl}\left(\frac{\partial \tilde{w}(x,l_y)}{\partial y}\right)^2 \right] dx \tag{4.42}$$

Substituting the total potential energy and the kinetic energy in Eq. (4.16), the mass and stiffness matrices are calculated according to Eq. (4.17). The approximate frequencies of the plate and the modal matrix are determined by solving the eigenvalue problem as outlined by Eq. (4.20).

As mentioned previously, in this work, Rayleigh's energy method is seen as a simplification of the Rayleigh-Ritz method by neglecting the non-diagonal terms of the mass and stiffness matrices. It was found that by using the beam mode shapes, Rayleigh's energy and the Rayleigh-Ritz methods gave similar results for the prediction of the frequencies and the response of the plate.

4.3.2 Dynamic Response for the GSSP Model

In order to decouple the equations of motion of the system, the following transformation of coordinates is used:

$$\boldsymbol{q} = \boldsymbol{U_m}\boldsymbol{\gamma} \tag{4.43}$$

where $\boldsymbol{U_m}$ is the modal matrix normalized with respect to the mass matrix, and $\boldsymbol{\gamma}$ is a vector of a new set of generalized coordinates $[\gamma_1, \gamma_2, ...\gamma_n]^T$ called modal coordinates. Using the principle of virtual work, the following variational equation is obtained [128]:

$$\delta \boldsymbol{q}^T \left(\boldsymbol{M}\ddot{\boldsymbol{q}} + \boldsymbol{K}\boldsymbol{q} - \boldsymbol{Q}\right) = 0 \tag{4.44}$$

$\boldsymbol{Q}$ is the generalized forces, which can be determined using Eq. (4.18). By inserting Eq. (4.43) in (4.44), the following set of decoupled equations are obtained:

$$\ddot{\gamma}_r + \tilde{\omega}_r^2\gamma_r(t) = \Gamma_r(t) \qquad \text{for } r = 1, 2, ... \tag{4.45}$$

where

$$[\Gamma_1, \Gamma_2, ...\Gamma_n]^T = \mathbf{\Gamma} = \boldsymbol{U_m}^T \boldsymbol{Q} \tag{4.46}$$

The general solution of Eq. (4.45) is [128]:

$$\gamma_r(t) = \frac{1}{\tilde{\omega}_r} \int_0^t \Gamma_r(\tau) \sin \tilde{\omega}_r (t - \tau) d\tau + \gamma_r(0) \cos(\tilde{\omega}_r t) + \frac{\dot{\gamma}_r(0)}{\tilde{\omega}_r} \sin(\tilde{\omega}_r t) d\tau \tag{4.47}$$

where $\gamma_r(0)$and $\dot{\gamma}_r(0)$ are the initial modal displacements and velocities, respectively. To apply actual machining forces, one has to resort to numerical methods to compute the convolution integral in Eq. (4.47). The solution for Eq. (4.45) can also be developed by direct numerical methods. Here, the Runge-Kutta-Fehlberg method was used [164].

4.3.3 Genetic Algorithms and Boundary Condition Calibration

To simulate the response of a pocket-side using a plate with torsional and translational springs, an off-line calibration for the stiffness coefficients of the springs needs to be performed. In this context, detailed FE models were used as virtual experiments to simulate the actual response of a pocket-side.

Description of the Calibration Procedure

For each pocket-side, an equivalent plate model is calibrated. The values of the stiffness of the springs of the plate are optimized by minimizing the error ψ between the response of the pocket-side resulting from the FE simulation of the pocket and the predictions calculated based on the GSSP model. Once the optimum values of the stiffness of the springs are determined, the plate model can be used to simulate the response of any point on the pocket-side under any loading condition. This calibration is repeated for all of the sides of the pocket. A near global optimization is required for the calibration of the spring values to avoid solutions at local optima, which can be expected in this case due to the large number of decision variables and the nature of the objective function. Real-coded Genetic Algorithm (GA) [165] is used in this research to determine the values of the optimum stiffness of the springs. Once these values are determined from the GA code, local optimization is performed using the Nelder-Mead method [166].

To reduce the computational effort during optimization, the response of the plate and the FE models are compared at four output points as shown in Fig. 4.2. Point P_A, where the force is applied, is at the centre of the pocket-side/plate. At this location, the force equally affects each opposing side of the plate. Point P_B, where the maximum displacement is expected, is at the middle of the top free edge. Points P_C and P_D are midway between point P_A and edges 2 and 3, respectively. These locations are chosen such that they capture the effects of the springs at the side edges. Under stable machining conditions and uniform chip load, machining forces are periodic and can be represented by Fourier transforms; thus a sinusoidal force is applied for the calibration with a frequency different from the pocket natural frequencies, to avoid resonance. It will be shown in Chapter 5, section 5.2 that this approach is not restrictive and the response due to machining loads and impact excitations are also accurately predicted.

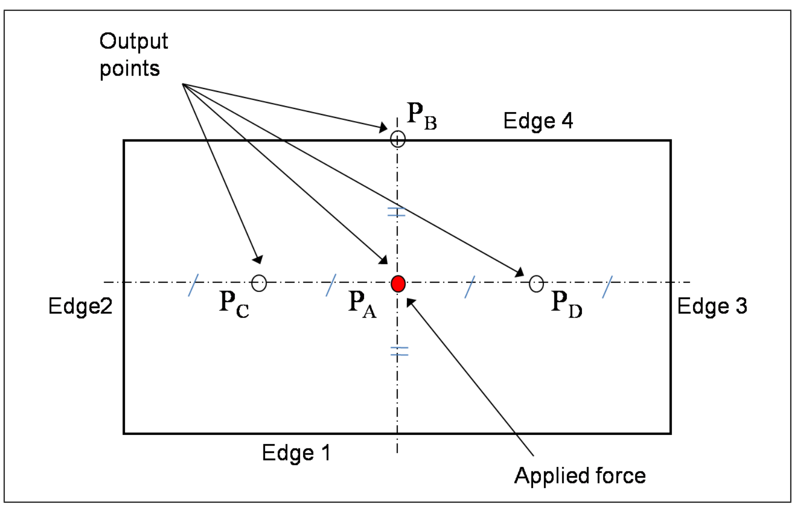

Figure 4.2: Schematic of the plate/pocket-side illustrating the location of the applied force and the output points for the response

Structure of the Genetic Algorithm Optimization Scheme

Although the formulation of the genetic algorithm differs from one problem to the other, depending on the complexity of the problem, the structure of the code has to include the following:

1. Decision variables: In this case there are eight variables that represent the distributed torsional and translational springs along the four boundaries. Although, the top edge of the pocket-side is a free edge (no springs), and the bottom edge is clamped (rigid), springs are assigned to both edges in order to allow more flexibility in the calibration procedure, and to include other effects such as adjacent pockets and edge clamps, if any.

2. Objective function: The objective function to be minimized is the error ψ, which can be expressed as:

$$\psi = \sum_{c=1}^{g} \sum_{e=1}^{s} \frac{\mid d_{ce} - \tilde{d}_{ce} \mid}{max \mid d \mid} \tag{4.48}$$

   where s is the number of time response points, g is the number of output points on the plate, and d_{ce} and $\tilde{d}_{ce}$ are the elements of the arrays $\boldsymbol{d}$ and $\tilde{\boldsymbol{d}}$ with dimensions $g \times s$, representing the displacement response of the pocket-side and the plate, respectively.

3. Constraints: In this case, no constraints are defined for the optimization algorithm.

4. Operators: They are intended either to randomize the search so as to break off one of the local optima or to improve the actual solution. The operators could be based on a two-point averaging method (cross-over) or single-point-alteration (mutation). The following three cross-overs and five mutations are implemented [165]: Arithmetic, simple, and heuristic cross-overs as, well as, uniform, whole uniform, non-uniform, boundary and Gaussian mutations.

Effect of the Change of Thickness of the Adjacent Sides on the Calibrated Stiffness of the Springs

During the machining of the pocket, the thicknesses of the adjacent-sides change. To reduce the number of times required for optimization, for a given load-application side, a correlation between the change of thickness of the adjacent-sides for a pocket and the calibrated stiffness of the rotational springs is determined and is expressed as:

$$r_n = r_c R^3 \tag{4.49}$$

where r_n and r_c are the new and the calibrated stiffness coefficients, respectively and R_t is the ratio of the new thickness to the original one. This relationship was determined empirically and based on the fact that the torsional stiffness of beams and plates is proportional to the cube of their thickness. Thus, once the calibrated values of the stiffness of the springs are determined, no further calibration is required even if the wall thicknesses vary. The validity of this relationship will be demonstrated in the results given in Chapter 5, section 5.2.2. Due to the high axial stiffness of the adjacent sides, the changes of the wall thicknesses have small effects on the stiffness of the translational springs. It was found that non-adjacent sides had negligible effects on the calibrated values of the stiffness of the springs.

4.4 Mathematical Formulation of the Multi-Span Plate (MSP) Model

The MSP model is based on developing a dynamics model for a multi-span plate to approximate the dynamics of thin-walled pockets. Similar to the GSSP model, one needs to generate trial functions that closely approximate the mode shapes of the multi-span plate. Using these trial functions, together with Rayleigh's energy and the Rayleigh-Ritz methods, the frequencies and the response of the multi-span plate can be approximated.

4.4.1 Boundary Conditions for the MSP Model

To describe the formulation of the MSP model, a multi-span plate is illustrated in Fig. 4.3. As can be seen, the spans are in the x-direction. The transverse vibration of span a with thickness h_a, will be designated as $w^{(a)}$. According to Eq. (4.1), the transverse vibration of span a can be expressed as:

$$D_a \left(\frac{\partial^4 w^{(a)}}{\partial x^4} + \frac{\partial^4 w^{(a)}}{\partial x^2 \partial y^2} + \frac{\partial^4 w^{(a)}}{\partial y^4} \right) + f_p(x, y, t) = m_a \frac{\partial^2 w^{(a)}}{\partial t^2} \tag{4.50}$$

where m_a is the mass per unit area of the a^{th} span and D_a is the flexural rigidity which can be written as:

$$D_a = \frac{E {h_a}^3}{12(1 - \nu^2)} \tag{4.51}$$

where h_a is the thickness of the a^{th} span. Based on the analysis performed in section 3.4,

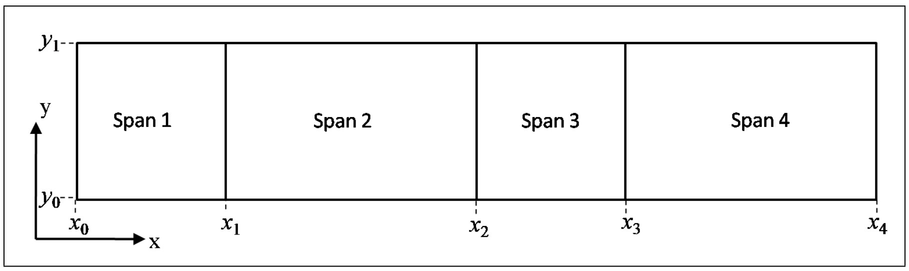

Figure 4.3: Representation of a multi-span plate

the following boundary conditions have to be applied in order to closely approximate the dynamics of the pocket:

At $x = x_a$, for $a = 1, 2, 3$

$$w^{(a)}\Big|_{(x=x_a)} = 0 \tag{4.52a}$$

$$w^{(a+1)}\Big|_{(x=x_a)} = 0 \tag{4.52b}$$

$$\left.\frac{\partial w^{(a)}}{\partial y}\right|_{(x=x_a)} = \left.\frac{\partial w^{(a+1)}}{\partial y}\right|_{(x=x_a)} \tag{4.52c}$$

$$D_a \left(\frac{\partial^2 w^{(a)}}{\partial x^2} + \nu \frac{\partial^2 w^{(a)}}{\partial y^2} \right)\Bigg|_{(x=x_a)} = D_{a+1} \left(\frac{\partial^2 w^{(a+1)}}{\partial x^2} + \nu \frac{\partial^2 w^{(a+1)}}{\partial y^2} \right)\Bigg|_{(x=x_a)} \tag{4.52d}$$

Eqs. (4.52a) and(4.52b) represent the conditions for zero displacement. Eqs. (4.52c) and (4.52d) represent the continuity of the rotations and the moments, respectively, about the edge $x = x_a$. For edges $x = x_1, x_4$, the following boundary conditions have to be specified:

$$w^{(4)}\Big|_{(x=x_4)} = 0 \tag{4.53a}$$

$$w^{(1)}\Big|_{(x=x_0)} = 0 \tag{4.53b}$$

$$\left.\frac{\partial w^{(4)}}{\partial y}\right|_{(x=x_4)} = \left.\frac{\partial w^{(1)}}{\partial y}\right|_{(x=x_0)} \tag{4.53c}$$

$$-D_4 \left(\frac{\partial^2 w^{(4)}}{\partial x^2} + \nu \frac{\partial^2 w^{(4)}}{\partial y^2}\right)\Bigg|_{(x=x_4)} = -D_1 \left(\frac{\partial^2 w^{(1)}}{\partial x^2} + \nu \frac{\partial^2 w^{(1)}}{\partial y^2}\right)\Bigg|_{(x=x_0)} \tag{4.53d}$$

Equations (4.53c) and (4.53d)represent the continuity of the rotations and the moments of span 1 about edge $x = x_0$ and span 4 about edge $x = x_4$. Clamped boundary conditions have to be applied at $y = y_0$ as follows:

$$w^{(a)} = 0 \tag{4.54a}$$

$$\frac{\partial w^{(a)}}{\partial y} = 0 \tag{4.54b}$$

where Eqs. (4.54a) and (4.54b) represent the conditions of zero displacement and slope, respectively. At $y = y_1$, free boundary conditions have to be applied and can be written as:

$$D_a \left(\frac{\partial^2 w^{(a)}}{\partial y^2} + \nu \frac{\partial^2 w^{(a)}}{\partial x^2}\right) = 0 \tag{4.55a}$$

$$D_a \left(\frac{\partial^3 w^{(a)}}{\partial y^3} + (2-\nu) \frac{\partial^3 w^{(a)}}{\partial x^2 \partial y}\right) = 0 \tag{4.55b}$$

where Eqs. (4.55a) and (4.55b) represent the conditions of zero moment and zero transverse shear, respectively.

4.4.2 Generation of the Trial Functions for the MSP Model

To approximate the mode shapes of the multi-span plate, the trial functions will be discretized in the x- and y-directions based on:

$$\overline{W}_{i,j}^{(a)} = \overline{X}_i^{(a)}(x)\, \overline{Y}_j^{(a)}(y), \quad x = x_{a-1} : x_a; \quad y = y_0 : 1; \quad 1 \leq a \leq s_x \tag{4.56}$$

where a is an index for the spans of the plate in the x-directions, x_{a-1} and x_a are the coordinates of the a^{th} span, and s_x is the total number of spans. For the a^{th} span, trial functions in the x-direction $\overline{X}_i^{(a)}$ and the y-direction $\overline{Y}_j^{(a)}$ are assigned. The trial functions in the x-direction are based on a multi-span beam model and the trial functions in the y-direction are generated using a clamped-free beam model. The advantage of using these beam mode shapes is that the displacements of the pocket are accurately described by including less than 20 approximate mode shapes in the model.

For the x-direction, the trial function will be generated using the equations of a four-span beam with dimensions corresponding to the dimensions of the spans of the plate. Each span of the beam is simply supported. Continuity conditions are satisfied between the internal edges of the beam as well as between the two external edges. The beam mode shapes are determined based on the Euler Bernoulli beam assumptions. The vibration of the a^{th} span of the beam can be expressed as:

$$\rho A_{ba} \frac{\partial^2 z_x^{(a)}}{\partial t^2} + EI_a \frac{\partial^4 z_x^{(a)}}{\partial x^4} = f(x,t) \tag{4.57}$$

where $z_x^{(a)}$, A_{ba}, and I_a are the transverse displacement, the area, and the moment of inertia, respectively of the a^{th} span. Based on the separation of variables, similar to Eq. (4.26), the solution of the beam response is expressed as:

$$z_x^{(a)}(x,t) = X^{(a)}(x)\Theta(t) \tag{4.58}$$

where $X^{(a)}$represents the spatial dependence for the a^{th} span and Θ gives the time dependence. The boundary-value problem can be expressed using Eq. (4.28) by replacing Z by $X^{(a)}$. For $x = x_a$, the following four boundary conditions could be specified:

$$X^{(a)}\Big|_{(x=x_a)} = 0 \tag{4.59a}$$

$$X^{(a+1)}\Big|_{(x=x_a)} = 0 \tag{4.59b}$$

$$\left.\frac{dX^{(a)}}{dx}\right|_{(x=x_a)} = \left.\frac{dX^{(a+1)}}{dx}\right|_{(x=x_a)} \tag{4.59c}$$

$$h_{xa}^3 \left. \frac{d^2X^{(a)}}{dx^2} \right|_{(x=x_a)} = h_{xa}^3 \left. \frac{d^2X^{(a+1)}}{dx^2} \right|_{(x=x_{a+1})} \tag{4.59d}$$

where h_{xa} is the thickness of the a^{th} span of the beam and is equal to the thickness of the corresponding span of the plate. Eqs. (4.59a) and (4.59b) represent the conditions of zero displacement at $x = x_a$, for spans a and $a+1$, respectively. Eqs. (4.59c) and (4.59d) represent the continuity of the rotations and the bending moments, respectively, about $x = x_a$. When applying this set of boundary conditions at $x = x_0$ and $x = x_4$, Eqs. (4.59) can be re-written as:

$$X^{(4)}\big|_{(x=x_{(4)})} = 0 \tag{4.60a}$$

$$X^{(1)}\big|_{(x=x_0)} = 0 \tag{4.60b}$$

$$\left. \frac{dX^{(4)}}{dx} \right|_{(x=x_4)} = \left. \frac{dX^{(1)}}{dx} \right|_{(x=x_0)} \tag{4.60c}$$

$$h_{x4}^3 \left. \frac{d^2X^{(4)}}{dx^2} \right|_{(x=x_4)} = h_{x1}^3 \left. \frac{d^2X^{(1)}}{dx^2} \right|_{(x=x_1)} \tag{4.60d}$$

For the a^{th} span, the solution of the boundary-value problem can be expressed as:

$$X^{(a)} = A_a \sin\beta_{xa}(\tilde{x}) + B_a \cos\beta_{xa}(\tilde{x}) + C_a \sinh\beta_{xa}(\tilde{x}) + D_a \cosh\beta_{xa}(\tilde{x}) \tag{4.61}$$

where $\tilde{x}$ is equal to $x - x_{a-1}$, A_a, B_a, C_a and D_a are the coefficients of the beam mode shape equation determined by satisfying the spatial boundary conditions and β_{xa} is described by the following equation:

$$\beta_{xa}^4 = \frac{\rho\omega_x^2}{\frac{1}{12}h_{xa}^2 E} \tag{4.62}$$

where ω_x is the natural frequency of the beam.

A total of 16 boundary conditions have to be satisfied for a four span beam. The equations are represented in the terms of the coefficients in Eq. (4.61), which results in a 16×16 matrix (16 equations and 16 coefficients). Different methods exist in the literature for solving for the coefficient of these equations. One way is to calculate the determinant of the 16×16 matrix. As the number of spans increases, this method will result in a substantial increase in the computation time. Instead, this system of equations could be reduced to four equations by using the method of transfer matrices where the coefficients of a given span are expressed in terms of the coefficients of the previous span [167, 168]. By using this method, increasing the number of spans does not affect the computation time. By inserting Eq. (4.61) in Eqs. (4.59), the following system of equations is obtained:

$$\begin{bmatrix} A_{a+1} \\ B_{a+1} \\ C_{a+1} \end{bmatrix} = \boldsymbol{\Phi_x}^{(a)} \begin{bmatrix} A_a \\ B_a \\ C_a \end{bmatrix} \tag{4.63}$$

where $\boldsymbol{\Phi_x^{(a)}}$ is the transfer matrix and has dimensions of 3×3. The coefficients of span 1 can be represented in terms of the coefficients of span 4 as a result of the continuity of the rotations and the moments about $x = x_0$ and $x = x_4$. Using the transformation in Eq. (4.63), the following equation can be derived:

$$\left(\prod_{a=s_x-1}^{a=1} \boldsymbol{\Phi_x}^{(a)} \right) \boldsymbol{\Phi_x}^{(s_x)} - \boldsymbol{I} \begin{bmatrix} A_{s_x} \\ B_{s_x} \\ C_{s_x} \end{bmatrix} = \mathbf{0} \tag{4.64}$$

The eigenvalues of the multi-span beam are determined by finding the nontrivial solutions of Eq. (4.64). The detailed derivation of Eqs. (4.63) and (4.64) are presented in Appendix B, section B.1. The i^{th} eigenfunctions of the a^{th} span of the beam in the x-direction will be denoted by $X_i^{(a)}$. These mode shapes will be used by replacing $\overline{X}_i^{(a)}$ in Eq. (4.56) by $X_i^{(a)}$.

The trial functions in the y-direction are based on a clamped-free beam model. The same equation of motion as in Eq. (4.23) is used. Using the separation of variables, a boundary-value problem is obtained and can be expressed by substituting Z in Eq. (4.28) by $Y(y)$ which represents the spatial dependence in the y-direction. The following spatial boundary conditions for the clamped-free beam have to be satisfied:

At $y = y_0$:

$$Y(y_0) = 0 \tag{4.65a}$$

$$\left.\frac{dY}{dy}\right|_{y=y_0} = 0 \tag{4.65b}$$

which represent the conditions for zero displacement and rotations, respectively.
At $y = y_1$

$$\left.\frac{d^2Y}{dy^2}\right|_{y=y_1} = 0 \tag{4.66a}$$

$$\left.\frac{d^3Y}{dy^3}\right|_{y=y_1} = 0 \tag{4.66b}$$

which represent the conditions for zero bending moment and shear forces, respectively. The following beam mode shape representation is used:

$$Y(y) = A_y \sin\beta_y(y) + B_y \cos\beta_y(y) + C_y \sinh\beta_y(y) + D_y \cosh\beta_y(y) \tag{4.67}$$

where A_y, B_y, C_y and D_y are the coefficients of the beam mode shape equation determined by satisfying the spatial boundary conditions. The equation for β_y can be expressed as:

$$\beta_y^4 = \frac{\rho\omega_y^2}{\frac{1}{12}h_y^2 E} \tag{4.68}$$

where ω_y is the natural frequency of the beam and h_y is the thickness of the beam. By inserting Eq. (4.67) in Eqs. (4.65) and (4.66), the following characteristic equation is obtained [128]:

$$\cos(\beta_y y_1)\cosh(\beta_y y_1) = -1 \tag{4.69}$$

By solving the characteristic equation, the eigenvalues and the mode shapes are determined. The j^{th} mode shape of the beam can be expressed as:

$$Y_j = A_{yj}\left[\sin\beta_{yj}y - \sinh\beta_{yj}y - \frac{\sin\beta_{yj}y_1 + \sinh\beta_{yj}y_1}{\cos\beta_{yj}y_1 + \cosh\beta_{yj}y_1}\left(\cos\beta_{yj}y - \cosh\beta_{yj}y\right)\right] \tag{4.70}$$

For each plate span a, the expression for Y_j is calculated and substituted for $\overline{Y}_j^{(a)}$ in Eq. (4.56).

It is necessary to evaluate the proposed trial functions in terms of satisfying the boundary conditions of the multi-span plate. For a multi-span plate with a uniform thickness, the trial functions satisfy the geometric and the dynamic boundary conditions of the plate at the edge $x = x_a$. For a plate with spans having different thicknesses, the geometric boundary conditions are satisfied; however, the dynamic boundary conditions are not satisfied. In this case, it is expected that the Rayleigh-Ritz method will provide more accurate results than Rayleigh's energy method. As can be seen from Eq. (4.70), although the thickness of each span could be different, the same trial function in the y-direction is used.

To estimate the frequencies of the multi-span plate, Rayleigh's energy method and the Rayleigh-Ritz methods are implemented in the same way as for the GSSP model. For Rayleigh's energy method, the maximum strain energy and the reference kinetic energy of each mode have to be evaluated. By substituting Eq. (4.56) in Eq. (4.9), the maximum strain energy for a given mode is determined as:

$$\overline{U}_{i,j} = \frac{1}{2}\sum_{a=1}^{s_x}\int_{x_{a-1}}^{x_a}\int_{y_0}^{y_1} D_a \overline{E}_{i,j}^{(a)} dydx \tag{4.71}$$

where $\overline{E}_{i,j}^{(a)}$ is expressed as:

$$\overline{E}_{i,j}^{(a)} = \left(\frac{\partial^2 \overline{W}_{i,j}^{(a)}}{\partial x^2}\right)^2 + \left(\frac{\partial^2 \overline{W}_{i,j}^{(a)}}{\partial y^2}\right)^2 + 2\nu \frac{\partial^2 \overline{W}_{i,j}^{(a)}}{\partial x^2}\frac{\partial^2 \overline{W}_{i,j}^{(a)}}{\partial y^2} + 2(1-\nu)\left(\frac{\partial^2 \overline{W}_{i,j}^{(a)}}{\partial x \partial y}\right)^2 \tag{4.72}$$

By substituting Eq. (4.56) in Eq. (4.6), the reference kinetic energy for a given mode can be written as:

$$\overline{T}_{i,j} = \frac{1}{2}\sum_{a=1}^{s_x}\int_{x_{a-1}}^{x_a}\int_{y_0}^{y_1} \left(\overline{W}_{i,j}^{(a)}\right)^2 dydx \tag{4.73}$$

The approximate natural frequencies of the multi-span plate are determined by evaluating Rayleigh's quotient expressed as:

$$\varpi_{i,j}^2 = \frac{\overline{U}_{i,j}}{\overline{T}_{i,j}} \tag{4.74}$$

Similar to the GSSP model, a vector $\overline{\boldsymbol{W}}$ of trial functions $\overline{W}_{ij}$ is defined such that the trial functions are listed in ascending order of their corresponding approximate natural frequencies. In order to generate a model with n degrees of freedom, the first n trial functions of the vector $\overline{\boldsymbol{W}}$ are selected and are referred to as $\tilde{W}_r$, for $r = 1, 2, ..., n$. To apply the Rayleigh-Ritz method, the response of the plate is approximated using Eq. (4.12) and the kinetic and strain energies are calculated by substituting Eq. (4.12) in Eq. (4.5) and Eq. (4.8), respectively. In this case, the total potential energy is equal to the strain energy of the plate. Using Lagrange's equations, the equations of motion are derived. Based on Eq. (4.16), the mass matrix $\boldsymbol{M}$ and the stiffness matrix $\boldsymbol{K}$ of the system are determined. By solving the eigenvalue problem, the frequencies $\tilde{\omega}_r$ and the modal matrix $\boldsymbol{U_m}$ are determined.

4.4.3 Dynamic Response for the MSP Model

To determine the response of the multi-span plate, one has to solve for the generalized coordinates $\boldsymbol{q}$ in Eq. (4.16). Using the same transformation as in Eq. (4.43), the modal coordinates $\boldsymbol{\gamma}$ are obtained. The vector of generalized forces $\boldsymbol{Q}$ is determined using Eq. (4.18). By applying the principle of virtual work, the equations of motion of the system are decoupled and the solution for the generalized coordinates is determined using Eqs. (4.44) to (4.47). As mentioned previously, in the Rayleigh' Energy method, the non-diagonal terms of the mass and stiffness matrices are ignored. For the GSSP model, these non-diagonal terms were negligible. Thus, the frequencies and the response obtained by using Rayleigh's energy method were similar to those obtained by the Rayleigh-Ritz method. However, for the case of the MSP model, these terms are more significant and thus, it is expected that the Rayleigh-Ritz method will offer higher accuracy when compared to Rayleigh's energy method, especially for the case of a plate with spans having different thicknesses.

4.5 Change of Thickness (CoT) Formulation

Up to this point, the thickness of each side of the pocket (unit-element) has been assumed uniform. It is necessary to develop a formulation that could approximate the change of thickness of a pocket-side during milling. In section 3.5, the change of thickness of a pocket-side for typical machining tool-paths was analyzed. It was proposed to discretize a plate to two spans in the x-direction and three spans in the y-direction in order to simulate the different machining tool-paths. To apply the proposed concept, the formulation of the change of thickness (CoT) will be developed for the MSP model. It should be also applied for the GSSP model.

For the four-span plate in Fig. 4.3, the previously described cases for the change of thickness will be applied to the first span. In the x-direction, span 1 will be divided in two sub-spans. In the y-direction, the multi-span plate is divided to three spans. Thus, eventually, the plate will have five spans in the x-direction and three spans in the y-direction, as shown in Fig. 4.4. Each span, denoted by indices (a,b), will have a thickness $h_p^{(a,b)}$, a flexural rigidity $D^{(a,b)}$ and a transverse vibration $w^{(a,b)}$. The total number of spans in the x- and y-directions are s_x and s_y, respectively.

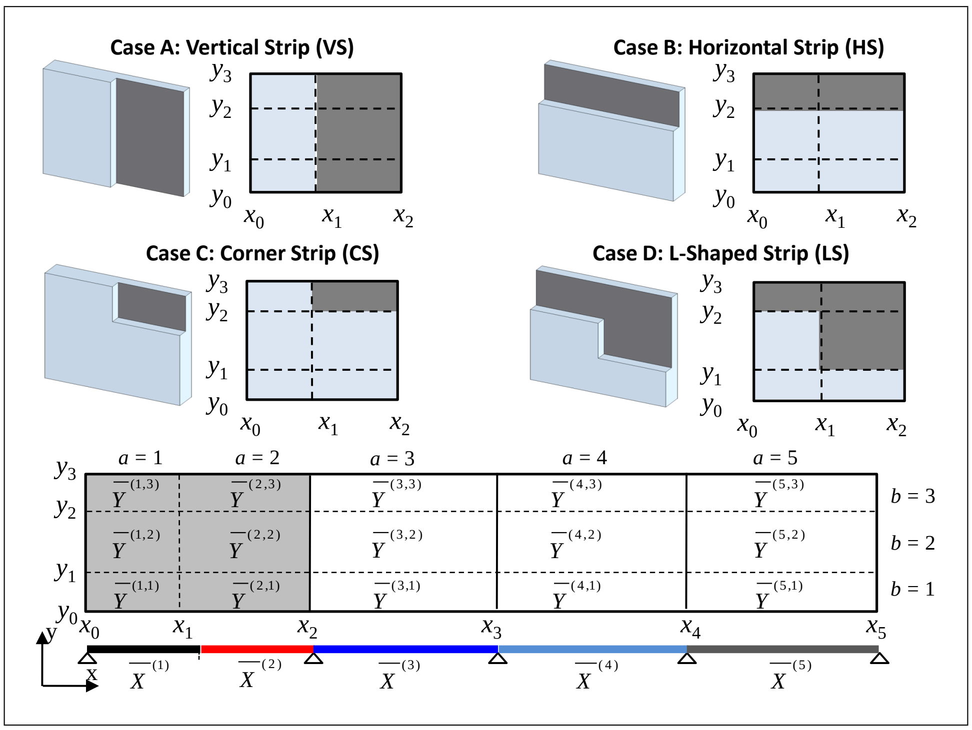

Figure 4.4: Illustration of the CoT formulation for the MSP model

The boundary conditions for the edges $x = x_0, x_2, x_3, x_4, x_5$, are based on Eqs. (4.52) by substituting $w^{(a)}$, h_a and D_a by $w^{(a,b)}$, $h_p^{(a,b)}$ and $D^{(a,b)}$, respectively. For edge $x = x_1$, the continuity of the rotations and the bending moments are satisfied according to Eqs. (4.52c) and (4.52d), respectively. In addition, the equations for the continuity of the displacements and the shear forces have to be satisfied and can be expressed as:

$$w^{(1,b)} = w^{(2,b)} \tag{4.75a}$$

$$D^{(1,b)}\left(\frac{\partial^3 w^{(1,b)}}{\partial x^3} + (2-\nu)\frac{\partial^3 w^{(1,b)}}{\partial x \partial y^2}\right) = D^{(2,b)}\left(\frac{\partial^3 w^{(2,b)}}{\partial x^3} + (2-\nu)\frac{\partial^3 w^{(2,b)}}{\partial x \partial y^2}\right) = 0 \tag{4.75b}$$

The boundary conditions at $y = y_0$ and $y = y_{s_y}$ are determined according to Eq. (4.54) and Eq. (4.55). The boundary conditions at $y = y_b$, for $b = 1, ..., s_y - 1$, are determined as:

$$w^{(a,b)} = w^{(a,b+1)} \tag{4.76a}$$

$$\frac{\partial w^{(a,b)}}{\partial y} = \frac{\partial w^{(a,b+1)}}{\partial y} \tag{4.76b}$$

$$D^{(a,b)}\left(\frac{\partial^2 w^{(a,b)}}{\partial y^2} + \nu\frac{\partial^2 w^{(a,b)}}{\partial x^2}\right) = D^{a,b+1}\left(\frac{\partial^2 w^{(a,b+1)}}{\partial y^2} + \nu\frac{\partial^2 w^{(a,b+1)}}{\partial x^2}\right) \tag{4.76c}$$

$$D^{(a,b)}\left(\frac{\partial^3 w^{(a,b)}}{\partial y^3} + (2-\nu)\frac{\partial^3 w^{(a,b)}}{\partial x^2 \partial y}\right) = D^{(a,b+1)}\left(\frac{\partial^3 w^{(2,b+1)}}{\partial y^3} + (2-\nu)\frac{\partial^3 w^{(2,b+1)}}{\partial x^2 \partial y}\right) = 0 \tag{4.76d}$$

To approximate the mode shapes of this multi-span plate, the trial functions will be discretized in the x- and y directions based on:

$$\overline{W}_{i,j}^{(a,b)} = \overline{X}_i^{(a)}(x)\,\overline{Y}_j^{(a,b)}(y), \quad x = x_{a-1} : x_a; \quad y = y_{b-1} : y_b; \quad 1 \leq a \leq s_x; \quad 1 \leq b \leq s_y \tag{4.77}$$

where $\overline{X}^{(a)}$ and the $\overline{Y}^{(a,b)}$ are the trial functions in the x- and y-directions, respectively. As can be seen, the trial function in the y-direction is a piece-wise function defined over s_y spans. For each set of spans with a given index a, a different trial function in the y-direction can be assigned. The trial functions in the x- and y-directions are based on multi-span beam models.

The x-direction trial function will be developed using a five-span beam. Based on the separation of variables as in Eq. (4.58), Eq. (4.61) is used to describe the mode shape of the beam in the x-direction. The boundary conditions at x_0, x_2, x_3, x_4, and x_5, are the same as described in section 4.4, Eqs. (4.59). At $x = x_1$, the following boundary conditions have to be applied to represent the continuity of the displacement, the rotation, the bending moment and the shear force:

$$X^{(1)}\Big|_{(x=x_1)} = X^{(2)}\Big|_{(x=x_1)} \tag{4.78a}$$

$$\frac{dX}{dx}^{(1)}\Bigg|_{(x=x_1)} = \frac{dX}{dx}^{(2)}\Bigg|_{(x=x_1)} \tag{4.78b}$$

$$h_{x1}^3 \; \frac{d^2X}{dx^2}^{(1)}\Bigg|_{(x=x_1)} = h_{x2}^3 \; \frac{d^2X}{dx^2}^{(2)}\Bigg|_{(x=x_1)} \tag{4.78c}$$

$$h_{x1}^3 \; \frac{d^3X}{dx^3}^{(1)}\Bigg|_{(x=x_1)} = h_{x2}^3 \; \frac{d^3X}{dx^3}^{(2)}\Bigg|_{(x=x_1)} \tag{4.78d}$$

By inserting Eq. (4.61) in Eqs. (4.59) and (4.78), the characteristic equation, the eigenfrequencies and the mode shapes can be determined similar to the four span beam for the MSP model (refer to section 4.4.2). The detailed derivation of the characteristic equation for the five-span beam is presented in Appendix B, section B.2.

The trial functions in the y-direction are based on a three-span clamped-free beam. Based on the separation of variables, the following spatial boundary conditions for the three-span clamped-free beam have to be satisfied:

At $y = y_0$:

$$Y^{(1)}(y_0) = 0 \tag{4.79a}$$

$$\frac{dY^{(1)}}{\partial y}\Bigg|_{y=y_0} = 0 \tag{4.79b}$$

Eqs. (4.79a) and (4.79b) represent the boundary conditions for zero displacement and rotations, respectively.

At $y = y_1, y_2$:

$$Y^{(b)}\Big|_{(y=y_b)} = Y^{(b+1)}\Big|_{(y=y_b)} \tag{4.80a}$$

$$\frac{dY}{dy}^{(b)}\Bigg|_{(y=y_b)} = \frac{dY}{dy}^{(b+1)}\Bigg|_{(y=y_b)} \tag{4.80b}$$

$$h_{yb}^3 \; \frac{d^2Y}{dy^2}^{(b)}\Bigg|_{(y=y_b)} = h_{y(b+1)}^3 \; \frac{d^2Y}{dy^2}^{(b+1)}\Bigg|_{(y=y_b)} \tag{4.80c}$$

$$h_{yb}^3 \left. \frac{d^3Y^{(b)}}{dy^3} \right|_{(y=y_b)} = h_{y(b+1)}^3 \left. \frac{d^3Y^{(b+1)}}{dy^3} \right|_{(y=y_b)} \tag{4.80d}$$

where h_{yb} is the thickness of the b^{th} span. Eqs. (4.80a) and (4.80c) represent the continuity of displacement and the shear force, respectively. Eqs. (4.80b) and (4.80d) represent the continuity of the rotation and the bending moments about $y = y_b$, respectively.

At $y = y_3$

$$\left. \frac{d^2Y^{(3)}}{dy^2} \right|_{y=y_3} = 0 \tag{4.81a}$$

$$\left. \frac{d^3Y^{(3)}}{dy^3} \right|_{y=y_3} = 0 \tag{4.81b}$$

Eqs. (4.81a) and (4.81b) represent the conditions of a free edge with zero bending moment and shear forces, respectively. For the b^{th} span of the beam, the following beam mode shape expression can be used:

$$Y^{(b)}(y) = A_b \sin\beta_{by}(\tilde{y}) + B_b \cos\beta_{by}(\tilde{y}) + C_b \sinh\beta_{by}(\tilde{y}) + D_b \cosh\beta_{by}(\tilde{y}) \tag{4.82}$$

where $Y^{(b)}$ represents the transverse displacement of the b^{th} span of the beam, $\tilde{y} = y - y_{b-1}$, y_b and y_{b-1} are the coordinates of the b^{th} span, A_b, B_b, C_b and D_b are the coefficients of the beam mode shape equation determined by satisfying the spatial boundary conditions. The equation for β_{yb} can be expressed as:

$$\beta_{yb}^4 = \frac{\rho\omega_y^2}{\frac{1}{12}h_{yb}^2 E} \tag{4.83}$$

where ω_y is the natural frequency of the beam. By inserting Eq. (4.82) in Eqs. (4.79), (4.80), and (4.81) and solving the characteristic equation, the eigenvalues and the mode shapes are determined. The characteristic equation is derived in detail in Appendix B, section B.3. The j^{th} mode shape of the b^{th} span is referred to as $Y_j^{(b)}$. For the spans of the plate with a given index a, the expression for $Y_j^{(b)}$ is calculated and substituted for $\overline{Y}_j^{(a,b)}$ in Eq. (4.77).

When applying the trial functions for the multi-span plate, the trial functions in the y-direction for $a = 1$ and 2 have to be the same or else the continuity of the displacements is violated at $x = x_1$. The trial functions in the y-direction for $a = 1, 2$ could be different from

the trial function for $a = 3, 4, 5$. To use the beam mode shapes in the different directions, one has to assign a thickness for each span of the x- and y-beams. The thickness of the different spans of the beam for the trial function in the x- direction can be determined as:
For $a = 1 : 5$

$$h_{xa} = \frac{\sum_{b=1}^{3}(y_b - y_{b-1})h_p^{(a,b)}}{y_3 - y_0} \tag{4.84}$$

This equation represents an average of the thicknesses of the plate spans based on the lengths of their corresponding spans in the y-direction. For the trial functions in the y-direction, the following equations are used to determine the thickness of the different spans of the beam:
For $a = 1$ and $a = 2$

$$h_{yb} = \frac{h_p^{(1,b)}(x_2 - x_1) + h_p^{(2,b)}(x_1 - x_0)}{x_2 - x_0} \tag{4.85a}$$

For $a = 3, 4, 5$,

$$h_{yb} = h_p^{(a,b)} \tag{4.85b}$$

Eq. (4.85a) is empirically determined and represents an average of the thicknesses based on the lengths of the spans in the x-direction.

In all the cases for the change of thickness, the continuity of the displacements and the rotations of the multi-span plate at the edges $y = y_b$ for $b = 0, 1, ..s_y$, are satisfied. The continuity of the displacements and the rotations of the plate at the edges $x = x_a$, for $a = 0, 1, ..., s_y$, are satisfied only when the same trial function in the y-direction is used for all spans. This is true for Case A (VS: vertical strip). For Cases B, C and D, the continuity of the rotation is violated along the edges x_0 and x_2 since the trial functions in the y-direction for $a = 1, 2$ are different from those for $a = 3$, $a = 4$ and $a = 5$. Given that the change of thickness during finishing operation in machining is small when compared to the actual thickness of the pocket side, it is still expected that these approximate mode shapes would give good results. This hypothesis is tested and confirmed in Chapter 5, section 5.3.

Once the trial functions are determined for the plate, Rayleigh's energy and the Rayleigh-Ritz method can be implemented to predict the frequencies of the plate using Eqs. (4.71) to (4.74) in section 4.4.2. The dynamic response can be predicted using the same procedure described in section 4.4.3.

4.6 Formulation for the Incorporation of the Fixture Constraints

In the review of the literature, it was shown that the contact nonlinearities due to the material properties and the geometry of the locators have negligible effect on the response of thin-walled structures away from the contact region. Thus, each locator can be applied at a single point with a rigid contact. For design purposes of the fixture layout, it is more convenient to assume that the fixture supports are perfectly rigid. In this case, the main goal is comparing the relative change in the displacement response from one layout to another. After optimizing the fixture layout, it is required to determine the effect of the stiffness of the locators on the absolute displacement of the workpiece. The objective in this case is either to perform some sensitivity analysis for the effect of the stiffness of the locators, or based on prior knowledge of the support stiffness (experimentally or through modelling), one can predict the response of the structure under such conditions. Thus, in the following sections, two formulations for the effect of the fixture supports will be presented. The first formulation, which will be referred to as Perfectly Rigid Support (PRS) deals with perfectly rigid supports. The second formulation, which will be referred to as Finite Stiffness Support (FSS) represents the effect of deformable supports. These two formulations are generalized and could be applied to both the GSSP and the MSP models.

According to the previous section, the approximate response of the plate can be expressed according to Eq. (4.12) where the trial functions and the generalized coordinates are denoted as $\tilde{W}_r$ and q_r, respectively. The equations of motion of the system are described according to Eq. (4.17), where $\boldsymbol{M}$ and $\boldsymbol{K}$ are the mass and stiffness matrices, respectively, $\boldsymbol{q}$ and $\boldsymbol{Q}$ are the vectors of generalized coordinates and forces, respectively.

4.6.1 Perfectly Rigid Support (PRS) Formulation

In this formulation, the perfectly rigid supports are represented by geometric (holonomic) constraints. For a total of k constrained points, the constraint equation for the u^{th} point can be represented as:

$$\tilde{w}(p_{cu}) = \sum_{r}^{n} \tilde{W}_r(p_{cu})q_r = 0 \qquad u = 1, 2, ..., k \tag{4.86}$$

where p_{cu} is the location of the u^{th} constrained point and n is the total number of included modes. Using Eq. (4.86), the constraints can be expressed as:

$$\boldsymbol{G}\boldsymbol{q} = \boldsymbol{0} \tag{4.87}$$

where $\boldsymbol{G}$ is the Jacobian matrix with dimensions $k \times n$ and can be expressed as:

$$\boldsymbol{G} = \begin{bmatrix} \tilde{W}_1(p_{c1}) & \tilde{W}_2(p_{c1}) & ... & \tilde{W}_n(p_{c1}) \\ \tilde{W}_1(p_{c2}) & \tilde{W}_2(p_{c2}) & ... & \tilde{W}_n(p_{c2}) \\ ... & ... & ... & ... \\ \tilde{W}_1(p_{ck}) & \tilde{W}_2(p_{ck}) & ... & \tilde{W}_n(p_{ck}) \end{bmatrix} \tag{4.88}$$

According to Eq. (4.87), there are k independent constraint equations, which allow the reduction of the number of generalized coordinates of the system to $n - k$. The vector of dependent coordinates, which will be referred to as $\boldsymbol{q_e}$, will be represented in terms of the vector of the independent coordinates, which will be designated as $\boldsymbol{q_o}$. The dimensions of $\boldsymbol{q_e}$ and $\boldsymbol{q_o}$ are $k \times 1$ and $(n-k) \times 1$, respectively. The equation of the constraints in (4.87) can be re-written in terms of $\boldsymbol{q_o}$ and $\boldsymbol{q_e}$ as:

$$\boldsymbol{G} \begin{Bmatrix} \boldsymbol{q_o} \\ \boldsymbol{q_e} \end{Bmatrix} = [\boldsymbol{G_o}\ \boldsymbol{G_e}] \begin{Bmatrix} \boldsymbol{q_o} \\ \boldsymbol{q_e} \end{Bmatrix} = \boldsymbol{G_o}\boldsymbol{q_o} + \boldsymbol{G_e}\boldsymbol{q_e} = \boldsymbol{0} \tag{4.89}$$

where $\boldsymbol{G_o}$ and $\boldsymbol{G_e}$ have dimensions of $k \times (n-k)$ and $k \times k$, respectively. They represent the matrices of the coefficients of $\boldsymbol{q_o}$ and $\boldsymbol{q_e}$, respectively. According to Eq. (4.89), the transformation between $\boldsymbol{q_o}$ and $\boldsymbol{q_e}$ can be expressed as:

$$\boldsymbol{q_e} = -\boldsymbol{G_e}^{-1}\boldsymbol{G_o}\boldsymbol{q_o} = \boldsymbol{G_m}\boldsymbol{q_o} \tag{4.90}$$

where $\boldsymbol{G_m}$ has dimensions of $k \times (n-k)$ and represents the transformation matrix between $\boldsymbol{q_e}$ and $\boldsymbol{q_o}$. A new set of generalized coordinates ϕ can be introduced such that

$$\boldsymbol{\phi} = \boldsymbol{q_o} \tag{4.91}$$

Using Eqs. (4.90) and (4.91), the transformation between $\boldsymbol{q}$ and $\boldsymbol{\phi}$ can be described as:

$$\boldsymbol{q} = \left\{ \begin{array}{c} \boldsymbol{q_o} \\ \boldsymbol{q_e} \end{array} \right\} = \left[\begin{array}{c} \boldsymbol{I} \\ \boldsymbol{G_m} \end{array} \right] \boldsymbol{\phi} = \boldsymbol{D}\boldsymbol{\phi} \tag{4.92}$$

where $\boldsymbol{D}$ has dimensions of $n \times (n-k)$. Substituting Eq. (4.92) into Eq. (4.17) and using the principle of virtual work, the following variational equation can be obtained:

$$\delta\boldsymbol{\phi}^T \left(\boldsymbol{M_c}\ddot{\boldsymbol{\phi}} + \boldsymbol{K_c}\boldsymbol{\phi} - \boldsymbol{D}^T\boldsymbol{Q} \right) = 0 \tag{4.93}$$

where the constrained mass matrix $\boldsymbol{M_c}$ and stiffness matrix $\boldsymbol{K_c}$ can be written as:

$$\boldsymbol{M_c} = \boldsymbol{D}^T\boldsymbol{M}\boldsymbol{D} \tag{4.94}$$

and

$$\boldsymbol{K_c} = \boldsymbol{D}^T\boldsymbol{K}\boldsymbol{D} \tag{4.95}$$

Since the variations associated with the minimum set of generalized coordinates $\boldsymbol{\phi}$, in Eq. (4.93), are all independent, the dynamic equations of motion in terms of the new generalized coordinates are obtained as:

$$\boldsymbol{M_c}\ddot{\boldsymbol{\phi}} + \boldsymbol{K_c}\boldsymbol{\phi} - \boldsymbol{D}^T\boldsymbol{Q} = 0 \tag{4.96}$$

By solving the eigenvalue problem, the modal matrix $\boldsymbol{U_c}$ and the approximate frequencies of the constrained system $\tilde{\omega}_c$ can be determined. The modal matrix is orthogonal with respect to the mass matrix $\boldsymbol{M_c}$ and the stiffness matrix $\boldsymbol{K_c}$. Using the orthogonality properties of $\boldsymbol{U_c}$, Eq. (4.96) can be decoupled and solved for $\boldsymbol{\phi}$.

4.6.2 Finite Stiffness Support (FSS) Formulation

In this formulation, the supports are modelled as springs with a finite stiffness. The spring forces are considered as external forces. The approximate response of the plate can be expressed using Eq. (4.12). For a total number of springs equal to k, the spring force f_u of the u^{th} spring can be approximated as:

$$f_u(x_u, y_u, t) = -k_u \tilde{w}(x_u, y_u, t) = -k_u \sum_{r=1}^{n} \tilde{W}_r(x_u, y_u) q_i(t) \tag{4.97}$$

where x_u and y_u are the spatial coordinate of the location of the spring, k_u is the stiffness of the u^{th} spring and n is the total number of mode shapes included in the approximation of the response. According to Eq. (4.18), the generalized force F_{ur} for the spring load can be determined as:

$$F_{ur} = \left(-k_u \sum_{i=1}^{n} \tilde{W}_i(x_u, y_u) q_i \right) \tilde{W}_r(x_u, y_u) \tag{4.98}$$

Using a matrix form, the vector of the generalized forces for a given spring force can be written as:

$$\boldsymbol{F_u} = -k_u \boldsymbol{\tilde{W}}(x_u, y_u) \boldsymbol{\tilde{W}}(x_u, y_u)^T \boldsymbol{q} \tag{4.99}$$

where $\boldsymbol{F_u} = [F_{u1}, F_{u2}, ..., F_{un}]^T$ and $\boldsymbol{\tilde{W}}(x_u, y_u) = [\tilde{W}_1(x_u, y_u), \tilde{W}_2(x_u, y_u), ...\tilde{W}_n(x_u, y_u)]^T$. According to Eq (4.99), the generalized forces for all springs can be expressed as:

$$\boldsymbol{F} = \sum_{u=1}^{k} \boldsymbol{F_u} = -\boldsymbol{K_s q} \tag{4.100}$$

where $\boldsymbol{K_s}$ is expressed as:

$$\boldsymbol{K_s} = \sum_{u=1}^{k} k_u \boldsymbol{\tilde{W}}(x_u, y_u) \boldsymbol{\tilde{W}}(x_u, y_u)^T \tag{4.101}$$

Based on Eqs. (4.17) and (4.100), the free vibration of a plate carrying k translational springs can be described as:

$$\boldsymbol{M\ddot{q}} + \boldsymbol{Kq} = -\boldsymbol{K_s q} \tag{4.102}$$

Assuming harmonic motions of the plate, the eigenvalue problem is set as:

$$\big(\boldsymbol{K}+\boldsymbol{K_s}\big)\boldsymbol{q_c}=\tilde{\omega}_c^2\boldsymbol{M}\boldsymbol{q_c} \tag{4.103}$$

where $\boldsymbol{q_c}$ and $\tilde{\omega}_c$ represent the eigenvector and the eigenfrequency of the constrained system. By solving this eigenvalue problem, the frequencies of the constrained plate and the eigenvector matrix are determined. The dynamic equations of motion of the constrained system, including the non-conservative external forces, can be written as:

$$\boldsymbol{M}\ddot{\boldsymbol{q}}+\big(\boldsymbol{K}+\boldsymbol{K_s}\big)\boldsymbol{q}=\boldsymbol{Q} \tag{4.104}$$

Based on the orthogonality properties of the calculated mode shape vectors, Eq. (4.104) can be decoupled and solved for $\boldsymbol{q}$ in a way similar to what was described in section 4.6.

4.7 Concluding Remarks

In this chapter, the mathematical formulations for the models proposed in Chapter 3 were developed. The first model, which is referred to as the Generalized Single-Span Plate (GSSP), represents the dynamics of a plate with torsional and translational springs at the boundaries. The dynamic response of the plate is approximated using Rayleigh's energy and the Rayleigh-Ritz method. Trial functions for the approximation of the plate mode shapes are generated using beam models with torsional and translation springs at the boundaries. A methodology for the calibration of the stiffness of the springs was proposed such that the model can represent the dynamics of a pocket-side. This methodology is based on global and local optimization techniques.

The second model, which is referred to as the Multi-Span Plate (MSP) model, represents the dynamics of a 3D generalized pocket using a multi-span plate with special boundary conditions. The approximate mode shapes of the multi-span plate are based on multi-span beam models. Similar to the previous model, both Rayleigh's energy and the Rayleigh-Ritz methods are used for the calculation of the frequencies and the response of the multi-span plate.

A new formulation, referred to as the Change of Thickness (CoT) formulation, was developed and implemented to represent the proposed cases for the milling of thin-walled pockets. In addition, the effects of the supports of the fixture were included in the dynamic models. Two formulations for the fixture supports were presented, the first, which is referred to as PRS formulation, represents perfectly rigid supports by using holonomic constraints and the second, which is designated as FSS formulation, represents deformable supports by using springs with a finite stiffness.

As will be demonstrated in Chapter 5, the developed models for the representation of the dynamics of thin-walled structures reduce the computational time by at least an order of magnitude when compared to FE models.

Chapter 5

Validation of the Dynamic Models Using FEM and Impact Tests

5.1 Introduction

In chapters 3 and 4, the development of new mathematical models for the dynamics of typical thin-walled structural components encountered in aerospace applications was presented. The objective of this chapter is to validate the mathematical formulations of these models and to demonstrate their ability to simulate accurately the dynamics of the thin-walled aerospace structures during milling. The chapter will be divided in four main sections including the validation of the GSSP model, the MSP model, the CoT formulation and the formulations representing the effect of the fixture supports (PRS and FSS). FE models and impact tests are used for the validation. As will be shown, the developed models permit the prediction of the response of pockets encountered in thin-walled aerospace structures with errors less than 10%, when compared to the FE models and the impact tests. The computation time is reduced by at least one order of magnitude.

5.2 Validation of the Generalized Single-Span Plate Model

The GSSP model is based on the representation of the different sides of a thin-walled structure using plates with translational and rotational springs at the boundaries. To validate this model, five sets of results will be presented. The first set of tests validates the developed model for a plate with torsional and translational spring against a corresponding FE plate. The second set of tests validates the capability of the GSSP model to predict accurately the dynamics of asymmetric pockets with oblique angles and different wall thicknesses. Sinusoidal forces, as well as force signals from actual machining experiments are applied. The third set of validation tests presents the results for the GSSP model for predicting the dynamics of a highly flexible square pocket. The fourth set of results will demonstrate the capability of the GSSP model to predict the dynamic response of a complex multiple-pocket structure with internal rib-walls and holes. As shown in Fig. 4.2, the responses are compared at four output points ($\mathrm{P_A}$, $\mathrm{P_B}$, $\mathrm{P_C}$, $\mathrm{P_D}$). To compare the FE model to the proposed model, the percentage error ϵ at a given point is calculated as follows:

$$\epsilon = \frac{A_f - A_p}{A_{max}} \times 100 \tag{5.1}$$

where A_f is the maximum amplitude of the response at the point under consideration, predicted using the FE model. The symbol A_p designates the maximum amplitude of the response at a given point calculated using the proposed model. The symbol A_{max} represents the maximum amplitude of the response of point $\mathrm{P_B}$, predicted using the FE model. For these four sets of results, the force will always be applied at point $\mathrm{P_A}$.

The fifth set of tests compares the responses determined from the GSSP and the FE models with those obtained experimentally from impact tests. In all cases, Rayleigh's energy method was used for the GSSP model with a maximum of 10 mode shapes versus 30 mode shapes in the FE models. The FE model was developed and analyzed in ABAQUS (version 6.4.) using 2D quadrilateral linear shell elements. Convergence analysis was performed to use a minimum number of elements without sacrificing the accuracy of the solution. Although this considerably reduced the computation time of the FE model, it was found that the developed GSSP model still offered much faster computation. General aluminum material properties were used: Young modulus E = 69×10^9 GPa, ν = 0.3 and ρ =2700 kg/m^3.

5.2.1 Set 1 of Tests: Validation of the GSSP Model Using a FE Model of a Plate

It is necessary to validate the developed approximate model of a plate with torsional and translational springs with a corresponding FE model of a plate. The dimensions of the plate are 200 mm $\times$ 100 mm $\times$ 2 mm. The different parameters chosen for this case study are summarized in Table 5.1. The values of the stiffness of the springs were chosen such that they do not represent a clamped or a free edge. A total of 1000 elements were used in the FE model. By comparing the first ten plate frequencies obtained from the FE and the GSSP models, an error less than 1.3% was obtained as reported in Table 5.2.

Table 5.1: List of parameters for the plate model

l_x	0.2 (m)	l_y	0.1(m)
K_{ox}	84×10^4 (N/m^2)	K_{oy}	102.5×10^4 (N/m^2)
K_{lx}	126×10^4(N/m^2)	K_{ly}	143.5×10^4 (N/m^2)
R_{ox}, R_{lx}	21.0×10^3 (N/m.rad)	R_{oy}, R_{ly}	20.5×10^3(N/m.rad)

Table 5.2: Comparison of the mode frequencies for the plate using the FE model and the GSSP model

Mode	1	2	3	4	5	6	7	8	9	10
FE Plate(Hz)	369	459	670	702	821	1108	1159	1636	1920	1937
GSSP model(Hz)	368	458	672	710	822	1098	1166	1636	1945	1948
Error %	0.3	0.3	0.2	1.2	0.03	0.9	0.5	0.01	1.3	0.6

A sinusoidal force with 30 N magnitude and 628 rad/s frequency was applied at the centre of the plate, i.e point P_A (x=100 mm, y=50 mm) in Fig. 4.2. The errors, in terms of the dynamic responses, are less than 1% at points P_A and P_B as depicted in Fig. 5.1 with a maximum amplitude of vibration of the FE plate of 170 μm. For this simple case, a substantial reduction in computational time (1 to 2 orders of magnitude) was achieved when comparing the developed model (< 2 seconds), with the FE model (> 100 seconds), using the same number of output points. Negligible differences have been found between the frequencies and responses determined using Rayleigh's energy method and the Rayleigh-Ritz method. This can be attributed to the choice of trial functions, which closely approximate the exact mode shapes of the plate.

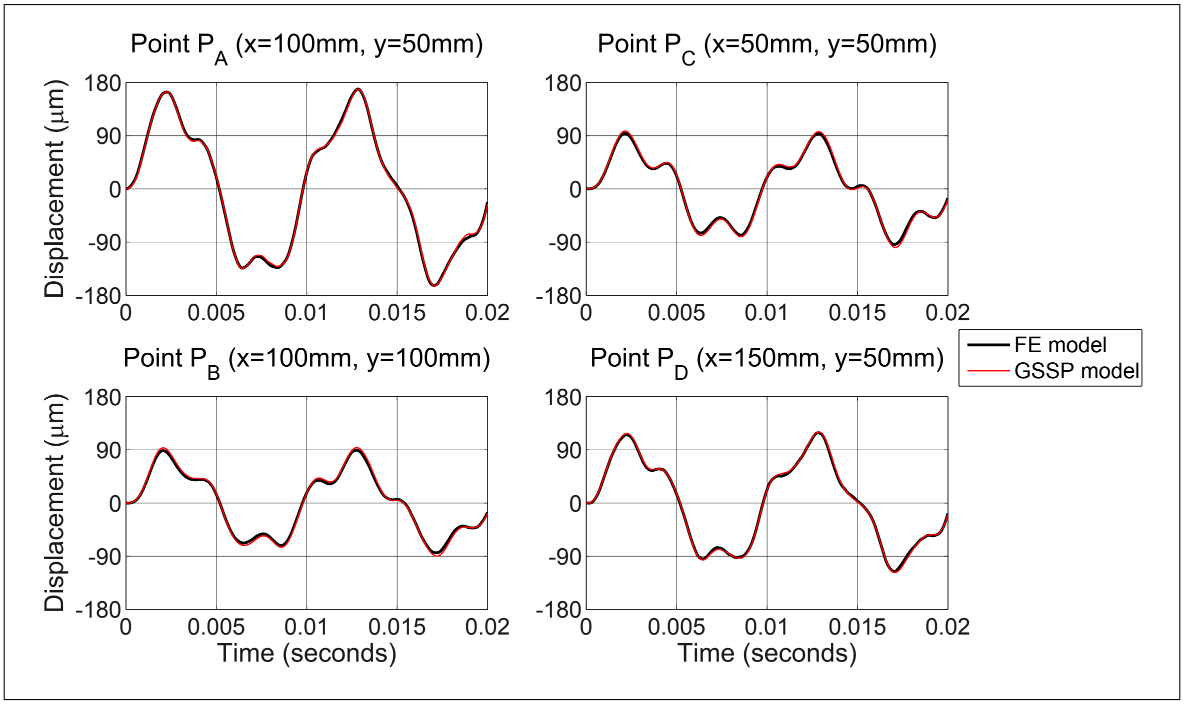

Figure 5.1: Comparison of the plate response predicted by the FE and the GSSP models under a sinusoidal load

5.2.2 Set 2 of Tests: Prediction of the Response of an Asymmetric Pocket

A general case of an asymmetric pocket with a clamped base was used in order to demonstrate the applicability of the GSSP model for the prediction of the response of pocket-type structures. The dimensions of the asymmetric pocket, shown in Fig. 5.2, are typical of flexible aerospace structures. The aspect ratios of the length and height to thickness are 66 and 33, respectively. A sinusoidal force with an amplitude of 60 N and a frequency of 300 rad/s was applied on side 1 (3 mm-thick). The point of load application P_A is located at x=100 mm and y=50 mm. The four output points P_A, P_B, P_C and P_D are shown in Fig. 5.2. A total of 1500 elements were used in the FE model.

Following the procedure described in section 4.3.3, the values of the stiffness of the springs resulting from the calibration, are reported in Table 5.3. The dynamic responses of the GSSP

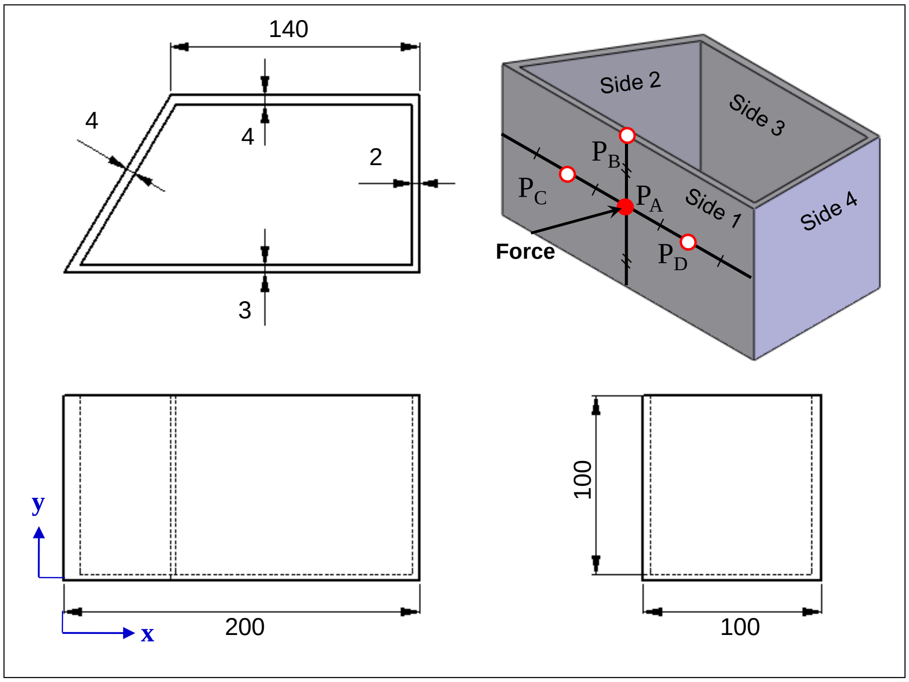

Figure 5.2: Dimensions of the asymmetric pocket in mm

and the FE models are shown in Fig. 5.3. The error in the prediction of the response at points P_A and P_B are less than 2%. This corresponds to an absolute error ≤ 3 μm, which is small compared to the plate thickness and to the typical tolerance value for the aerospace structural components (±125 μm). The errors in prediction of the responses at points P_C and P_D are less than 1.0%. The simulation time of the developed model is less than 2 seconds, while the computation time for the FE model is greater than 3 minutes.

Table 5.3: Calibrated stiffness values of the springs for the asymmetric pocket

K_{ox}	10×10^7 (N/m^2)	K_{oy}	5×10^7 (N/m^2)
K_{lx}	10×10^7(N/m^2)	K_{ly}	1.2×10^4 (N/m^2)
R_{ox}	1.1×10^4 (N/m.rad)	R_{oy}	4.0×10^5(N/m.rad)
R_{lx}	2.3×10^3 (N/m.rad)	R_{ly}	48(N/m.rad)

To demonstrate the necessity for calibration, two plate models with standard boundary conditions (i.e. simply supported, clamped, free) were analyzed and compared to the pocket-side response. The first model represents a plate simply supported at the two side edges, clamped at the bottom edge and free on the top edge (SCSF). This model represents a more flexible structure than the pocket-side since the edges are free to rotate. The second

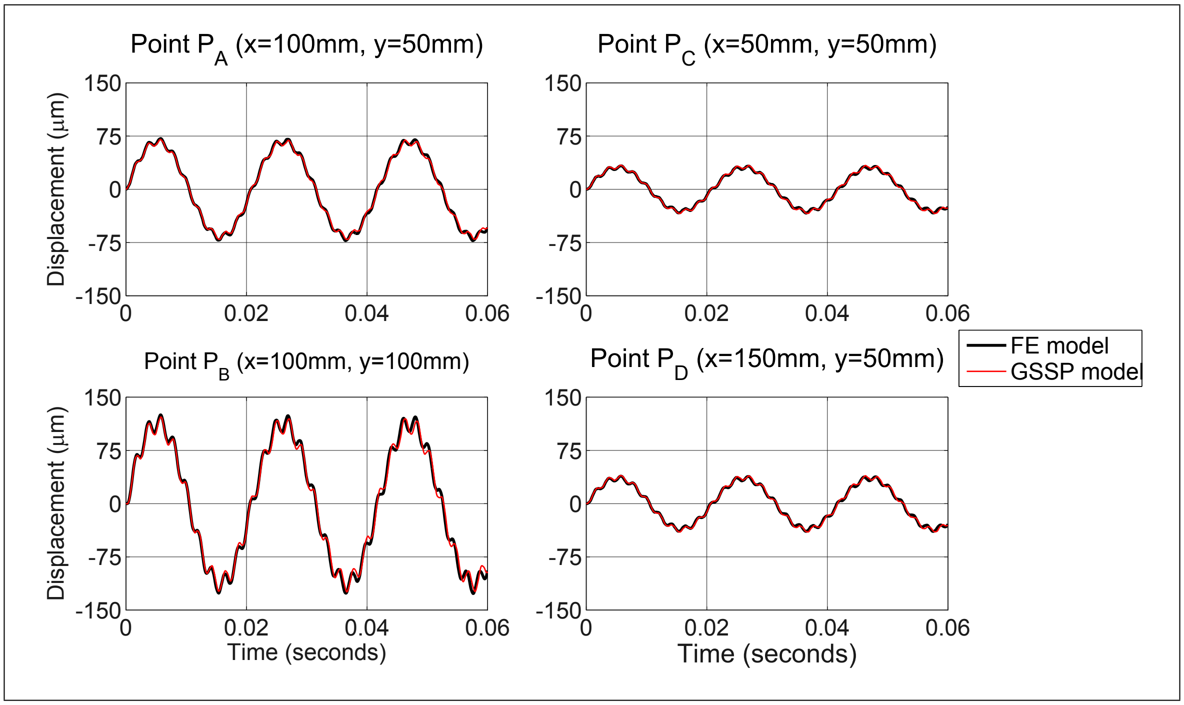

Figure 5.3: Comparison of the asymmetric pocket responses predicted by the FE and the GSSP models under a sinusoidal load (300 rad/s)

case is a plate clamped at the side and bottom edges, and free on the top edge (CCCF). This represents the other extreme, where the plate is more rigid than the actual pocket-side since the rotations of the side edges are completely constrained. A sinusoidal force with an amplitude of 60 N and a frequency of 300 rad/s was applied at point P_A. The responses obtained from these two plate models and the FE model of the pocket at points P_A and P_B are shown in Fig. 5.4. It is found that the first model overestimates the response by 30% in terms of the maximum amplitude of vibration, when compared to the FE response. The second plate model underestimates the maximum amplitude of vibrations by 22%.

The GSSP model was tested by using the same pocket while applying a sinusoidal force of 60 N amplitude and 3770 rad/s frequency (600 Hz/36000 rpm) at point P_A. The frequency of the force simulates the high rotational speeds encountered in high speed machining. As seen in Fig. 5.5, an excellent matching in the prediction of the responses using the GSSP and the FE models is still achieved, both in terms of frequency content and vibration amplitude, with a maximum error at point P_B of less than 4%. This demonstrates that the proposed model can predict accurately the response for higher frequency forces that are different from

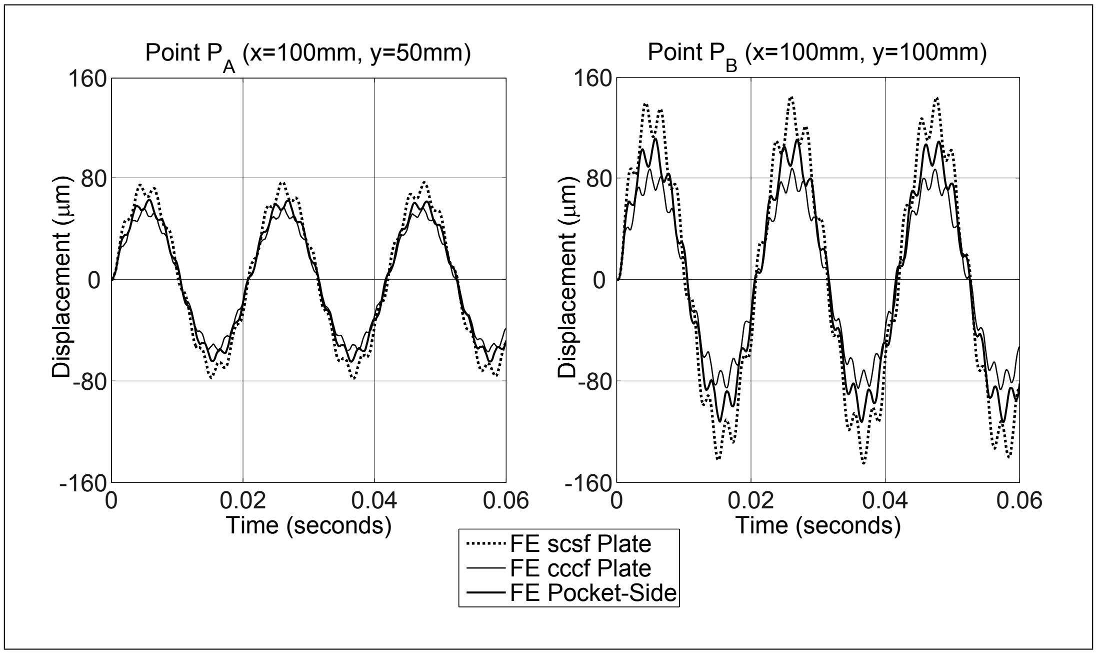

Figure 5.4: Comparison of the responses of the SCSF and CCCF plates to the response of the asymmetric pocket using FEM

those used for the calibration of the model.

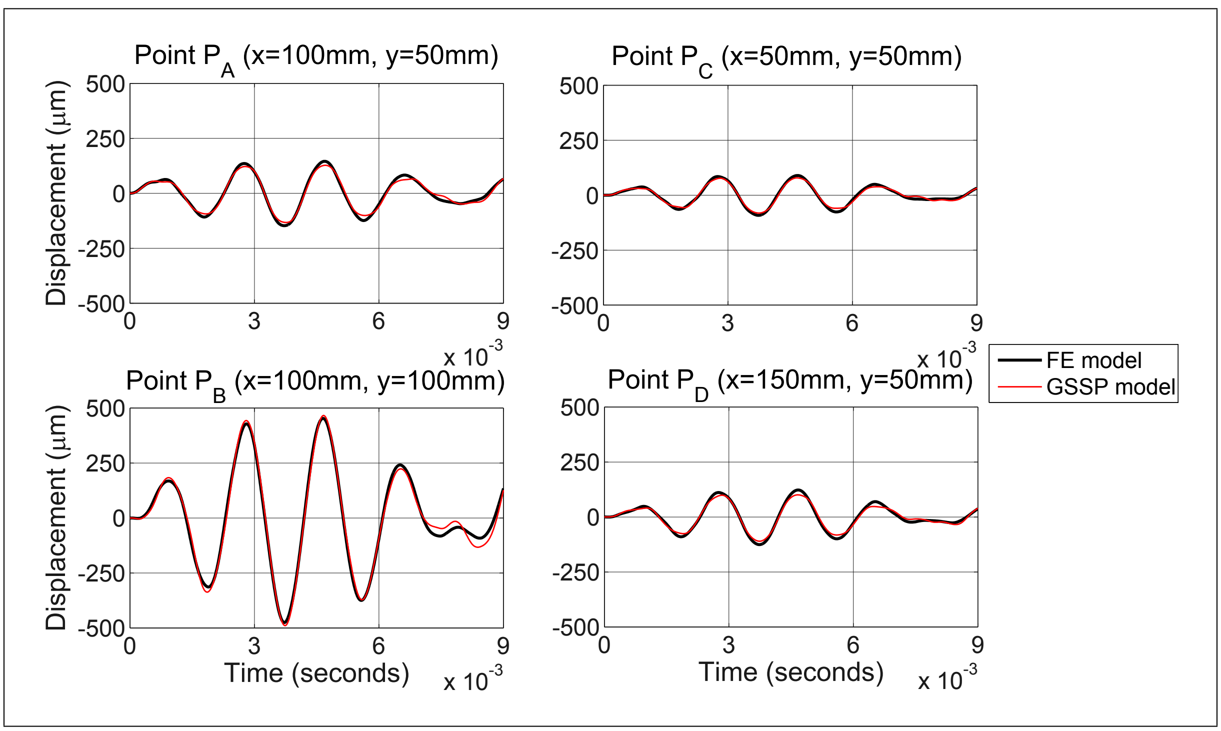

Figure 5.5: Comparison of the asymmetric pocket responses predicted by the FE and the GSSP models under a sinusoidal load (3770 rad/s)

A milling experiment was conducted on a 5-axis high-speed, horizontal machining centre, Makino A88ϵ, in order to generate an actual machining force signal as shown in Fig. 5.6a. In this experiment, a 2-flute, 19 mm flat end-mill cutter was used to finish a pocket made of Al 6065 at 3,180 rpm corresponding to a surface speed of 3.16 m/s. A 0.25 mm and 40 mm radial and axial depth of cuts were used to reproduce practical finishing operations. The force signal during the milling process was measured using a 3-component piezoelectric dynamometer (Kistler, model # 9255B). This machining force was applied at point P_A both in the detailed FE and the simplified GSSP models, as shown in Fig. 5.6b. A comparison of the results can be seen in Fig. 5.7. At point P_A, the relative error in the responses is 2%, while at point P_B, where the maximum deflection occurs, the error is less than 4% (5 μm absolute error). Thus, with a maximum amplitude of vibration of 128 μm, both the GSSP and the FE models will indicate that the part is almost out of tolerance (±125μm).

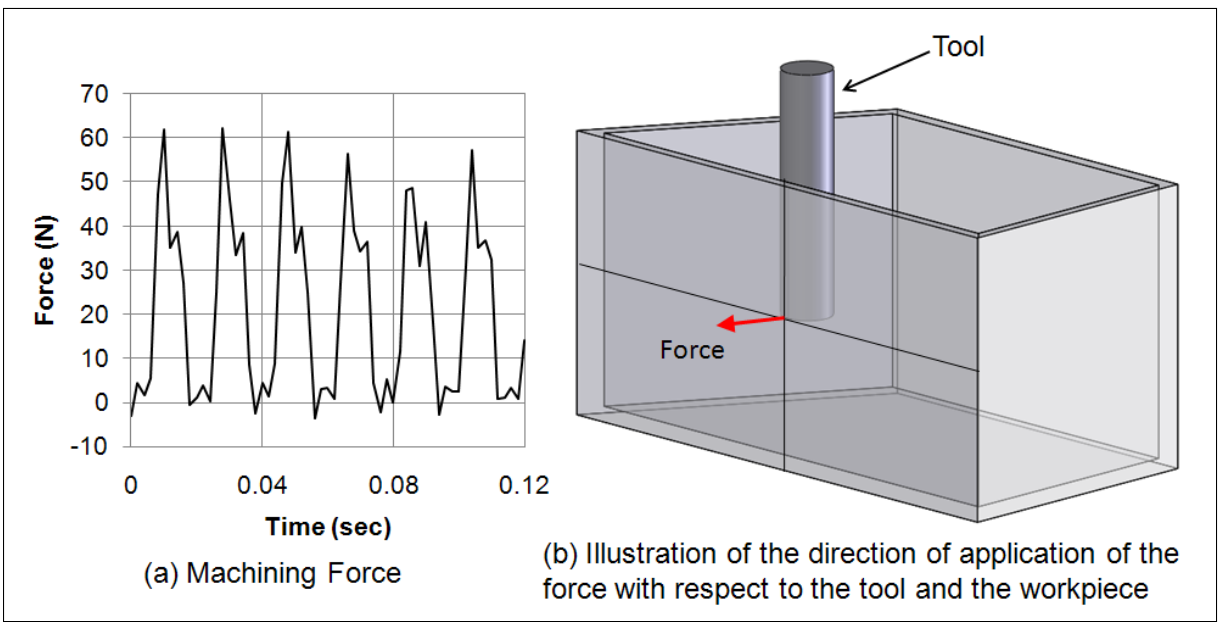

Figure 5.6: Measured machining force and an illustration of the direction of the force with respect to the tool and the workpiece

It is necessary to validate the correlation established in section 4.3.3 between the change of thickness of the adjacent sides and the calibrated stiffness of the rotational springs (refer to Eq. (4.49)). Using the asymmetric pocket in Fig. 5.2, the wall thicknesses of the adjacent sides were incrementally varied from 4 mm to 2 mm for side 2 and from 2 mm to 1 mm

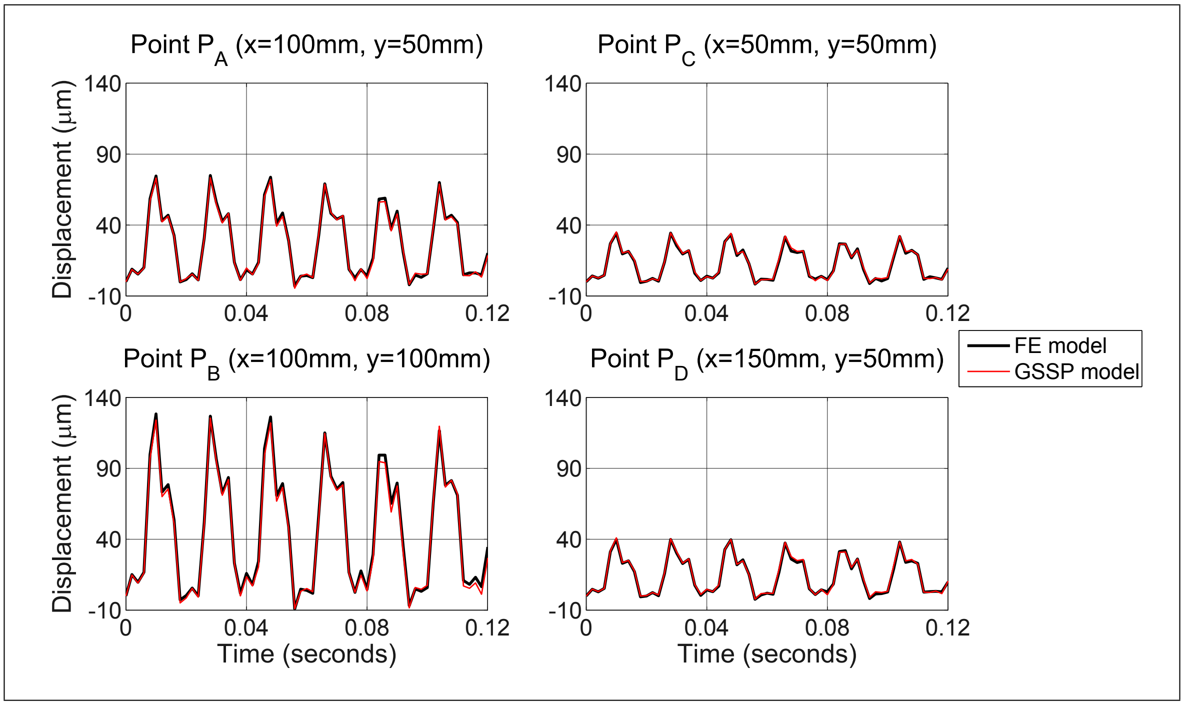

Figure 5.7: Comparison of the asymmetric pocket responses predicted by the FE and the GSSP models under an actual machining load

for side 4. For a given new thickness of an adjacent side, a new spring stiffness has to be determined. One way to determine it is through optimization. In Fig. 5.8, the graphs on the left show the optimization function ψ (refer to Eq. (4.48)) plotted versus the spring stiffness, for different thicknesses of sides 2 and 4. As can be seen, for each new thickness, a corresponding optimum spring stiffness is determined.

Instead of using optimization, new spring values are calculated using the relationship in Eq. (4.49). In Fig. 5.8, the graphs on the right show the stiffness values determined through optimization or calculated using Eq. (4.49) versus the ratio R_t of the new to the old thickness. The springs stiffness coefficients, which are determined through optimization and calculation, are in excellent agreement. Thus, once the calibrated stiffness values of the rotational springs are determined, no further calibration is required for different wall thicknesses. As mentioned previously, due to the high axial stiffness of the adjacent sides, the changes of thickness has a small effect on the translational spring stiffness. The effect of the change of thickness of the non-adjacent sides on the response of the load-application side is negligible.

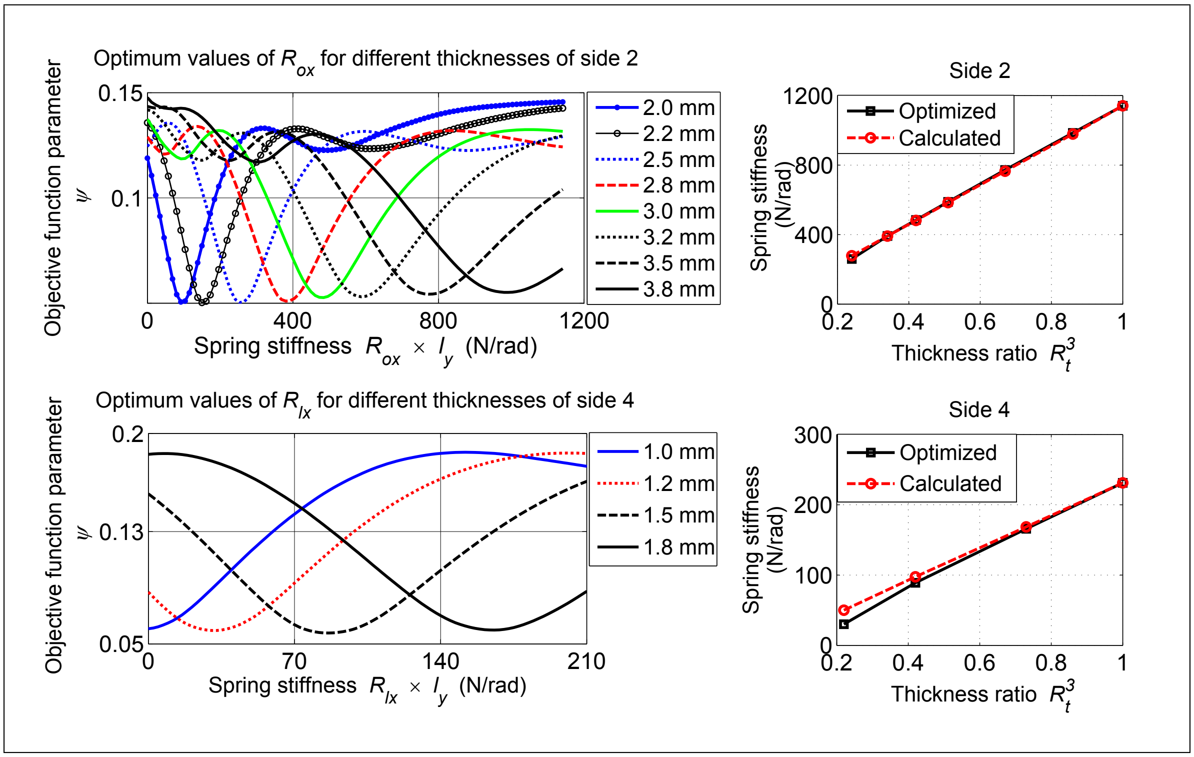

Figure 5.8: Correlation between the rotational spring stiffness and the change of the thickness of the adjacent wall

5.2.3 Set 3 of Tests: Prediction of the Response of a Highly Flexible Square Pocket

Another validation of the model is performed by using a highly flexible pocket structure where the aspect ratios of the length-to-thickness and height-to-thickness are 100 and 50, respectively. Although not common, this level of flexibility is sometimes encountered in aerospace structures. The dimension of this square pocket is 200 mm × 100 mm × 2 mm. Due to the symmetry, the pocket has repeated natural frequencies for different mode shapes, which are not accounted for in the GSSP model. The calibrated values of the stiffness of the springs are shown in Table 5.4. Due to the symmetry of the pocket, the number of optimization variables is six instead of eight since the values for K_{ox} and R_{ox} are the same as K_{lx} and R_{lx}, respectively. In the FE model, a total of 2200 elements was used to model the square pocket with a clamped base.

A Comparison of the responses of the FE pocket versus the GSSP model is shown in

Table 5.4: Calibrated stiffness values of the springs for the square pocket

K_{ox}	3.2×10^6 (N/m^2)	K_{oy}	5×10^7 (N/m^2)
K_{lx}	3.2×10^6(N/m^2)	K_{ly}	5×10^6 (N/m^2)
R_{ox}	3.4×10^3 (N/m.rad)	R_{oy}	0(N/m.rad)
R_{lx}	3.4×10^3 (N/m.rad)	R_{ly}	392(N/m.rad)

Fig. 5.9. A sinusoidal force with 30 N amplitude and 300 rad/s was applied at point P_A. The maximum displacement has a large magnitude of 210 μm. Although some pocket frequencies are absent from the GSSP model, the agreement in the response of the GSSP and the FE models is still remarkably good with a maximum error in response at points P_A and P_B of less than 2%. This corresponds to an absolute error of 4 μm. These errors are within the prediction requirements, set in the objectives of this research and are still small when compared to a tolerance of ±125 μm. Thus, for the extreme case of flexibility, the GSSP model can still offer accurate results in substantially smaller computational times with at least one order of magnitude reduction in the computation time when compared to the FE model.

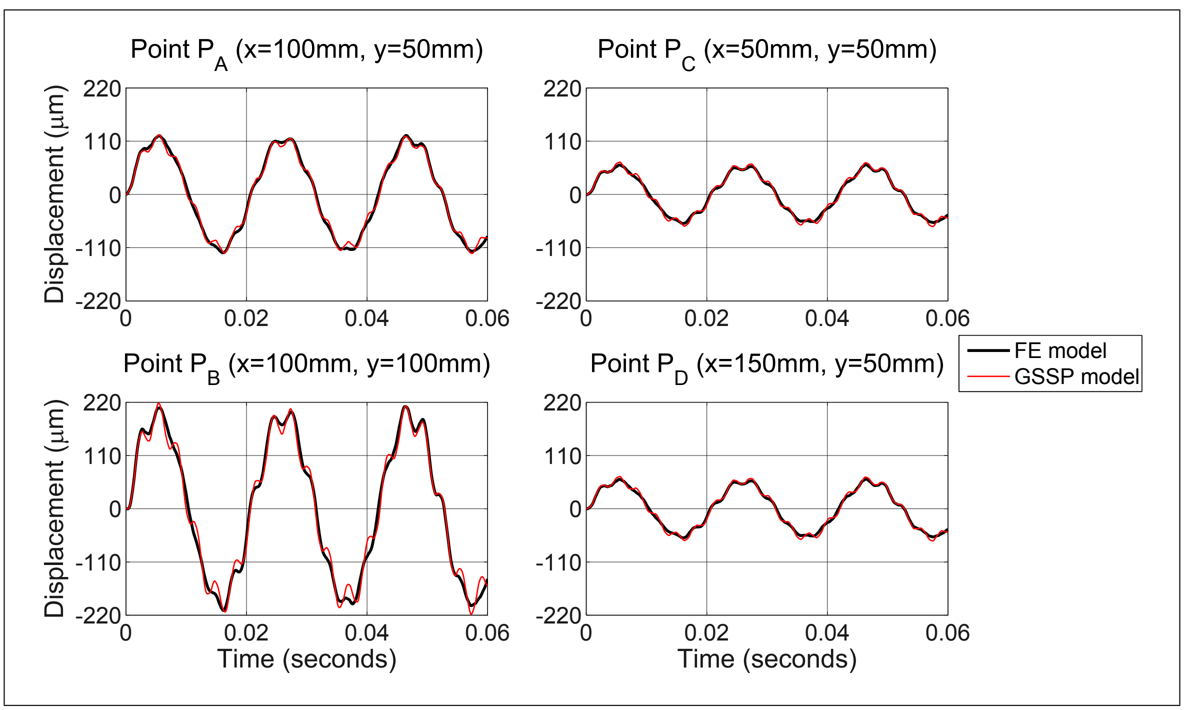

Figure 5.9: Comparison of the square pocket responses predicted by the FE and the GSSP models under a sinusoidal load (300 rad/s)

5.2.4 Set 4 of Tests: Prediction of the Response of a Complex Multiple Pocket Structure

To demonstrate the generality of the GSSP model, the model was validated using a complex thin-walled structure having the shape and the dimensions shown in Fig. 5.10. The load application point is indicated by the arrows and the dotted circle. A sinusoidal load was applied with an amplitude of 60 N and a frequency of 600 rad/s. The response was calculated at four output points (refer to Fig. 4.2). In the FE model the base of the structure was clamped and a total of 3200 elements were used.

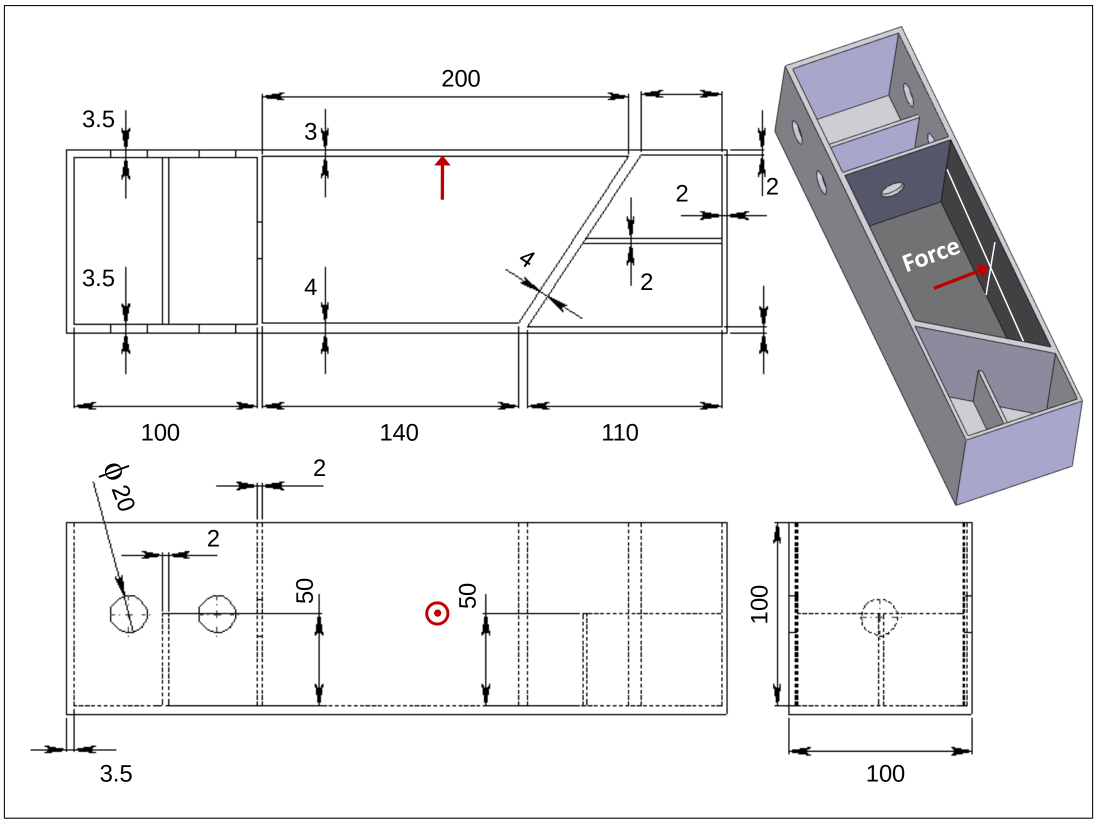

Figure 5.10: Dimensions of the multiple pocket structure in mm

The calibrated values of the stiffness of the springs, which were determined using the procedure outlined in section 4.3.3, are reported in Table 5.5. The responses determined using the FE and the GSSP models are shown in Fig. 5.11. As can be seen, an excellent matching in the response is obtained with predictions errors at points P_A and P_B of less than 4.5%. This corresponds to an absolute error of 5.5 µm. The GSSP model offered at least one to two orders of magnitude reduction in the computation time when compared to the FE model. These results demonstrate the capability of the GSSP model to predict accurately and efficiently the dynamic response of complex thin-walled structures.

Table 5.5: Calibrated stiffness values of the springs for the multiple pocket structure

K_{ox}	10×10^7 (N/m^2)	K_{oy}	5×10^7 (N/m^2)
K_{lx}	10×10^7(N/m^2)	K_{ly}	4.9×10^3 (N/m^2)
R_{ox}	2.1×10^4 (N/m.rad)	R_{oy}	4.0×10^5(N/m.rad)
R_{lx}	1.5×10^4 (N/m.rad)	R_{ly}	3.8×10^2 (N/m.rad)

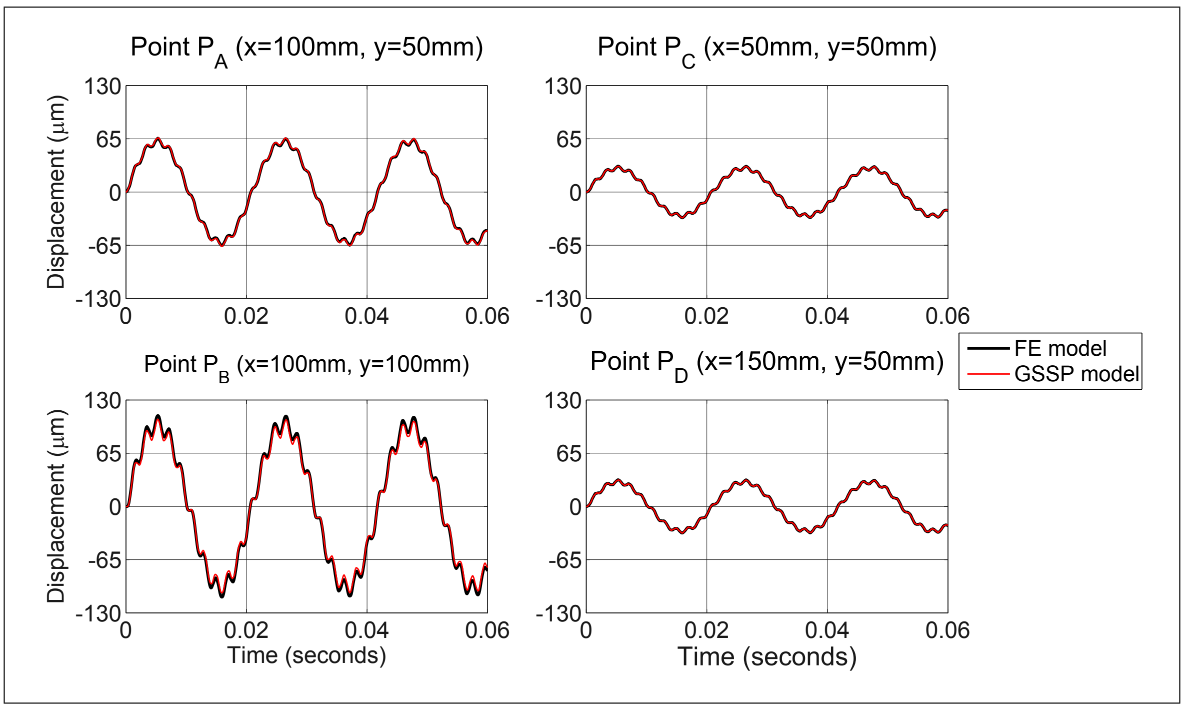

Figure 5.11: Comparison of the multiple-pocket structure response predicted by the FE and the GSSP models under a sinusoidal load (300 rad/s)

5.2.5 Set 5 of Tests: Experimental Validation Through Impact Experiments

The objective of this test is to verify the accuracy of the FE models, as well as, to validate the GSSP model. This is achieved by comparing the responses predicted by the GSSP and the FE models to the actual experimental results of two pockets with different dynamic characteristics. The dimensions of these two pockets are shown in Fig. 5.12a and Table 5.6. For pockets 1 and 2, a total of 1000 and 1800 elements were used, respectively, in the FE model. An illustration of the pocket with a contactless probe to measure the dynamic displacement of the side of the pocket and the probe holder is shown in Fig. 5.12b. The rigid probe holder is fixed to the solid base of the pocket. This solid base represent the boundary conditions of a clamped edge. Due to the non-uniformity of the wall thicknesses, they were determined based on an average of 9 to 15 points on each side using a coordinate measuring machine (Mitutoyo, model: MACH 806). To demonstrate the generality of the approach, the corner radius in pocket 1 was represented in the FE model as a sharp corner. The calibrated spring values, determined using the methodology described in section 4.3.3, are shown in Tables 5.7 and 5.8. The use of these spring values in the GSSP model gives results that are in very good agreement in terms of the displacement response with the predictions of the FE model with errors less than 6%.

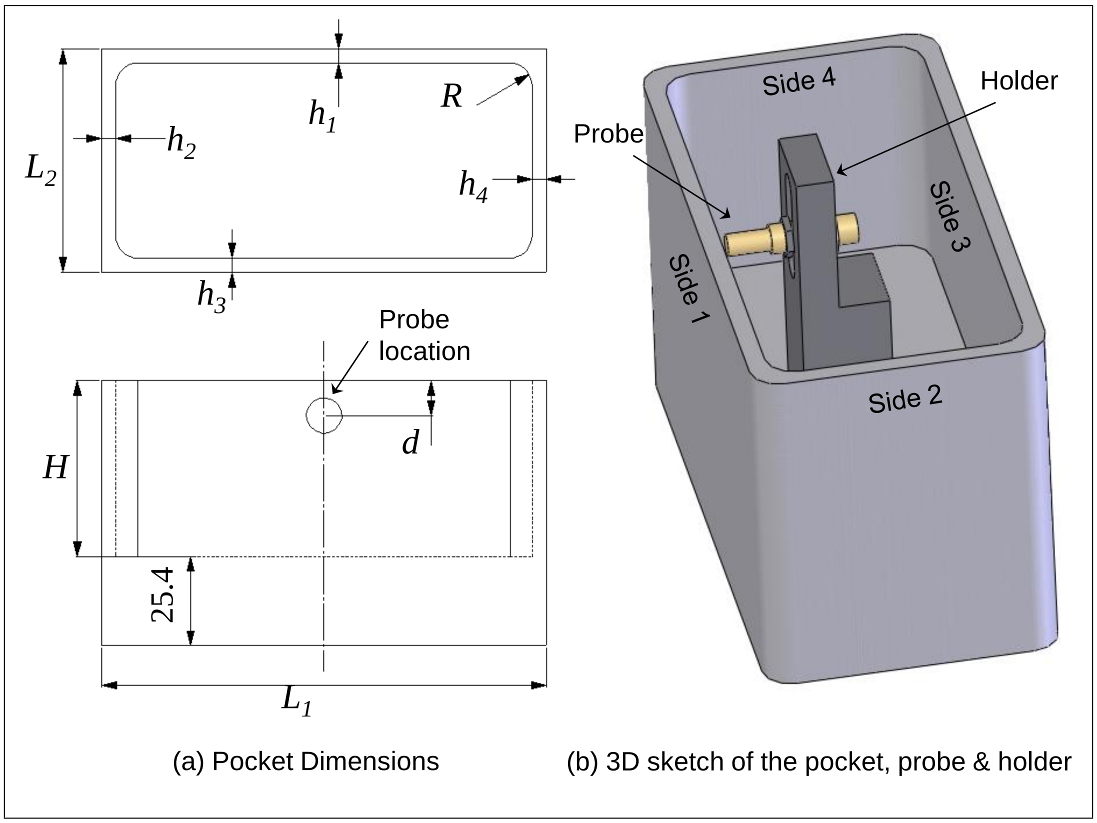

Figure 5.12: Representation for the dimensions of the pockets used for the experimental validation of the GSSP model

Table 5.6: Dimensions (in mm) of pockets 1 and 2, for the experimental validation of the GSSP model

	L_1	L_2	H	h_1	h_2	h_3	h_4	R	d
Pocket 1	101	50	51	1.57 ±0.06	1.55 ±0.07	1.53 ±0.06	1.51 ±0.08	4.76	3.5
Pocket 2	102	51	101	3.25 ±0.05	3.20 ±0.04	3.33 ±0.05	3.25 ±0.05	0	10

Table 5.7: Calibrated stiffness values of the springs for pocket 1

K_{ox}	4.2×10^6 (N/m^2)	K_{oy}	1.0×10^8 (N/m^2)
K_{lx}	5.2×10^6 (N/m^2)	K_{ly}	1.5×10^5 (N/m^2)
R_{ox}	2.2×10^3 (N/m.rad)	R_{oy}	1.0×10^7(N/m.rad)
R_{lx}	6.4×10^3 (N/m.rad)	R_{ly}	0(N/m.rad)

Table 5.8: Calibrated stiffness values of the springs for pocket 2

K_{ox}	1.0×10^8 (N/m^2)	K_{oy}	1.0×10^8 (N/m^2)
K_{lx}	1.0×10^8 (N/m^2)	K_{ly}	4.7×10^5 (N/m^2)
R_{ox}	1.1×10^4 (N/m.rad)	R_{oy}	3.9×10^6(N/m.rad)
R_{lx}	1.5×10^4 (N/m.rad)	R_{ly}	1.2×10^4 (N/m.rad)

The experimental frequencies of the pockets were determined using an Impulse Force Test Hammer system. The system consists of impulse hammers with automatically-actuated piezoelectric units (PCB 086C04 and PCB 086D05) for pockets 1 and 2, respectively and an accelerometer (PCB 352C23). The comparison of the first two natural frequencies determined experimentally and through the FE model is presented in Table 5.9. For the first pocket, the errors in the 1^{st} and 2^{nd} frequencies are less than 7% and 4%, respectively. For the second pocket, the errors are less than 0.1% and 3%, respectively.

Table 5.9: Comparison of the experimental frequencies and the FE frequencies of pockets 1 and 2 for the first two modes

		Experimental Frequency(Hz)	FE Frequency (Hz)	% Error
Pocket 1	Mode 1	896	959	7.0
	Mode 2	1001	1037	3.6
Pocket 2	Mode 1	1326	1325	0.08
	Mode 2	2701	2764	2.33

Using the hammers (PCB 086C04) and (PCB 086D05), which also measure the forces, an impact force was applied on side 1 of pockets 1 and 2, respectively. The responses were measured using the contactless displacement sensor (KAMAN, model 1UEP) illustrated in Fig. 5.12b. The measured forces were applied in the FE and the GSSP models in order to compare the predicted and measured responses. There are three different measurement errors including the errors due to the accuracy of the probe ε_p, the accuracy of the force measurement transducer ε_f and the uncertainty of the position of the load-application point ε_l.

The calibration of the probe was performed by using linear fitting with a coefficient of determination (R^2) of 0.997 and a measurement error ε_1 of ± 3 μm. For the errors in the force measurement ε_2, the transducer of the hammer has a linearity of ± 1%, according to the manufacturer specifications. Since the model is linear, one can assume that the measured force linearly affect the measured vibration. Thus a 1% error in the force measurement is translated to a 1% error in the probe measurements. Thus, ε_2 is determined in μm as ±1% of the maximum amplitude of the measured vibration. The uncertainty of the position of the load-application is estimated to be within ± 2 mm. To determine the effect of the force position on the response, using the FE model, the load was applied at four points on the circumference of a circle with a radius of 2 mm and a centre at the nominal position of the load. The amplitude of the peak displacement was calculated for each case and compared to a nominal case in which the load is applied at the centre of the circle. The error ε_3 is determined in μm as the average of the differences between the amplitudes of the peaks of the four cases and the amplitude of the peak of the nominal case. The total error in measurement ε_t can be calculated as:

$$\varepsilon_t = \left(\sum_{i=1}^{3} \varepsilon_i^2 \right)^{\frac{1}{2}} \tag{5.2}$$

The experimental responses for the first and second pockets, shown in Fig. 5.13, are in excellent agreement with the GSSP model predictions. The measurement errors, calculated for each pocket according to Eq. (5.2), are shown in Table 5.10. The percentage deviation between the maximum amplitude of the experimental data and those of the FE and the

GSSP model are less than 1% for the first pocket (1.6 μm) with a total measurement error of ± 8.0 μm. For the second pocket, the predictions errors are 6% (7.5 μm) for the FE model and 2% (2.6 μm) for the GSSP model with a total measurement error of ± 6.0 μm.

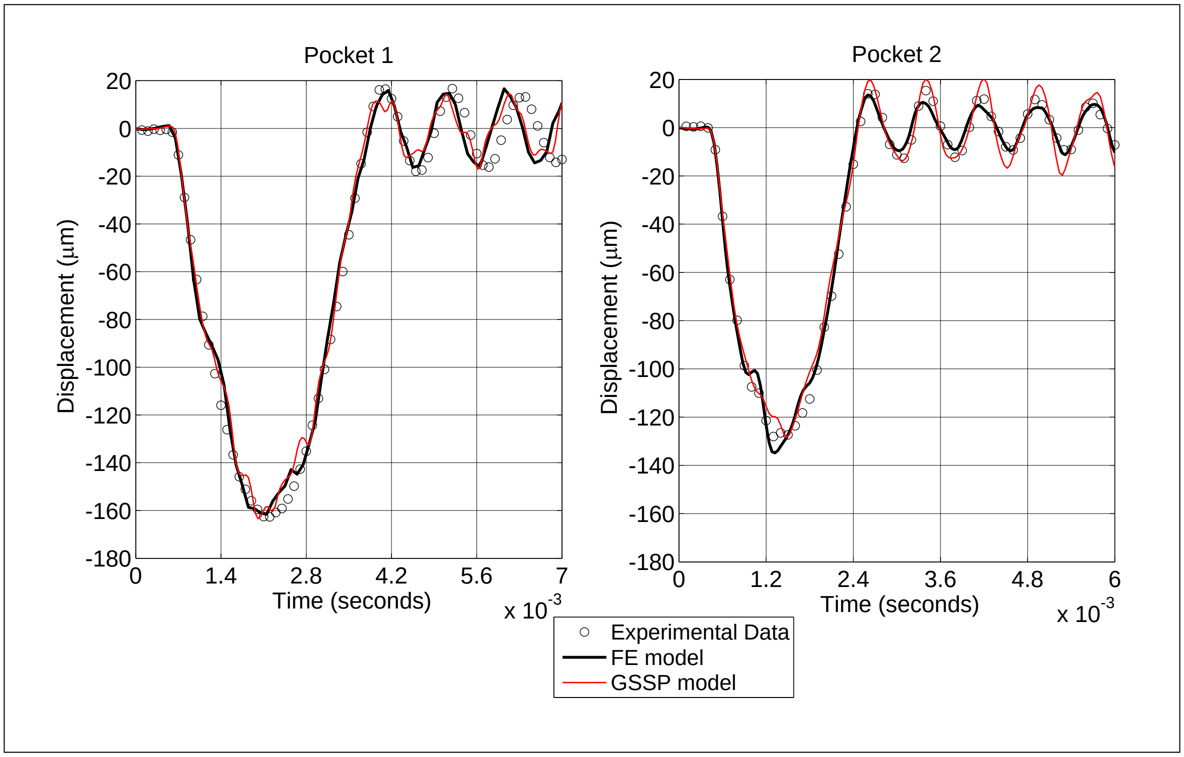

Figure 5.13: Comparison of the responses from experiment, FE model and GSSP model for pockets 1 and 2

Table 5.10: Measurement errors for the impact test for pockets 1 and 2

Error type	Pocket 1	Pocket 2
ε_1 (μm)	± 3.0	± 3.0
ε_2 (μm)	± 1.6	± 1.4
ε_3 (μm)	± 7.2	± 5.0
ε_t (μm)	± 8.0	± 6.0

Although the GSSP model was calibrated using a sinusoidal force, excellent matching of the response is achieved under impact loading as well. This shows that both the FE and the GSSP models can be considered as high-fidelity representations of the pocket dynamics. For these two cases, no damping was included since the structural damping coefficients of the pockets were found to be less than 1.0%.

5.3 Validation of the Multi-Span Plate Model

The validation of the MSP model includes two main sets of validations results. Set 1 will compare the MSP model to FE multi-span plates. Set 2 will include the comparison of the frequencies and the responses for different types of pockets using the MSP and FE models. Referring to Fig. 4.2, the response will be calculated at the same output points (P_A, P_B, P_C and P_D) located on the first span of the plate and the corresponding side of the pocket. Point P_A will be located at the centre of the span/side, P_B at the middle of the free edge and P_C and P_D midway between point P_A and the side edges. The prediction errors will be calculated using Eq. (5.1). No impact tests were performed to validate the MSP model since an extensive experimental validation through machining tests was performed for the MSP model and will be presented in Chapter 6. An additional validation case will be presented in section 5.5.4 to demonstrate the applicability of the MSP model for the prediction of the dynamic response of pockets with internal rib-walls. Similar to the previous sections, the FE models are based on 2D quadrilateral linear shell elements. The same aluminum material properties were used (E = 69×10^9 GPa, ν = 0.3 and ρ =2700 kg/m^3).

5.3.1 Set 1 of Tests: Validation of the MSP Model Against FE Models of Multi-Span Plates

For the developed multi-span plate model, there is neither analytical nor approximate solutions in the literature. In order to validate its formulation, the MSP model was compared to FE models of different multi-span plates. The frequencies and the responses of two four-span plates will be analyzed. Both plates have the same width and length; however, the first multi-span plate has uniform thicknesses for all spans and the second has non-uniform thicknesses. The width of the two multi-span plates is 100 mm. The other dimensions are given in Table 5.11. In both cases, Rayleigh's energy method and the Rayleigh-Ritz method are implemented and the results are compared. The calculation of the MSP model included 10 mode shapes as opposed to 30 mode shapes in the FE model with a total of 2500 elements.

The frequencies of multi-span plate 1 (with uniform thicknesses), evaluated using the FE

Table 5.11: Dimensions of the multi-span plate for the validation of the MSP model

Multi-span plate #	Dimensions	span 1	span 2	span 3	span 4
1	Length (mm)	200	100	200	100
	Thickness (mm)	3.0	3.0	3.0	3.0
2	Length (mm)	200	100	200	100
	Thickness (mm)	3.0	2.0	4.0	3.5

model and the MSP model, are listed in Table 5.12. The maximum error in the frequencies determined using the Rayleigh-Ritz method and Rayleigh's energy method are less than 1.5% and 3.0%, respectively. Although the Rayleigh-Ritz method offers better accuracy, both methods allow us to predict accurately the frequencies of the multi-span plate. This was expected since the proposed trial mode shapes satisfy the geometric and natural boundary conditions for the vertical edges of multi-span plates with uniform thicknesses. It should be noticed that increasing the number of included mode shapes does not affect the prediction of the first frequencies in the case of Rayleigh's energy method. The responses of the four points on the first span are shown in Fig. 5.14. For this case, a 30 N force with a frequency of 1256 rad/s (200 Hz or 12,000 rpm) was applied at the centre of the free edge, i.e. at point P_B (x=100 mm, y = 100 mm). The maximum error of the response at point P_B is less than 6% for the Rayleigh-Ritz method, and less than 11% for Rayleigh's energy method. It can be seen that an excellent matching is achieved using the Rayleigh-Ritz method in terms of frequency and amplitude. Rayleigh's energy method also offers excellent predictions of the frequencies and relatively good prediction of the dynamic response with a slightly better computational efficiency.

Table 5.12: Comparison of the mode frequencies of multi-span plate 1 (with uniform thicknesses) predicted by the FE model and the MSP model

	Mode	1	2	3	4	5	6	7	8	9	10
	FE (Hz)	465	500	923	1094	1232	1476	1841	1848	1991	2194
Rayleigh-Ritz	MSP (Hz)	468	505	933	1108	1248	1495	1853	1862	2015	2222
	Error %	0.9	0.9	1.1	1.2	1.3	1.3	0.6	0.9	1.2	1.3
Rayleigh	MSP (Hz)	475	510	950	1124	1266	1511	1872	1875	2041	2245
	Error %	2.4	2.0	3.0	2.8	2.8	2.3	1.7	1.5	2.5	2.3

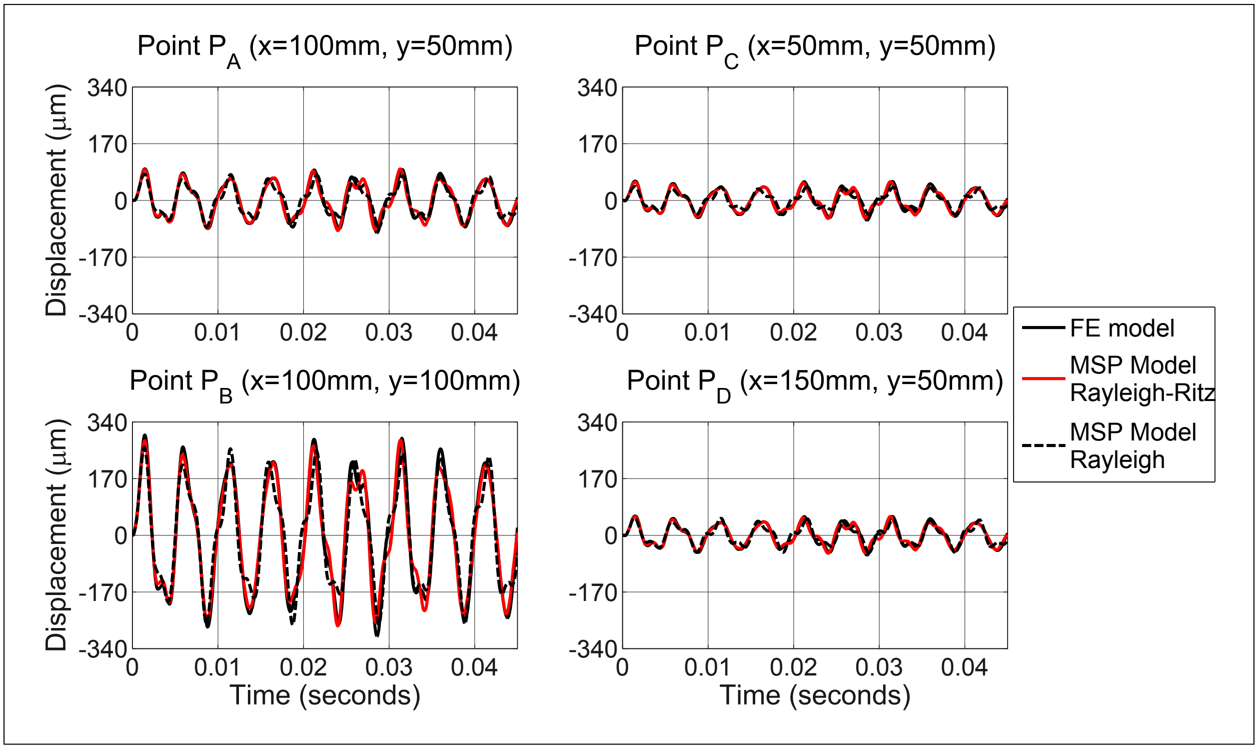

Figure 5.14: Comparison of the responses of multi-span plate 1 (with uniform thicknesses) predicted by the FE and the MSP models under a sinusoidal load

For multi-span plate 2 (with non-uniform thicknesses), the predictions of the frequencies using the two MSP formulations, are listed in Table 5.13. The errors in frequencies between the MSP and the FE models are less than 2% when the Rayleigh-Ritz method was implemented. Using Rayleigh's energy method, the errors in the frequencies of the first six mode shapes are less than 6%; however, for higher mode shapes the error become relatively large, as expected. For the same applied loading and output points as in the previous case, the responses determined using the FE and the MSP models are shown in Fig. 5.15. The errors in the response predicted by the MSP model using the Rayleigh-Ritz method are less than 3.5%. This corresponds to an absolute error of 11 μm. There is generally a reasonable agreement in the responses when using Rayleigh's energy method; however, the error at point P_B is greater than 15%. Based on these results and in order to maintain consistency, the responses for all the coming validation cases, will be calculated using the Rayleigh-Ritz method.

Table 5.13: Comparison of the mode frequencies of multi-span plate 2 (with non-uniform thicknesses) predicted by the FE model and the MSP model

	Mode	1	2	3	4	5	6	7	8	9	10
	FE (Hz)	468	594	931	1133	1264	1583	1817	1889	2030	2424
Rayleigh-	MSP (Hz)	472	600	942	1147	1281	1607	1835	1921	2061	2452
Ritz	Error %	1.0	1.0	1.2	1.2	1.3	1.5	1.0	1.7	1.5	1.2
Rayleigh	MSP (Hz)	495	594	970	1196	1264	1624	1991	2087	2351	2398
	Error %	5.9	0.02	4.3	5.5	0.03	2.6	9.6	10.5	15.9	1.0

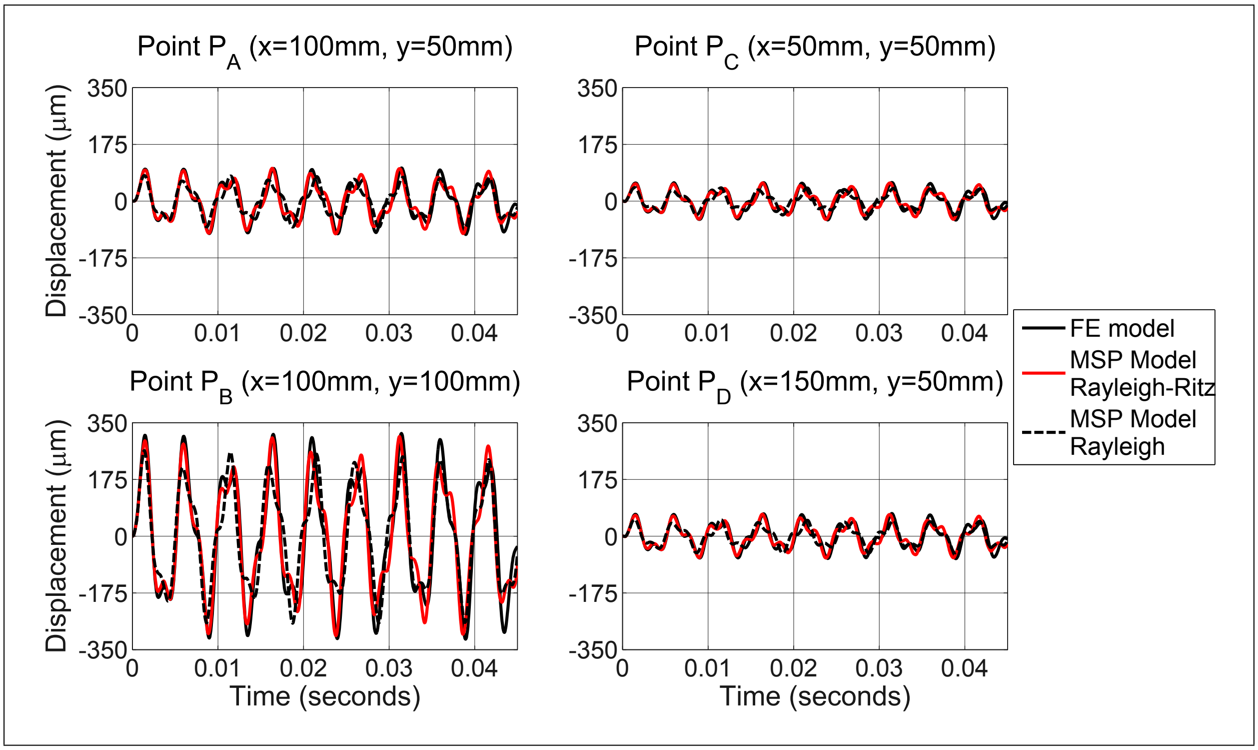

Figure 5.15: Comparison of the responses of multi-span plate 2 (with non-uniform thicknesses) predicted by the FE and the MSP models under a sinusoidal load

5.3.2 Set 2 of Tests: Validation of the MSP Model Against FE Models of Asymmetric Pockets

Now that the MSP model was validated against FE models of multi-span plates, it is necessary to compare the response of different pockets to the corresponding MSP model. To show the generality of the approach, the validations are performed for different pocket shapes. The strategy for the validation is to start with a rectangular pocket, then modify its shape by changing the dimensions of its sides and the angles of its corners. In such a way, one could see the effect of the gradual change of the pocket shape on the response. The general shape of the pocket is shown in Fig. 5.16 and the dimensions are listed in Table 5.14. The output points, where the responses are calculated, are on side 1, as shown in Fig. 5.16. The total number of elements for the six pockets ranged between 2200 to 2600.

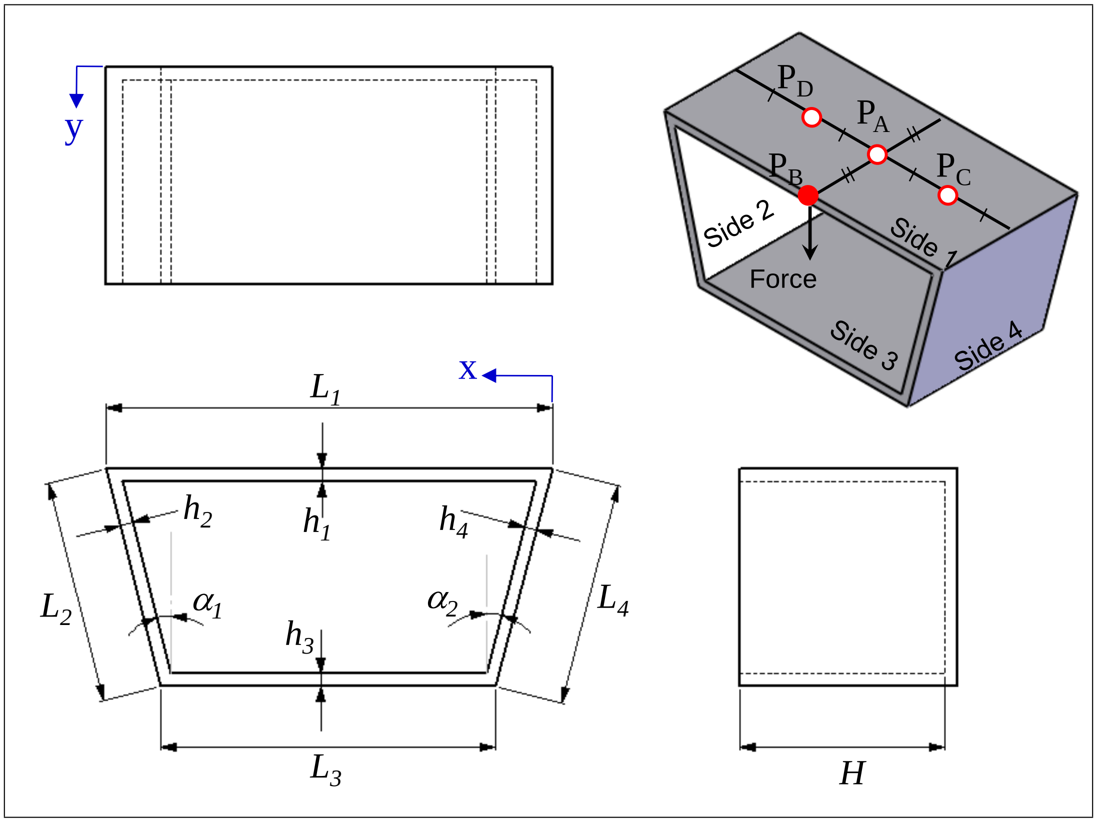

Figure 5.16: Representation of the dimensions of the generalized pocket used for the validation of the MSP model

Table 5.14: Dimensions (in mm) of the pockets for the validation of the MSP model

	L_1	L_2	L_3	L_4	h_1	h_2	h_3	h_4	H	α_1	α_2
Pocket 1	150.0	100.0	150.0	100.0	3.0	3.5	4.0	2.0	80	0	0
Pocket 2	150.0	101.6	132.0	100.0	3.0	3.5	4.0	2.0	80	10	0
Pocket 3	150.0	106.6	113.0	100.0	3.0	3.5	4.0	2.0	80	20	0
Pocket 4	150.0	115.6	92.0	100.0	3.0	3.5	4.0	2.0	80	30	0
Pocket 5	150.0	130.6	66.0	100.0	3.0	3.5	4.0	2.0	80	40	0
Pocket 6	200.0	130.6	58.0	115.6	3.0	3.5	4.0	2.0	80	40	30

The frequencies for pocket 1 calculated using a FE model and the MSP model of the pocket are listed in Table 5.15. The maximum error in the predictions of the frequencies is less than 3.5%. This close agreement in the frequencies can be attributed to the good approximation of the mode shapes. The first four mode shapes of the pocket using the FE and the MSP models are shown in Fig. 5.17. By unfolding the pocket sides, one can see the agreement between the mode shapes of the pocket and the multi-span plate. For the first mode shape, sides 1 and 3 move outwards, while sides 2 and 4 move inward. Correspondingly, spans 1 and 3 move up and spans 2 and 4 move down. For mode 2, sides 1, 2 and 4 move outward and side 3 moves inward. In the multi-span plate, spans 1, 2, 4 move down and span 3 moves up. For mode 3, the maximum deflection is seen on side 4 and span 4, while one can notice a sine wave shape on side 1 and span 1. For mode 4, the maximum amplitude is at side 2 and span 2. The shape of a sine wave can be seen at sides 1 and 3 and spans 1 and 3.

Table 5.15: Comparison of the mode frequencies of pocket 1 predicted by the FE model and the MSP model

Mode	1	2	3	4	5	6	7	8	9	10
FE (Hz)	756	949	1126	1533	1880	2323	2427	2871	2910	3484
MSP (Hz)	768	969	1143	1565	1926	2388	2488	2926	2956	3592
Error %	1.6	2.1	1.5	2.1	2.4	2.8	2.5	1.9	1.6	3.1

A sinusoidal force of 30 N amplitude and 1256 rad/s frequency was applied at the centre of the free edge of side/span 1, i.e point P_B (x=75 mm, and y = 80 mm). The responses at the four output points for the FE and the MSP models are shown in Fig. 5.18. The error in the prediction of the responses at points P_B and P_A, are less than 5.5 % and 4.5 %, respectively. The maximum amplitude of vibration at point P_B is 155 μm. As shown in Fig. 5.18, the responses calculated using the MSP model and the FE pocket are in close agreement in terms of the global amplitude and the instantaneous time response. For this case, 20 mode shapes were used for the MSP model versus 30 mode shapes in the FE model. The computation time to determine the responses was reduced by at least one order of magnitude when compared to the FE calculations. When 30 mode shapes were used in the MSP model, the errors in the response at point P_B were less than 4.5%.

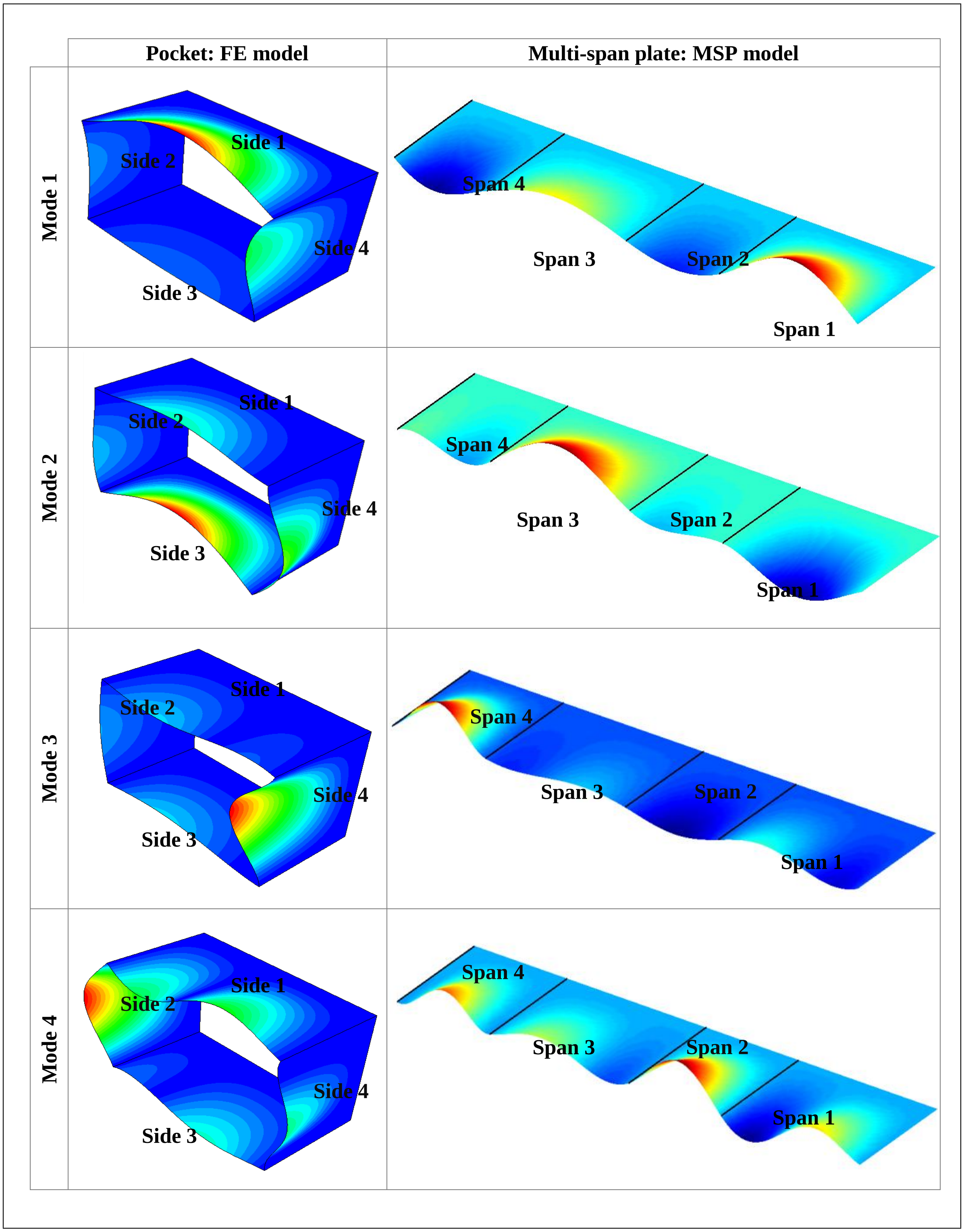

Figure 5.17: Comparison of the first four mode shapes of pocket 1 using the FE and the MSP models

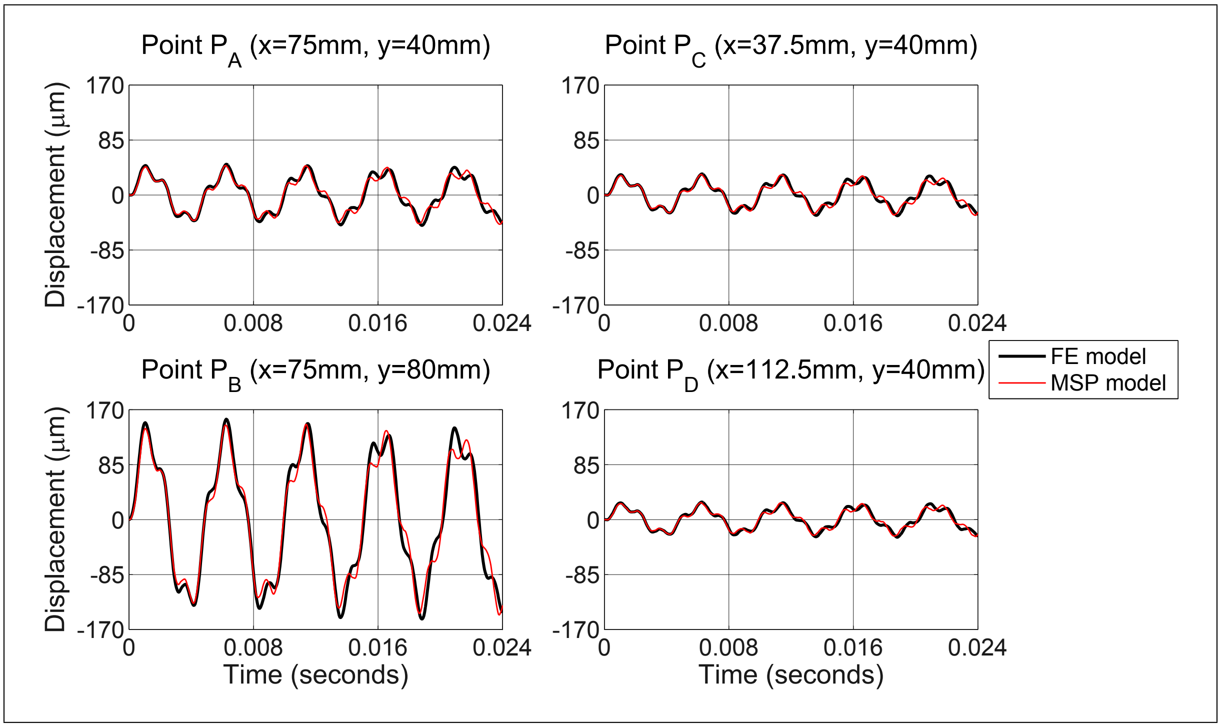

Figure 5.18: Comparison of the responses of pocket 1 predicted by the FE and the MSP models under a sinusoidal load

For pockets 2, 3, 4 and 5, similar agreement in the predictions of the frequencies of the pockets are achieved with errors less than 6%. The responses at point P_B, for pockets 2, 3, 4 and 5, are shown in Fig. 5.19. The frequency, amplitude and location of the load are similar to those applied for pocket 1. One can see that an excellent matching is achieved in the responses with predictions errors of less than 5%. It can be also noticed that small variations exist between the response of the different pockets. This shows that for a given side (e.g. side 1), variations in the dimensions of the adjacent sides has negligible effect on its response. This is one of the reasons why the concept of a multi-span plate can accurately simulate the response of rectangular and non-rectangular pockets.

The comparison of the frequencies of pocket 6, which has a trapezoidal shape, are listed in Table 5.16, with prediction errors less than 5%. The responses at the four points on side 1 are shown in Fig. 5.20. The errors for all points are less than 3%. Although the amplitude of the applied force was equal to 30 N, the maximum amplitude of vibration is 223 μm. This large amplitude of vibration and small applied force highlight the main challenge in machining such structures.

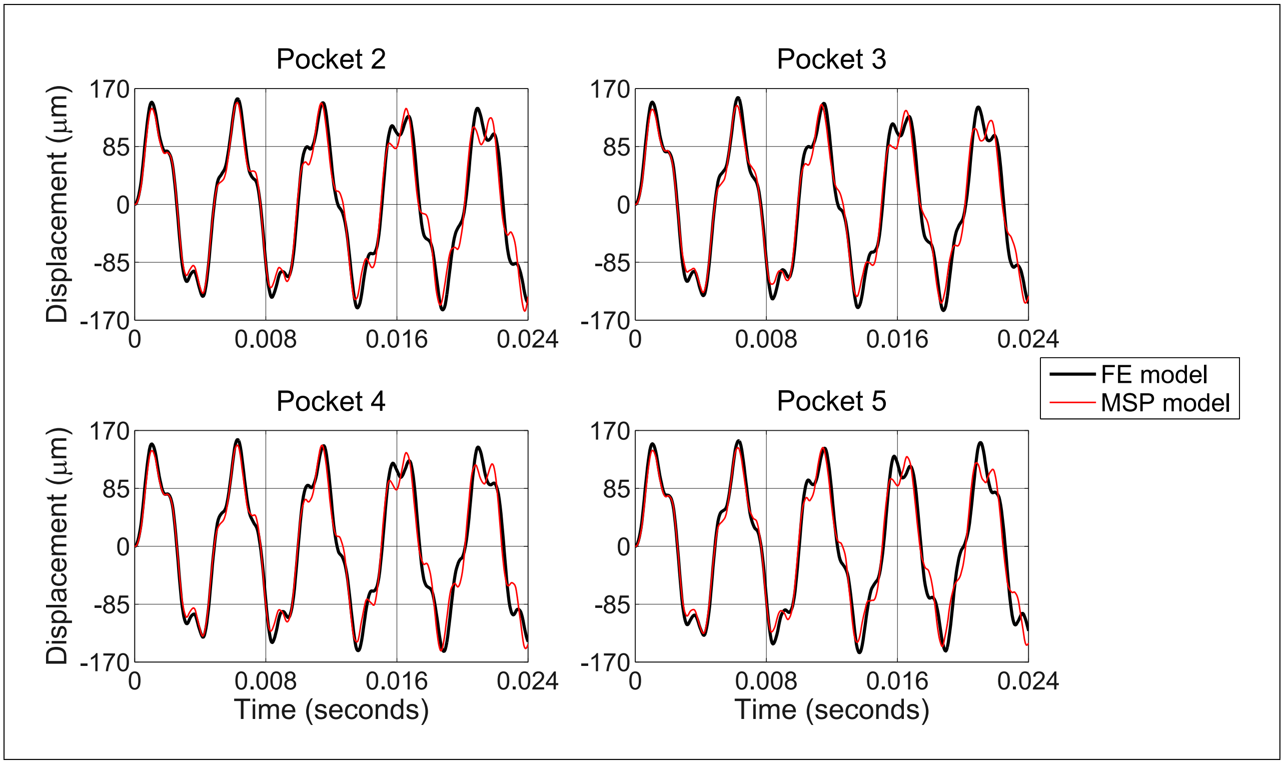

Figure 5.19: Comparison of the responses at point P_B for pockets 2, 3, 4 and 5 predicted by the FE and the MSP models under a sinusoidal load

Table 5.16: Comparison of the mode frequencies of pocket 6 predicted by the FE model and the MSP model

Mode	1	2	3	4	5	6	7	8	9	10
FE (Hz)	593	864	1040	1252	1986	2224	2264	2603	2726	3329
MSP (Hz)	600	882	1067	1278	2027	2259	2337	2706	2756	3413
Error %	1.2	2.1	2.6	2.1	2.1	1.6	3.2	4.0	1.1	2.5

To validate the model for different loading conditions, the frequency of the load was increased to 3896 rad/s (620 Hz, 37200 rpm) while maintaining its amplitude and location unchanged. This frequency is chosen such that it is close to the first natural frequency of pocket 6 and thus, resonance is expected. As seen in Fig. 5.21, the responses are still in excellent agreement. Thus, the MSP model can provide accurate predictions for the responses of thin-walled pockets in resonance.

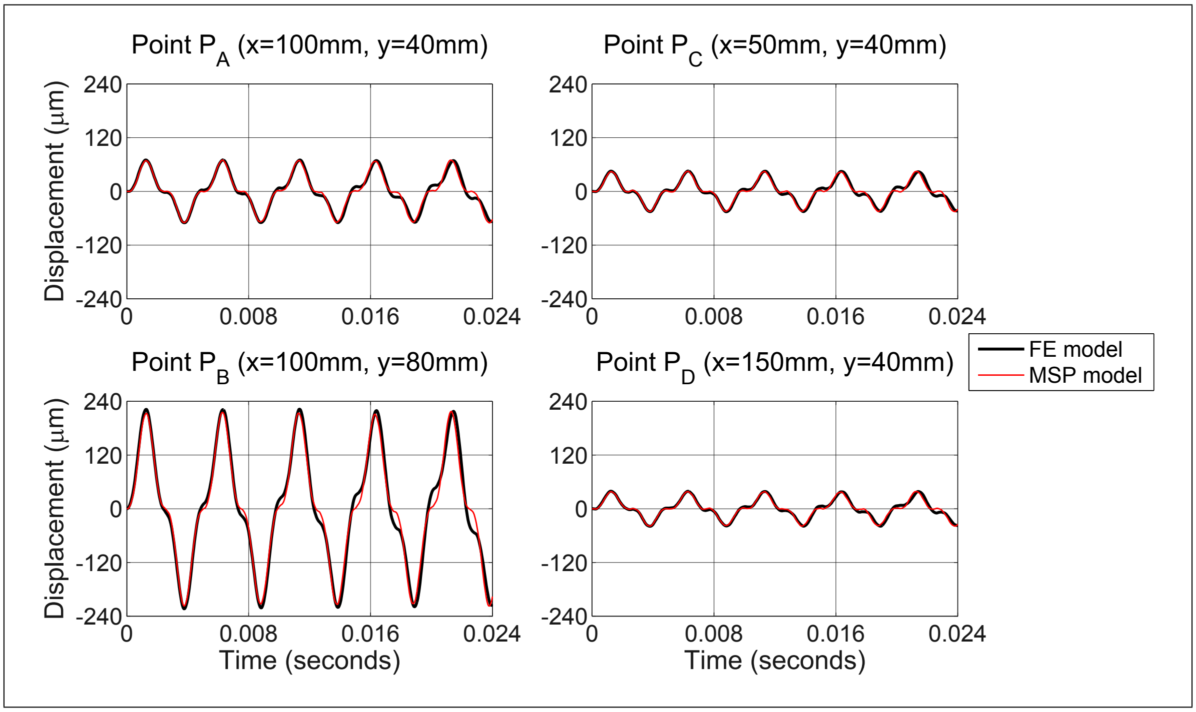

Figure 5.20: Comparison of the responses of pocket 6 predicted by the FE and the MSP models under a sinusoidal load (1256 rad/s)

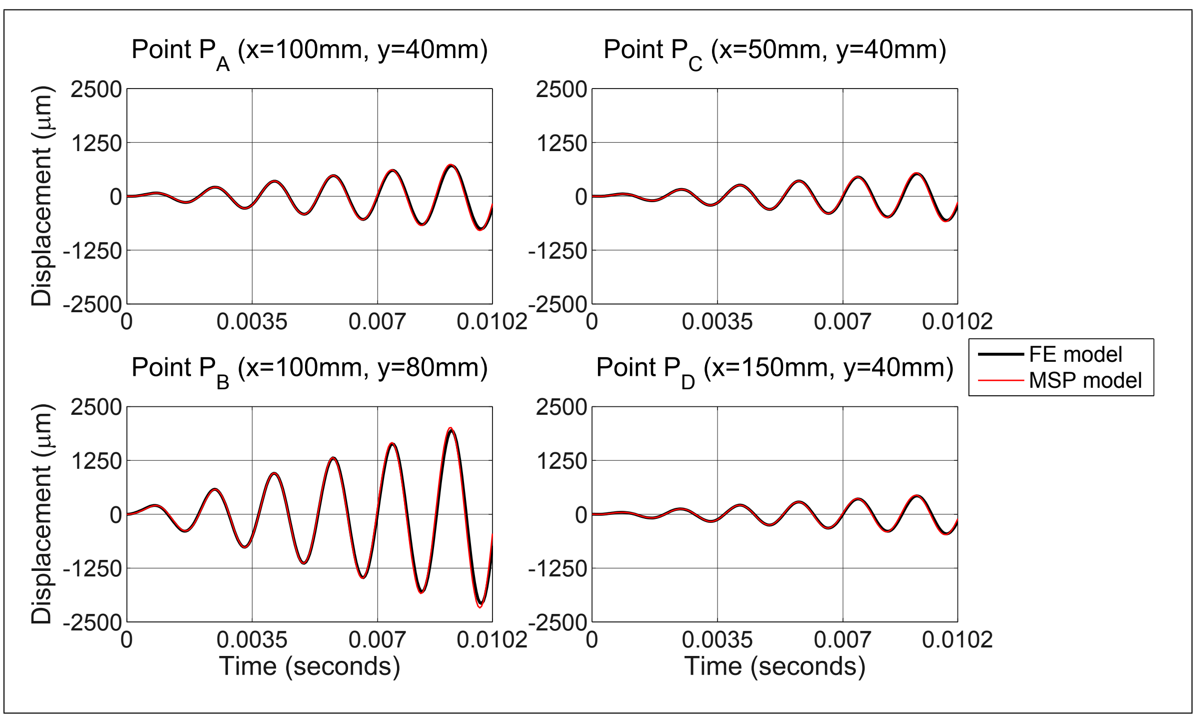

Figure 5.21: Comparison of the responses of pocket 6 predicted by the FE and the MSP models under a sinusoidal load (3896 rad/s)

5.4 Validation of the Change of Thickness (CoT) Formulation

As mentioned in section 4.5 and as shown in Fig. 5.22, there are different cases for the change of thickness which can be represented by a vertical strip (VS) for case A, horizontal strip (HS) for case B, corner strip (CS) for case C and L-shaped strip (LS) for case D. In Fig. 5.22, the original and the new (reduced) thicknesses are referred to as h_o and h_n, respectively. The dimensions of the strips are determined by the x and y coordinates. As mentioned in section 4.5, the MSP model will include five spans in the x-direction and three spans in the y-directions. Spans 1 and 2 in the x-direction represent side 1 of the pocket, and spans 3, 4 and 5 represent sides 2, 3 and 4, respectively.

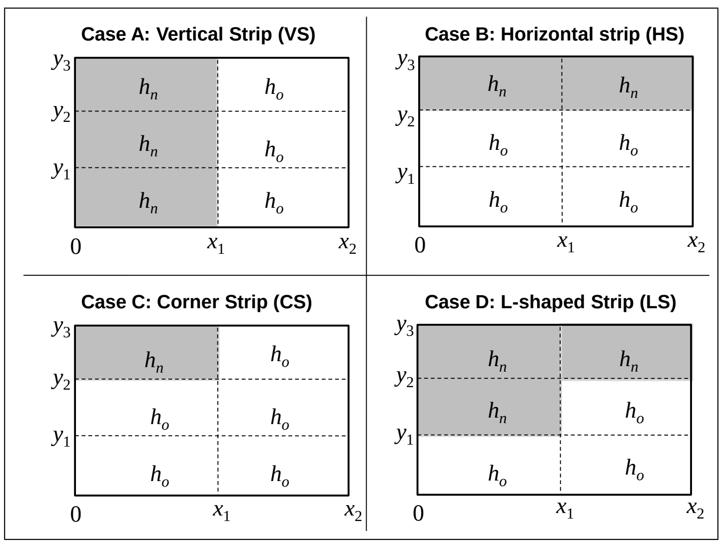

Figure 5.22: Illustration for the cases of the change of thickness used in the validation of the MSP model with the CoT formulation

To validate the MSP model with the CoT formulation, these four cases for the change of thickness were simulated on side 1 of pocket 6 (refer to Table 5.14). According to Fig. 5.22, x_1 and x_2 are equal to 100 mm and 200 mm, respectively, and y_1, y_2 and y_3 are equal to 26.6 mm, 53.3 mm and 80 mm, respectively. The original and the new thicknesses are equal to 3 mm and 2 mm, respectively. For the machining of such thin-walled structures, this is considered as a large change of thickness since it will lead to relatively high cutting forces and thus more vibrations. For the validation of the capability of the proposed model in capturing the effect of the change of thickness, these selected values represent an extreme case. The frequencies of the four cases are listed in Table 5.17. An excellent matching in frequencies is achieved with errors less than 5% for the first 10 frequencies of all the cases. One can note that if the MSP model were used with a uniform thickness for spans 1 and 2, this would have produced very large errors in the predictions of the frequencies.

Table 5.17: Comparison of the mode frequencies of pocket 6 for different configurations for the change of thickness predicted by the FE model and the MSP model with the CoT formulation

Case	Mode	1	2	3	4	5	6	7	8	9	10
Case A	FE (Hz)	515	792	980	1146	1717	2105	2117	2219	2523	2819
(VS)	MSP (Hz)	520	807	1001	1179	1748	2131	2170	2265	2619	2876
	Error %	1.0	2.0	2.1	2.8	1.8	1.2	2.5	2.1	3.8	2.0
Case B	FE (Hz)	611	825	1004	1146	1762	2133	2215	2471	2516	2859
(HS)	MSP (Hz)	612	859	1026	1182	1783	2225	2265	2528	2581	2967
	Error %	0.1	4.0	2.2	3.1	1.2	4.3	2.3	2.3	2.6	3.8
Case C	FE (Hz)	605	825	1030	1209	1854	2167	2217	2558	2634	3104
(CS)	MSP (Hz)	609	852	1058	1243	1892	2239	2268	2669	2716	3244
	Error %	0.6	3.3	2.7	2.8	2.0	3.3	2.3	4.3	3.1	4.5
Case D	FE (Hz)	580	802	979	1107	1669	2089	2194	2320	2443	2746
(LS)	MSP (Hz)	581	839	988	1155	1671	2184	2250	2385	2518	2864
	Error %	0.2	4.6	0.9	4.4	0.1	4.6	2.6	2.8	3.1	4.3

For all the cases, a load was applied at point P_B (x = 100 mm, y = 80 mm) with an amplitude of 30 N and a frequency of 1256 rad/s on side 1. For case A (vertical strip), the responses at the four locations shown in Fig. 5.16 are presented in Fig. 5.23. The errors in the response at point P_B is less than 2.5 % with a maximum amplitude of vibration of 383 μm. The errors for the other points are less than 1.0%. Although the applied force is relatively low (30 N), the amplitude of vibrations is very high. This explains why such a change in thickness is not common in the machining of thin-walled structures since in such case the cutting forces will be even higher than 30 N and may lead to chatter. As discussed in section 4.5, for case A (VS), the close agreement between the MSP and the FE models is expected since the trial functions satisfy all the geometric boundary conditions.

For case B (horizontal strip), the responses are shown in Fig. 5.24. The error in the prediction of the response at point P_B is less than 4.0 % with a maximum amplitude of vibration of 344 μm, while the errors at the other points are less than 1.0%. For this case,

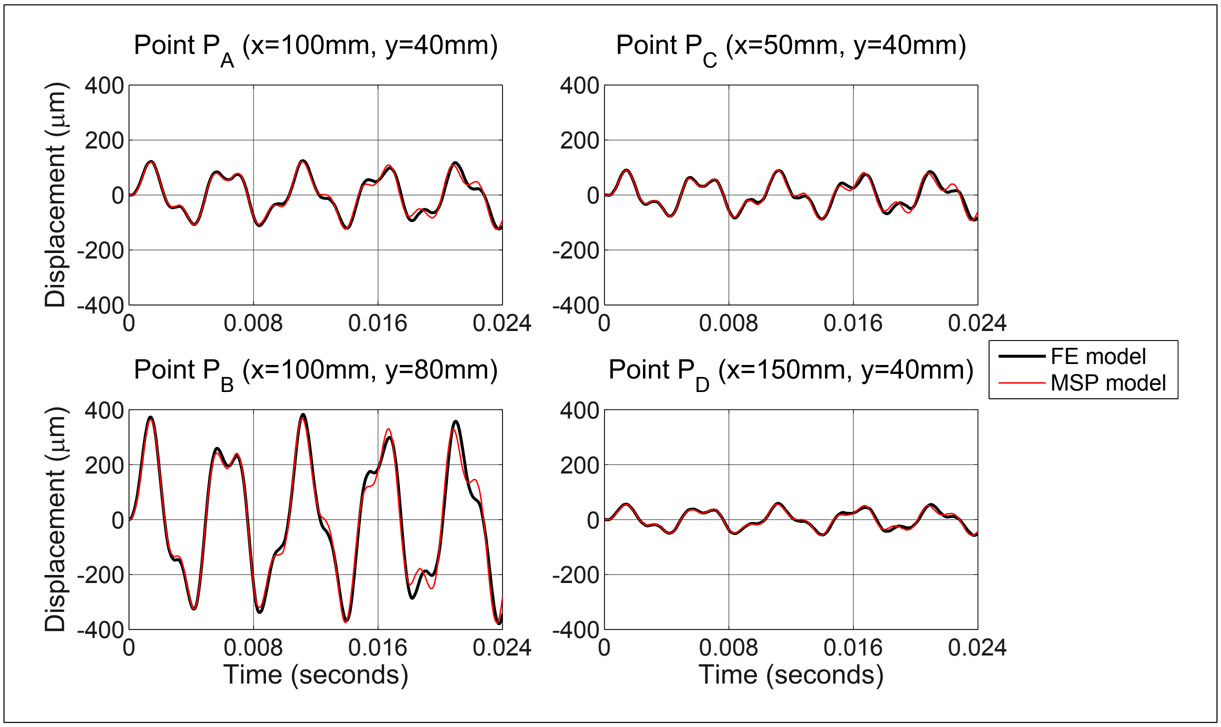

Figure 5.23: Comparison of the responses of pocket 6 predicted by the FE model and the MSP model with the CoT formulation for Case A: Vertical strip

the trial functions satisfy all the geometric boundary conditions expect for the continuity of the rotations about edges $x = x_0$ and $x = x_2$. One can see that a close agreement in the response is still achieved.

The responses for case C (corner strip), and case D (L-shaped strip) are shown in Fig. 5.25 and Fig. 5.26, respectively. The error at point $\mathrm{P_B}$ is less than 6.5% and 3% for cases C and D, respectively. The close agreement in the responses for these two cases shows that the CoT formulation can simulate the continuous change of thickness with relatively high accuracy.

An extensive effort was performed for the validation of the CoT formulation using 162 different FE models. The response of eighteen different rectangular pockets, with nine cases for the change of thickness for each pocket were evaluated. A general 3D sketch of the pocket is shown in Fig. 5.27. All pockets have a width W_d of 100 mm. The eighteen pockets were categorized into three sets (Set E, Set F, Set G) with lengths L of 200 mm, 150 mm, and 100 mm, respectively. The eighteen pockets are generated by varying the height H and the thicknesses of the sides as reported in Table 5.18.

Different scenarios for the change of thickness were implemented based on the four cases

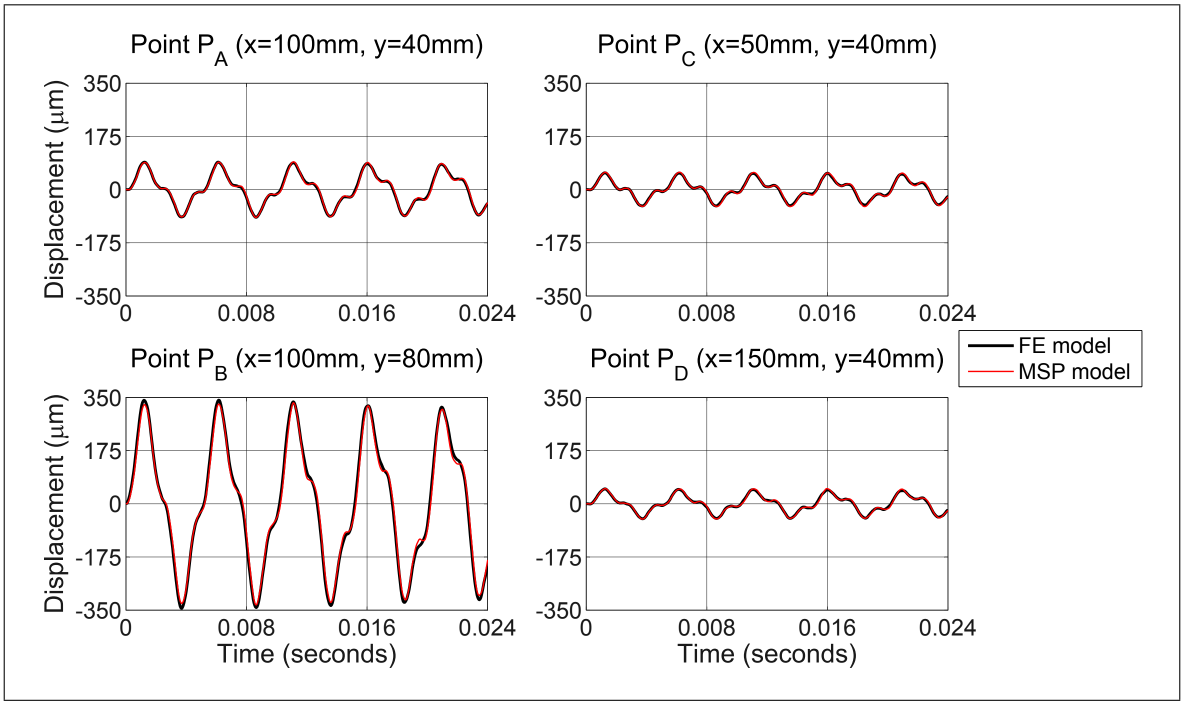

Figure 5.24: Comparison of the responses of pocket 6 predicted by the FE model and the MSP model with the CoT formulation for Case B: Horizontal strip

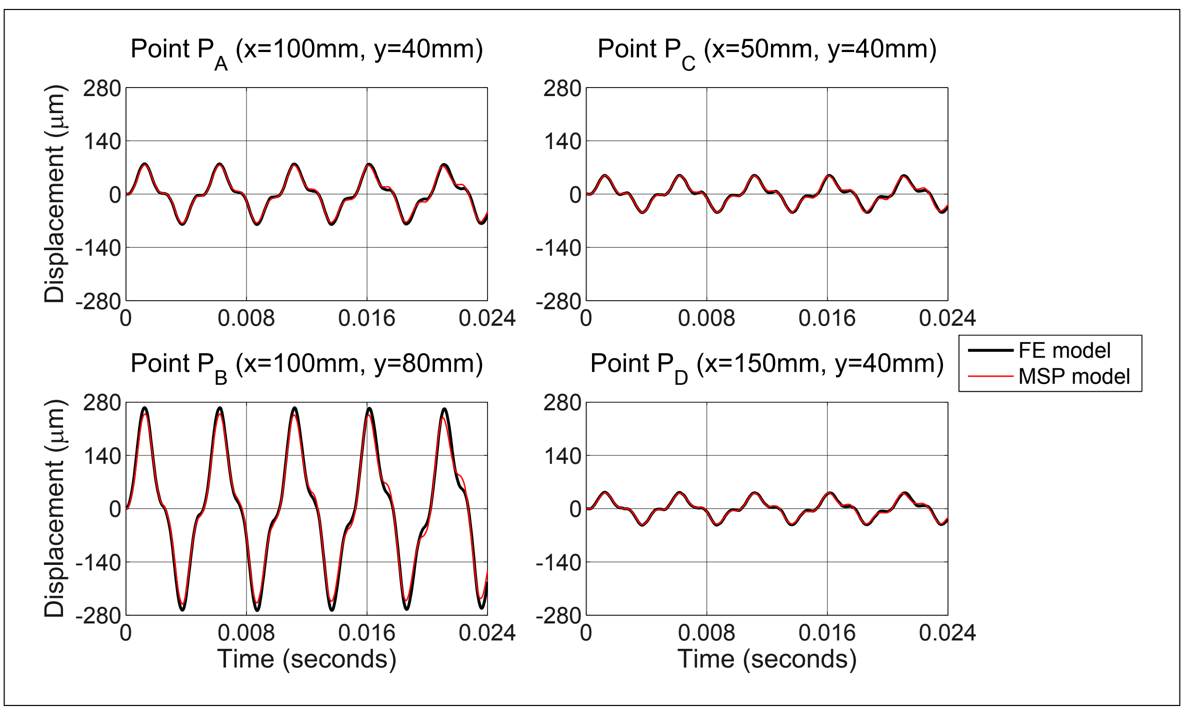

Figure 5.25: Comparison of the responses of pocket 6 predicted by the FE model and the MSP model with the CoT formulation for Case C: Corner strip

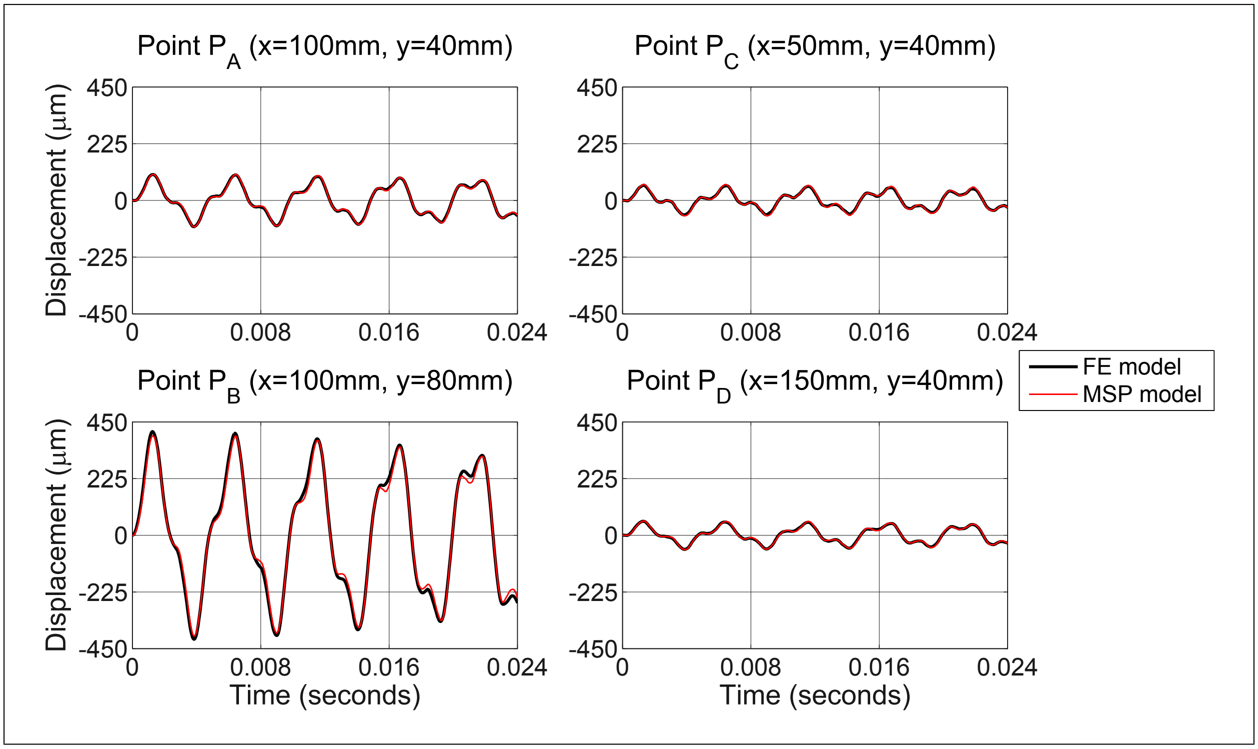

Figure 5.26: Comparison of the responses of pocket 6 predicted by the FE model and the MSP model with the CoT formulation for Case D: L-shaped strip

Table 5.18: Pocket dimensions (in mm) for the validation of the CoT formulation

	Height (H)			Thickness (h)			
No.	Set E (L=200 mm)	Set F (L=150 mm)	Set G (L=100 mm)	Side 1	Side 2	Side 3	Side 4
1	80	60	60	3	3	3	3
2	80	60	60	3	4	2	4
3	80	60	90	4	2	3	2
4	120	90	90	3	3	3	3
5	120	90	90	3	4	2	4
6	120	90	90	4	2	3	2

presented in Fig 5.22. The change of thickness for all cases was applied by selecting a non-uniform strip on side 1 and assigning to it a different thickness. The dimensions of the strip are determined by μ_1 and μ_2, which represent a fraction of the length L and μ_3 and μ_4 which represent a fraction of the height H. To establish the limits of the CoT formulation, the new (reduced) thickness is half the original one. As mentioned previously, such large change of thickness, is not likely to occur in the machining of thin-walled structures since this will lead

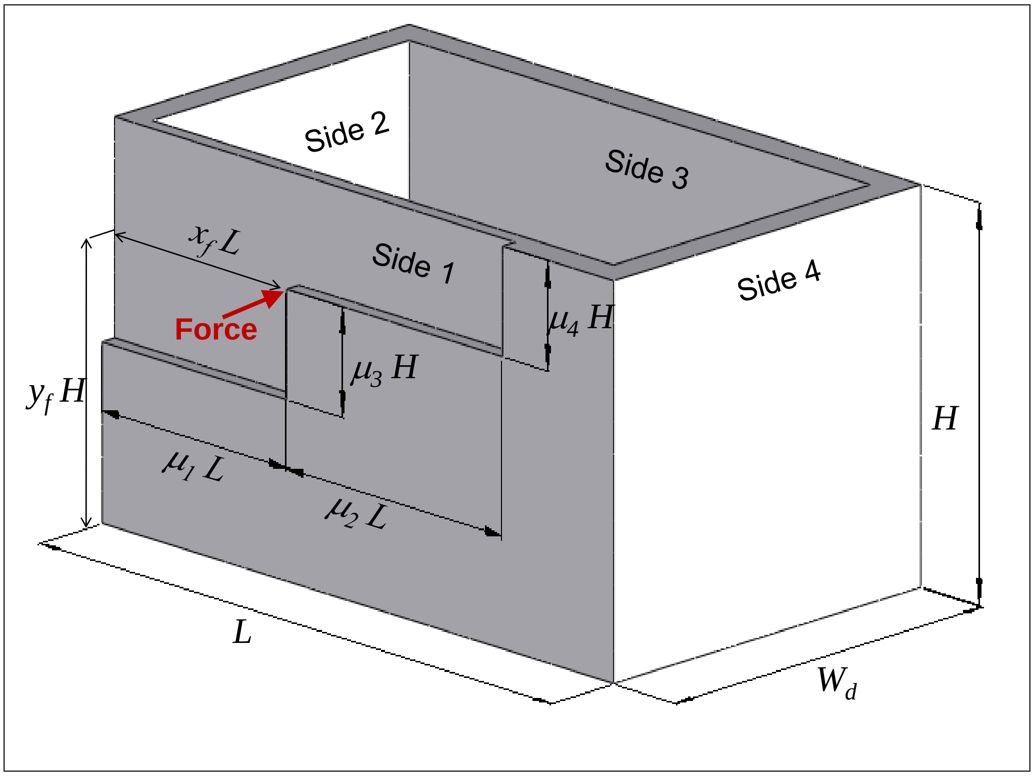

Figure 5.27: 3D sketch for the representation of the different pockets and cases for the change of thickness

to very high forces, chatter and damage of the workpiece or the cutting tool. The lengths and heights of the strips and the location of the applied force are presented in Table 5.19. The coordinates of the point of load application are determined by x_f and y_f. For each case, a force of 10 N amplitude and 1256 rad/s frequency was applied on side 1 at $(x_f L,\ y_f H)$. The pocket response was evaluated at the point of load application using a FE model and the corresponding MSP model.

Table 5.19: Dimensions of the strips for the validation of the CoT formulation

	Case								
Variable	1	2	3	4	5	6	7	8	9
μ_1	0.0	1/4	0.5	3/4	1.0	0.5	1.0	1.0	1.0
μ_2	0.0	0.0	0.0	0.0	0.0	0.5	1/4	0.5	3/4
μ_3	0.0	0.5	0.5	0.5	0.5	0.5	1/3	1/3	1/3
μ_4	0.0	0.0	0.0	0.0	0.0	0.5	1/3	1/3	1/3
x_f	0.5	1/4	0.5	3/4	0.5	0.5	1/4	0.5	3/4
y_f	1.0	1.0	1.0	1.0	1.0	1.0	2/3	2/3	2/3

A summary of the prediction errors in the maximum amplitude of vibration for the 162 cases is shown in Fig. 5.28. The errors are calculated relative to the maximum amplitude of the response of the FE model at the point of load application and not relative to the maximum displacement of the whole side. The figure shows that for all the cases, expect for Pocket G3 (cases 5,9), the errors are less than 10%. The slightly large error for Pocket G3 (case 5) can be attributed to the fact that not all the geometric boundary conditions are satisfied and that the change of thickness is very high. For the other cases, given the large change of thickness, the model provides an accurate calculation of the responses. An example of the obtained responses for pockets E1, E3, G1, and G3 (case 6) are shown in Fig. 5.29. An excellent agreement in the responses is achieved in all the cases.

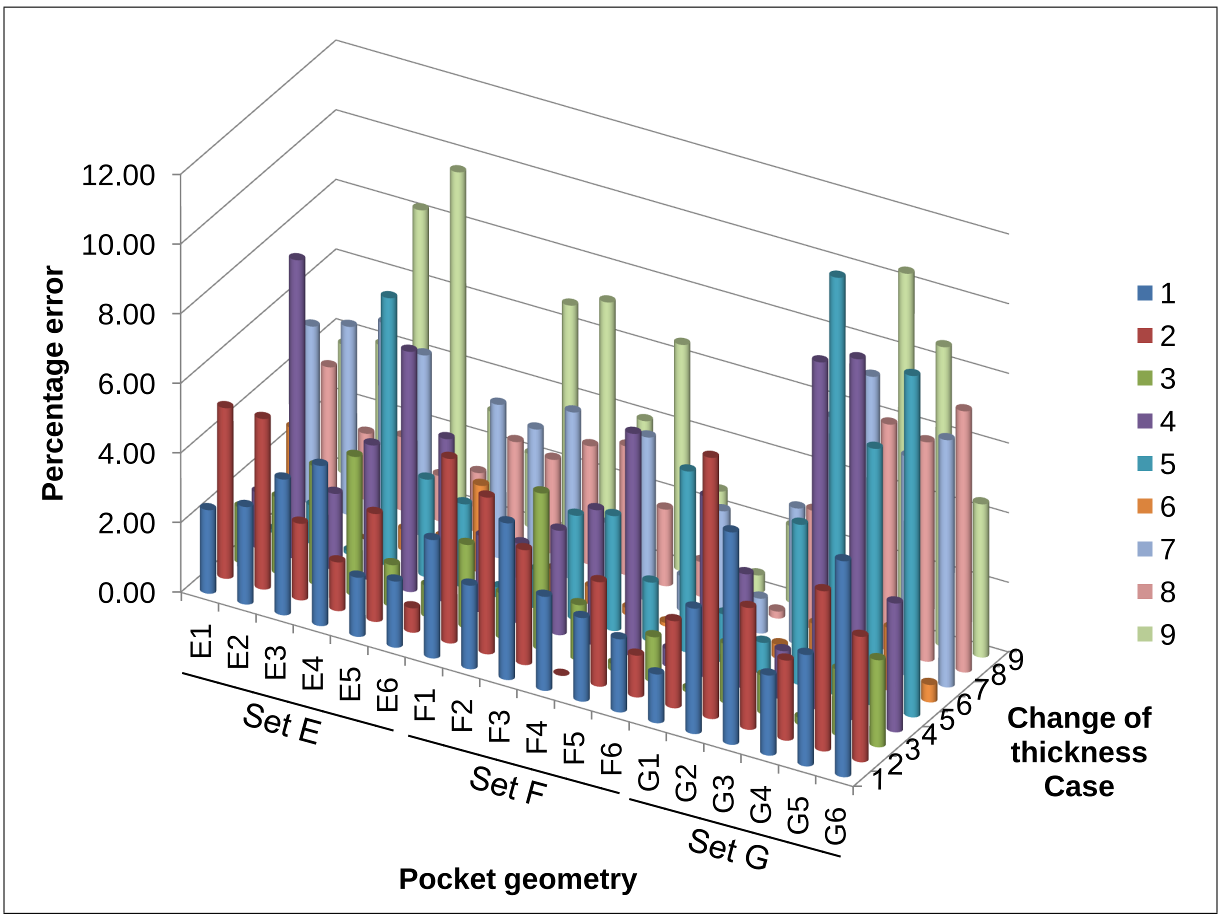

Figure 5.28: Prediction errors of the MSP model with the CoT formulation for different cases

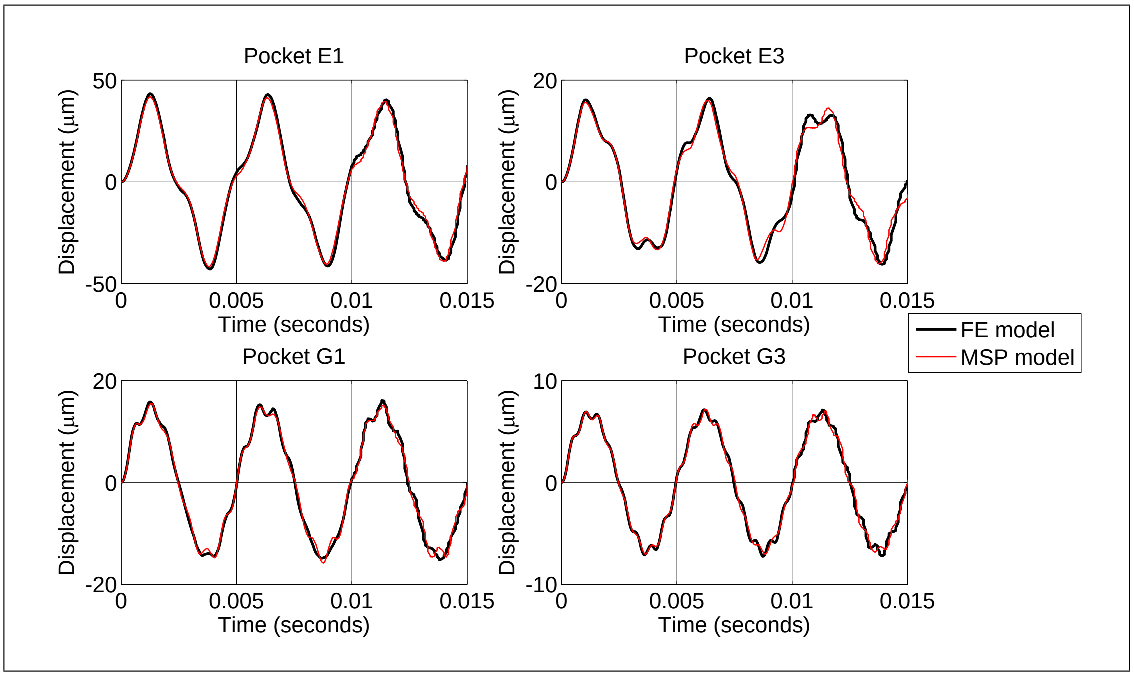

Figure 5.29: The responses of pockets E1, E3, G1 and G3 for case 6 of the change of thickness predicted by the FE model and the MSP model with the CoT formulation

5.5 Validation of the Formulations for the Effect of the Fixture Supports

In section 4.6, two formulations were presented to model perfectly rigid and deformable supports. To validate these formulations, two different fixture layouts, which are illustrated in Fig. 5.30 were applied in the FE model of pocket 6 (refer to Fig. 5.16 and Table 5.14) and compared to the corresponding MSP model with the proposed support formulations.

5.5.1 Validation of the Perfectly Rigid Support (PRS) Formulation

The Perfectly Rigid Support (PRS) formulation, presented in section 4.6.1, is based on representing the support using holonomic constraints. For pocket 6, point P_A (x=100 mm, y=40 mm), which is at the centre of side 1, was rigidly constrained. The comparison of the frequencies of the FE model and the MSP model with the PRS formulation is listed in Table 5.20 with errors in frequencies less than 4.5%. A force of 30 N and 1256 rad/s was

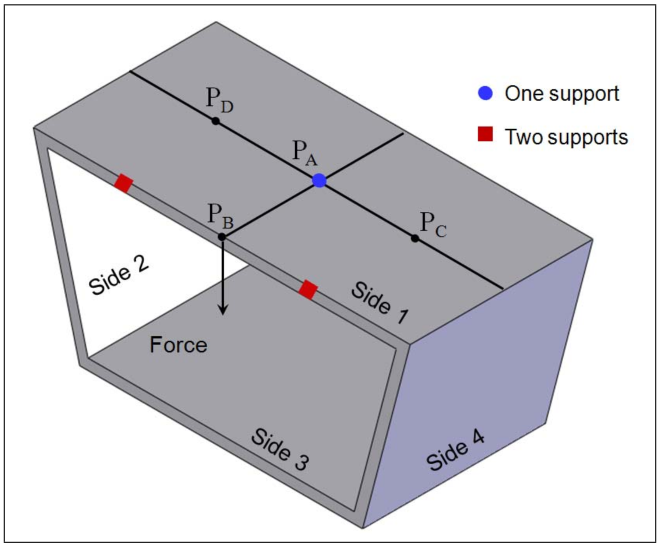

Figure 5.30: Illustration of the support locations on pocket 6

applied on side 1 at point P_B (x=100 mm, y=80 mm). The responses determined using the FE model of the pocket and the MSP model are shown in Fig. 5.31. The error at point P_B is less than 8% with a maximum amplitude of vibration of 82 µm. This corresponds to an absolute error less than 6.5 µm. As seen for the response of point P_A, the constraint is satisfied since the vibrations are zero. The errors at points P_C and P_D are less than 1.5%. As compared to the response of the same pocket without constraints (refer to Fig. 5.20), a reduction in the amplitude of vibration of 140 µm (≈ 65%) was achieved by applying only one constraint on the pocket side and thus the amplitude of vibration falls within the typical tolerance requirements of ± 125 µm.

Table 5.20: Comparison of the mode frequencies of pocket 6 with one support predicted by the FE model and the MSP model with the PRS formulation

Mode	1	2	3	4	5	6	7	8	9	10
FE (Hz)	833	988	1080	1271	2071	2234	2308	2609	3318	3347
MSP (Hz)	850	1031	1113	1301	2116	2248	2384	2704	3386	3482
Error %	2.1	4.4	3.1	2.3	2.2	0.6	3.3	3.7	2.1	4.0

Instead of using one support at the centre of side 1, i.e point P_A, two points (x=50 mm, y=80 mm and x=150 mm, y=80 mm) on the free edge of side 1 were rigidly constrained as illustrated in Fig. 5.30. The frequencies of the FE model and the MSP model are listed

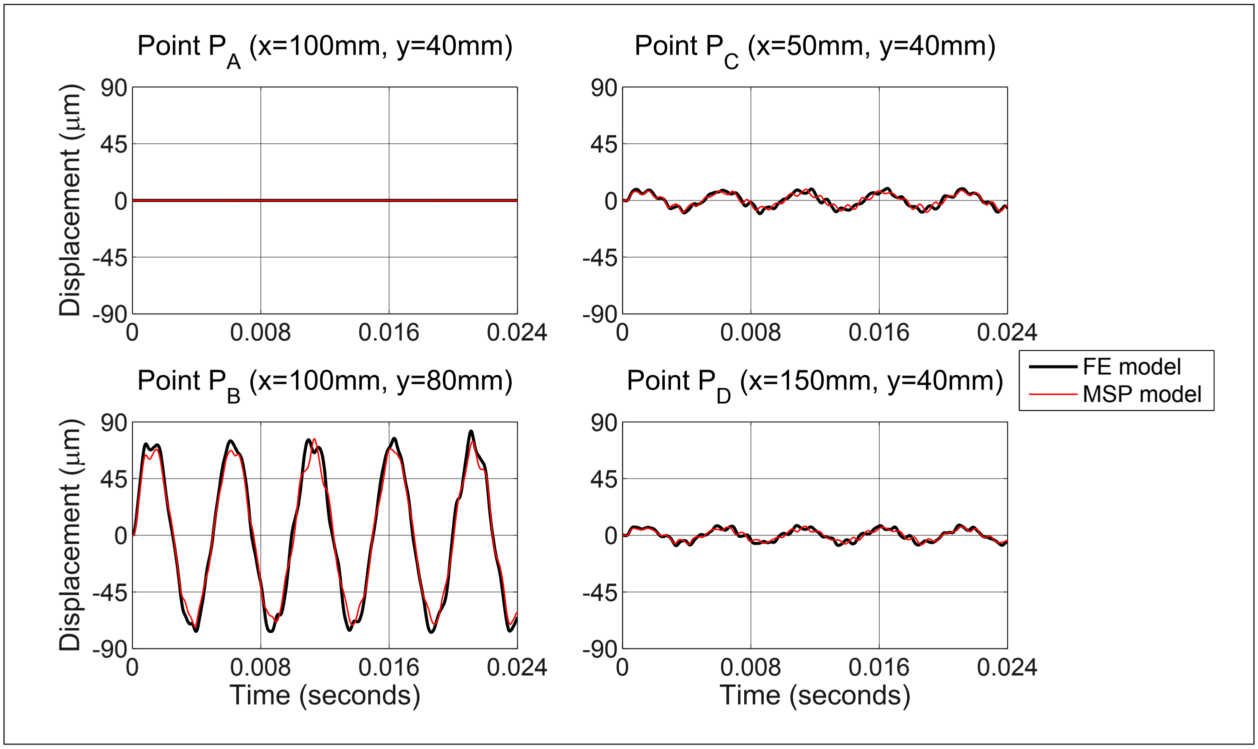

Figure 5.31: Comparison of the responses of pocket 6 with one rigid support predicted by the FE model and the MSP model with the PRS formulation

in Table 5.21. As can be seen the errors are less than 6.0%. The frequency, amplitude and location of the applied force are similar to the previous case (one support). The responses determined using the FE model of the pocket and the MSP model were calculated and are shown in Fig. 5.32. The error in the prediction of the response at point P_B is less than 7% with a maximum amplitude of vibration of 72 μm. This corresponds to an absolute error of less than 5.0 μm. The errors at the other points are less than 3%. As compared to the same pocket with one support, a reduction in the amplitude of vibration of 10 μm only (12%) was achieved by applying two constraints on the pocket side. Thus, for this particular case, a two support fixture layout did not substantially reduce the vibrations when compared to a support applied at a single point. The same pocket and loading were tested when constraints were added at the middle of the free edge of sides 2, 3 and 4. Almost the same response was achieved for the points on side 1 with the same maximum amplitude. This shows that the effect of the supports on adjacent sides (sides 2, 3, 4) on the response of the load application side (side 1) is negligible, as explained in section 3.2.4.

Table 5.21: Comparison of the mode frequencies of pocket 6 with two supports predicted by the FE model and the MSP model with the PRS formulation

Mode	1	2	3	4	5	6	7	8	9	10
FE (Hz)	877	1097	1220	2067	2220	2265	2411	2638	3306	3508
MSP (Hz)	892	1134	1280	2133	2247	2399	2496	2726	3449	3619
Error %	1.8	3.4	4.9	3.2	1.2	5.9	3.5	3.3	4.3	3.2

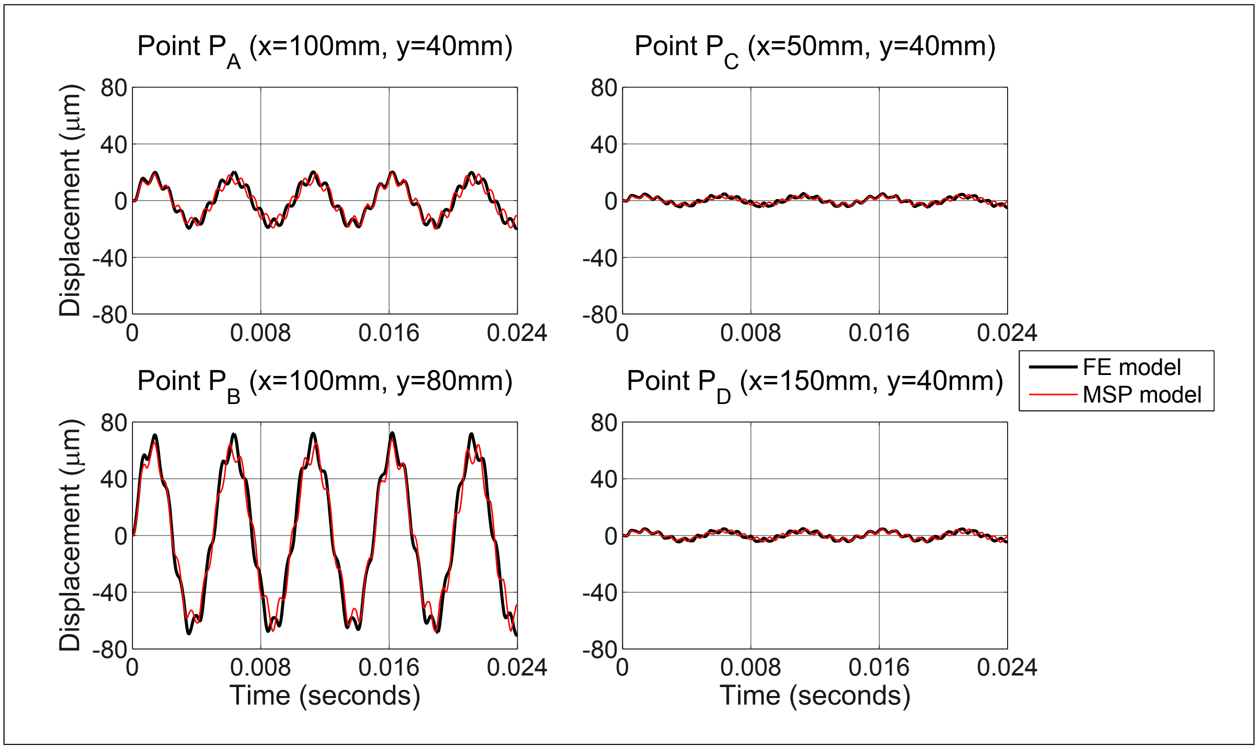

Figure 5.32: Comparison of the responses of pocket 6 with two rigid supports predicted by the FE model and the MSP model with the PRS formulation

5.5.2 Validation of the Finite Stiffness Support (FSS) Formulation

The objective here is to validate the Finite Stiffness Support (FSS) formulation for the effect of the supports presented in section 4.6.2, which is based on springs with a finite stiffness. The same cases presented in section 5.5.1 for one and two supports were repeated with deformable supports having a stiffness 3×10^6 N/m. As will be seen in Chapter 6, section 6.2.3, this stiffness value corresponds to the stiffness of the supports used during the machining experiments. The errors in the prediction of the frequencies for both cases were less than 4.5 %. The same amplitude, frequency and location of the applied load were used for the cases with one or two flexible supports, as the corresponding cases with rigid supports. The responses for the case with one support at point P_A are shown in Fig. 5.33. The error at point P_B is less than 3%, which corresponds to an absolute error of 3.3 μm with a maximum amplitude of vibrations of 115 μm. The error at point P_A (100, 40) relative to the maximum displacement of this point (not the maximum displacement of the whole side), is less than 2.0%. This shows that the formulation of the flexible supports is able to capture accurately the response of the structure even at the location of the support.

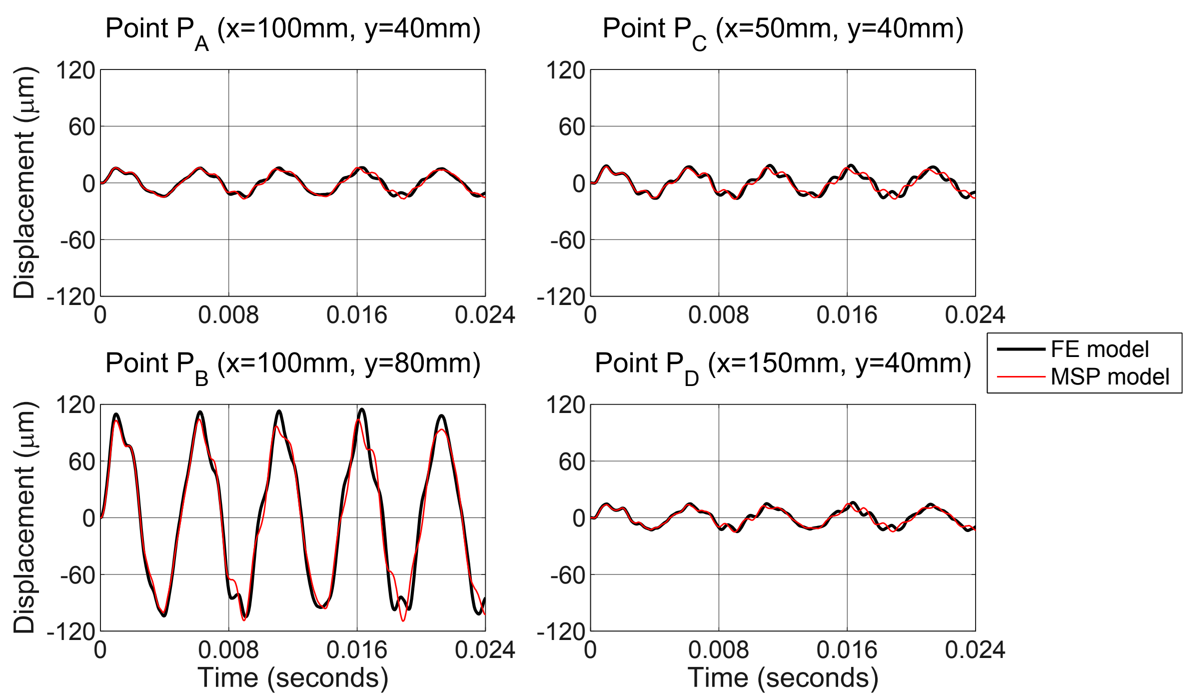

Figure 5.33: Comparison of the responses of pocket 6 with one support predicted by the FE model and the MSP model with the FSS formulation

For the case of two point supports, the response is shown in Fig. 5.34. The error in the response at point P_B (100, 80) is less than 5% and the errors at the other points are less than 2%. The maximum amplitude of vibration is 80 μm. When comparing the flexible supports to the rigid supports, the reduction in the amplitude of vibration is ≈ 63% when using one rigid support and ≈ 50% when using one flexible support, instead of no supports. In both cases, a substantial reduction in the vibration amplitude was achieved. Similarly, using two supports instead of no supports lead to a reduction in amplitude of 67% and 65% for the rigid and flexible supports, respectively. As a conclusion, for the initial design of the fixture layout, the designer could assume the supports to be perfectly rigid in order not to include a large number of variables in the optimization of the fixture layout. However, for the fine tuning of the fixture layout, it might be necessary to include the effect of the flexibility of the supports for accurate predictions of the cutting forces and the surface topography of the machined workpiece.

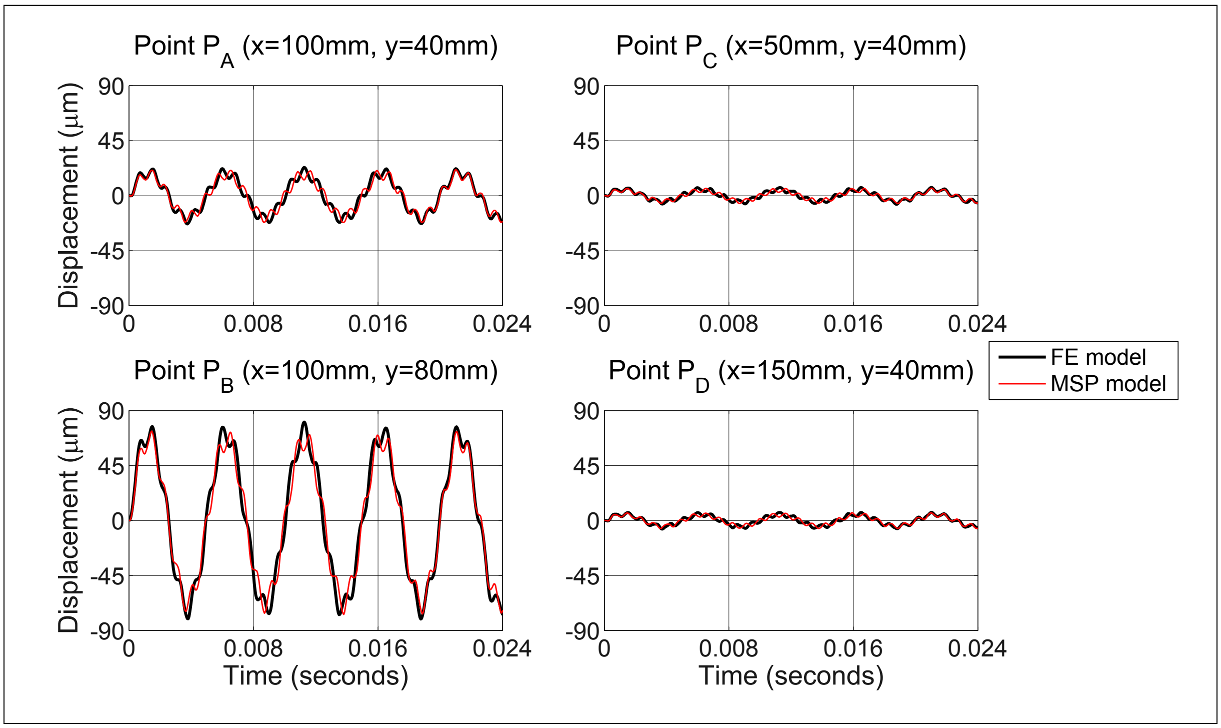

Figure 5.34: Comparison of the responses of pocket 6 with two supports predicted by the FE model and the MSP model with the FSS formulation

5.5.3 Validation of the PRS and the FSS Formulations while Including the CoT Formulation

It is necessary to validate the CoT formulation with the proposed formulations to represent the effect of the fixture supports. Thus, two points at x=50 mm, y=80 mm and x=150 mm, y= 80 mm were rigidly constrained one side 1 of pocket 6. The change of thickness according to case D (L-shaped strip) (refer to Fig. 5.22) was also applied on side 1 as illustrated in

Fig. 5.35. Both the PRS and FSS formulations were implemented. For the FSS formulation, a spring stiffness of 10^8 N/m was used to simulate a perfectly rigid support. The errors in frequencies for both cases were less than 6% when compared to the FE model. The responses are shown in Fig. 5.36, with a maximum error in the prediction of the responses of less than 8.0% for both formulations. As can be seen, the FSS can be used to represent both deformable and perfectly rigid supports.

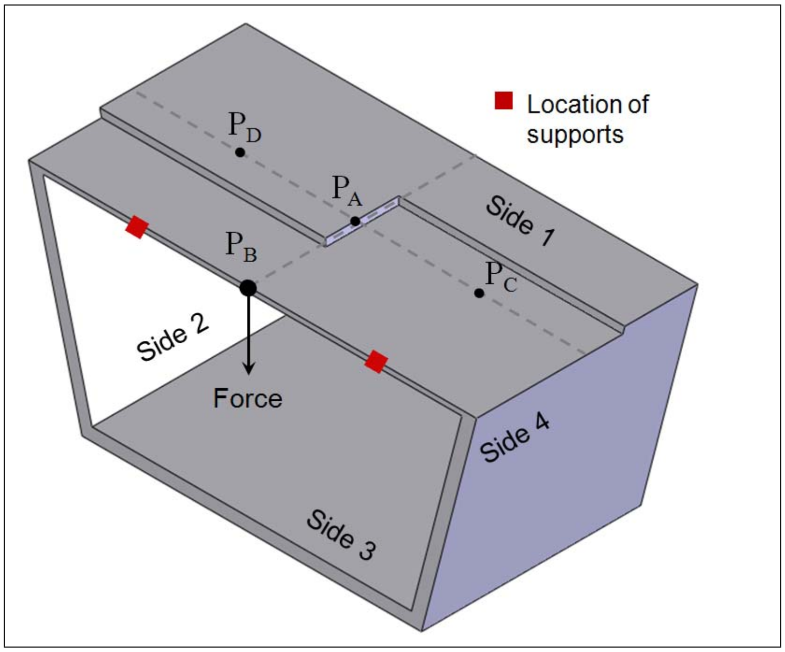

Figure 5.35: Illustration of the support locations and the change of thickness with an L-shaped strip on side 1 of pocket 6

It is noteworthy that simulating the dynamic response of the pocket shown in Fig. 5.35, while considering the continuous change of thickness for all the sides and five different fixture layouts, would require approximately 90 to 100 hours computation time using a FE model. Consequently, the FE models are not adopted for fixture design in the aerospace industry due to their extensive computational requirements. Compared to this, the computation time for the above-mentioned cases is reduced to less than one hour using the models and formulations presented in this thesis. This significant reduction of computation time (one to two orders of magnitude) will allow the use of these newly developed models and formulations for interactive fixture design.

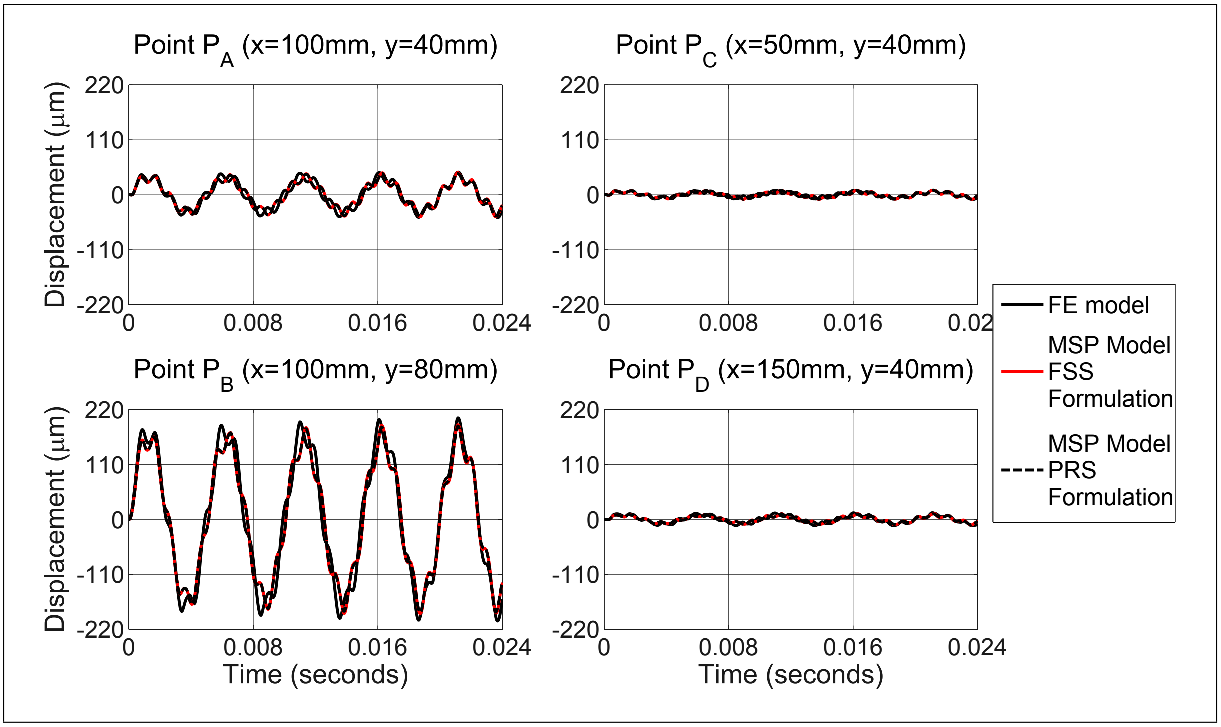

Figure 5.36: Comparison of the responses of pocket 6 predicted by the FE model and the MSP model with the PRS and the FSS formulations while including the CoT formulation

5.5.4 Use of the FSS Formulation with the MSP Model to Predict the Response of a Pocket with Internal Rib-Walls

As mentioned in Chapter 3, section 3.2, one of the types of thin-walled aerospace structures that need to be represented is a pocket with internal rib-walls. In Fig. 5.37, a rectangular pocket with rib-walls across its length and width is illustrated. In the FE model, the base of the pocket was clamped and a total of 1500 of elements was used. A force of 30 N amplitude and 1256 rad/s was applied at point P_B (100, 80) on side 1 and the response was calculated at four output points as shown in Fig. 5.37. To represent the effect of the internal rib-walls, the FSS formulation was implemented in the MSP model by adding two springs on each side at the positions corresponding to the top and the middle of the rib-wall as illustrated by the squares in Fig. 5.37. To simulate the high axial rigidity of the rib-walls, a stiffness of 10^7 N/m was used for all the springs.

The comparison of the frequencies determined using the MSP model and the frequencies of the corresponding modes in the FE model are reported in Table 5.22 with errors less than

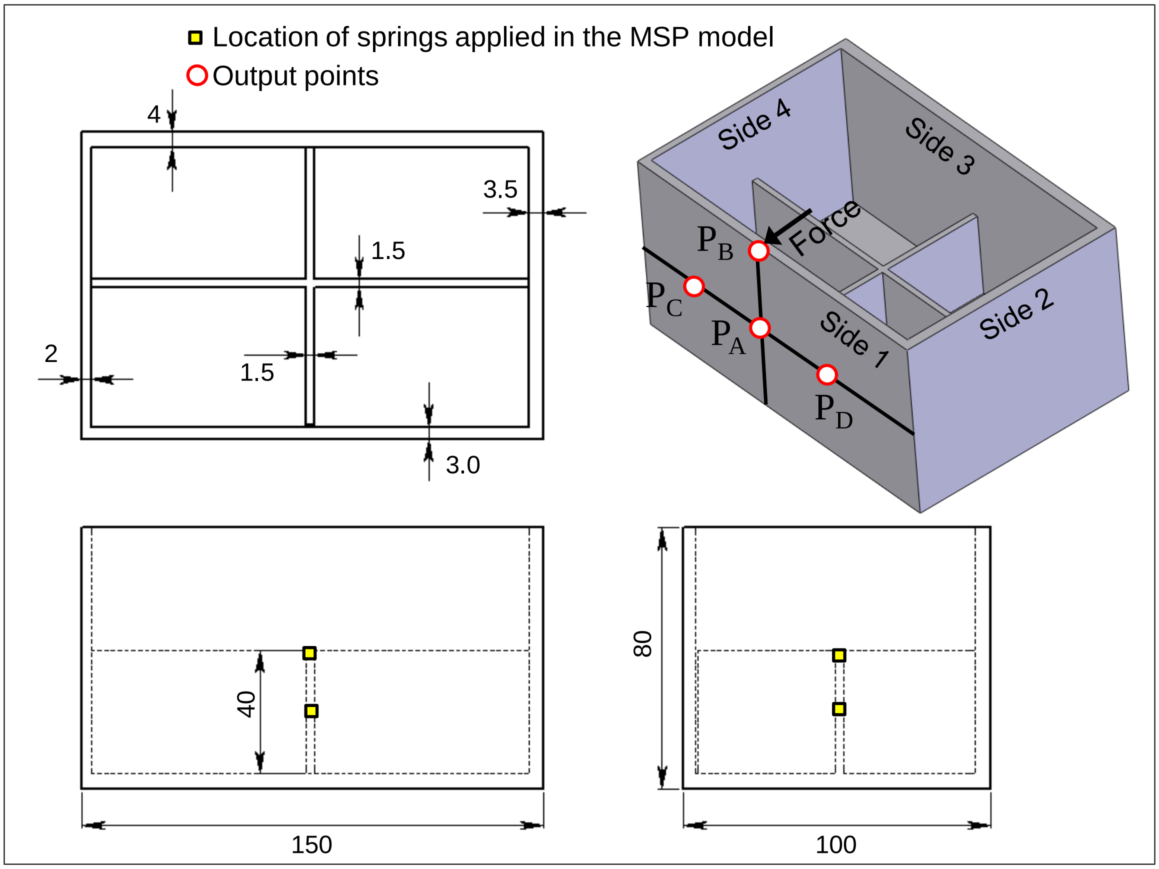

Figure 5.37: Dimensions (in mm) of the pocket with internal rib-walls

3.5%. The responses predicted using the MSP and the FE model are shown in Fig. 5.38. The error at points P_B, where the load is applied, is less than 1.0% with a maximum amplitude of vibration of 80 µm. The error at point P_A is less than 3%. These results show that the MSP model can accurately predict the response of the pocket even at the position of the rib-wall.

Table 5.22: Comparison of the mode frequencies of the pocket with internal rib-wall predicted by the FE model and the MSP model with the FSS formulation

Mode	1	2	3	4	5	6	7	8	9	10
FE (Hz)	1207	1418	1524	1797	2060	2423	2875	3382	3891	4004
MSP (Hz)	1234	1434	1553	1822	2111	2479	2924	3463	4015	4134
Error %	2.2	1.1	1.9	1.4	2.5	2.3	1.7	2.4	3.2	3.2

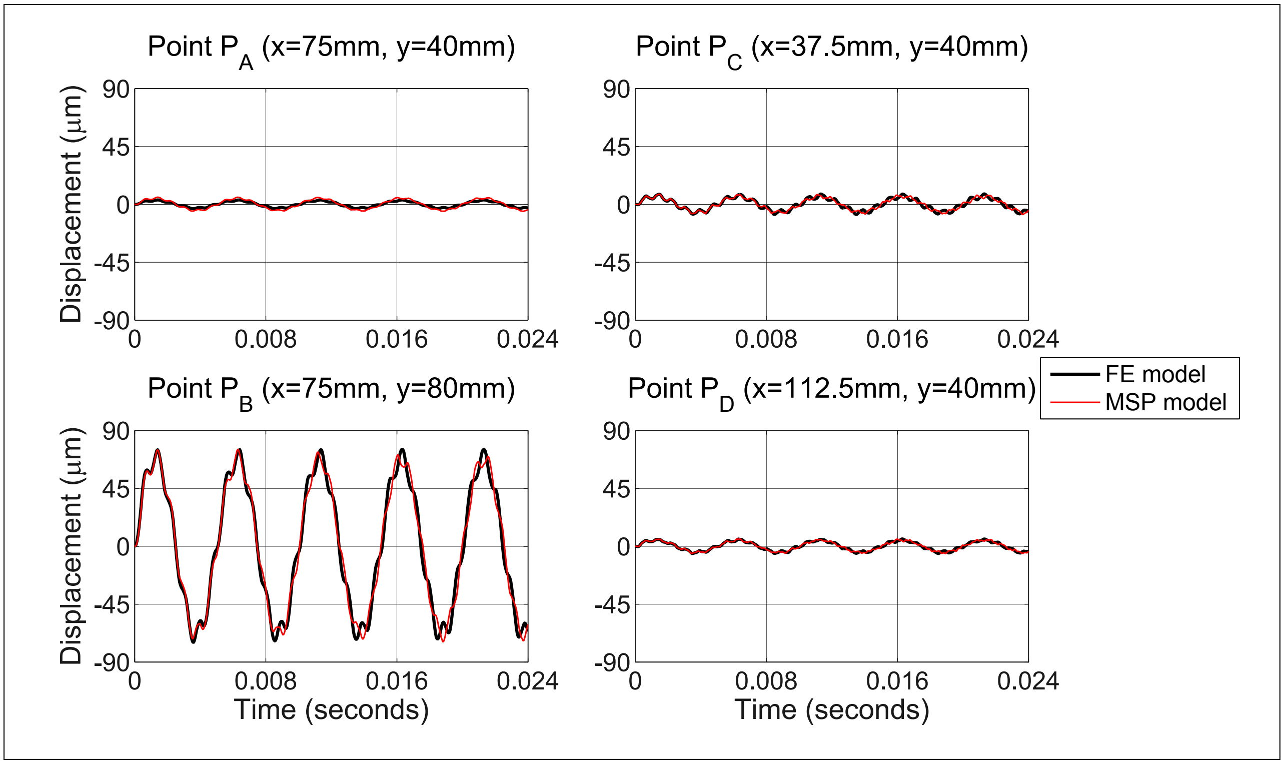

Figure 5.38: Comparison of the response of the pocket with internal rib-wall predicted by the FE model and the MSP model with the FSS formulation

5.6 Summary of the Results

In this chapter, extensive validations of the mathematical models with respect to FE models was presented. The validation cases were chosen so that they represent typical pockets encountered in thin-walled aerospace structures in terms of the shape, dimensions, features and types of loading during machining. The GSSP model was validated for different thin-walled structures and different types of loadings (sinusoidal, impact and real machining forces). Experimental impact tests were performed for the validation of the model as well as for the verification of the FE model. In all cases, an excellent agreement in response was found with errors less than 5 % when comparing the GSSP model with the FE model. The proposed model offered at least one order of magnitude reduction in the computation time. Similarly, the MSP model was validated for different pocket shapes and different loads. The comparison of Rayleigh's energy method and the Rayleigh-Ritz method was performed and it was shown that for pockets with non-uniform thicknesses, the Rayleigh-Ritz method offers better accuracy in terms of the predictions of the frequencies and the responses with errors less than 6%. The CoT formulation was validated using different pocket shapes and change of thickness scenarios. An extensive analysis for 162 cases for the change of thickness was performed and it was shown that the proposed formulation can accurately represent the varying dynamics of the structures. The PRS and FSS formulations for rigid and flexible supports were validated using different fixture layouts applied on a pocket. Using these different validations cases, it was shown that the proposed models can accurately represent the effect of the fixture layout on the dynamics of thin-walled structures during milling. An excellent agreement in the prediction of the frequencies and the responses have been found with errors less than 10 % and at least one order of magnitude reduction in computation time when compared to FEM, thus satisfying the objectives set for this research program.

Chapter 6

Experimental Validation of the Dynamic Models Through the Machining of Thin-Walled Pockets

6.1 Introduction

In the previous chapter, the developed dynamic models were validated against FE models and experimental impact tests. This chapter will detail the experimental validation of the MSP model, the CoT formulation, and the FSS formulation, through the machining of thin-walled workpieces. The chapter will include the description of the experimental setup, the different model parameters, the procedure to prepare and conduct the experiment, error analysis and the comparison of the results for the machining of a rectangular pocket, with and without supports. The effect of the dynamics of the measurement systems on the output signals will also be discussed. This will include, a brief review of the literature, the analysis of the problem by the mean of a two-degree of freedom model and the development and the validation of a new methodology for the compensation of the dynamics of the measurement system in the measured force signal.

6.2 Description of the Experiment

The setup in the experiments was comprised of a machining centre, force and displacement measurement systems, a fixture for locating and clamping the workpiece, and the cutting tools. The setup, the test procedures and the calibration of different measurement systems are discussed in the coming subsections.

6.2.1 Experimental Setup

All tests were carried out on a 5-axis high-speed, high-power horizontal machining centre Makino A88ϵ, with the following characteristics: 50 kW spindle, a maximum spindle speed of 18,000 rpm, a maximum feed rate of 50 m/min, a tool clamping force of 19.6 kN and an HSK 100A spindle adapter. The large machining envelope (900 $\times$ 800 $\times$ 970 mm) has the capability to machine medium size components used in the aerospace industry. The machine has a high thermal stability and rigidity; these characteristics reduce the thermal and the machine vibration errors.

The acquisition of the data was performed using an 8 channel data acquisition card (National Instruments, model NI PCI-4472) and a software application developed in LabView (version 8.0). All signals were recorded with a high sampling frequency of 12,000 Hz to capture the characteristics of the dynamics of the measurement system.

The setup consisting of the workpiece, the workpiece fixture, and the dynamometer is shown in Fig. 6.1. A 3-component force measurement dynamometer (Kistler 9255B) was fixed to the moving table of the machining centre. The dynamometer coordinate system, referred to as DCS, is also shown in the figure. In the z-direction, the dynamometer has a rigidity of 3 kN/µm and a natural frequency of 2.0 kHz, when mounted on a flange. In the x- and y-directions, the dynamometer has a rigidity and a natural frequency of 2 kN/µm and 1.7 kHz, respectively. The calibrated measurement range is 0 to 4 kN in the z-direction and 0 to 2 kN in the x- and y-directions. The dynamometer has a linearity of $\pm$ 1%. In these experiments, the cutting forces in the z-direction were the input to the model.

A rectangular pocket was machined from Aluminum 6060 with the dimensions shown in Fig. 6.2. The bottom thick base of the workpiece was necessary to simulate clamped boundary conditions at the bottom of the pocket. The grooves at the base of the workpiece were used to fix the probe and support holders inside the pocket, since all the machining was performed from outside. The 1/4" threaded holes were used to fix the supports to the

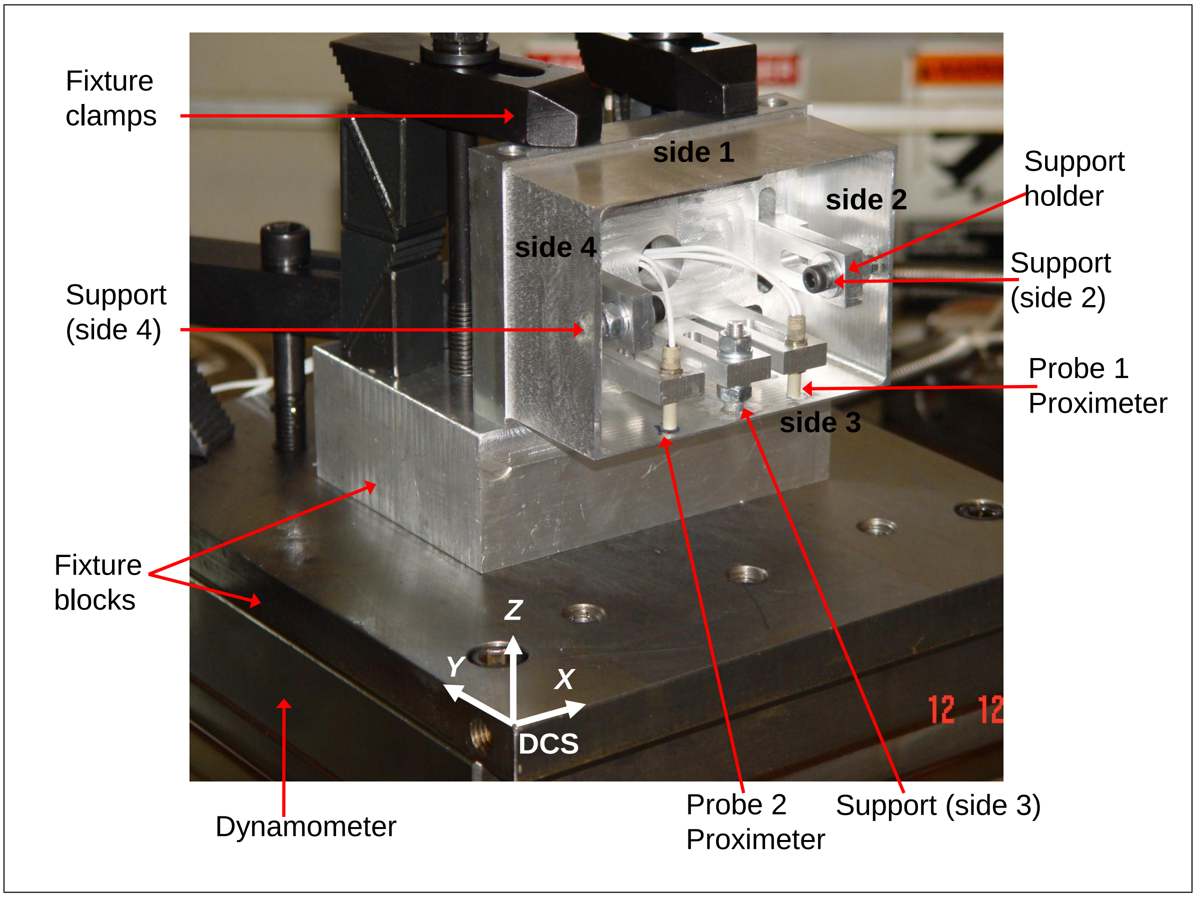

Figure 6.1: Picture of the setup including the workpiece, the fixture, the probes and the dynamometer

sides of the pocket as illustrated in Fig. 6.1.

The vibrations of the thin-walled pockets were measured by three contactless position sensors (probes 1 and 2: KAMAN, model 1UEP and probe 3: BENTLY model 3300 REBAM). The diameters and the lengths of probes 1 and 2 are 6.35 mm and 30 mm, respectively, while those of probe 3 are 10 mm and 50 mm, respectively. Cubic regression functions were used for the calibration of probes 1 and 2 (KAMAN) and a linear function was used for probe 3 (Bently), as shown in Fig. 6.3. The coefficients of determination R^2 for the calibration functions of probes 1, 2 and 3 are 0.9998, 0.9997 and 0.9996, respectively. The errors due to calibration will be discussed in section 6.4.

To take into account the magnetic effect of the fixture on the probe measurements, the probes were calibrated while mounted on the probe holder. The probe holder was designed in a way to have relatively high rigidity, and to maintain a minimum distance from the

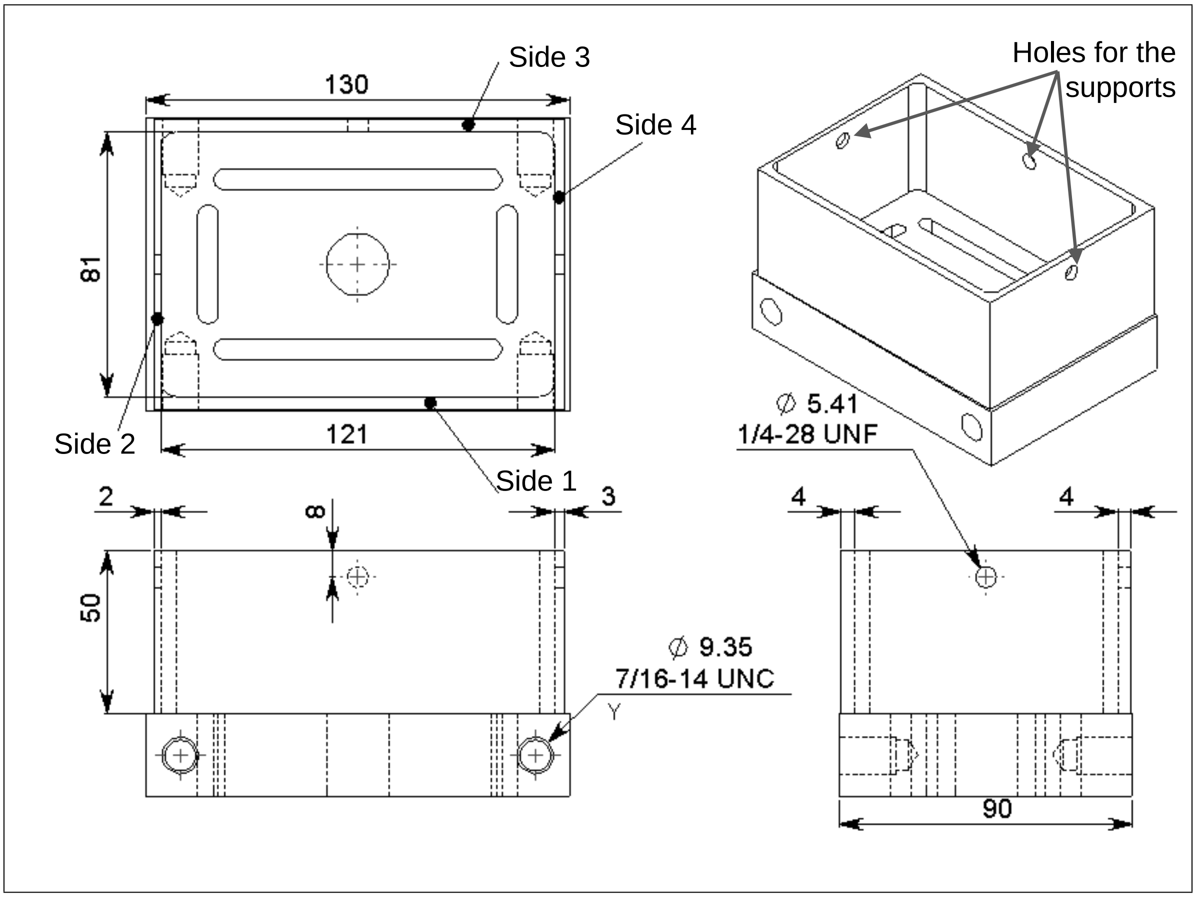

Figure 6.2: Dimensions of the rectangular pocket in mm

support to the face of the probe, as recommended by the manufacturer. The dimensions of the probe holder used in this experiment are shown in Fig. 6.4. The same design of the probe holders was used to hold the fixture supports (locators). The supports were threaded aluminum pins with a diameter of 6.35 mm. As shown in Fig. 6.1, the supports (pins) fit inside the threaded holes on the pocket sides. Epoxy adhesive was added to eliminate any relative motion between the pin and the workpiece.

A two-flute Cobalt M42 end-mill with a 15.875 mm diameter and a 30° helix angle was used for the machining of the pocket from outside. The tool was mounted on a balanceable HSK 100A tool holder, as shown in Fig. 6.5. The whole assembly was balanced up to 20,000 rpm with a permissible unbalance of 9.22 g (balancing grade: G2.5).

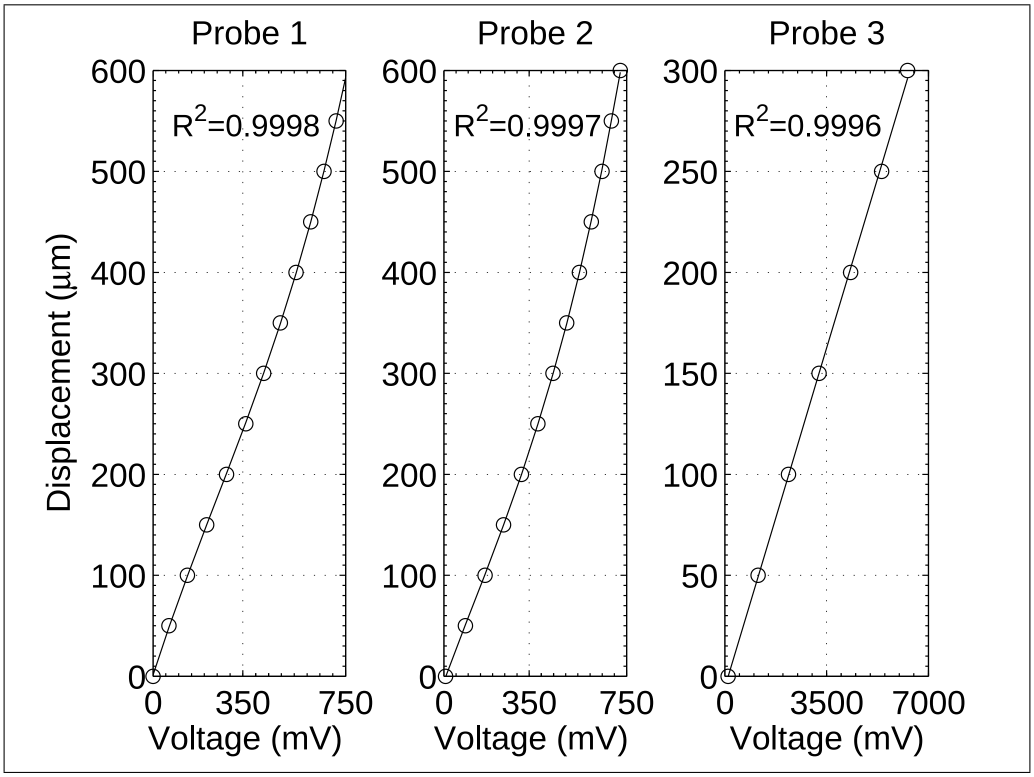

Figure 6.3: Calibration curves for probes 1, 2 and 3

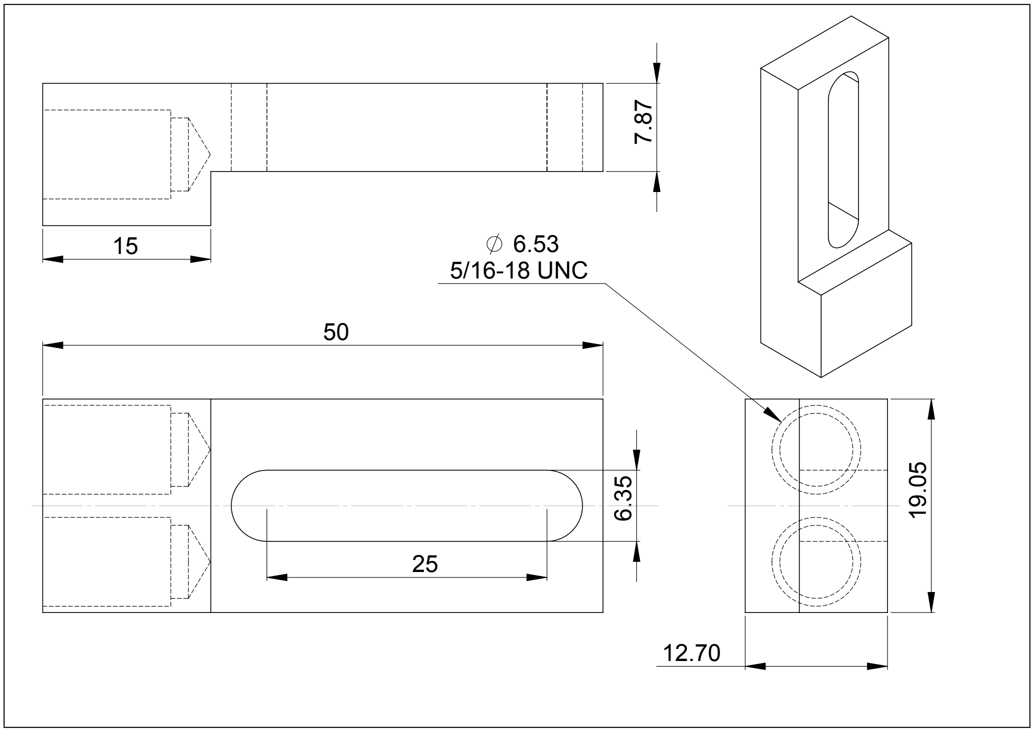

Figure 6.4: Probe holder dimensions in mm

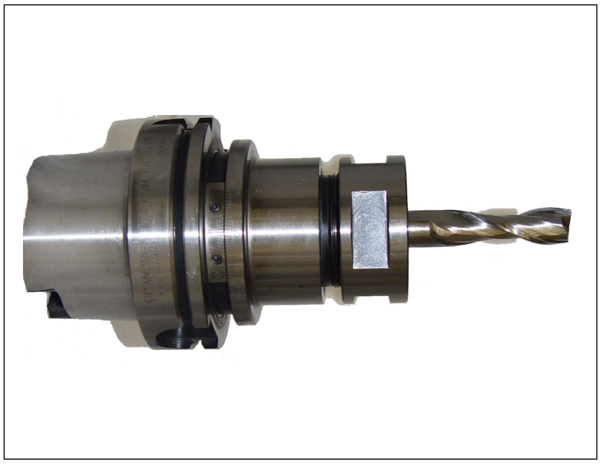

Figure 6.5: Picture of the end-mill mounted on the tool holder

6.2.2 Experimental Procedures

A solid block was opened using a two-flute end mill with a diameter of 3/4 inch (19.05 mm). A 1.0 mm machining allowance was left on each wall from inside. A semi-finishing machining path with a radial depth of cut of 0.5 mm was performed on the inside walls of the pocket using a four-flute end mill with a diameter of 7/16 inch (11.11 mm). Finally, the walls were finished using a four-flute end mill with a diameter of 1/4 inch (6.35 mm) to produce the desired corner fillets. A 0.5 mm thickness is machined from the outside of the walls of the pocket. After these machining processes, the block had the dimensions shown in Fig. 6.2.

After opening the pocket, the workpiece was removed and the tool and the holder in Fig. 6.5 were mounted on the spindle. The forces were measured while cutting in air to determine the effect of any tool/spindle unbalance on the forces. The stability lobes were determined for the tool-workpiece material combination to properly select the cutting parameters. The probes and the holders were then installed inside the pocket, which was mounted on the dynamometer as shown in Fig. 6.1.

The machining started on the outside of side 1 without any fixture supports for the walls of the pocket. The measurement of the displacement of side 1 was performed using the three contactless probes shown in Fig. 6.6a. After finishing the machining of side 1, three supports were installed on sides 2, 3, and 4 and two probes were placed facing side 3 as illustrated in Fig. 6.6b. The block was flipped such that side 3 is at the bottom. The workpiece coordinate system (WCS) is always located at the lower right corner of the machined side of the pocket. To ensure the accuracy of the force measurements, the distance in the z-direction (with respect to DCS) between the force application point (cutting tool) and the face of the dynamometer was maintained less than 100 mm, as recommended by the dynamometer supplier. Thus, during the machining of sides 1 and 3, the pocket was placed such that the side which is machined is closer to the dynamometer top face as shown in Fig. 6.6. Moreover, the workpiece was always positioned near the centre of the dynamometer. During the machining of one side, the thicknesses of the other sides remained unchanged.

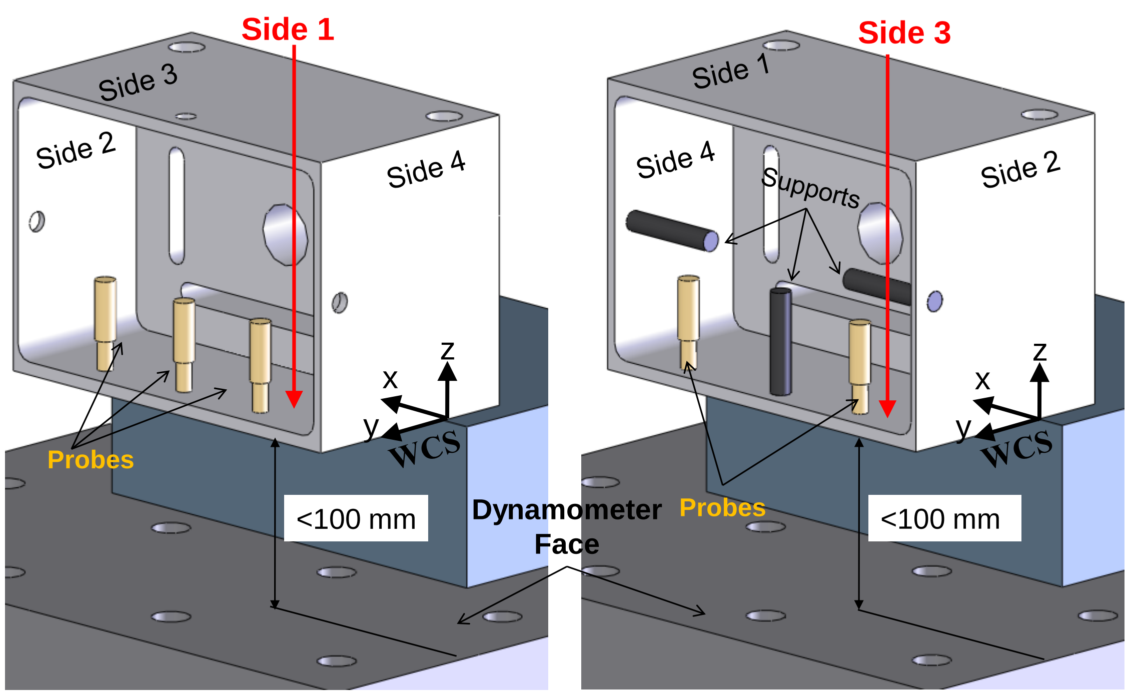

(a) 3D Illustration of the set up during the machining of side 1

(b) 3D Illustration of the set up during the machining of side 3

Figure 6.6: Illustration of the setup during the machining of sides 1 and 3

For each of sides 1 and 3, the machining started at the top free edge of the side until reaching the bottom (fixed end). An illustration of the machining paths is shown in Fig. 6.7. The position of the tool relative to the top edge of the side will be referred to as the tool-path depth (d_p). Thus, the axial depth of cut (d_y) is the distance between a given tool-path depth and the previous one. For each tool-path depth, two machining paths were performed. All the measurement are done during the first path. The radial depth of cut of the first path is designated as d_z. Thus, during this path, the thickness is reduced by an amount d_z as shown in Fig. 6.7a. Then during the second path, the tool moves by 0.2 mm in the z-direction (with respect to WCS) as presented in Fig. 6.7b. The role of this path is to clean any under- or over- cut from the first path. In addition, it ensures that at a given tool-path depth, the tool does not touch the workpiece at the previous tool-path depths. This is illustrated in Fig. 6.7c. In this way, the force location can be determined accurately. At the end of each case, after reaching the bottom of the side, the stability lobes of the side were determined at the expected most flexible point. From the stability lobes of the workpiece and the tool, the cutting parameters for the next thickness were chosen. At some instances, the selected cutting parameters still resulted in chatter, especially at the initial tool-path depths. As a consequence, the cutting parameters were modified until chatter was eliminated or reduced to an acceptable level.

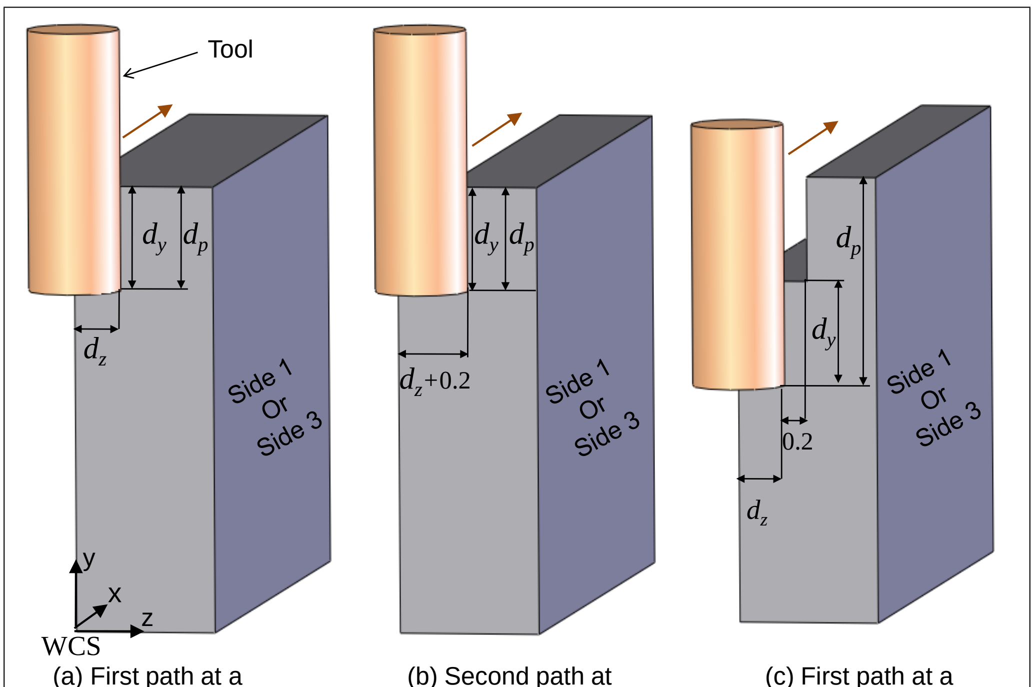

Figure 6.7: Description of the tool path used for machining the side of the pocket

Table 6.1 shows the sequence for the reduction of the thickness of sides 1 and 3. There are two sets of results, one for the pocket without supports (machining side 1) and the second for the pocket with supports (machining side 3). There are four cases in each set of results. At a given tool-path depth d_p, the intermediate thickness designate the thickness of the wall after the first machining tool path. The final thickness is the thickness of the wall after the second tool path. The name for each case is assigned according to the initial and final thicknesses. The details of the feed rates and the spindle speeds for each case will be presented in section 6.5, Tables 6.5 and 6.6. During the machining of side 1, the thicknesses of sides 2, 3 and 4 were 2.0 mm, 4.0 mm and 3.0 mm, respectively. During the machining of side 3, the average thickness of side 1 was found to be 1.20 mm.

Table 6.1: Thicknesses and radial and axial depths of cut for the different cases

Side	Set	Case	Initial thickness (mm)	Intermediate thickness (mm)	Final thickness (mm)	d_y (mm)	d_z (mm)
Side 1	No supports	4.0 - 3.2	4.0	3.4	3.2	2.0	0.6
	No supports	3.2 - 2.4	3.2	2.6	2.4	2.0	0.6
	No supports	2.4 - 1.8	2.4	2.0	1.8	1.5	0.4
	No supports	1.8 - 1.3	1.8	1.5	1.3	1.0	0.3
Side 3	With supports	4.0 - 3.0	4.0	3.2	3.0	4.0	0.8
	With supports	3.0 - 2.1	3.0	2.3	2.1	3.0	0.7
	With supports	2.1 - 1.5	2.1	1.7	1.5	1.0	0.4
	With supports	1.5 - 1.0	1.5	1.2	1.0	1.0	0.3

The probe locations for the pocket without and with support are shown in Fig. 6.6 and are specified in Table 6.2. All the dimensions are determined with respect to the origin of the workpiece coordinate system WCS. The probe measures the average vibration of the surface in-front of its face. To compare the experimental results with the MSP model, for each probe position, an average of 5 points was used in the MSP model. One point was located at the centre of the probe, and the remaining 4 points were equally distributed on a circle with a diameter equal to the diameter of the probe.

Table 6.2: Probe locations

	Side 1 without supports		Side 3 with supports	
	x (mm)	y (mm)	x (mm)	y (mm)
Probe 1	62.0	43.0	88	42.5
Probe 2	30.0	43.0	33	42.5
Probe 3	92.5	41.5	—	—

6.2.3 Parameters Used in the Developed Dynamic Models

For the comparison of the results, the machining forces in the z-direction are input to the MSP model with the CoT and the FSS formulations. The probe measurements and the predicted responses are compared.

In the MSP model, the following workpiece material properties were used: Young's modulus $E = 69 \times 10^3$ MPa, Poisson's ratio $\nu = 0.3$ and density $\rho = 2700$ kg/m^3. In all cases, the load was treated as a line load. The calculation of the response was performed using the explicit Runge-Kutta (4,5) integration through the MATLAB function "ode45" with a relative tolerance error of 10^{-5}, an absolute tolerance error of 10^{-6} and a maximum time step of 10^{-5} s. According to the analysis presented in Chapter 5, it was sufficient to include 10 mode shapes in the MSP model for the comparison of the results of the pocket without supports. This was confirmed with some additional convergence analysis in which the number of included mode shapes were incrementally increased from 5 modes to 25 modes. It was found that the difference between the results for 10 modes and 25 modes are less than 0.3% in terms of the maximum amplitude of vibration. For the pocket with supports, 20 mode shapes were used to better describe the response since the supports add extra dynamic constraints to the equations. To approximate the continuous change of thickness during machining at a given depth of cut, the thickness value was updated five times.

For the set of results of the pocket with supports, the FSS formulation for deformable supports was used to account for the support and the holder flexibility. The stiffness of the support/ holder system is affected by the material and geometric properties of the support and the holder in addition to the effect of the interface between the support and its holder, and the support and the workpiece. An estimated stiffness of 3.0 $\times 10^6$ N/m was used through out all the cases. To determine this estimated value of the stiffness, preliminary tap tests were performed by applying impacts on the top of the support holder and measuring the response at the same point. An estimated stiffness was determined from the transfer function. This stiffness value was input to the model as an initial guess for the calibration of the support stiffness. The calibration was performed for only one case and one depth of cut by matching the response from the model and the experiment at the support location.

6.3 Dynamics of the Force Measurement System

Different types of transducers can be used for the force measurement either by mounting them on the workpiece or on the spindle holding the cutting tool. When discussing the force measurement system, two factors need to be considered. The first is the dynamic characteristics of the force measurement system and the second is the nature of the applied force. As mentioned previously in the experimental setup, the measurements of the forces were performed using a rigid dynamometer, with a natural frequency of 2 KHz in the z-direction (the direction of concern). Based on standard guidelines, accurate measurement up to 1/3 of the natural frequency of the transducer can be achieved [169]. This corresponds to a maximum rotational speed of 20,000 rpm for an end mill with 2 flutes, similar to the one used in this experiment. However, due to the extra mass of the workpiece and the fixture, the natural frequency of the dynamometer is further decreased [170, 171]. In addition, the workpiece and the fixture act as a mechanical filter, which distorts the force signal [172].

The dynamometer measurements are accurate for roughing operations of rigid workpieces due to the large static component of the forces [173]. For finishing operations, the milling process has the following characteristics, which are directly reflected on the force signal:

- Small radial depths of cut, which lead to small immersion angles as compared to an immersion angle of 180° in the case of slotting. This results in a highly intermittent force with impulse-like signal. Even at lower frequencies, this force can still excite the dynamometer natural frequencies [171].

- Due to the small radial and axial depths of cut, the force amplitude is low. Thus the signal to noise ratio is low [171].
- For relatively small tool diameters, a higher rotational tool speed is required. This leads to high frequency forces, which can excite the dynamometer natural frequencies.

One of the traditional solutions to such problem is the accelerometric compensation, in which the inertial effect of the dynamometer top plate is subtracted from the force signal [174, 175, 176]. However, in many instances, this technique leads to large inaccuracies and phase distortion in the neighbourhood of the natural frequency of the measurement system [172]. Also, this technique is useful only for point measurements, where the excitation and the response are at the same point [169]. A modification of this method was achieved by using multiple accelerometers to measure the vibration of the top plate of the dynamometer in three directions [177, 178]. The Frequency Response Function (FRF) between the input force and the resultant acceleration was used to determine the stiffness and the mass matrices of the dynamometer and to retrieve the original signal. Another technique was proposed based on experimentally determining the transfer function between the input force and the output signal from the dynamometer. By using inverse filtering of the transfer function, the applied forces are then obtained from the measured force signals [170, 172]. It was shown that a Kalman filter could also be implemented to filter out the effect of structural modes on the force measurement [179]. In all previous studies, the workpiece was rigid, and thus the material removal action did not substantially change its dynamic characteristics. Thus, the dynamics of the workpiece was either ignored or identified once at the beginning of the experiment. For the machining of thin-walled structures, the change of thickness considerably affects the dynamics of the system, and thus the implementation of these approaches is not practical. For the measurement of the forces during the milling of thin-walled structures, De Lacalle *et al.* [171] suggested the use of spindle speeds lower than 6000 rpm, and using a dynamometer with a higher natural frequency. However, it was pointed out that these types of dynamometers have lower measurement range, which reduces their applicability. Moreover, limiting the spindle speed below 6000 rpm is not practical since for finishing operations, smaller tools are used, and thus a higher spindle speed is required. In the coming sections, a new methodology to determine the actual cutting forces from the measured signal during the milling of thin-walled structures will be presented.

6.3.1 Two Degree of Freedom Model

To understand the nature of the problem, a simple two degree of freedom model was formulated and is shown in Fig. 6.8. The dynamometer is represented by a mass m_D, a damping c_D and a stiffness k_D. The displacement of the top plate of the dynamometer is designated by z_D. For simplicity, the workpiece, with a displacement z_1, is represented by a one degree of freedom model with a mass m_1, a damping c_1, and a stiffness k_1. An input force f is applied on mass m_1. The values of the parameters of the model, which are listed in Table 6.3, were extracted from impact tests on the side of the pocket and the dynamometer.

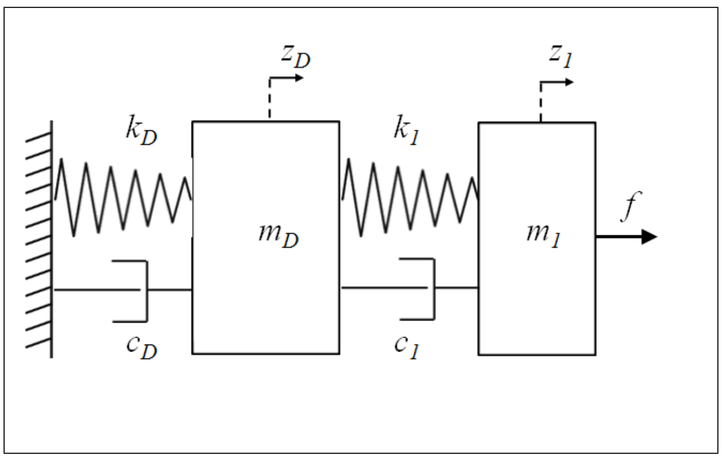

Figure 6.8: Schematic of a two degree of freedom model

Table 6.3: Parameters of the two degree of freedom model

Workpiece		Dynamometer	
m_1	0.01 (kg)	m_D	4.0 (kg)
c_1	8.9(N.s/m)	c_D	5030 (N.s/m)
k_1	7.8 $\times 10^5$ (N/m)	k_D	6.3 $\times 10^8$ (N/m)

The shape of the input force f was determined based on a simple 2D mechanistic force model for a 2-flute, 15.875 mm diameter tool, a 10,000 rpm spindle speed and a 1 mm radial depth of cut. These parameters were chosen based on actual cutting experiments. The output signal of the dynamometer results from the deformation of the piezo-electric crystal inside it [172, 178]. Accordingly, the output signal (force) could be represented as $k_D \times z_D$ for the model in Fig. 6.8. The comparison of the input force and the output force using this model is shown in Fig. 6.9. Due to the dynamics of the system, the output signal was completely distorted, and its amplitude was increased by more than 250%, as compared to the input force signal. A comparison of the Fast Fourier Transform (FFT) of these input and output signals is shown in Fig. 6.10. The harmonics of the tooth passing frequency was present in both signals. In the input signal, the amplitudes of these harmonics have a peak at the first tooth passing frequency and then they decrease gradually. Nevertheless, due to the dynamics of the workpiece and the measurement system, the peak amplitude of the output signal was found at a frequency of 1330 Hz, which is close to the natural frequency of the workpiece.

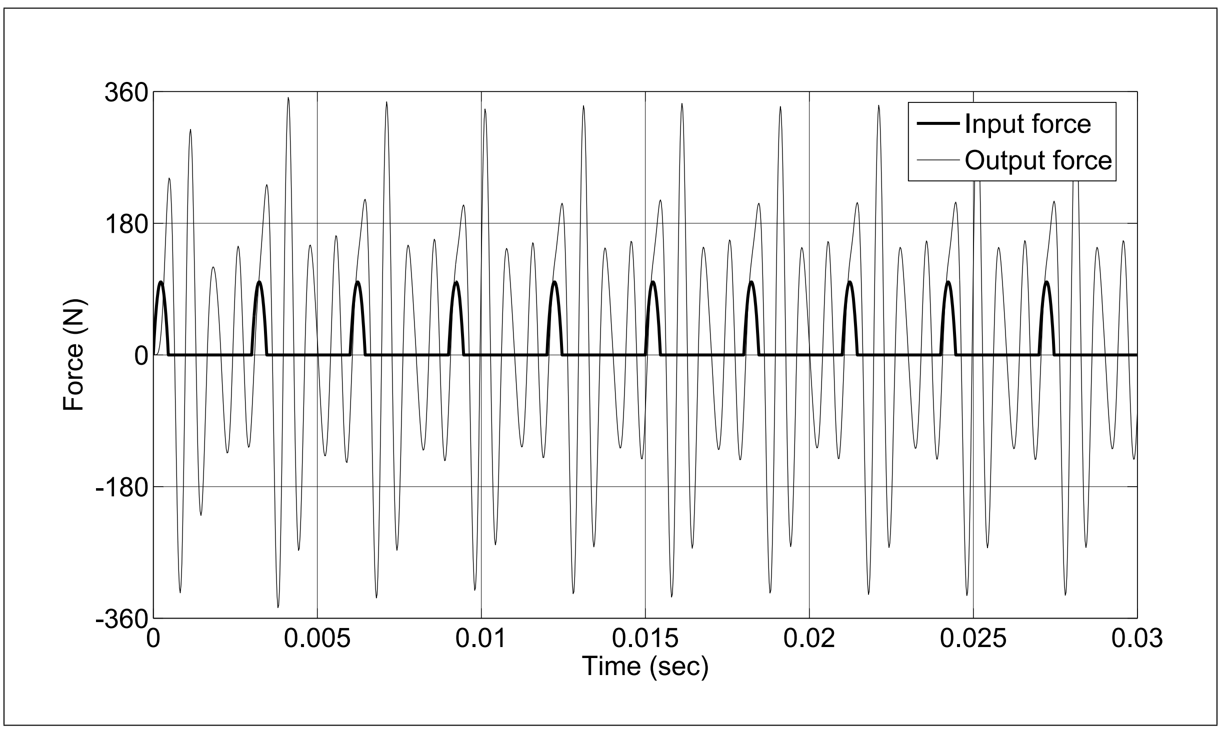

Figure 6.9: Comparison of the theocratical input force and the output force obtained using the two degrees of freedom model

Different cutting parameters were examined, and it was observed that in order to minimize the distortion of the output signal, a large radial depth of cut (or a small tool diameter),

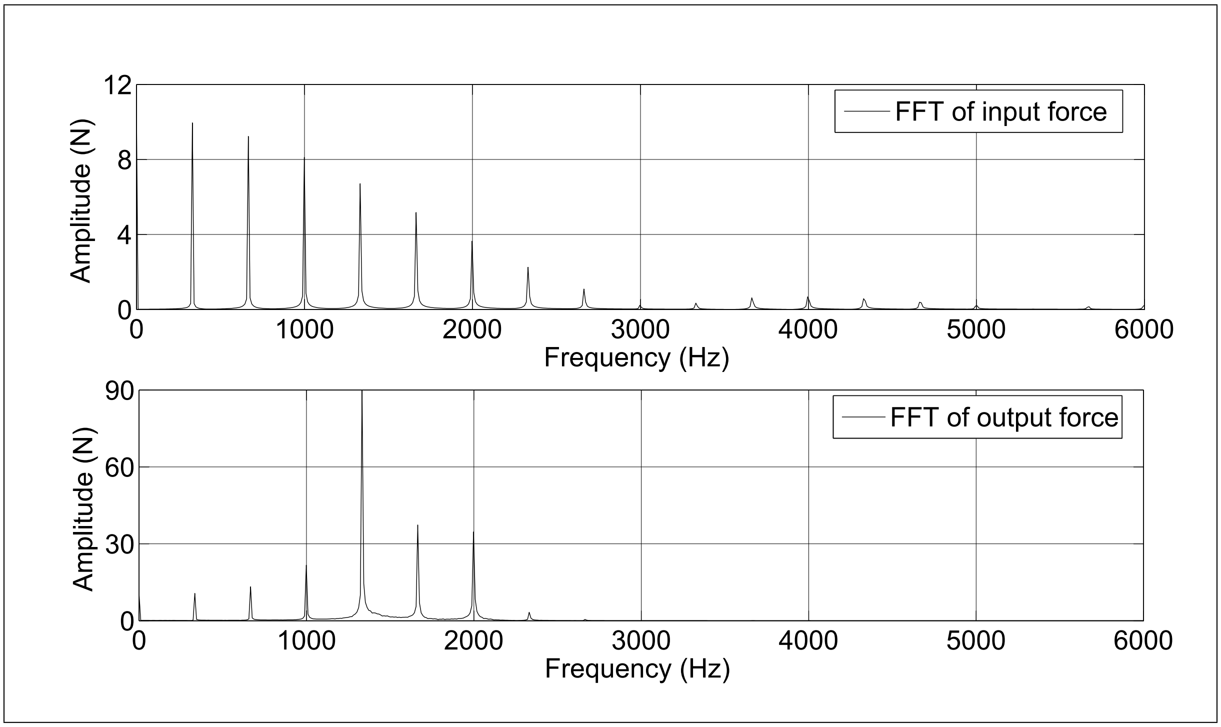

Figure 6.10: FFT of the input and output forces using the two degrees of freedom model

and a spindle speed lower than 2,000 rpm, were required. These values are not practical for the purpose of finishing operations and can still give rise to other problems such as large deviations from specified tolerances in the case of large immersion angles, chatter due to tool deflection for tools with small diameters, and higher forces in the case of low cutting speeds. Instead, a methodology is required to compensate for the dynamics of the measurement system and the workpiece.

6.3.2 Proposed Methodology for the Identification of the Transfer Function of the Force Measurement System

By reviewing the literature, the inverse filtering techniques were found to be a promising solution for this problem. However, it was necessary to account for the change of the workpiece dynamics due to the change of thickness of its sides during machining. The proposed methodology is based on modelling the workpiece and the fixture as a two degree of freedom system while representing the dynamic characteristics of the dynamometer by a multi-mode transfer function, determined experimentally. This model can be represented schematically as shown in Fig. 6.11 where m_1, c_1, k_1 and m_2, c_2, k_2 are the mass, the damping and the stiffness for the first and second degrees of freedom of the workpiece and the fixture, respectively. The displacement of the first and second mass are designated by z_1 and z_2 while the displacement of the face of the dynamometer is represented by z_D.

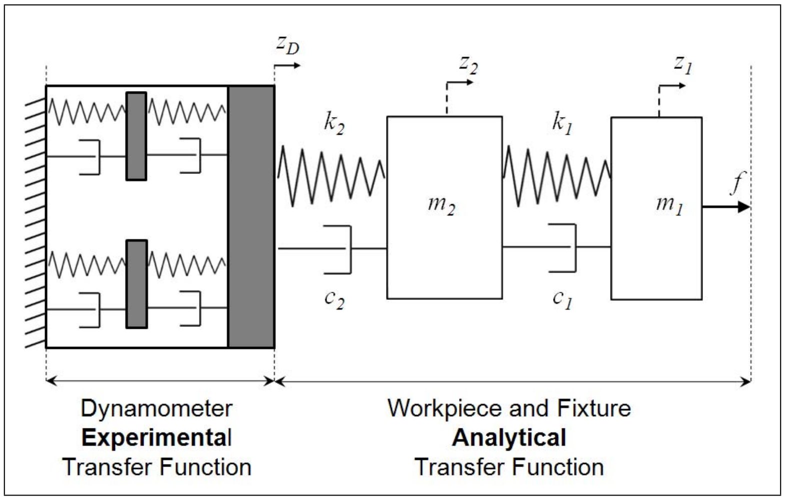

Figure 6.11: Schematic illustration of the model representing the workpiece, the fixture and the dynamometer setup

The flow chart shown in Fig. 6.12 represents the steps for the development and the validation of the proposed methodology for the extraction of the input machining forces from the dynamometer measurements:

1. **Identification of the dynamometer transfer function**: Impact tests are performed to characterize the transfer function (T_F) between the input force (F_{in}) and the output signal from the dynamometer (F_D), as well as the transfer function (T_x) between the input force and the displacement of the dynamometer top plate (z_D). The dynamometer is fixed on the table of the machining centre.

2. **Optimization of the parameters of the workpiece/fixture model**: Based on the cutting parameters (spindle speed, and radial and axial depths of cut) that were used during the machining of the pocket side at a given thickness (h) and tool-path depth d_p, the idealized shape of the machining force signal (F_s) is determined. The transfer function representing the dynamics of the system (workpiece, fixture and

dynamometer) and relating the input machining force to the output measurement from the dynamometer is designated as T_{sys}. This transfer function is obtained by combining the transfer function (T_w) of the workpiece and the fixture and the two transfer functions T_F and T_x (see Appendix C for the detailed formulation). The transfer function T_w depends on the following unknown parameters of the workpiece and the fixture (m_1, m_2, c_1, c_2 and k_1, k_2). To determine these parameters, the idealized machining force F_s is input to the combined transfer function T_{sys}. A global optimization such as Genetic Algorithms is used to determine the optimum parameters that minimizes the error between the output force from the model (F_o) and the force signal (F_m) which was measured during the machining experiments for the same thickness h and tool-path depth d_p. Once the transfer function T_{sys} is identified for a given h and d_p, it can be inverted an multiplied by the force measurement of the dynamometer to obtain the real cutting forces.

To validate the proposed methodology, a known input force F_{in} (e.g. impact force) is applied on the workpiece while the whole set-up is mounted. The output force measurement of the dynamometer F_D is multiplied by the inverse of the system transfer function $[T_{sys}]^{-1}$ to obtain the compensated force signal F_c. This force is then compared to the input force F_{in}. If the two forces are in agreement, then the transfer function T_{sys} can accurately represent the dynamics of the workpiece-fixture-dynamometer system.

6.3.3 Details of the Formulation of the Dynamics of the Force Measurement System

To be able to use the different transfer functions, the variables are transformed to the frequency domain. The force and the displacement variables described earlier including F_{in}, F_D, F_s, F_o, F_m, z_D, z_1, and z_2 represent the Discrete Fourier Transform (DFT) of their corresponding time signal variables. The identification of the two transfer functions (T_w and T_x) was based on an average of 5 impact (tap) tests. For these tests, the force was applied and measured using an impulse hammer with automatically-actuated piezoelectric units (PCB 086D05). The displacement of the top face of the dynamometer was obtained by measuring

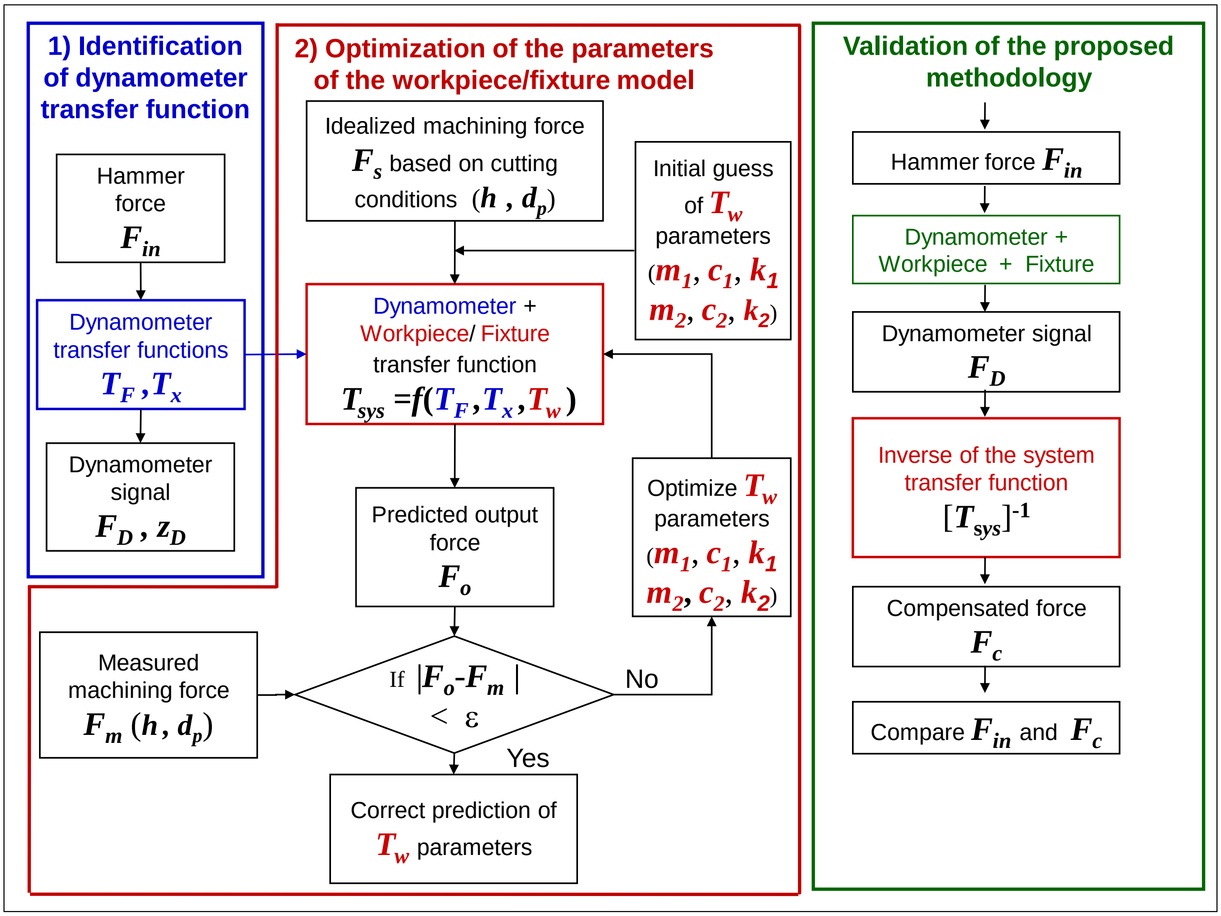

Figure 6.12: Flow chart for the identification of the transfer function of the workpiece-dynamometer system

the acceleration at the centre of the dynamometer using a piezoelectric accelerometer (PCB 352C68) and then double integrating the measured signal.

Once identified, these transfer functions were used in the optimization. The optimization was performed using Genetic Algorithms with three cross-overs (arithmetic, simple, and heuristic) and five mutation operators (uniform, whole uniform, non-uniform, boundary and Gaussian mutations). The frequencies at which the magnitude of the force F_m has peaks are determined. These frequencies are sorted in a descending order according to the amplitude of their corresponding force peak and are referred to as ω_s for $s = 1, 2, \ldots$. The objective function ψ_e used to determine the error between the measured force and the predicted output force from the model is defined as follows:

$$\psi_e = \left(\sum_{s=1}^{3} \left[F_o(\omega_s) - F_m(\omega_s) \right]^2 \right)^{\frac{1}{2}} \tag{6.1}$$

where $F_o(\omega_s)$ and $F_m(\omega_s)$ are the magnitude of the DFT of the output force from the model (F_o) and the measured force (F_m), respectively, evaluated at ω_s. Increasing the number of maximum peaks in the objective function negligibly affected the final transfer function in most cases. Nevertheless, in some instances, it was found that a high number of peaks resulted in the divergence of the optimization scheme.

Since the sampling frequency was 12,000 Hz, the range of frequency in the DFT was 0 to 6,000 Hz. The high frequency range (4,000 Hz to 6,000 Hz) was removed from the signal for several reasons. Due to aliasing problems, the range of frequencies from 0.4 to 0.5 of the sampling frequency does not contains accurate data to describe the system [180]. Moreover, by analyzing the frequency content of the hammer forces, it was observed that the impacts could excite the structure up to a frequency close to 3,000 Hz. Consequently, keeping the frequencies in the higher range resulted in large numerical errors and erroneous results. Finally, it was found that the content of the signal in the higher range did not affect the amplitude or the shape of the signal.

6.3.4 Validation of the Proposed Methodology for the Identification of the Transfer Function of the Force Measurement System

Tap tests were performed on side 1 at the base of the pocket while the whole setup was mounted. Applying the force on the base of the pocket allowed us to have large amplitude impacts with sufficient energy content to excite the frequencies of the system, with good coherence, and without damaging the workpiece. The transfer function T_{sys} was determined through the procedure described in section 6.3.2 for the case of machining side 1 with a thickness h of 3.2 mm and at a tool-path depth d_p of 42 mm. This case was selected so that the tool-path depth is close to the point where the impact force (F_{in}) for validation is applied.

Figure 6.13 shows the input force of the hammer F_{in}, the dynamometer measurements, and the compensated force, in addition to the optimized transfer function T_{sys}. The error between the maximum amplitudes of the hammer force and the dynamometer measured force is more than 110%. By applying the proposed methodology, the error in amplitude was reduced to less than 3%, as shown in Fig. 6.13. It can be seen that the proposed methodology reduced the amplitude of the overshoot after the impact by more than 90% relative to the maximum amplitude of the hammer ($\approx$ 1800 N). While the forces after the impact should be equal to zero, the measured forces have some residual vibrations. The proposed methodology was able to substantially reduce these residual vibrations; however, it did not completely eliminate it. To recuperate the correct force signal, these oscillations have to be discarded. Similarly, when the proposed methodology is applied to the measured machining forces, some oscillations could appear for the time interval when the flutes of the tool are not engaged in the workpiece. These small amplitude oscillations will also be discarded. Ten validation cases were performed and the average of the errors was found to be 8.0%.

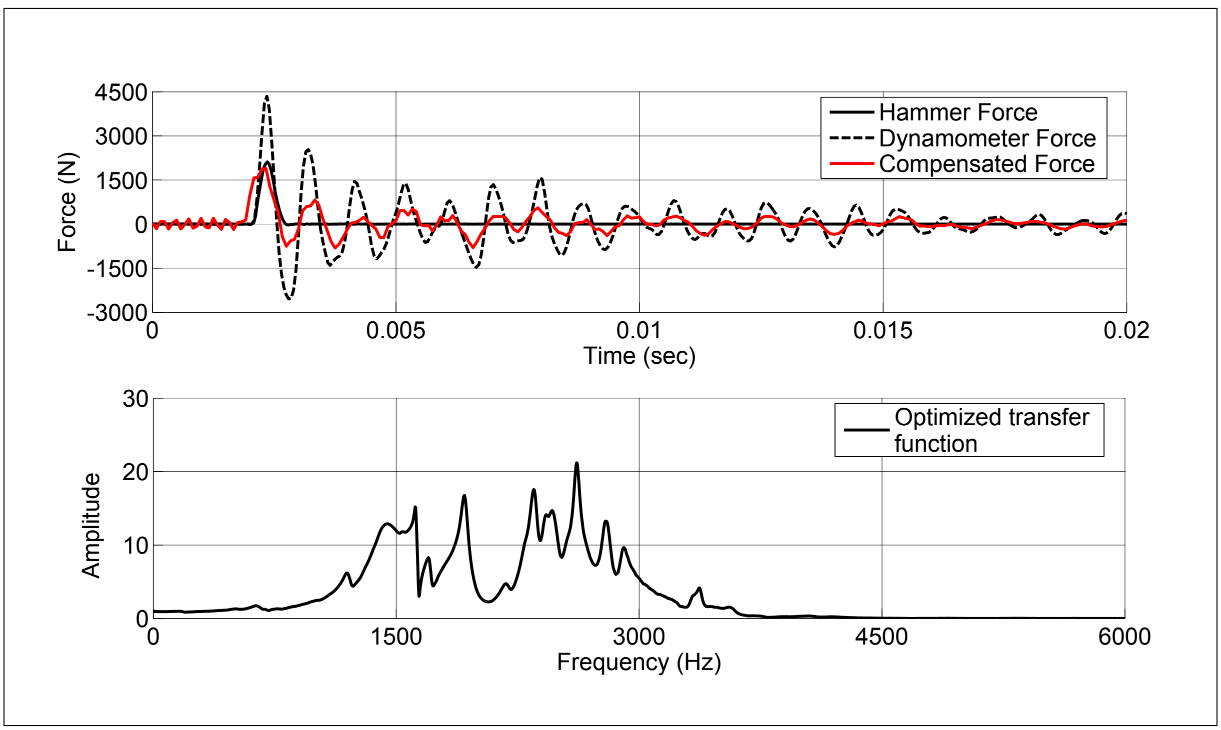

Figure 6.13: Comparison between the hammer, dynamometer and compensated forces for the validation of the proposed methodology

6.4 Error Analysis of the Measurement System

To be able to validate the predictions of the proposed dynamic models experimentally, the errors in the measurements of the forces and the displacements have to be accounted for. Depending on the type of the experiment, different error analysis techniques could be applied. The experiments could be categorized as multiple or single sample experiments. The multiple sample experiment involves the repetition of the experiment for the same conditions to quantify the uncertainties in the measurements. In the single sample experiment, the uncertainty in the measurement is established analytically by combining the errors resulting from the different measurement devices [181].

In the machining experiment, described in this chapter, there are many factors that could affect the forces including the tool wear, the uniformity of the workpiece thickness, tool run-out, material nonlinearities, the tool signature on the workpiece, and chatter. Thus it is very difficult to repeat the different tests with exactly the same conditions. For this reason, the experiment is considered as a single-measurement experiment.

For the displacement measurements, there are two main sources of errors. The first is the error due to the lack of accuracy of the measurements of the probe (ε_{p1}). For a given displacement (u_a), the probe outputs a voltage, which is transformed to an equivalent displacement (u_c) through the calibration curve (refer to Fig. 6.3). At a 95% confidence level, the error interval is represented by twice the standard deviation σ_u, where σ_u can be calculated as follows [182]:

$$\sigma_u = \left[\frac{1}{N} \sum (u_c - u_a)^2 \right]^{\frac{1}{2}} \tag{6.2}$$

The mean, the standard deviations (σ_u), the error interval ($2\sigma_u$), and the number of points (N) for probes 1, 2 and 3, are shown in table 6.4.

The second source of error is due to the dynamic response of the probe holder (ε_{p2}). This error is determined from the transfer function of the probe holder relating the machining forces on the side of the pocket to the vibration of the probe holder. Tap tests were performed by applying impacts on the side of the pocket and measuring the response on the support holder. The transfer function, determined from the impact tests, is shown on Fig. 6.14.

Table 6.4: Measurement errors due to the accuracy of the probes

	Mean	Standard Deviation σ_u	Error interval $(2\sigma_u)$	No. of points (N)
Probe 1	0.67 μm	0.47 μm	1.6 μm	26
Probe 2	1.10 μm	0.72 μm	2.5 μm	26
Probe 3	1.28 μm	1.12 μm	3.4 μm	14

For each individual measurement (at a given tool-path depth), the forces are input to this transfer function to determine the corresponding response. The maximum of the absolute displacement for this response is used as the bound of the error interval corresponding to the probe dynamics. In most experiments, this error was less than ± 4 μm. The total measurement error for each probe is calculated as:

$$\varepsilon_m = \left[\varepsilon_{p1}^2 + \varepsilon_{p2}^2\right]^{\frac{1}{2}} \tag{6.3}$$

The maximum measurement error for probes 1, 2 and 3 was found to be less than 8.0 μm, 6.7 μm, and 6.9 μm, respectively.

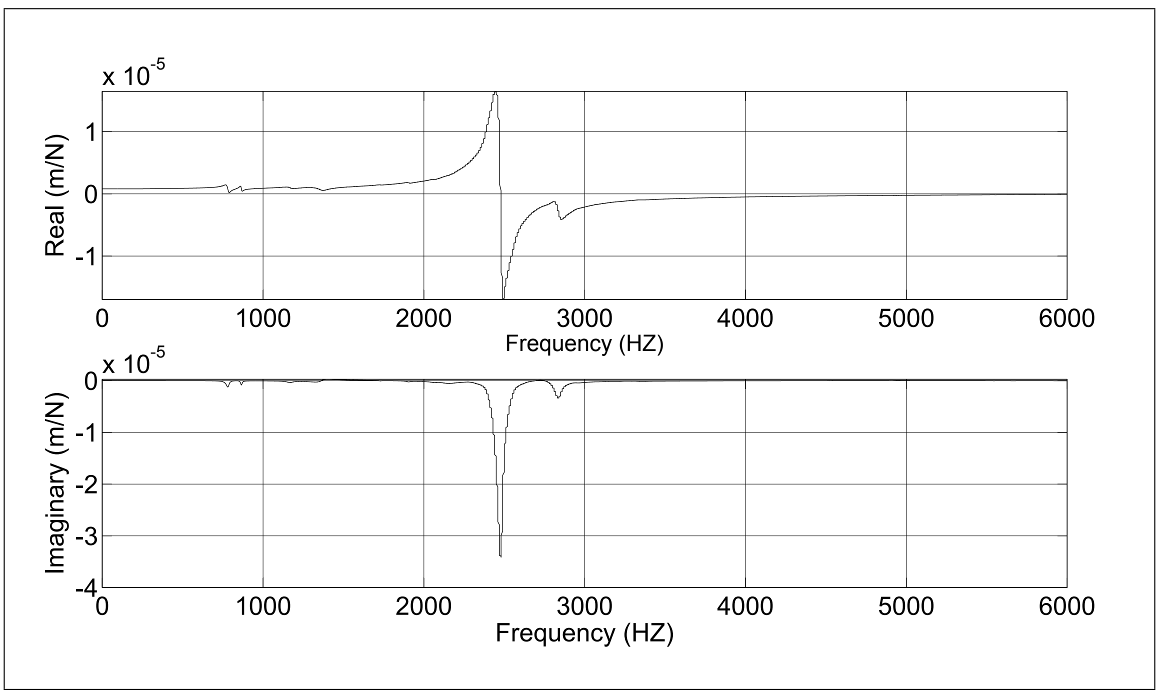

Figure 6.14: Example of the transfer function of the support holder

For the force measurement, two sources of errors are present. The first is the error due to the nonlinearity of the dynamometer (ε_{f1}). As previously mentioned in the specification of the dynamometer (refer to section 6.2), this error is within ±1%. The second source of error is due to the dynamics of the measurement system (dynamometer) (ε_{f2}). According to the validation presented in 6.3.4, the compensated forces have an error of ±8.0%. This percentage will represent the measurement error due to the dynamics of the force measurement system. The total force measurement error was found to be equal to 8.1%. This value was calculated as follows:

$$\varepsilon_f = \left[\varepsilon_{f1}^2 + \varepsilon_{f2}^2\right]^{\frac{1}{2}} \tag{6.4}$$

Assuming that the system is linear, the calculated response w_c can be expressed as:

$$w_c = mf_c \tag{6.5}$$

where m represents the slope of the curve and f_c is the compensated force, which is input to the MSP model. Knowing that the force has an error ε_f, introducing a corresponding error ε_c to the calculated displacement and substituting in Eq. (6.5), the following equation is obtained:

$$w_c \pm \varepsilon_c w_c = m(f_c \pm \varepsilon_f f_c) \tag{6.6}$$

By dividing the left hand side of Eq. (6.6) by w_c and the right hand side by mf_c, it will be found that the percentage error ε_c of the calculated displacement is equal to the force measurement percentage error. One needs to multiply ε_c by the calculated instantaneous displacement in order to estimate the effect of the force measurement errors on the displacement in μm.

According to this analysis, the measured displacement will have an error band of $\pm\varepsilon_m$ to represent the measurement errors of the probe. The displacement calculated by the models will have an error band of $\pm\varepsilon_c w_c$ due to the measurement errors of the force.

6.5 Experimental Results

As mentioned previously, the objective of this chapter is to compare the vibration measured during real cutting experiment versus the calculated response from the developed models. During the experiments, two conditions were monitored: chatter and tool wear. Since the objective of this experiment is to validate the model under stable conditions, the results are focused on the cases with no chatter or very low level of chatter and low or medium level of tool wear. As will be seen, for the cases with undesirable conditions such as high level of chatter or tool wear, the accuracy of the model is still reasonable, which further validates the model. The levels of chatter were determined qualitatively based on the surface finish of the machined area and the magnitude of the recorded cutting forces. For the tool wear there are two extremes. The first is when the tool is new and the second is when the edge of the tool starts to chip. All the cases in between these two extreme conditions are considered as having low or medium tool wear depending on how long the tool has been used.

The error ϵ_c between the measured and the calculated responses, at a given location of a probe, is expressed as follows:

$$\epsilon_c = \left| \frac{d_c - d_m}{d_m} \right| \times 100 \tag{6.7}$$

where d_c and d_m are the maximum of the calculated and measured displacements, respectively. The error could have been calculated relative to the maximum displacement of the pocket side. However, since only three probes were used for the measurements, the location where the global maximum displacement of the side occurred was not detected during the experiment.

6.5.1 Validation Test Results under Stable Cutting Conditions

A summary of the cases that will be presented for the cutting tests under stable conditions is shown in Table 6.5. Several cases were evaluated at different tool-path depths with and without supports. The identification name of each case (e.g. 3.2-2.4) represents the change of thickness during machining from 3.2 mm to 2.4 mm. For each case, two tool-path depths were selected to compare the measured versus the calculated response of the side of the pocket. For each set of results (pocket without and with supports), the cases are presented in an ascending order based on the relative measurement errors. By analyzing the different cases, it was found that the relative errors in the measurements were higher in the cases with very thick or very thin sides. For the case where the machining was performed on a thick side, the amplitude of the vibrations was relatively small and the relative measurement errors were high. On the other extreme, very thin sides experienced more chatter, leading to higher errors in the force compensation.

Table 6.5: Summary of the test cases with stable cutting conditions

Stable conditions (*no / low chatter and no, low, medium tool wear*)						
Set	Case	Tool-path depth d_p (mm)	Spindle speed (rpm)	Feed rate (mm/min)	Chatter	Tool wear
1- No supports	3.2-2.4	10.0 16.0	9000 9300	3600 2790	low	low
2- No supports	4.0-3.2	2.0 20.0	8000	3200	none	none low
3- No supports	2.4-1.8	15.0 21.0	12300	4200	none	medium
4- With supports	2.1-1.5	11.5 15.5	6000	3600	none	none
5- With supports	3.0-2.1	9.0 18.0	8900	1780	low	low
6- With supports	4.0-3.0	8.0 12.0	8900	1600	none	none

Test Cases for Machining the Pocket Without Supports

For each of these cases, tap tests were performed on side 1 before machining, and the workpiece frequencies were determined and compared to those calculated from the model. The responses for test case 3.2-2.4 at a tool-path depth of 10 mm are presented in Fig 6.15. In this figure, two types of plot can be seen; the plots on the left show an envelop for the peaks of the responses during the whole machining path. The envelop represents the average of the negative peaks of the response. For the sake of clarity, the envelops for the positive peaks were not included since their amplitudes were relatively small. The measurement errors of the probes are represented with error bars around the measured response. The measurement errors of the force, input to the proposed dynamic models, are indicated by a shaded band around the envelope of the calculated response. The location of the probe is indicated by a solid vertical line. The plots on the right represent the time responses at the location of each probe. This type of plot permits the comparison of the dynamic characteristics of the measured and the calculated responses. It is expected that some deviations in the responses could occur near the edges of the side of the pocket. These deviations are due to the assumptions made in the model concerning the approximation of the boundary conditions (refer to section 4.4.2). For this reason, the area within the tool position 0 to 20 mm and 100 to 120 mm are shaded. Practically, for the purpose of the design of the fixture layout, any deviation at these regions is not of a significance, since the vibrations are expected to be low at the edges as compared to the centre.

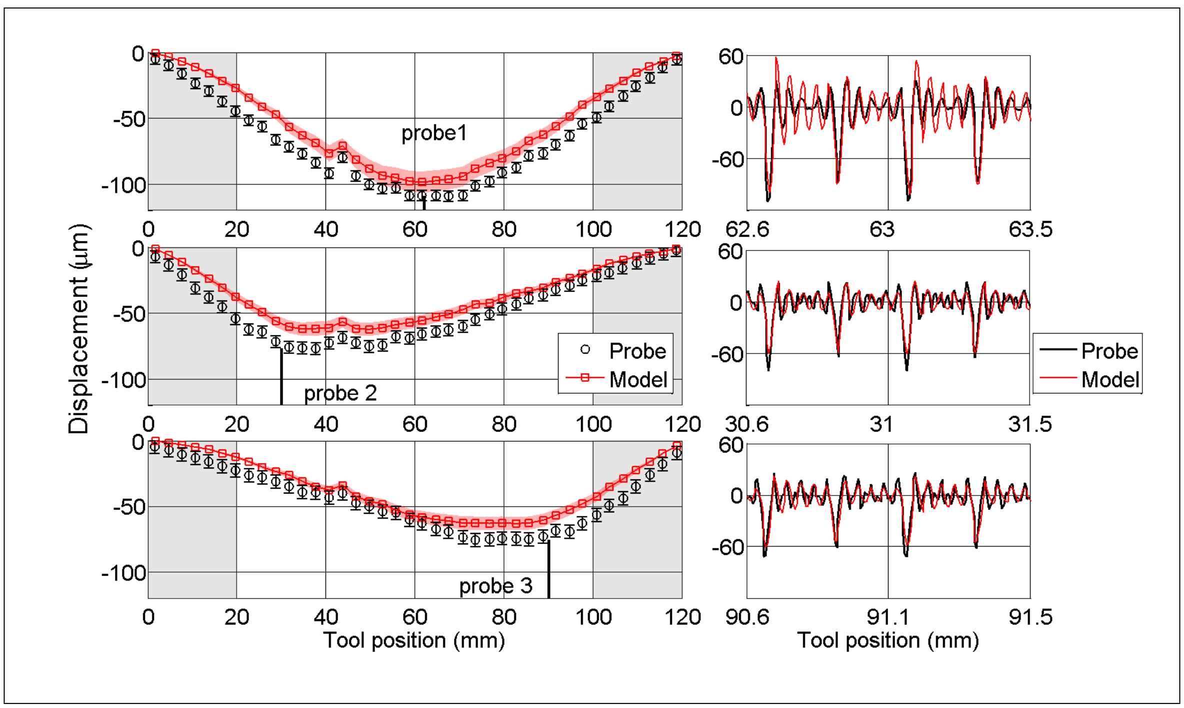

Figure 6.15: Pocket without supports; the results for the displacements of test case 3.2 -2.4, at a tool-path depth of 10.0 mm

Based on the tap tests before machining for test case 3.2-2.4, the frequencies of the first 3 mode shapes were found to be 1576 Hz, 1812 Hz, and 2046 Hz, as compared to the calculated ones 1614 Hz, 1898 Hz and 2055 Hz with errors less than 2.5%, 4.5% and 0.5%, respectively. As reported in Table 6.1, the radial and axial depth of cut for this case are 0.6 mm and 2.0 mm, respectively. The errors between the envelops of the calculated and the measured responses at probes 1, 2 and 3 were found to be 5.4%, 10.8% and 12.8%. As can be seen, the shape of the envelops of the measured and the calculated responses are in close agreement, even at the region where sudden change occur (tool positions between 42 mm to 45 mm). This certainly validates the accuracy of the response predicted from the model, as well as the accuracy of the compensated force signal since this same discontinuity can be found in the force signal shown in Fig. 6.16. The responses from the model at the corners of the pocket were still in good agreement with the measurements. For the calculated and the measured time responses presented in Fig. 6.15, the frequencies of the free vibration portion of the responses were calculated and the error was found to be less than 7.5%. Thus, the dynamic characteristics of the machined pocket are captured accurately in the model in terms of amplitude and frequency. The thickness before the machining was measured at different locations on the pocket side. Variations less than 50 μm was observed. This thickness uniformity is one of the factors that contributed to the close agreement between the model and the experiment.

Damping is an important factor to determine so that the vibration of the system could be properly described. As seen in Fig. 6.15, as the tool moves away from the probe location, the response is damped. To describe the damping, one needs to differentiate between the time intervals when the flutes of the cutting tool are in-cut and out-of-cut. When the flutes are out-of-cut, no external forces are applied on the pocket side. Thus the main source of damping is the structural damping. For these time intervals, a damping of 0.02 was used in the model. This value was determined from different tap tests performed on the side of the pocket. During the time interval when the flutes are in-cut, an additional damping is present, due to the interaction between the workpiece and the tool. At these instances a higher damping is expected due to the rubbing effect between the workpiece and the clearance face of the tool [114]. The damping value used in the model was determined through the calibration of the damping ratio for each case at only one depth of cut, by matching the measured and the calculated responses. Once determined, this value was used for the other

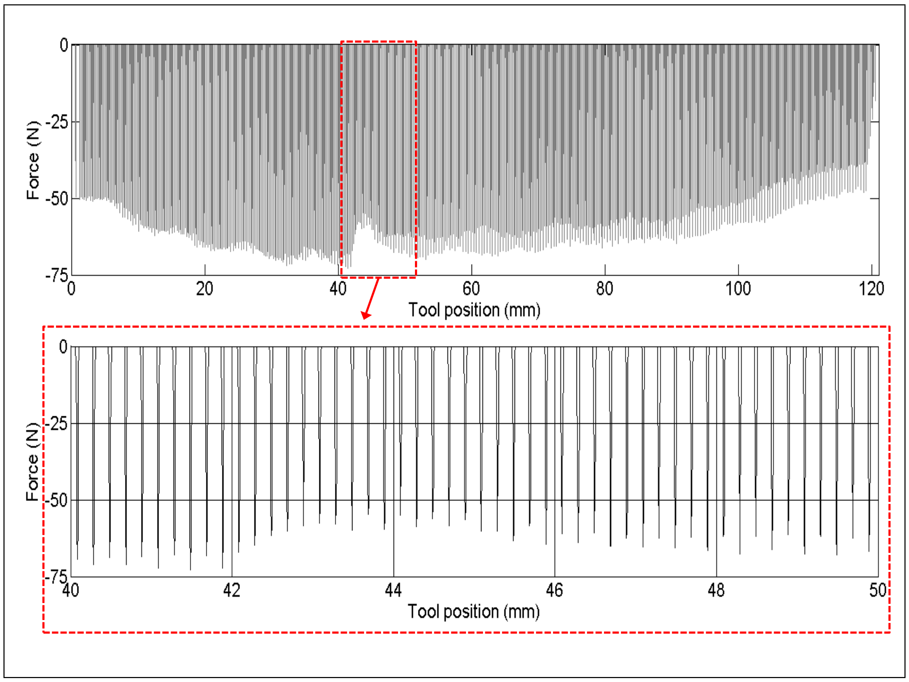

Figure 6.16: Compensated force for test case 3.2 - 2.4, at a tool-path depth of 10 mm

depths of cut. The value of this damping ratio for test cases 4.0-3.2 and 3.2-2.4 was found to be 0.07. For test case 2.4-1.8, with smaller radial depths of cut, the damping ratio was 0.2. This is expected due to the potential rubbing between the tool and the workpiece. In general, the rubbing can be related to the maximum chip thickness during cutting. For a chip thickness lower than a certain value, rubbing is likely to occur [183]. The minimum chip thickness depends on many factors including the corner radius of the tool and the cutting speed. The chip thickness is related to the feed per tooth f_z. In roughing operations, where the difference between the entrance and the exit angles of the flute are greater than 90°, the feed per tooth is equal to the maximum chip thickness. For smaller depths of cut, the maximum chip thickness is much lower than the feed per tooth. This is shown in Fig. 6.17 where the maximum chip thickness is represented by the segment AB. In these experiments, to avoid rubbing, higher feed rates were used such that the value of the maximum chip thickness AB was greater or equal to 0.05 mm. Nevertheless, in many instances, these high feed rates resulted in chatter and were reduced leading to more rubbing and higher damping.

The responses for the same test case at a depth of cut of 16 mm is shown in Fig. 6.18. The errors ψ_c between the envelops of the measured and the calculated responses at probes 1, 2,

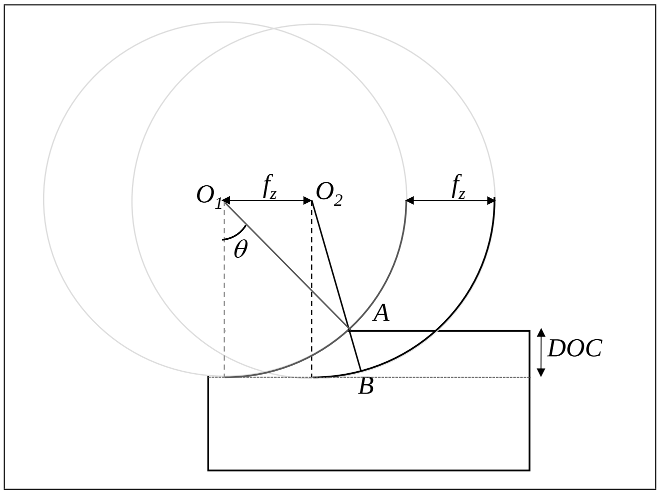

Figure 6.17: Illustration of the relation between the feed per tooth f_z and the maximum chip thickness

and 3 were found to be 5.0%, 10.9%, and 1.7%, respectively. Based on the time response plots, the error in the frequencies of the free vibration of the calculated and measured responses was found to be less than 1.0%. Within the measurement errors, one can see excellent agreement in the shape of the envelopes of the calculated and measured responses as well as the dynamic characteristics of the time responses. For this case, a slightly less agreement was found near the corners of the pocket, as expected. A slightly higher damping was expected for this tool-path depth as a result of some rubbing between the tool and the workpiece. The feed per tooth at this tool-path depth was 0.15 mm/th, as compared to a 0.2 mm/th in the previously presented results. Other depths of cut were evaluated for this test case and showed the same agreement between measured and predicted responses.

For test case 4.0-3.2, the errors between the calculated and the measured frequencies of the first three mode shapes were found to be less than 3.5%. The results for test case 4.0-3.2 at 2 mm and 20 mm tool-path depths are shown in Fig. 6.19 and Fig. 6.20, respectively. For the first tool-path depth (2 mm), the errors between the envelops of the measured and the calculated responses for the three probes were found to be 9.7%, 4.0% and 5.0%, respectively. Similar to the previous cases, a good agreement is seen between the calculated and the measured responses. A good agreement is seen between the calculated and the measured time responses in terms of the frequency content of the free vibration oscillations. Due to the displacement measurement errors, some deviations appear between the measured

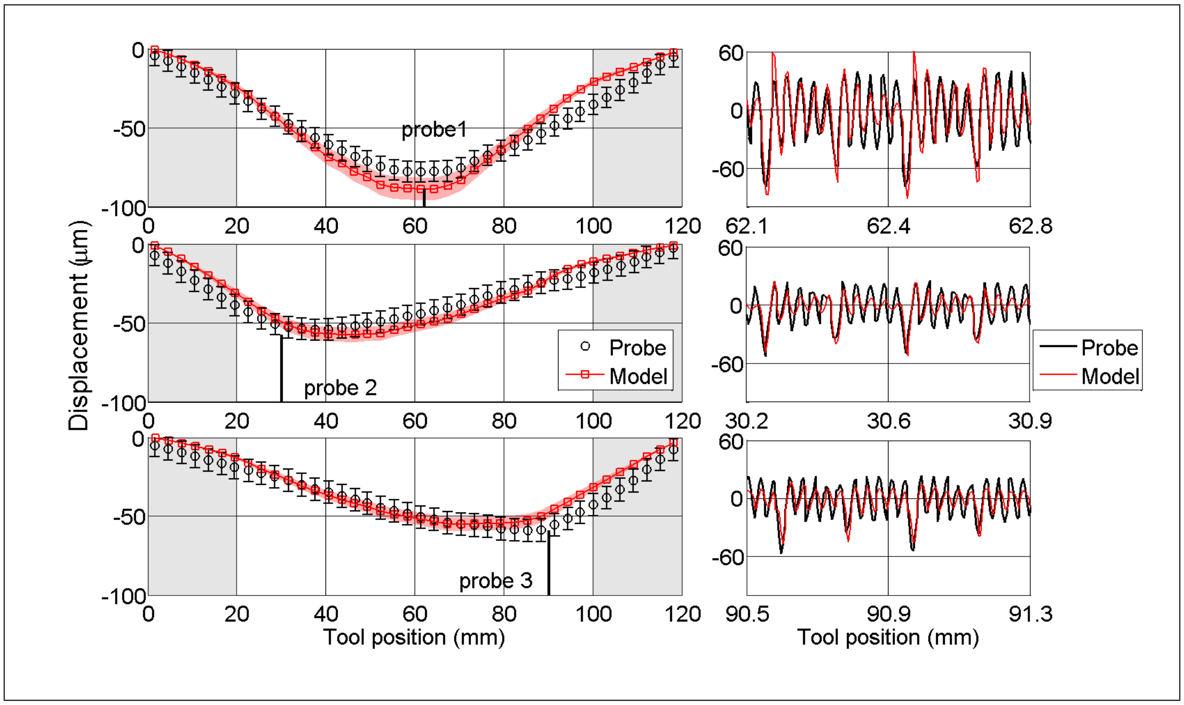

Figure 6.18: Pocket without supports; the results for the displacements of test case 3.2 -2.4, at a tool-path depth of 16.0 mm

and calculated low amplitude free vibration oscillations. At 20 mm tool-path depth, the same level of agreement was achieved, with errors between the envelops of the measured and the calculated responses for probes 1, 2 and 3 of 9.4%, 6.7% and 5.6%, respectively.

For a thinner wall thickness, as in test case 2.4-1.8, the first 3 frequencies of the pocket before machining were found experimentally to be equal to 1290 Hz, 1170 Hz, and 1960 Hz. These values are compared to 1283 Hz, 1810 Hz and 2015 Hz with errors less than 0.5%, 2.5% and 3.0% when the model was used. As mentioned previously, for test case 2.4-1.8, with a radial and axial depth of cut of 0.4 mm and 1.0 mm respectively, the damping of the system was expected to be higher due to potential rubbing between the workpiece and the system. Another reason for this high damping could be the wear observed on the tool. Figure 6.21 presents the responses during the machining at a tool-path depth of 15 mm. All the machining paths previous to this tool-path depth resulted in very high chatter, which eventually led to some non-uniformity of the machined areas. Since this non-uniformity was not taken into account in the model, some deviations were expected between the measured and the calculated responses. Moreover, the non-uniformity of the thickness might have

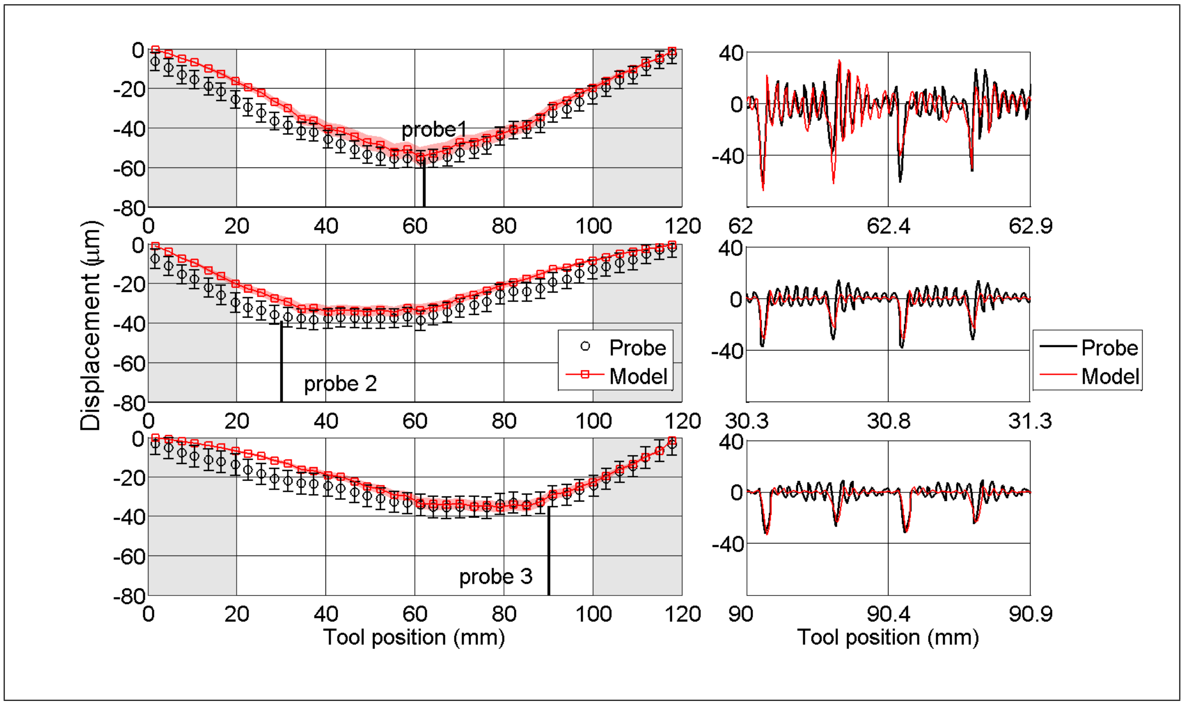

Figure 6.19: Pocket without supports; the results for the displacements of test case 4.0 -3.2, at a tool-path depth of 2.0 mm

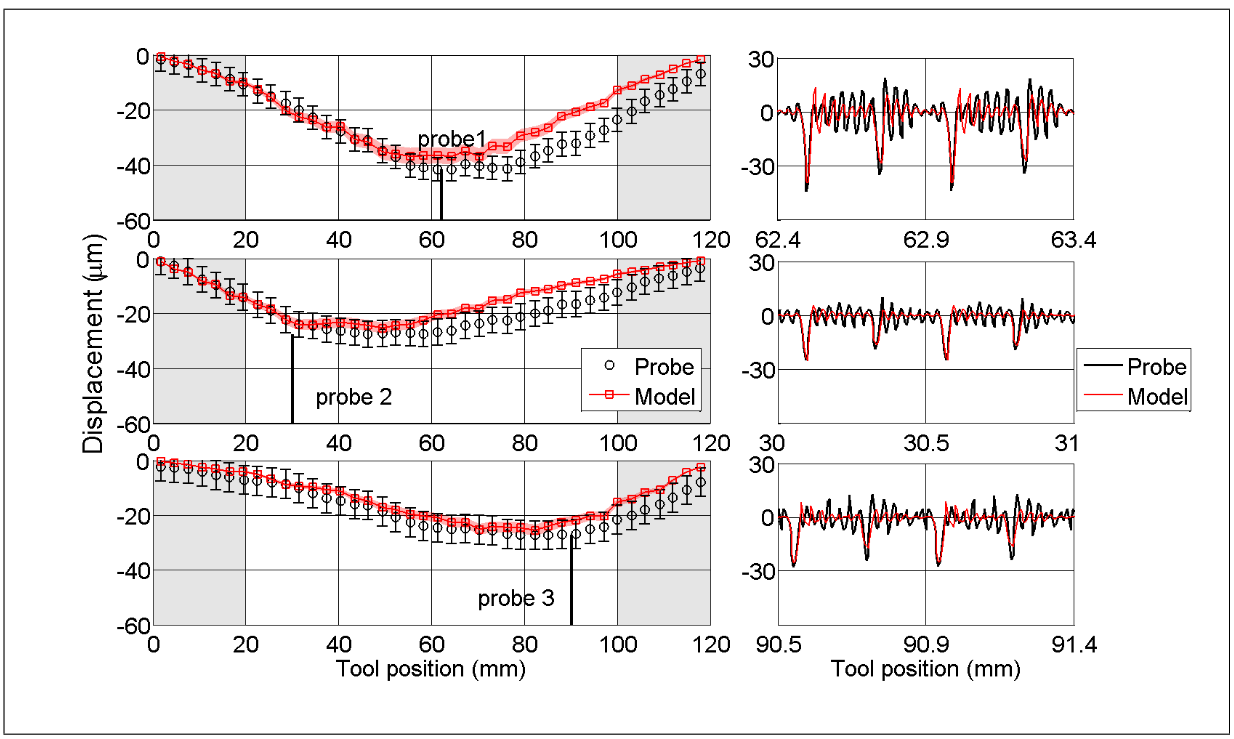

Figure 6.20: Pocket without supports; the results for the displacements of test case 4.0 -3.2, at a tool-path depth of 20.0 mm

resulted in the tool touching the workpiece at regions away from the specified tool-path depth. This might have affected the point of load application. As seen in Fig. 6.21, the errors between the envelops of the measured and the calculated responses were found to be less than 4.0%, 6.5%, and 1.0%, respectively. Less agreement is seen between the shape of the envelops of the responses for the tool positions at 70 mm to 80 mm for probe 2, and 20 mm to 30 mm for probe 3. One can see, however, that the results are in close agreement, considering the measurement errors, especially in the force signal. Negligible errors in frequencies, between the measured and the calculated responses, can be seen in the time responses at probes 1 and 3. For the time responses at probe 2, some differences exist, which could be a result of some local errors in the probe measurements or in the compensation of the force signal.

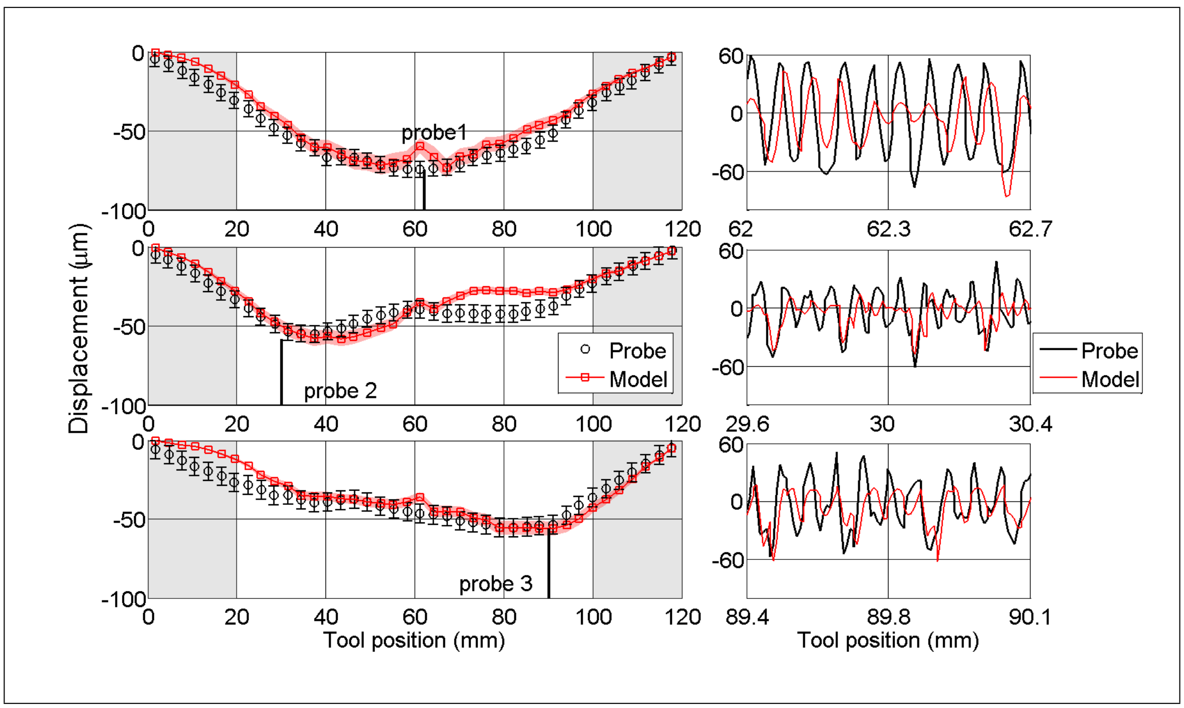

Figure 6.21: Pocket without supports; the results for the displacements of test case 2.4 -1.8, at a tool-path depth of 15.0 mm

Similar agreement in the response can be seen for the same test case at a tool-path depth of 21 mm (refer to Fig. 6.22). The errors between the envelops of the measured and the calculated responses are 11.4%, 11.8%, and 4.6%, for probes 1, 2 and 3, respectively. Within the measurement errors, some deviations can be seen between the envelops of the measured and the calculated responses due to the non-uniformity of the thicknesses, the rubbing of the tool, and the tool wear. For the time responses, excellent agreement in terms of frequency of the free vibration oscillations is seen at probe 1. Some deviations between the measured and the calculated time responses can be seen at probes 2 and 3. This is mainly attributed to the errors in the compensated forces. The rotational speed of the tool in this test case was relatively higher (12,300 rpm) than previous ones. Since a 2-flute tool was used, the force frequency was double that of the spindle speed. Although the methodology for the compensation of the forces was shown to produce good results in all the previous cases, for high frequency force signals, it was hard to match all the peaks of the forces, especially at the tooth-passing frequency. Other results at different tool-path depths were evaluated for this case, and similar agreement was found.

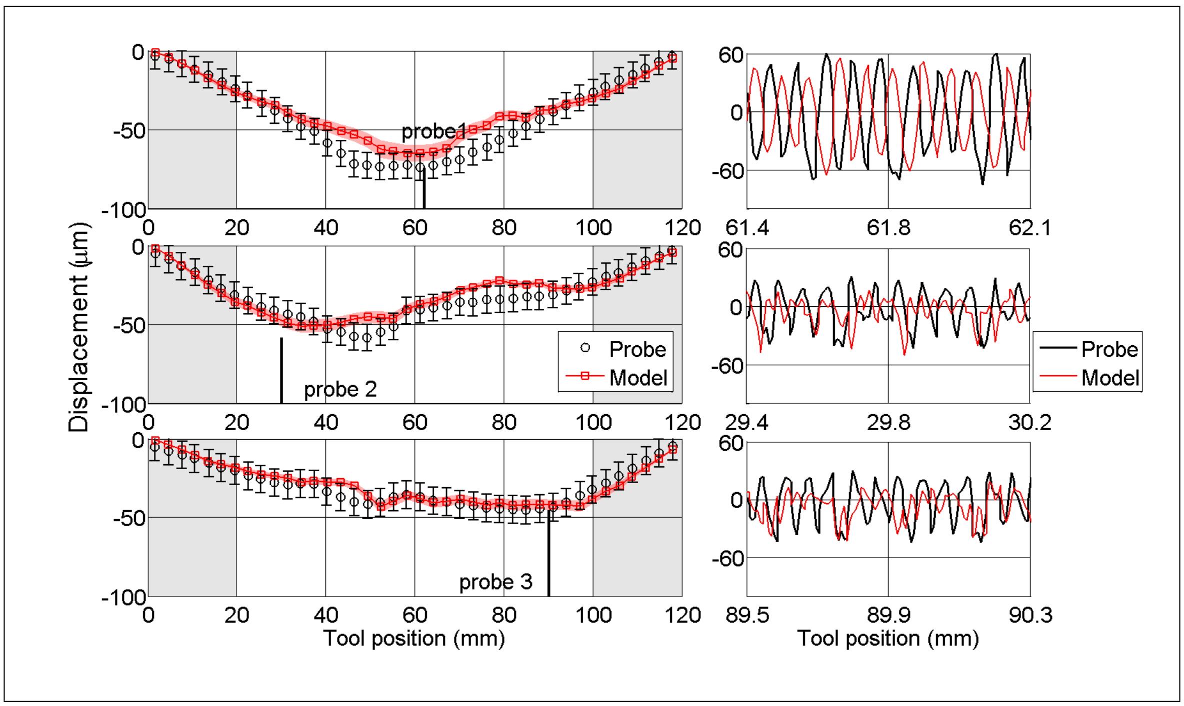

Figure 6.22: Pocket without supports; the results for the displacements of test case 2.4 -1.8, at a tool-path depth of 21.0 mm

It should be noted that for all test cases, the relative measurement errors for the machining at a tool-path depth larger than 25 mm were high due to the low amplitudes of the vibration of the side, and thus the evaluation of the results were limited to the range up to this depth. During the machining of the final thickness of side 1 (test case 1.8-1.3), high chatter occurred, therefore the results for this case will be presented in section 6.5.2.

Test Cases for Machining the Pocket with Supports

For this set of results, the same types of plots were used to compare the responses from the MSP model and the measurements. Only two probes were used in the measurement due to space limitation inside the pocket. As previously described, there was one support on each side of the pocket, except side 1. All the machining tests were performed on side 3. The stiffness of the supports were determined based on tap tests as mentioned in section 6.2.3. For all the test cases, a damping factor of 0.1 was determined for the forced vibration intervals through the calibration procedure described earlier. A damping factor of 0.02 was estimated for the free vibration intervals.

The results for test case 2.1-1.5 will be presented first since relatively large amplitudes of vibration were achieved, with a stable cutting process leading to the lowest errors in the measurements. The results for a tool-path depth of 11.5 mm are shown in Fig 6.23. The location of the support is indicated by the dashed line at a tool position of 60 mm. Similar to the previous set of results, it was expected that some deviations could exist near the corners of the pocket due to the assumptions embed in the model in relation to the boundary conditions. In addition, some deviations were expected at the support location. This is a result of the simplifying assumptions in the modelling of the support. These deviations were expected at the portions of the envelop away from the probe location, where the amplitudes of measured vibrations were relatively small (tool position 0 to 55 mm for probe 1 and 65 mm to 120 mm for probe 2), which is indicated by the shaded areas. For this tool-path depth, the agreement was still very good in these regions. The errors between the envelops of the measured and the calculated responses at probes 1 and 2 were found to be less than 1.5% and 1%, respectively. In the time response graphs, it can be seen that the predictions of the model follow faithfully the measurements. The frequencies of the free oscillations of the measured and the calculated time responses were found to be 2500 Hz and 2340 Hz, respectively, with an error less than 6.5%.

The results for the tool-path depth of 15.5 mm is shown in Fig. 6.24. The errors between the envelops of the responses at probes 1 and 2 were found to be less than 5.5% and 1.5%,

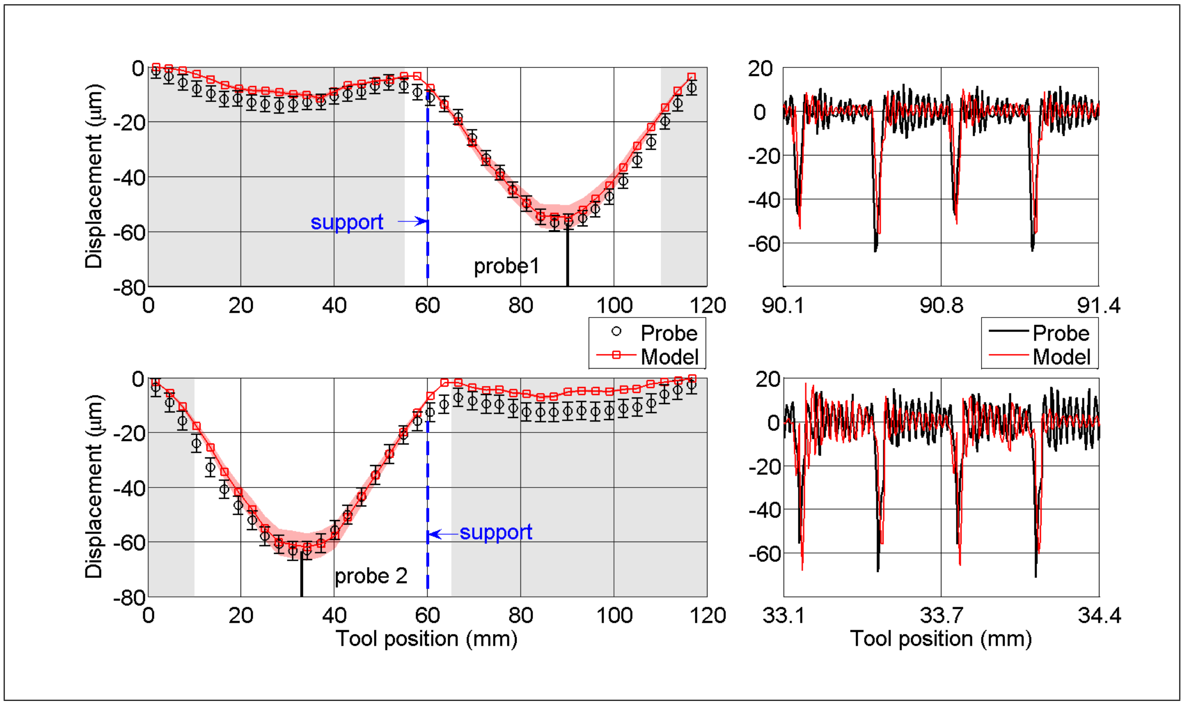

Figure 6.23: Pocket with supports; the results for the displacements of test case 2.1 -1.5, at a tool-path depth of 11.5 mm

respectively. As expected, minor deviations are seen in the shaded regions (tool position 0 - 50 mm) for probe 1 and (tool position 65 mm -120 mm) for probe 2. The frequencies of the free vibration oscillation of the measured and the calculated time responses are in close agreement. For probe 1, the amplitudes of the free vibration oscillations from the model predictions are smaller than those from the measurements. This is mainly attributed to the estimated value of the damping. Other tool-path depths were evaluated, and similar agreement was achieved.

For test case 3.0-2.1, the results for the 9.0 mm tool-path depth are shown in Fig. 6.25. The errors between the envelops of the measured and the calculated responses were found to be 3.0% and 13.0%, respectively for probes 1 and 2. The errors in measurement are slightly higher due to the higher forces, which resulted in larger amplitudes of vibration of the probe holder, as compared to the previous case. As expected, some deviations exist at tool position 0 to 50 mm for probe 1, which is due to the simplifying assumption for the support modelling and the boundary conditions near the pocket corner.

The results for the same test case at a tool-path depth of 18 mm are shown in Fig. 6.26.

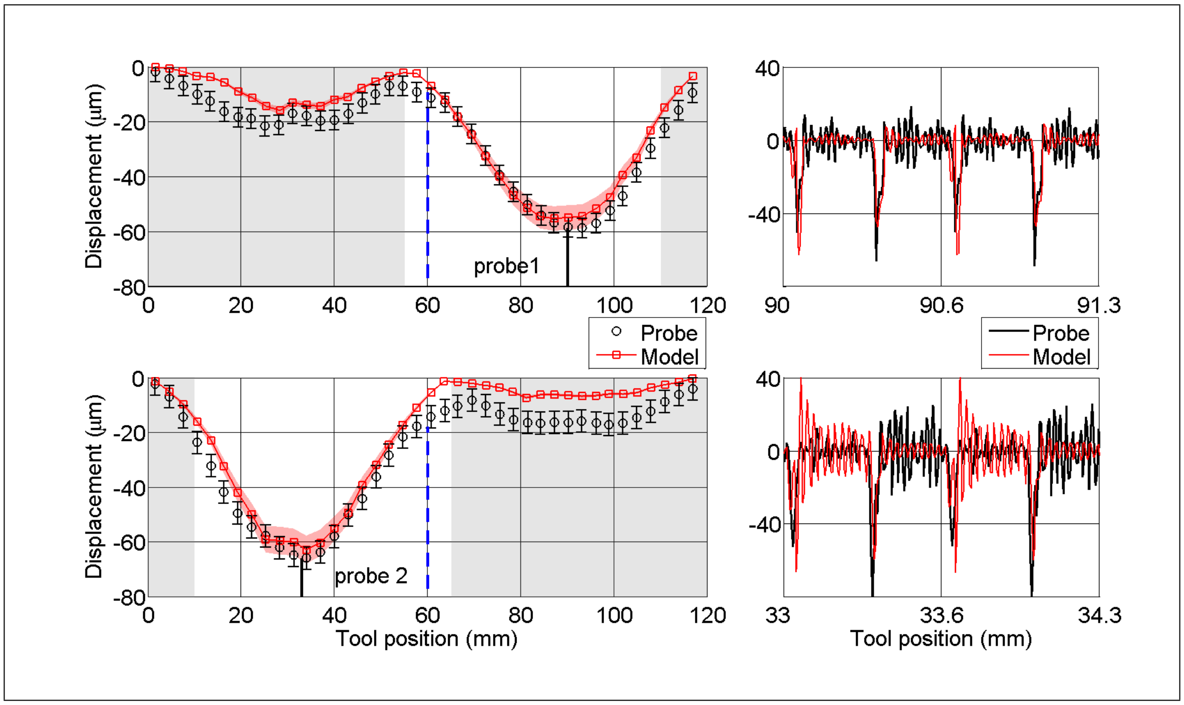

Figure 6.24: Pocket with supports; the results for the displacements of test case 2.1 -1.5, at a tool-path depth of 15.5 mm

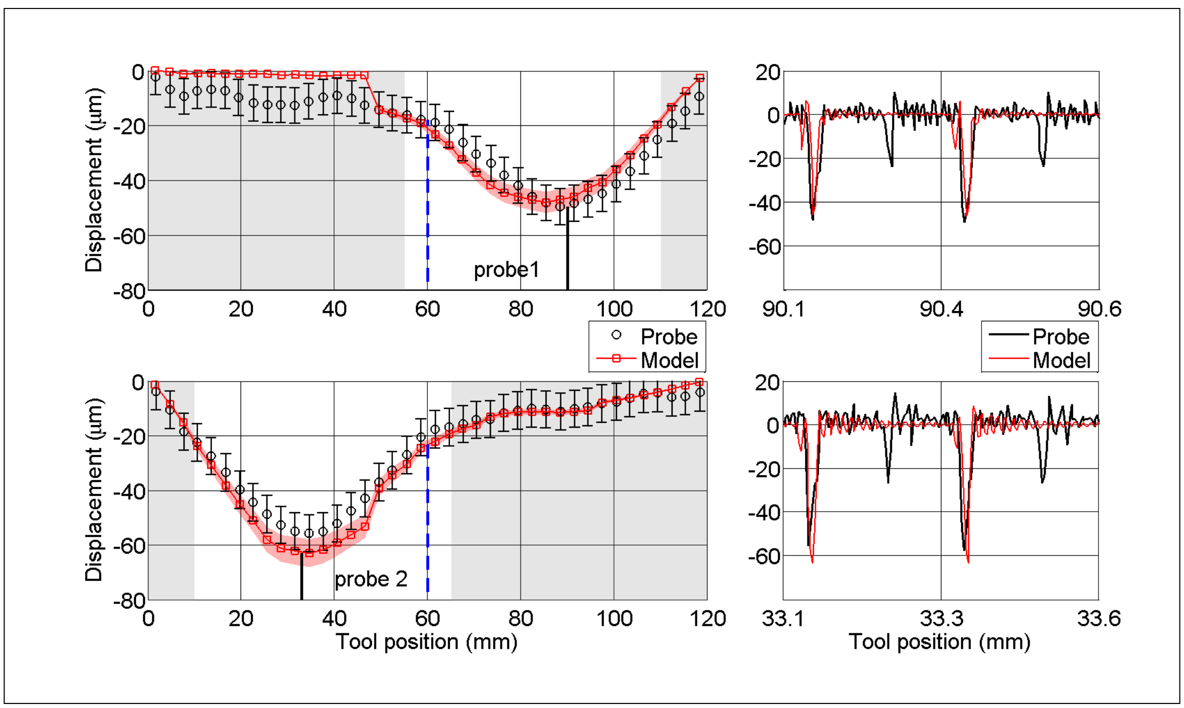

Figure 6.25: Pocket with supports; the results for the displacements of test case 3.0 -2.1, at a tool-path depth of 9.0 mm

The errors between the envelops of the measured and the calculated responses were found to be 3.4% and 4.0%, at probes 1 and 2, respectively. The amplitude of the calculated displacement is very low at tool position 0 to 50 mm for probe 1 and 70 mm to 120 mm for probe 2. This is again due the simplifying assumptions for the support and the boundary conditions of the MSP model. The errors in the frequencies of the free vibration response of the measured and the calculated time responses were found to be less than 3.0% and 1.0%, respectively for the tool-path depths 9.0 mm and 18.0 mm. These negligible errors in frequency show that the model can capture accurately the dynamic characteristics of the system. Through the analysis of the measured time responses in Fig. 6.25 and Fig. 6.26, it can be seen that for two consecutive peaks, representing the engagement of the two flutes of the cutting tool, one was smaller than the other. This could be a result of a tool-run out. Due to the dynamics of the measurement systems, these small peaks were masked (filtered) and were very difficult to retrieve in the compensated force signal. This explains why in the calculated time response these small peaks were missing.

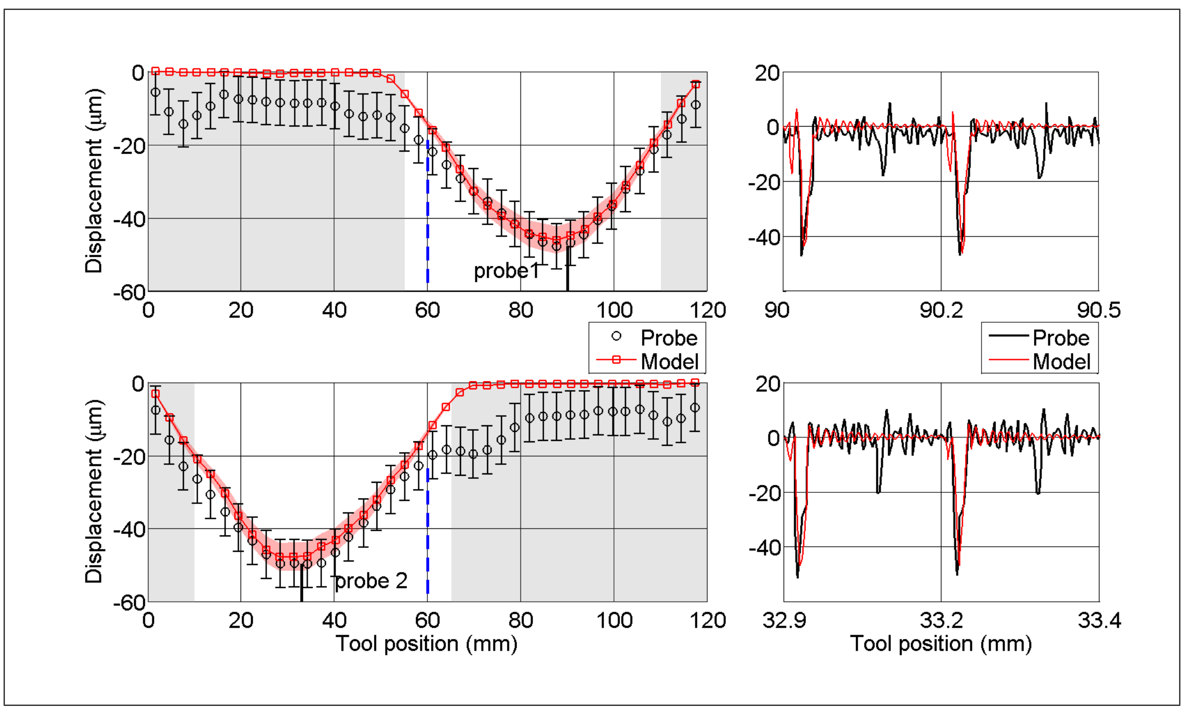

Figure 6.26: Pocket with supports; the results for the displacements of test case 3.0 -2.1, at a tool-path depth of 18.0 mm

For test case 4.0-3.0, the wall thickness was relatively thick. As seen in Fig 6.27, the amplitudes of the vibrations at a tool-path depth of 8 mm were less than 40 μm. The errors between the envelops of the measured and the calculated responses have been estimated to be 3.5% and 9.0%, respectively for probes 1 and 2. At tool position equal to 60 mm, one can notice a sudden change in the envelop of the measured response, which is a result of a sudden change in the force. At this tool position, the tool path intersects with the support location leading to the tool cutting the support. Due to the difference between the material of the support and the workpiece, an abrupt change in the cutting forces occurs.

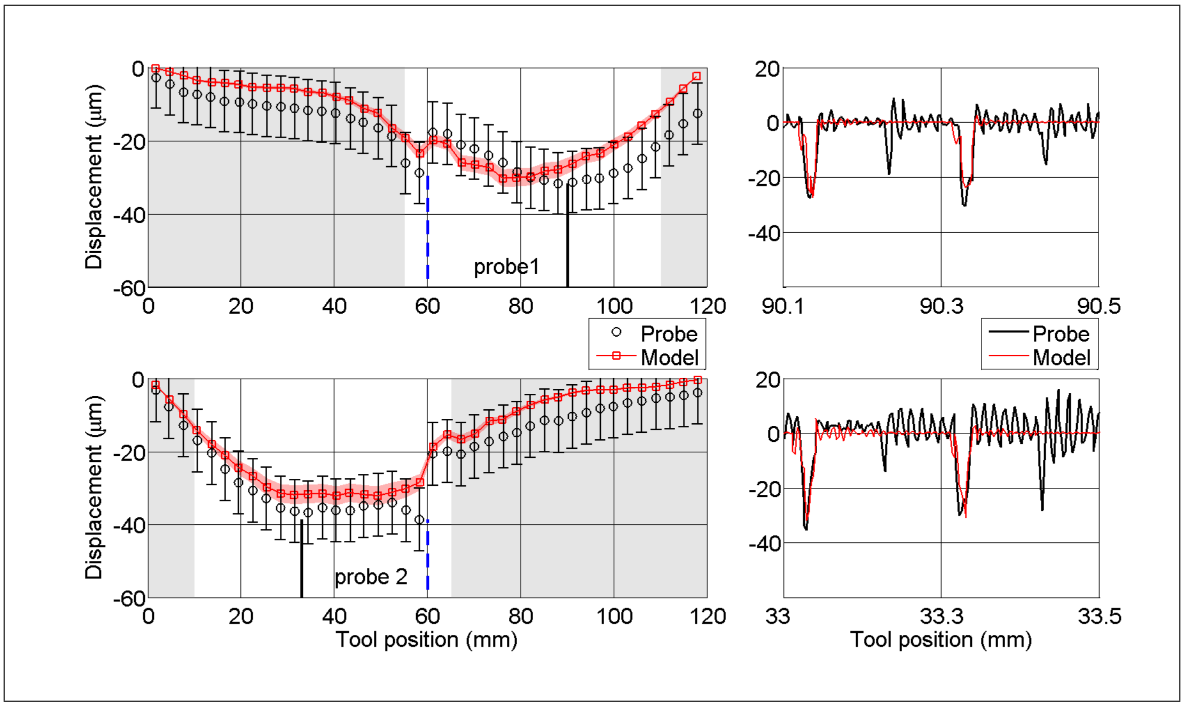

Figure 6.27: Pocket with supports; the results for the displacements of test case 4.0 -3.0, at a tool-path depth of 8.0 mm

The results for the machining at 12 mm tool-path depth are shown in Fig 6.28. The errors between the envelops of the measured and the calculated responses are less than 5.0%. There were some deviations in the envelops at tool positions 90 mm to 120 mm. For both tool-path depths, the errors of the frequencies of the free vibration oscillations of the measured and the calculated time responses were found to be less than 1%. It was very difficult to compare the difference in the amplitudes of the free vibration intervals since these amplitudes for the measured results were less than 10 μm. These are compared to the probe measurement errors of ≈ ±5 μm. It is important to note that for this large thickness, the model is still providing accurate results in terms of the maximum amplitudes of displacement, the frequencies of the time response and the general nature of the dynamic behaviour.

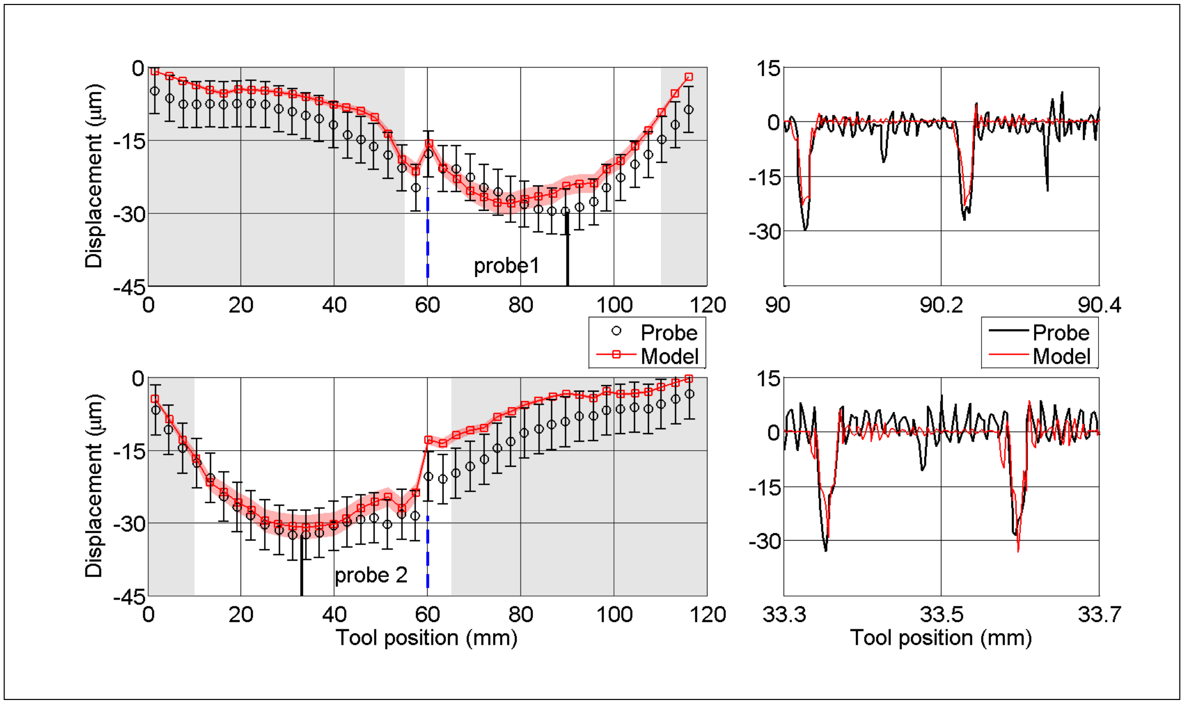

Figure 6.28: Pocket with supports; the results for the displacements of test case 4.0 -3.0, at a tool-path depth of 12.0 mm

6.5.2 Validation Test Results under Unstable Cutting Conditions

To demonstrate the applicability of the model in the cases where machining instability is encountered, some results are presented for the cases with high chatter or tool wear. In these cases, the amplitudes of the vibrations were relatively high. It has to be noted that from the fixture designer point of view, the objective is not to predict accurately the vibrations during chatter, but rather to know roughly the extent by which the vibrations exceed a predefined tolerance limit. Based on this, it will be shown that the model was still able to predict the time response of the side of the pocket, without and with supports, with relatively good accuracy. The test cases with machining instability that will be presented are listed in Table 6.6.

For test case 1.8-1.3, chatter occurred during the machining at most of the tool-path

Table 6.6: Summary of the test cases with unstable cutting conditions

Unstable machining conditions (*medium to high chatter or high tool wear*)						
Set	Case	Tool-path depth d_p (mm)	Spindle speed (rpm)	Feed rate (mm/min)	Chatter	Tool wear
1- No supports	1.8-1.3	8.0	10000	2000	high	high
2- No supports	3.2-2.4	2.0	9000	4500	high	low
3- With supports	1.5-1.0	14.0	6000	3600	medium	high

depths. Based on the tap tests that were performed before machining in this test case, the following 3 frequencies were determined 1035 Hz, 1703 Hz, and 1855 Hz. The error in the frequencies between the model and the measurements were found to be 2.2%, 0.7% and 5.7%, respectively. Figure 6.29 shows the results for test case 1.8-1.3 at a tool-path depth of 8.0 mm. During machining, high chatter and high tool wear were observed. A relatively good matching was, however, achieved between the maximum of the envelops of the measured and the calculated responses with errors of 5.5% and 12%, and 4% at probes 1, 2 and 3, respectively.

It should be noted, that the errors in the compensation of the forces should have been higher. As shown in the figure, there are some deviations in the shapes of the envelops. This can be explained as follows: At the time intervals where some instability occurs, the measured force is distorted, and as a consequence, it is very hard to compensate for the dynamics of the measurement system. By analyzing the time responses of the measured and the calculated results, one can see excellent matching in terms of the amplitude and the frequency of the vibration.

Figure 6.30 shows the results for test case 3.2-2.4 at the first tool-path depth. For this case, only the chatter was observed, while the tool wear was relatively low. The errors between the envelops of the measured and the predicted responses were found to be less than 4%, 6% and 4%, respectively at probes 1, 2 and 3. Some deviations between the envelops of the measured and the calculated responses can be seen near the edges of the side (tool position 10 mm to 20 mm and 90 mm to 100 mm). Similar to the previous test case, an excellent matching was found between the calculated and the measured time responses.

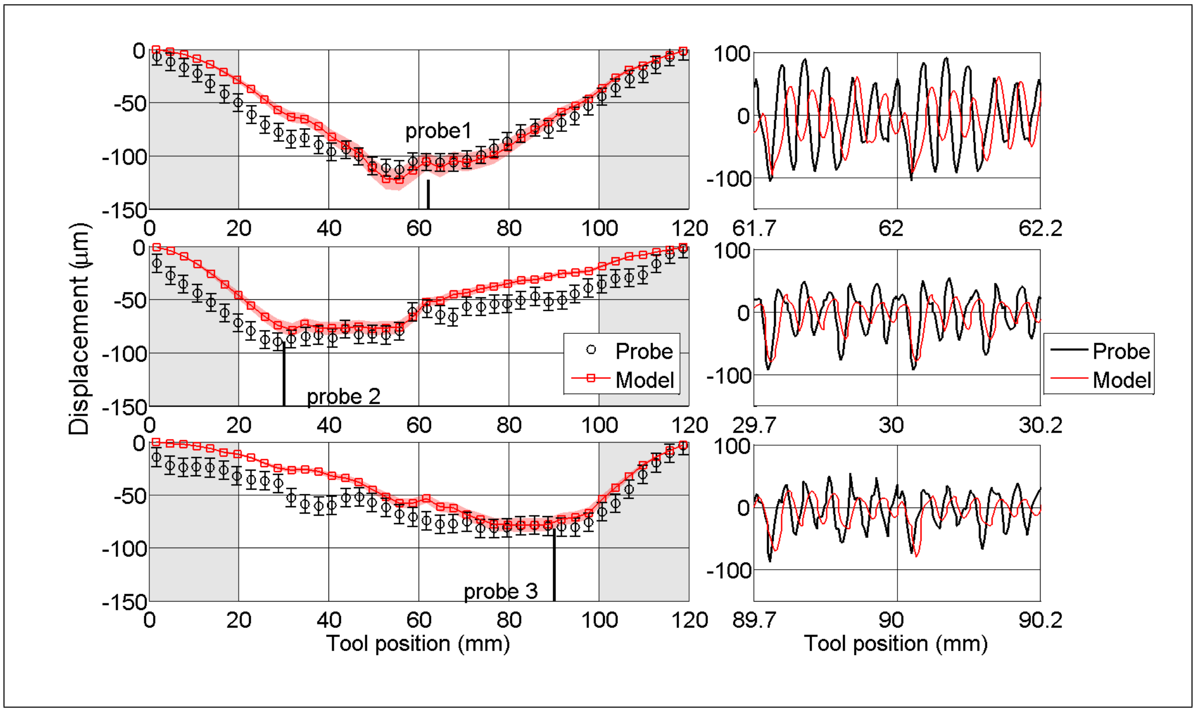

Figure 6.29: Pocket without supports; the results for the displacements of test case 1.8 -1.3, at a tool-path depth of 8.0 mm

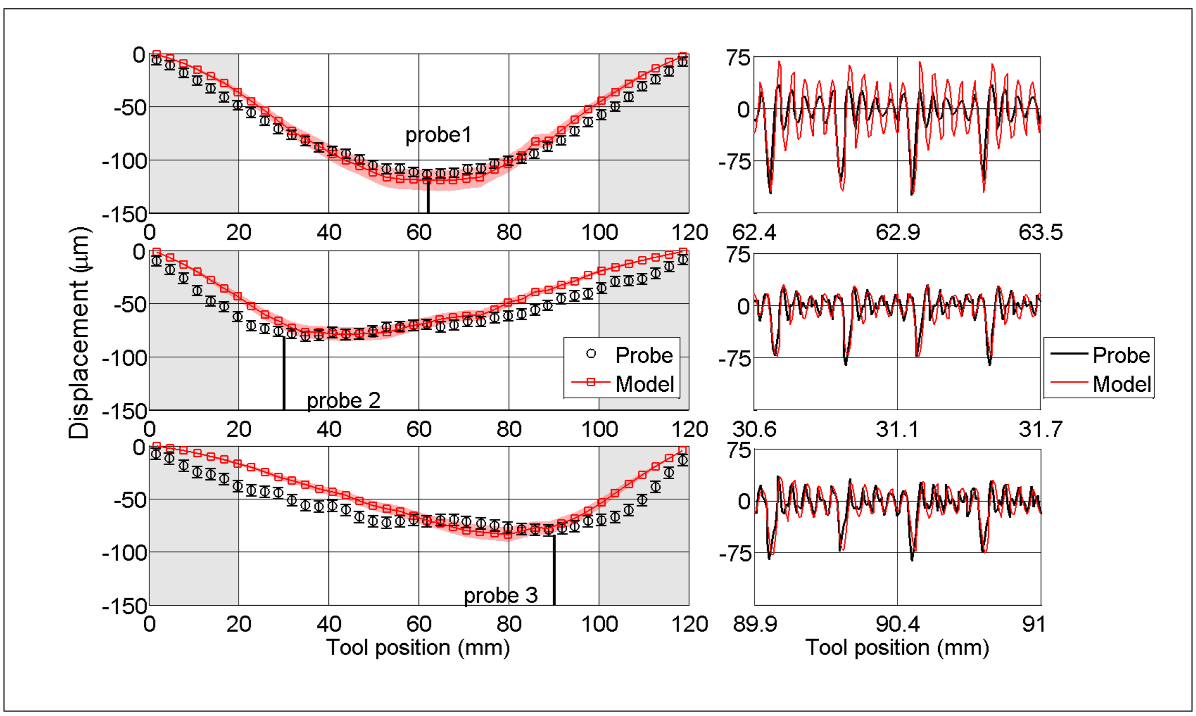

Figure 6.30: Pocket without supports; the results for the displacements of test case 3.2 -2.4, at a tool-path depth of 2.0 mm

For test case 1.5-1.0, with supports, the results are shown in Fig. 6.31 for a tool-path depth of 14 mm. Due to the very small thickness of the side of the pocket, very high chatter was experienced during the machining, which resulted in a maximum amplitude of vibration of 217 μm. The errors between the envelops of the measured and the calculated responses were found to be 9.0% and 5.7% at probes 1 and 2, respectively. The error between the frequency of the free vibration of the measured and the calculated responses were found to be less than 1%. It can be seen that although the matching between the two envelops is not as good as the cases with stable conditions, almost all of the dynamic characteristics of the time responses (frequency and amplitudes) are in very close agreement.

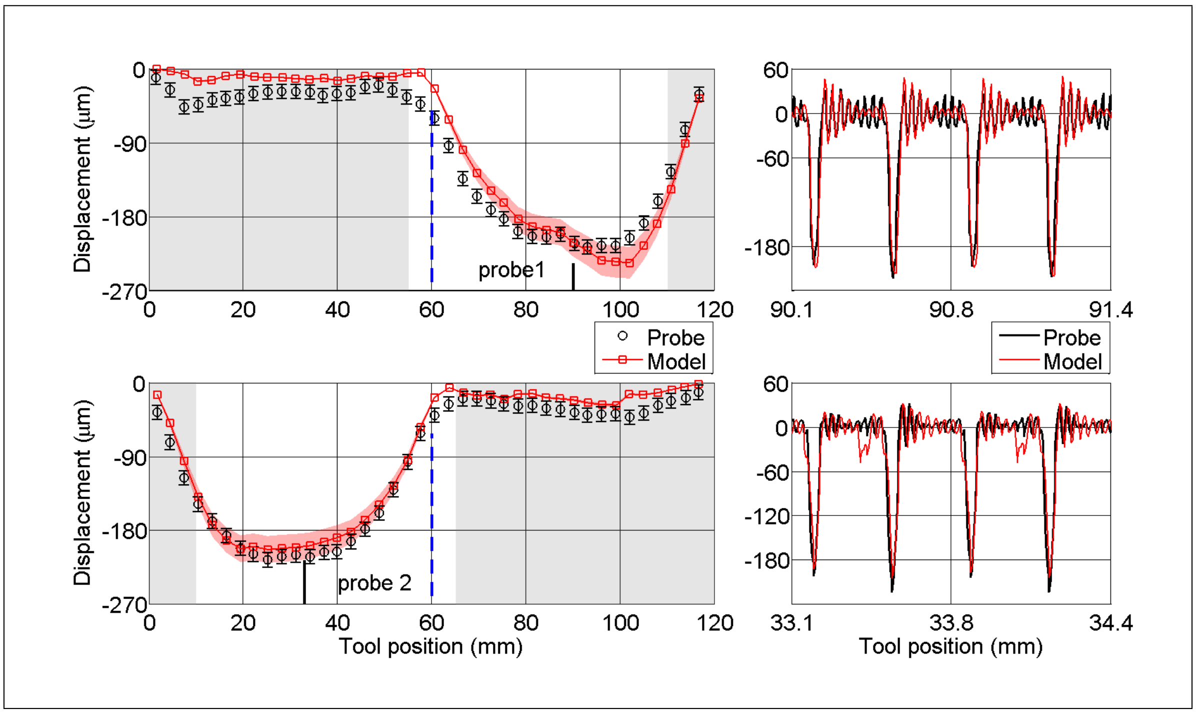

Figure 6.31: Pocket with supports; the results for the displacements of test case 1.5 -1.0, at a tool-path depth of 14.0 mm

6.6 Summary of the Results

In this chapter, experimental validation results were presented for machining a rectangular pocket, with and without supports. The results covered different side thicknesses, different tool-path depths, and different cutting parameters. The agreement between the calculated and the measured responses were evaluated based on the natural frequencies of the pocket before the machining of each side (for the cases without support), the maximum amplitude of the vibration during machining and the frequency of the free vibration of the time responses. It was shown that under stable cutting conditions (low chatter and tool wear), the model predictions were in excellent agreement with the measured responses taking into account the measurement errors. The predictions error for most of the cases were less than 10%. At some instances, deviations occurred between the measurements and the predictions of the model due to the differences between the model assumptions and the experimental conditions including the uniformity of the side thickness, the modelling of the support contact, the value of the damping ratio, and the continuity conditions at the edges of the side of the pocket. Although the model was not intended for cases with high chatter and tool wear, it still provided reasonably good agreement with the measurements with errors less than 10%. The presented results demonstrate the validity of the model in predicting the dynamic behaviour of thin-walled pockets during real machining applications, while accurately capturing the effect of the fixture supports on the dynamics of the pocket sides. In addition, a new methodology was developed to account for the dynamics of the force measurement system while taking into account the dynamics of the workpiece. This methodology was validated for different cases and the errors between the input force and the compensated force were found to be $\approx 8.0\%$.

Chapter 7

Conclusions and Recommendations for Future Research Work

7.1 Conclusions

This research is focused on the modelling of the dynamics of thin-walled aerospace structures during milling while taking into account the effects of the fixture layout. The following conclusions can be drawn from the performed analyses and the obtained results:

1. According to the review of the current practices in the aerospace industry, it was found that the fixture design relies mainly on the designer's experience and general conservative guidelines. For the fixture design of flexible workpieces, few models take into account the dynamics of thin-walled structures. These models ignore the continuously varying dynamic characteristics of the workpiece due to the material removal action. In addition, they are based on computationally demanding formulations. It was concluded that a computationally efficient model was required to represent the effect of the fixture layout on the dynamics of thin-walled aerospace structures during milling while taking into account the continuous change of thickness of the workpiece.

2. An analysis of typical aerospace structural components was performed and a generalized unit-element with the shape of an asymmetric pocket was identified to represent the dynamics of these components. Two different models were proposed in this research for the prediction of the dynamics of the identified unit-element. The proposed models were developed using Rayleigh's energy method and the Rayleigh-Ritz method.

3. The first model, which was referred to as Generalized Single-Span Plate (GSSP) model, was based on discretizing the pocket to plates with torsional and translational springs at the boundaries. The role of the springs was to take into account the effect of the adjacent walls and adjacent pockets. The stiffness values of the springs were determined through an off-line calibration based on FE models using Genetic Algorithms as an optimization technique. The approximate mode shapes were based on beams with torsional and translational springs at the boundaries. Numerical validations through FE models of typical aerospace structural components and experimental validations through impact tests were performed. The prediction errors of the GSSP model were found to be less than 5% when compared to FE models and experimental measurements. The computational time is reduced by one to two orders of magnitude.

4. The second model, which was referred to as the Multi-Span Plate Model (MSP), was based on representing the dynamics of a generalized 3D pocket by a 2D multi-span plate. A new set of trial functions based on multi-span beam and clamped-free beam models were used. These trial functions allowed an accurate approximation of the response of the multi-span plate with few mode shapes. Numerical validations of the MSP model were performed using different FE models of thin-walled pockets and various frequencies of loading. It was shown that the prediction error of the model is less than 6%.

5. Four general scenarios were identified for the change of thickness during the milling of thin-walled pockets. A change of thickness (CoT) formulation was developed and implemented in the MSP model to represent these cases. Multi-span beam models were used for the trial functions in both the x- and y-directions. An extensive FE validation of the CoT formulation was performed for different aspect ratios of rectangular and non-rectangular pockets and various change of thickness schemes. It was shown that the proposed model can accurately capture the dynamic effect of the change of thickness with prediction errors of less than 9%.

6. Two different formulations were developed to represent the effect of the fixture layout for rigid and flexible supports. The first, which was referred to as Perfectly Rigid

Support (PRS) formulation, simulates the effect of a rigid support using holonomic constraints. The second formulation, which was referred to as Finite Stiffness Support (FSS) formulation, uses springs with finite stiffness to represent flexible supports. The proposed formulations were validated by implementing them in the MSP model, with and without the CoT formulation. It was found that an excellent agreement between the predictions of the proposed models and the FE models was achieved with errors less than 10% and at least one order of magnitude reduction in the computation time.

7. The MSP model and the CoT and the FSS formulations were validated experimentally by conducting machining tests of a thin-walled pocket, with and without supports. It was shown that the developed models are able to predict the changes in the dynamics of the workpiece during milling for a wide range of thicknesses varying from 4 mm to 1 mm, with predictions errors of 10 -13%. It was also found that the models can still predict accurately the responses for cases with machining instability due to high chatter and tool wear.

8. A new methodology was proposed and validated in order to account for the errors due to the dynamics of the force measurement system. It was shown that the proposed methodology reduced the measurement errors from more than 100% to an average error of 8%.

7.2 Contributions to Knowledge

1. New conceptual developments have been made by representing complex thin-walled aerospace structures using a generalized unit-element with the shape of an asymmetric pocket. In addition, new concepts were introduced to represent the 3D asymmetric pocket with a 2D plate. These new concepts made it possible to develop models and formulations for the prediction of the dynamic response of thin-walled aerospace structures while taking into account the effect of the fixture layout and the continuous change of thickness during milling.

2. A new model was developed to represent the dynamics of complex thin-walled aerospace structures through an off-line calibration of a plate with torsional and translational springs. This simplified semi-analytical model offers a reduction in the computation time by at least one order of magnitude compared to available FE models and a prediction error of less than 5%.

3. A new model was developed for the representation of the dynamics of a 3D pocket using a 2D analytical multi-span plate model. This model can predict the dynamic responses of various types of aerospace structures with at least one order of magnitude reduction in computation time compared to FE models and prediction errors less than 6%. Although not generalized as the previous model, this model eliminates the need for calibration.

4. A new formulation was developed to simulate possible cases for the change of thickness during milling of thin-walled pockets. The prediction errors were found to be less than 9% when compared to FE models. To date, no analytical model is available to represent the continuous change of thickness of thin-walled structures.

5. Two different formulations were proposed for the modelling of the effect of the fixture layout. The first formulation is based on the use of holonomic constraints and the second is based on springs with finite stiffness.

6. By integrating the developed dynamic models and the proposed formulations for the effect of the fixture supports, a generalized analytical model for the analysis of the effect of the fixture layout on the dynamics of thin-walled structures was developed while taking into account the continuous change of thickness of the workpiece and the effect of rigid and deformable fixture supports. These integrated models meet the conflicting requirements of prediction accuracy and computational efficiency as set by the aerospace industry.

7. A novel methodology was developed to account for the dynamics of the measurement system, as well as the dynamics of the workpiece.

Impact on industry: To date, no fixture design software exists that includes the effect of the vibrations of thin-walled workpieces during machining. The developed models will bridge this gap and provide an interactive prediction capability to suit the industrial applications. This will substantially improve the productivity and lower the machining cost. Based on these models, optimization of the fixture layout could be performed within reasonable time frames, thus decreasing the design and development time.

7.3 Recommendations for Future Research Work

The present study provides a starting point for the analysis of the effect of the fixture layout on the dynamics of thin-walled structures during milling while taking into account the continuous change of thickness of the workpiece. The following topics could be pursed for future research work:

1. Integration of the developed dynamic models with 5-axis mechanistic force models in order to determine the effect of the cutting parameters such as the feed-rate, the radial and axial depths of cut, and the spindle speed on the cutting forces and the integrity of the machined surface.

2. Extension of the developed models to deal with other non-structural aerospace thin-walled components such as turbine blades.

3. Deriving expressions for the stiffness of the springs in the GSSP model, as function of the dimensions of the adjacent sides and pockets. This will eliminate the need for calibration through FE models.

4. Modelling of the process damping of low immersion milling and its effect on the vibration of thin-walled structures.

5. Developing an expert system for the design of fixtures while taking into account the static and the dynamic deflections of thin-walled workpieces. This should also include the implementation of different optimization schemes.

Bibliography

[1] G. S. A. Shawki and M. M. Abdel-Aal, "Rigidity considerations in fixture design - contact rigidity at locating elements," *International Journal of Machine Tool Design and Research*, vol. 6, no. 1, pp. 31–43, 1966.

[2] B. Li and S. N. Melkote, "Improved workpiece location accuracy through fixture layout optimization," *International Journal of Machine Tools and Manufacture*, vol. 39, no. 6, pp. 871–883, 1999.

[3] B. Li and S. N. Melkote, "Fixture clamping force optimisation and its impact on workpiece location accuracy," *International Journal of Advanced Manufacturing Technology*, vol. 17, no. 2, pp. 104–113, 2001.

[4] W. Michael Yu and L. Tong, "A full contact model for fixture kinematic analysis," vol. 2 of *Proceedings IEEE/RSJ International Conference on Intelligent Robots and Systems*, pp. 1602–1607, IEEE, 2002.

[5] U. D. Batyrov, "Factors affecting setting errors of pallet fixtures," *Soviet Engineering Research*, vol. 4, no. 4, pp. 67–69, 1984.

[6] B. M. Bazrov and A. I. Sorokin, "Effect of clamping sequence on workpiece mounting accuracy," *Soviet Engineering Research*, vol. 2, no. 10, pp. 92–95, 1982.

[7] R. O. Mittal, P. H. Cohen, and B. J. Gilmore, "Dynamic modeling of the fixture-workpiece system," *Robotics and Computer-Integrated Manufacturing*, vol. 8, no. 4, pp. 201–217, 1991.

[8] M. Estrems, H. T. Sanchez, and F. Faura, "Influence of fixtures on dimensional accuracy in machining processes," *International Journal of Advanced Manufacturing Technology*, vol. 21, no. 5, pp. 384–390, 2003.

[9] R. A. Marin and P. M. Ferreira, "Analysis of the influence of fixture locator errors on the compliance of work part features to geometric tolerance specifications," *ASME Journal of Manufacturing Science and Engineering*, vol. 125, no. 3, pp. 609–616, 2003.

[10] G. H. Qin, W. H. Zhang, and M. Wan, "A mathematical approach to analysis and optimal design of a fixture locating scheme," *International Journal of Advanced Manufacturing Technology*, vol. 29, no. 3-4, pp. 349–359, 2006.

[11] G. S. A. Shawki and M. M. Abdel-Aal, "Rigidity considerations in fixture design - contact rigidity at locating elements," *International Journal of Machine Tool Design and Research*, vol. 6, no. 1, pp. 31–43, 1966.

[12] A. de Sam Lazaro and D. A. King, "Automated design of machining fixtures: tolerance and sequential operations," *Intelligent Systems Engineering*, vol. 1, no. 2, pp. 172–184, 1992.

[13] E. C. DeMeter, "Restraint analysis of fixtures which rely on surface contact," *ASME Journal of Engineering for Industry*, vol. 116, no. 2, pp. 207–215, 1994.

[14] Q. A. Sayeed and E. C. De Meter, "Machining fixture design and analysis software," *International Journal of Production Research*, vol. 32, no. 7, pp. 1655–1674, 1994.

[15] B. Li, S. N. Melkote, and S. Y. Liang, "Analysis of reactions and minimum clamping force for machining fixtures with large contact areas," *International Journal of Advanced Manufacturing Technology*, vol. 16, no. 2, pp. 79–84, 2000.

[16] M. Y. Wang and D. M. Pelinescu, "Contact force prediction and force closure analysis of a fixture rigid workpiece with friction," *ASME Journal of Manufacturing Science and Engineering*, vol. 125, no. 2, pp. 325–332, 2003.

[17] S. Satyanarayana and S. N. Melkote, "Finite element modeling of fixture-workpiece contacts: single contact modeling and experimental verification," *International Journal of Machine Tools and Manufacture*, vol. 44, no. 9, pp. 903–913, 2004.

[18] S. N. Melkote and S. P. Siebenaler, "Prediction of workpiece deformation in a fixture system using the finite element method," *International Journal of Machine Tools and Manufacture*, vol. 46, no. 1, pp. 51–58, 2006.

[19] A. Raghu and S. N. Melkote, "Prediction of workpiece location error due to fixture geometric errors and fixture-workpiece compliance," vol. 14 of *ASME Manufacturing Engineering Division, MED*, pp. 273–280, ASME, New York, 2003.

[20] A. Raghu and S. N. Melkote, "Analysis of the effects of fixture clamping sequence on part location errors," *International Journal of Machine Tools and Manufacture*, vol. 44, no. 4, pp. 373–382, 2004.

[21] G. H. Qin, W. H. Zhang, and M. Wan, "Analysis and optimal design of fixture clamping sequence," *ASME Journal of Manufacturing Science and Engineering*, vol. 128, no. 2, pp. 482–493, 2006.

[22] G. Qin, W. Zhang, Z. Wu, and M. Wan, "Systematic modeling of workpiece-fixture geometric default and compliance for the prediction of workpiece machining error," *ASME Journal of Manufacturing Science and Engineering*, vol. 129, no. 4, pp. 789–801, 2007.

[23] E. C. De Meter, W. Xie, S. Choudhuri, S. Vallapuzha, and M. W. Trethewey, "A model to predict minimum required clamp pre-loads in light of fixture-workpiece compliance," *International Journal of Machine Tools and Manufacture*, vol. 41, no. 7, pp. 1031–1054, 2001.

[24] E. C. De Meter, S. Choudhuri, and S. Vallapuzha, "An evaluation of a linear clamp pre-load model with respect to milling operations," vol. 1 of *2001 IEEE/ASME International Conference on Advanced Intelligent Mechatronics. Proceedings*, pp. 308–313, IEEE, 2001.

[25] H. T. Sanchez, M. Estrems, and F. Faura, "Fixturing analysis methods for calculating the contact load distribution and the valid clamping regions in machining processes," *International Journal of Advanced Manufacturing Technology*, vol. 29, no. 5-6, pp. 426–435, 2006.

[26] H. T. Sanchez, M. Estrems, and F. Faura, "Analysis and compensation of positional and deformation errors using integrated fixturing analysis in flexible machining parts," *International Journal of Advanced Manufacturing Technology*, vol. 29, no. 3-4, pp. 239–252, 2006.

[27] L. Shaogang, L. Zheng, Z. H. Zhang, and D. H. Wen, "Optimal fixture design in peripheral milling of thin-walled workpiece," *International Journal of Advanced Manufacturing Technology*, vol. 28, no. 7-8, pp. 653–658, 2006.

[28] S. Ratchev, K. Phuah, and S. Liu, "FEA-based methodology for the prediction of part-fixture behaviour and its applications," *Journal of Materials Processing Technology*, vol. 191, no. 1-3, pp. 260–264, 2007.

[29] Y. J. G. Liao and S. J. Hu, "Flexible multibody dynamics based fixture-workpiece analysis model for fixturing stability," *International Journal of Machine Tools and Manufacture*, vol. 40, no. 3, pp. 343–362, 2000.

[30] Y. G. Liao and S. J. Hu, "An integrated model of a fixture-workpiece system for surface quality prediction," *International Journal of Advanced Manufacturing Technology*, vol. 17, no. 11, pp. 810–819, 2001.

[31] F. Gu, S. N. Melkote, S. G. Kapoor, and R. E. DeVor, "Model for the prediction of surface flatness in face milling," *ASME Journal of Manufacturing Science and Engineering*, vol. 119 (a), no. 4, pp. 476–484, 1997.

[32] G. Liao, "Predictive model for workpiece surface error due to machining processes," *Society of Manufacturing Engineers*, no. MR99-247, pp. 1–12, 1999.

[33] Q. A. Sayeed and E. C. de Meter, "Mixed-integer programming model for fixture layout optimization," *ASME Journal of Manufacturing Science and Engineering*, vol. 121, no. 4, pp. 701–708, 1999.

[34] Q. A. Sayeed and E. C. De Meter, "Compliance based MIP model and heuristic for support layout optimization," *International Journal of Production Research*, vol. 37, no. 6, pp. 1283–1301, 1999.

[35] L. Masset and J. F. Debongnie, "Machining processes simulation: specific finite element aspects," *Journal of Computational and Applied Mathematics*, vol. 168, no. 1-2, pp. 309–320, 2004.

[36] N. Kaya and F. Ozturk, "The application of chip removal and frictional contact analysis for workpiece-fixture layout verification," *International Journal of Advanced Manufacturing Technology*, vol. 21, no. 6, pp. 411–419, 2003.

[37] M. J. Hockenberger and E. C. De Meter, "Application of Meta functions to the quasi-static analysis of workpiece displacement within a machining fixture," *ASME Journal of Manufacturing Science and Engineering*, vol. 118, no. 3, pp. 325–331, 1996.

[38] M. Hockenberger and E. De Meter, "A preliminary investigation into the use of Meta functions for the dynamic analysis of workpiece displacement within a machining fixture," *Transactions of NAMRI/SME*, vol. 23, pp. 325–330, 1995.

[39] J. H. Yeh and F. W. Liou, "Contact condition modelling for machining fixture setup processes," *International Journal of Machine Tools and Manufacture*, vol. 39, no. 5, pp. 787–803, 1999.

[40] B. Li and S. N. Melkote, "Optimal fixture design accounting for the effect of workpiece dynamics," *International Journal of Advanced Manufacturing Technology*, vol. 18, no. 10, pp. 701–707, 2001.

[41] M. R. Behzadi and B. Arezoo, "Static and dynamic models for predicting the effects of supports on machining flatness and roughness," *Proceedings of the Institution of*

Mechanical Engineers, Part B (Journal of Engineering Manufacture), vol. 216, no. 5, pp. 735–742, 2002.

[42] B. Fang, R. E. Devor, and S. G. Kapoor, "Influence of friction damping on workpiece-fixture system dynamics and machining stability," *ASME Journal of Manufacturing Science and Engineering*, vol. 124, no. 2, pp. 226–233, 2002.

[43] I. Deiab, *Effect of fixture dynamics on the face milling process.* PhD thesis, McMaster University, 2003.

[44] H. Deng, *Analysis and Synthesis of Fixturing Dynamic Stability in Machining Accounting for Material Removal Effect.* PhD thesis, Georgia Institute of Technology, 2006.

[45] E. C. De Meter, "Fast support layout optimization," *International Journal of Machine Tools and Manufacture*, vol. 38, no. 10-11, pp. 1221–1239, 1998.

[46] M. Daimon, T. Yoshida, N. Kojima, H. Yamamoto, and T. Hoshi, "Study for designing fixtures considering dynamics of thin-walled plate- and box-like workpieces," vol. 34 of *CIRP Annals*, pp. 319–322, Technische Rundschau, Berne, Switz, 1985.

[47] C.-H. Chu, M. W. Trethewey, E. C. De Meter, and C.-Y. Wu, "Modeling and analysis of workpiece static and dynamic structural characteristics for machining operations," vol. 1 of *Proceedings of the International Modal Analysis Conference - IMAC*, pp. 325–331, SEM, Bethel, CT, 1997.

[48] J. K. Rai and P. Xirouchakis, "Finite element method based machining simulation environment for analyzing part errors induced during milling of thin-walled components," *International Journal of Machine Tools and Manufacture*, vol. 48, no. 6, pp. 629–643, 2008.

[49] Y. Kang, Y. Rong, and J. A. Yang, "Geometric and kinetic model based computer-aided fixture design verification," *ASME Journal of Computing and Information Science in Engineering*, vol. 3, no. 3, pp. 187–199, 2003.

[50] Y. Kang, Y. Rong, and J. C. Yang, "Computer-aided fixture design verification, part 2: tolerance analysis," *International Journal of Advanced Manufacturing Technology*, vol. 21, no. 10-11, pp. 836–841, 2003.

[51] R. T. Meyer and F. W. Liou, "Fixture analysis under dynamic machining," *International Journal of Production Research*, vol. 35, no. 5, pp. 1471–1489, 1997.

[52] S. Kashyap and W. R. DeVries, "Finite element analysis and optimization in fixture design," *Structural Optimization*, vol. 18, no. 2-3, pp. 193–201, 1999.

[53] E. Y. T. Tan, A. S. Kumar, J. Y. H. Fuh, and A. Y. C. Nee, "Modeling, analysis, and verification of optimal fixturing design," *IEEE Transactions on Automation Science and Engineering*, vol. 1, no. 2, pp. 121–132, 2004.

[54] K. Kulankara, S. Satyanarayana, and S. N. Melkote, "Iterative fixture layout and clamping force optimization using the Genetic Algorithm," *ASME Journal of Manufacturing Science and Engineering*, vol. 124, no. 1, pp. 119–125, 2002.

[55] R. J. Guyan, "Reduction of stiffness and mass matrices," *American Institute of Aeronautics and Astronautics Journal*, vol. 3, no. 2, p. 380, 1965.

[56] Y. Liao, "A generic algorithm-based fixture locating positions and clamping schemes optimization," in *Proceedings of the Institution of Mechanical Engineers, Part B: Journal of Engineering Manufacture*, vol. 217, pp. 1075–1083, 2003.

[57] S. Vallapuzha, E. C. De Meter, S. Choudhuri, and R. P. Khetan, "An investigation into the use of spatial coordinates for the Genetic Algorithm based solution of the fixture layout optimization problem," *International Journal of Machine Tools and Manufacture*, vol. 42, no. 2, pp. 265–275, 2002.

[58] S. Vallapuzha, E. C. De Meter, S. Choudhuri, and R. P. Khetan, "An investigation of the effectiveness of fixture layout optimization methods," *International Journal of Machine Tools and Manufacture*, vol. 42, no. 2, pp. 251–263, 2002.

[59] G. Prabhaharan, K. P. Padmanaban, and R. Krishnakumar, "Machining fixture layout optimization using FEM and evolutionary techniques," *International Journal of Advanced Manufacturing Technology*, vol. 32, no. 11-12, pp. 1090–1103, 2007.

[60] M. Anjanappa, D. K. Anand, and J. A. Kirk, "Identification and optimal control of thin rib machining," vol. 6 of *ASME Dynamic Systems and Control Division DSC*, pp. 15–23, ASME, New York, 1987.

[61] M. Anjanappa, D. K. Anand, and J. A. Kirk, "Application of stochastic optimal control to thin rib machining," *IEEE Proceedings D Control Theory and Applications*, vol. 138, no. 3, pp. 228–236, 1991.

[62] J. Tlusty, S. Smith, and W. R. Winfough, "Techniques for the use of long slender end mills in high-speed milling," *CIRP Annals - Manufacturing Technology*, vol. 45, no. 1, pp. 393–396, 1996.

[63] S. Smith and D. Dvorak, "Tool path strategies for high speed milling aluminum workpieces with thin webs," *Mechatronics*, vol. 8, no. 4, pp. 291–300, 1998.

[64] W. Zhao, N. He, K. Wu, and L. He, "High efficiency milling of thin-walled components of airplane," *Key Engineering Materials*, vol. 259-260, pp. 814–818, 2004.

[65] K. Wu, N. He, W. H. Liao, and W. Zhao, "Optimization of cutting parameters in high speed milling of thin-walled structure components," *Key Engineering Materials*, vol. 259-260, pp. 809–813, 2004.

[66] S. Herranz, F. J. Campa, L. N. Lopez de Lacalle, A. Rivero, A. Lamikiz, E. Ukar, J. A. Sanchez, and U. Bravo, "The milling of airframe components with low rigidity: a general approach to avoid static and dynamic problems," *Proceedings of the Institution of Mechanical Engineers, Part B (Journal of Engineering Manufacture)*, vol. 219, no. B11, pp. 789–801, 2005.

[67] Y. Altintas, *Manufacturing Automation: Metal Cutting Mechanics, Machine Tool Vibrations, and CNC Design*. Cambridge University Press, 2000.

[68] Y. Altintas and P. Lee, "General mechanics and dynamics model for helical end mills," *CIRP Annals - Manufacturing Technology*, vol. 45, no. 1, pp. 59–64, 1996.

[69] S.-M. Wang, C.-H. Chiou, and Y.-M. Cheng, "An improved dynamic cutting force model for end-milling process," *Journal of Materials Processing Technology*, vol. 148, no. 3, pp. 317–327, 2004.

[70] H. El Mounayri, A. D. Spence, and M. A. Elbestawi, "Milling process simulation - a generic solid modeller based paradigm," *ASME Journal of Manufacturing Science and Engineering*, vol. 120, no. 2, pp. 213–221, 1998.

[71] P. A. Clayton, T. El-Wardany, M. A. Elbestawi, and D. Viens, "A mechanistic force model of the 5-axis milling process," *American Society of Mechanical Engineers, Manufacturing Engineering Division, MED*, vol. 11, pp. 979–987, 2000.

[72] R. E. Devor, W. A. Kline, and W. J. Zdeblick, "Mechanistic model for the force system in end milling with application to machining airframe structures," *Manufacturing Engineering Transactions*, pp. 297–303, 1980.

[73] F. Ismail, M. A. Elbestawi, R. Du, and K. Urbasik, "Generation of milled surfaces including tool dynamics and wear," *ASME Journal of Engineering for Industry*, vol. 115, no. 3, pp. 245–252, 1993.

[74] C. Sim and M. Yang, "Prediction of the cutting force in ball-end milling with a flexible cutter," *International Journal of Machine Tools and Manufacture*, vol. 33, no. 2, pp. 267–284, 1993.

[75] E. Budak and Y. Altintas, "Peripheral milling conditions for improved dimensional accuracy," *International Journal of Machine Tools and Manufacture*, vol. 34, no. 7, pp. 907–918, 1994.

[76] H.-Y. Feng and C.-H. Menq, "Flexible ball-end milling system model for cutting force and machining error prediction," *ASME Journal of Manufacturing Science and Engineering*, vol. 118, no. 4, pp. 461–469, 1996.

[77] C. L. Liao and J. S. Tsai, "Dynamic response analysis in end milling using pre-twisted beam finite elements," *Journal of Materials Processing Technology*, vol. 40, no. 3-4, pp. 407–432, 1994.

[78] O. E. E. K. Omar, T. El-Wardany, E. Ng, and M. A. Elbestawi, "An improved cutting force and surface topography prediction model in end milling," *International Journal of Machine Tools and Manufacture*, vol. 47, no. 7-8, pp. 1263–75, 2007.

[79] W. A. Kline, R. E. Devor, and I. A. Shareef, "Prediction of surface accuracy in end milling," *ASME Journal of Engineering for Industry*, vol. 104, no. 3, pp. 272–278, 1982.

[80] J. W. Sutherland and R. E. Devor, "Improved method for cutting force and surface error prediction in flexible end milling systems," *ASME Journal of Engineering for Industry*, vol. 108, no. 4, pp. 269–279, 1986.

[81] J.-S. Tsai and C.-L. Liao, "Finite-element modeling of static surface errors in the peripheral milling of thin-walled workpieces," *Journal of Materials Processing Technology*, vol. 94, no. 2, pp. 235–246, 1999.

[82] S. Ratchev, E. Govender, S. Nikov, K. Phuah, and G. Tsiklos, "Force and deflection modelling in milling of low-rigidity complex parts," *Journal of Material Processing Technology*, vol. 143-144, pp. 796–801, 2003.

[83] S. Ratchev, W. Huang, S. Liu, and A. A. Becker, "Modelling and simulation environment for machining of low-rigidity components," *Journal of Materials Processing Technology*, vol. 153-154, no. 10, pp. 67–73, 2004.

[84] S. Ratchev, S. Liu, W. Huang, and A. A. Becker, "Milling error prediction and compensation in machining of low-rigidity parts," *International Journal of Machine Tools and Manufacture*, vol. 44, no. 15, pp. 1629–1641, 2004.

[85] S. Ratchev, S. Liu, W. Huang, and A. A. Becker, "A flexible force model for end milling of low-rigidity parts," *IJournal of Materials Processing Technology*, vol. 153-154, no. 10, pp. 134–138, 2004.

[86] S. Ratchev, S. Nikov, and I. Moualek, "Material removal simulation of peripheral milling of thin wall low-rigidity structures using FEA," *Advances in Engineering Software*, vol. 35, no. 8-9, pp. 481–491, 2004.

[87] S. Ratchev, S. Liu, and A. A. Becker, "Error compensation strategy in milling flexible thin-wall parts," *Journal of Materials Processing Technology*, vol. 162-163, pp. 673–681, 2005.

[88] S. Ratchev, S. Liu, W. Huang, and A. A. Becker, "An advanced FEA based force induced error compensation strategy in milling," *International Journal of Machine Tools and Manufacture*, vol. 46, no. 5, pp. 542–551, 2006.

[89] H. Guo, D. W. Zuo, S. H. Wang, L. L. Xu, M. Wang, and J. Hu, "The application of FEM technology on the deformation analysis of the aero thin-walled frame shape workpiece," *Key Engineering Materials*, vol. 315-316, pp. 174–179, 2006.

[90] Y. Kang, Z. Wang, J. Wu, and C. Jiang, "Numerical prediction of static form errors in the end milling of thin-walled workpiece," International Technology and Innovation Conference 2006, pp. 816 –824, Institute of Engineering and Technology, 2006.

[91] A. Tang, Z. Liu, and H. Ma, "Modeling and simulation of big deformations of thin walled plate in end milling process," 2007 IEEE International Conference on Automation and Logistics, pp. 2384–2388, IEEE, 2007.

[92] A. Tang and Z. Liu, "Deformations of thin-walled plate due to static end milling force," *Journal of Materials Processing Technology*, vol. 206, no. 1-3, pp. 345–351, 2008.

[93] Y. Altintas, D. Montgomery, and E. Budak, "Dynamic peripheral milling of flexible structures," *ASME Journal of Engineering for Industry*, vol. 114, no. 2, pp. 137–145, 1992.

[94] M. A. Davies and B. Balachandran, "Impact dynamics in milling of thin-walled structures," *Nonlinear Dynamics*, vol. 22, no. 4, pp. 375–392, 2000.

[95] J. Kanchana, V. Prabhu Raja, R. Prakash, and P. Radhakrishnan, "Dynamics of high-speed machining of aerospace structures using finite-element analysis," *Defence Science Journal*, vol. 52, no. 4, pp. 403–408, 2002.

[96] M. L. Campomanes and Y. Altintas, "An improved time domain simulation for dynamic milling at small radial immersions," *ASME Journal of Manufacturing Science and Engineering*, vol. 125, no. 3, pp. 416–422, 2003.

[97] G. Peigne, H. Paris, and D. Brissaud, "A model of milled surface generation for time domain simulation of high-speed cutting," *Proceedings of the Institution of Mechanical Engineers, Part B (Journal of Engineering Manufacture)*, vol. 217, no. B7, pp. 919–930, 2003.

[98] G. Peigne, H. Paris, D. Brissaud, and A. Gouskov, "Impact of the cutting dynamics of small radial immersion milling operations on machined surface roughness," *International Journal of Machine Tools and Manufacture*, vol. 44, no. 11, pp. 1133–1142, 2004.

[99] R. Sagherian and M. A. Elbestawi, "A simulation system for improving machining accuracy in milling," *Computers in Industry*, vol. 14, no. 4, pp. 293–305, 1990.

[100] F. Abrari, *Multi-axis milling of flexible parts*. PhD thesis, McMaster University, 1998.

[101] S. A. Tobias, *Machine Tool Vibration*. Blackie, 1965.

[102] N. H. Hanna and S. A. Tobias, "Theory of nonlinear regenerative chatter," *ASME Journal of Engineering for Industry*, pp. 247–255, 1974.

[103] J. Tlusty and F. Ismail, "Basic non-linearity in machining chatter," *Annals of the CIRP*, vol. 30, no. 1, pp. 299–304, 1981.

[104] J. Tlusty and F. Ismail, "Special aspects of chatter in milling," *Journal of Vibration, Acoustics, Stress, and Reliability in Design*, vol. 105, no. 1, pp. 24–32, 1983.

[105] D. Ruxu, M. A. Elbestawi, and B. C. Ullagaddi, "Chatter detection in milling based on the probability distribution of cutting force signal," *Mechanical Systems and Signal Processing*, vol. 6, no. 4, pp. 345–62, 1992.

[106] Y. Altintas and E. Budak, "Analytical prediction of stability lobes in milling," *CIRP Annals - Manufacturing Technology*, vol. 44, no. 1, pp. 357–362, 1995.

[107] F. Ismail and E. Soliman, "New method for the identification of stability lobes in machining," *International Journal of Machine Tools and Manufacture*, vol. 37, no. 6, pp. 763–774, 1997.

[108] S. D. Merdol and Y. Altintas, "Multi frequency solution of chatter stability for low immersion milling," *ASME Journal of Manufacturing Science and Engineering*, vol. 126, no. 3, pp. 459–466, 2004.

[109] F. Ismail and R. Ziaei, "Chatter suppression in five-axis machining of flexible parts," *International Journal of Machine Tools and Manufacture*, vol. 42, no. 1, pp. 115–122, 2002.

[110] L. N. L. de Lacalle, U. Bravo, O. Altuzarra, J. A. Sanchez, and F. J. Campa, "Stability limits of milling considering the flexibility of the workpiece and the machine," *International Journal of Machine Tools and Manufacture*, vol. 45, no. 15, pp. 1669–1680, 2005.

[111] F. J. Campa, L. N. De Lopez Lacalle, U. Bravo, S. Herranz, and E. Ukar, "Determination of cutting conditions for the stable milling of flexible parts by means of a three-dimensional dynamic model," vol. 16-1 of *ASME Manufacturing Engineering Division, MED*, pp. 667–674, ASME, New York, 2005.

[112] F. J. Campa, L. N. L. de Lacalle, A. Lamikiz, and J. A. Sanchez, "Selection of cutting conditions for a stable milling of flexible parts with bull-nose end mills," *Journal of Materials Processing Technology*, vol. 191, no. 1-3, pp. 279–282, 2007.

[113] V. Thevenot, L. Arnaud, G. Dessein, and G. Cazenave-Larroche, “Influence of material removal on the dynamic behavior of thin-walled structures in peripheral milling,” *Machining Science and Technology*, vol. 10, no. 3, pp. 275–87, 2006.

[114] S. Seguy, G. Dessein, and L. Arnaud, “Surface roughness variation of thin wall milling, related to modal interactions,” *International Journal of Machine Tools and Manufacture*, vol. 48, no. 3-4, pp. 261–74, 2008.

[115] I. Mane, V. Gagnol, B. C. Bouzgarrou, and P. Ray, “Stability-based spindle speed control during flexible workpiece high-speed milling,” *International Journal of Machine Tools and Manufacture*, vol. 48, no. 2, pp. 184–94, 2008.

[116] A. M. Y. Cunedioglu and H. Akcay, “Frequency domain analysis of model order reduction techniques,” *Finite Elements in Analysis and Design*, vol. 42, pp. 367–403, 2006.

[117] J. Pang, R. Dukkipati, W. N. Patten, and G. Sheng, “Comparative analysis of model-reduction methods,” *Heavy Vehicle Systems*, vol. 10, no. 3, pp. 224–253, 2003.

[118] J. O’Callahan, “A procedure for an improved reduced system (IRS) model,” in *Proceedings of the 7th International Modal Analysis Coneference*, pp. 17–21, 1989.

[119] J. Gu, *Efficient Model Reduction Methods for Structural Dynamics Analyses*. Ph.d. thesis report, Department of Mechanical Engineering, University of Michigan, 2000.

[120] M. I. Friswell, S. D. Garvey, and J. E. T. Penny, “Model reduction using dynamic and iterated IRS techniques,” *Journal of Sound and Vibration*, vol. 186, no. 2, pp. 311–323, 1995.

[121] R. L. Kidder, “Reduction of structural frequency equations,” *AIAA Journal*, vol. 11, no. 6, p. 892, 1973.

[122] N. Bouhaddi and R. Fillod, “Model reduction by a simplified variant of dynamic condensation,” *Journal of Sound and Vibration*, vol. 191, no. 2, pp. 233–250, 1996.

[123] A. Y. T. Leung, "Simple dynamic structure method," *Earthquake Engineering and Structural Dynamics*, vol. 16, no. 6, pp. 827–837, 1988.

[124] L. Meirovitch, *Analytical Methods in Vibrations*. New York, Macmillan, 1967.

[125] Z.-D. Ma, "Development of a new mode-superposition technique for modal frequency response analysis of coupled acoustic-structural systems," *Finite Elements in Analysis and Design*, vol. 14, no. 2-3, pp. 209–223, 1993.

[126] E. L. Wilson, M. W. Yuan, and J. M. Dickens, "Dynamic analysis by direct superposition of Ritz vectors," *Earthquake Engineering and Structural Dynamics*, vol. 10, no. 6, pp. 813–821, 1982.

[127] B. Nour-Omid and R. W. Clough, "Dynamic analysis of structures using Lanczos coordinates," *Earthquake Engineering and Structural Dynamics*, vol. 12, no. 4, pp. 565–577, 1984.

[128] L. Meirovitch, *Principles and Techniques of Vibrations*. Prentice Hall, 1997.

[129] J. Craig, R. R. and M. C. C. Bampton, "Coupling of substructures for dynamic analyses," *AIAA Journal*, vol. 6, no. 7, pp. 1313–1319, 1968.

[130] S. Wen-Hwa, G. Jianmin, G. M. Hulbert, and M. Zheng-Dong, "On the use of multiple quasi-static mode compensation sets for component mode synthesis of complex structures," *Finite Elements in Analysis and Design*, vol. 35, no. 2, pp. 119–140, 2000.

[131] S. M. Dickinson and G. B. Warburton, "Vibration of box-type structures," *Journal of Mechanical Engineering Science*, vol. 9, no. 4, pp. 325–335, 1967.

[132] J. Yuan and S. M. Dickinson, "The flexural vibration of rectangular plate systems approached by using artificial springs in the Rayleigh-Ritz method," *Journal of Sound and Vibration*, vol. 159, no. 1, pp. 39–55, 1992.

[133] N. Popplewell, "The vibration of a box-type structure I. Natural frequencies and normal modes," *Journal of Sound and Vibration*, vol. 14, no. 3, pp. 357–365, 1971.

[134] N. Popplewell, "The vibration of a box-type structure II. Response to a travelling pressure wave," *Journal of Sound and Vibration*, vol. 18, no. 4, pp. 521–531, 1971.

[135] D. J. Gorman, "A comprehensive study of the free vibration of rectangular plates resting on symmetrically-distributed uniform elastic edge supports," *ASME Journal of Applied Mechanics*, vol. 56, no. 4, pp. 893–899, 1989.

[136] G. B. Warburton, "The vibration of rectangular plates," *Proceedings of the Institution of Mechanical Engineers*, vol. 168, pp. 371–384, 1954.

[137] E. M. Forsyth and G. B. Warburton, "Transient vibration of rectangular plates," *Journal of Mechanical Engineering Science*, vol. 2, no. 4, pp. 325–330, 1960.

[138] S. M. Dickinson, "The buckling and frequency of flexural vibration of rectangular isotropic and orthotropic plates using Rayleigh's method," *Journal of Sound and Vibration*, vol. 61, no. 1, pp. 1–8, 1978.

[139] P. A. A. Laura and R. O. Grossi, "Transverse vibrations of rectangular plates with edges elastically restrained against translation and rotation," *Journal of Sound and Vibration*, vol. 75, no. 1, pp. 101–107, 1981.

[140] P. A. Laura and R. H. Gutierrez, "Transverse vibrations of thin, elastic plates with concentrated masses and internal elastic supports," *Journal of Sound and Vibration*, vol. 75, no. 1, pp. 135–143, 1981.

[141] G. B. Warburton and S. L. Edney, "Vibrations of rectangular plates with elastically restrained edges," *Journal of Sound and Vibration*, vol. 95, no. 4, pp. 537–551, 1984.

[142] C. Filipich, P. A. A. Laura, C. E. Gianetti, and L. E. Luisoni, "Vibrations of rectangular, stepped thickness plates with edges elastically restrained against rotation," *International Journal of Mechanical Sciences*, vol. 20, no. 3, pp. 149–158, 1978.

[143] D. V. Bambill, R. E. Rossi, V. Jederlinic, and C. A. Rossit, "Vibrations of a rectangular plate with a free edge in the case of discontinuously varying thickness," *Ocean Engineering*, vol. 24, no. 1, pp. 45–49, 1997.

[144] P. A. A. Laura, R. O. Grossi, and G. I. Carneiro, "Transverse vibrations of rectangular plates with thickness varying in two directions and with edges elastically restrained against rotation," *Journal of Sound and Vibration*, vol. 63, no. 4, pp. 499–505, 1979.

[145] P. A. A. Laura, C. P. Filipich, and V. H. Cortinez, "Vibrations of beams and plates carrying concentrated masses," *Journal of Sound and Vibration*, vol. 117, no. 3, pp. 459–465, 1987.

[146] D. Avalos, H. Larrondo, and P. Laura, "Vibrations of a simply supported plate carrying an elastically mounted concentrated mass," *Ocean Engineering (Pergamon)*, vol. 20, no. 2, pp. 195 – 205, 1993.

[147] J. R. Wu and W. H. Liu, "Vibration of rectangular plates with edge restraints and intermediate stiffeners," *Journal of Sound and Vibration*, vol. 123, no. 1, pp. 103–113, 1988.

[148] R. H. Gutierrez and P. A. A. Laura, "Transverse vibrations of rectangular plates elastically restrained against rotation along the edges with varying stiffener length," *Journal of Sound and Vibration*, vol. 101, no. 1, pp. 122–124, 1985.

[149] W. H. Liu and C. C. Huang, "Free vibration of a rectangular plate with elastically restrained and free edges," *Journal of Sound and Vibration*, vol. 119, no. 1, pp. 177–183, 1987.

[150] A. S. Veletsos and N. M. Newmark, "Determination of natural frequencies of continuous plates hinged along two opposite edges," *ASME Journal of Applied Mechanics*, vol. 23, no. 1, pp. 97–102, 1956.

[151] R. Szilard, *Theories and Appications of Plate Analysis: Classical, Numericad and Engineering Methods*. John Wiley and Sons, Inc., 2004.

[152] I. Elishakoff and A. Sternberg, "Eigenfrequencies of continuous plates with arbitrary number of equal spans," *ASME Journal of Applied Mechanics*, vol. 46, no. 3, pp. 656–662, 1979.

[153] D. J. Gorman and L. Garibaldi, "Accurate analytical type solutions for free vibration frequencies and mode shapes of multi-span bridge decks: The span-by-span approach," *Journal of Sound and Vibration*, vol. 290, no. 1-2, pp. 321–336, 2006.

[154] L. Ercoli and P. A. A. Laura, "Transverse vibrations of continuous rectangular plates of variable thickness taking into account additional complicating factors," vol. 98-6 of *ASME Pressure Vessels and Piping Division PVP*, pp. 195–198, ASME, New York, 1985.

[155] L. Ercoli and P. A. A. Laura, "Analytical and experimental investigation on vibrating, continuous rectangular plates of non-uniform thickness," *Journal of Sound and Vibration*, vol. 112, no. 3, pp. 447–454, 1987.

[156] S. Marchesiello, A. Fasana, L. Garibaldi, and B. A. D. Piombo, "Dynamics of multi-span continuous straight bridges subject to multi-degrees of freedom moving vehicle excitation," *Journal of Sound and Vibration*, vol. 224, no. 3, pp. 541–561, 1999.

[157] Anon, "Transverse vibrations of continuous rectangular plates. A comparison of results," *Applied Acoustics*, vol. 26, no. 2, pp. 149–154, 1989.

[158] K. T. Truong and J. Davidson, "Free vibration of a rectangular plate of nonuniform thickness," vol. 101 of *ASME Pressure Vessels and Piping Division PVP*, pp. 81–87, ASME, New York, 1986.

[159] Y. K. Cheung and L. G. Tham, *Finite Strip Method*. CRC Press, 1998.

[160] B. W. Golley and J. Petrolito, "Free and forced vibration analysis of continuous plates," pp. 1–11, University of Newcastle, Newcastle, Aust, 1982.

[161] J. A. Puckett and G. J. Lang, "Compound strip method for free vibration analysis of continuous plates," *Journal of Engineering Mechanics*, vol. 112, no. 12, pp. 1375–1389, 1986.

[162] J. Petrolito and B. W. Golley, "Dynamic analysis of orthotropic plates using finite strip-elements," pp. 1127–1132, A.A. Balkema, Rotterdam, Neth, 1991.

[163] B. W. Golley and J. Petrolito, "Finite strip-elements for the dynamic analysis of orthotropic plate structures," *Journal of Sound and Vibration*, vol. 163, no. 3, pp. 479–491, 1993.

[164] R. L. Burden and J. D. Faires, *Numerical Analysis.* Thomson Books/Cole, 2005.

[165] Z. Michalewicz and D. Fogel, *How to Solve It: Modern Heuristics.* Springer-Verlag Berlin Heidlberg, 2002.

[166] S. Rao, *Engineering Optimization.* John Willey and Sons, Inc., 2002.

[167] H.-P. Lin and S. Chang, "Free vibration analysis of multi-span beams with intermediate flexible constraints," *Journal of Sound and Vibration*, vol. 281, no. 1-2, pp. 155 – 169, 2005.

[168] R.-T. Wang, "Vibration analysis of a multi-span beam," *Chung-Kuo Chi Hsueh Kung Ch'eng Hsueh Pao/Journal of the Chinese Society of Mechanical Engineers*, vol. 15, no. 1, pp. 88 – 93, 1994.

[169] D. Erwin, *Modal Testing : Theory, Practice, and Application.* Baldock, Hertfordshire, England ; Philadelphia, PA : Research Studies Press, 2000.

[170] L. R. Castro, P. Vieville, and P. Lipinski, "Correction of dynamic effects on force measurements made with piezoelectric dynamometers," *International Journal of Machine Tools and Manufacture*, vol. 46, no. 14, pp. 1707–1715, 2006.

[171] L. N. L. de Lacalle, A. Lamikiz, J. A. Sanchez, and I. F. de Bustos, "Recording of real cutting forces along the milling of complex parts," *Mechatronics*, vol. 16, no. 1, pp. 21–32, 2006.

[172] S. A. Jensen, Y. C. Shin, and P. Davies, "Inverse filtering of unwanted system dynamics in cutting force measurement," vol. 58 of *ASME, Dynamic Systems and Control Division DSC*, pp. 167–174, ASME, New York, 1996.

[173] L. Castro, P. Vieville, and P. Lipinski, "Experimental methodology destined to establish the frequency response function (FRF) between a dynamic force and the signals emitted by a piezoelectric dynamometer," *Materials Science Forum*, vol. 526, pp. 85–90, 2006.

[174] R. L. Kegg, "Cutting dynamics in machine tool chatter – contribution to machine tool chatter research – 3," *ASME Journal of Engineering for Industry*, vol. 87, no. 4, pp. 464–470, 1965.

[175] Y. Tanaka and N. Ikawa, "Accelerometer applications to tool dynamometers with improved dynamic response," vol. 18, no. 2, pp. 353–359, 1970.

[176] W. A. Knight and M. M. Sadek, "Correction for dynamic errors in machine tool dynamometers," *Annals of the CIRP*, vol. 19, no. 2, pp. 237–245, 1971.

[177] N. Tounsi and A. Otho, "Dynamic cutting force measuring," *International Journal of Machine Tools and Manufacture*, vol. 40, no. 8, pp. 1157–1170, 2000.

[178] N. Tounsi and A. Otho, "Dynamometer performance modeling and experimental assessment," *ASME Journal of Dynamic Systems, Measurement and Control*, vol. 122, no. 3, pp. 477–482, 2000.

[179] S. S. Park and Y. Altintas, "Dynamic compensation of spindle integrated force sensors with Kalman filter," *ASME Journal of Dynamic Systems, Measurement and Control*, vol. 126, no. 3, pp. 443–452, 2004.

[180] W. S. Smith, *The Scientist and Engineer's Guide to Digital Signal Processing.* California Technical Pub, 1998.

[181] S. J. Kline and F. A. McClintock, "Describing uncertainties in single sample experiments," *Mechanical Engineering*, vol. 75, no. 1, pp. 3–8, 1953.

[182] E. O. Doebelin, *Measurement Systems : Application and Design.* Boston: McGraw-Hill, 2004.

[183] H. A. Kishawy and M. A. Elbestawi, "Effects of process parameters on material side flow during hard turning," *International Journal of Machine Tools and Manufacture*, vol. 39, no. 7, pp. 1017–1030, 1999.

[184] J. R. Vinson, *The Behavior of Thin Walled Structures : Beams, Plates, and Shells.* Prentice Hall, 1989.

Appendix A

Boundary Conditions and Trial Functions for a Plate with Torsional and Translational Springs

This appendix has two section. In the first section, the boundary conditions for a plate with torsional and translation springs will be presented. The second section includes the detailed expression of the characteristic equation and the mode shape of a beam with torsional and translational springs.

A.1 Boundary Conditions for a Plate with Torsional and Translational Springs

The boundary conditions for a rectangular plate with torsional and translational springs at the boundaries can be represented at each edge as follows [184]:

At $x = 0$

$$\frac{\partial^3 w}{\partial x^3} + (2 - \nu)\frac{\partial^3 w}{\partial x \partial y^2} - \frac{K_{xo}}{D_E} w = 0 \tag{A-1a}$$

$$D_E\left[\frac{\partial^2 w}{\partial x^2} + \nu\frac{\partial^2 w}{\partial y^2}\right] + R_{xo}\frac{\partial w}{\partial x} = 0 \tag{A-1b}$$

At $x = l_x$

$$\frac{\partial^3 w}{\partial x^3} + (2 - \nu)\frac{\partial^3 w}{\partial x \partial y^2} - \frac{K_{xl}}{D_E} w = 0 \tag{A-2a}$$

$$D_E\left[\frac{\partial^2 w}{\partial x^2} + \nu\frac{\partial^2 w}{\partial y^2}\right] + R_{xl}\frac{\partial w}{\partial x} = 0 \tag{A-2b}$$

Eqs (A-1) and (A-2) represent the force and moment balance at $x = 0$ and $x = x_l$, respectively.

At $y = 0$

$$\frac{\partial^3 w}{\partial y^3} + (2-\nu)\frac{\partial^3 w}{\partial y \partial x^2} - \frac{K_{yo}}{D_E} w = 0 \tag{A-3a}$$

$$D_E\left[\frac{\partial^2 w}{\partial y^2} + \nu\frac{\partial^2 w}{\partial x^2}\right] + R_{yo}\frac{\partial w}{\partial y} = 0 \tag{A-3b}$$

At $y = l_y$

$$\frac{\partial^3 w}{\partial y^3} + (2-\nu)\frac{\partial^3 w}{\partial y \partial x^2} - \frac{K_{yl}}{D_E} w = 0 \tag{A-4a}$$

$$D_E\left[\frac{\partial^2 w}{\partial y^2} + \nu\frac{\partial^2 w}{\partial x^2}\right] + R_{yl}\frac{\partial w}{\partial y} = 0 \tag{A-4b}$$

Eqs (A-3) and (A-4) represent the force and moment balance at $x = 0$ and $x = x_l$, respectively.

A.2 Beam with Torsional and Translational Springs

The characteristic equation for a beam with torsional and translation springs at the boundaries can be obtained by using the separation of variables according to Eq. (4.26) and substituting Eq. (4.32) in Eqs. (4.30) and (4.31). The expression for the characteristic equation can be written as:

$$\sum_{i=1}^{6} \kappa_i = 0 \tag{A-5}$$

where κ_i is expressed as follows:

$$\kappa_1 = \left(\frac{EI\beta\left(EI\beta^3\right)^2}{k_0} + \frac{r_0 r_l k_l}{EI\beta}\right)(\cos\beta l_u \cosh\beta l_u - 1) \tag{A-6a}$$

$$\kappa_2 = \left(-\frac{k_l r_l EI\beta^3}{k_0} - r_0 EI\beta^3\right)(\cos\beta l_u \cosh\beta l_u + 1) \tag{A-6b}$$

$$\kappa_3 = \left(-2r_l EI\beta^3 - 2\frac{r_0 k_l EI\beta^3}{k_0}\right)(\cos\beta l_u \cosh\beta l_u) \tag{A-6c}$$

$$\kappa_4 = \left(2\frac{r_l r_0 EI\beta^5}{k_0} - 2k_l EI\beta\right)(\sin\beta l_u \sinh\beta l_u) \tag{A-6d}$$

$$\kappa_5 = \left(-\frac{k_l\,(EI)^2\,\beta^4}{k_0} - (EI)^2\,\beta^4 + k_l r_l + k_l r_0\right)(\cos\beta l_u \sinh\beta l_u - \sin\beta l_u \cosh\beta l_u) \tag{A-6e}$$

$$\kappa_6 = \left(\frac{(r_0 + r_l)\,(EI\beta^3)^2 - r_0 k_l r_l \beta^2}{k_0} - r_l r_0 \beta^2\right)(\cos\beta l_u \sinh\beta l_u + \sin\beta l_u \cosh\beta l_u) \tag{A-6f}$$

For Eqs. (A-6a) to (A-6f), the second bracket in each equation represent the characteristic equation for a beam model with certain standard boundary conditions. For example, Eqs. (A-6a) and (A-6b) represent the characteristic equation for a free-free beam and clamped- free beam, respectively. The eigenvalues of the beam with torsional and translational springs are determined by finding the values of β_r which satisfy Eq. (A-5). By substituting the calculated values of β_r in Eq. (4.32) and then satisfying the spatial boundary conditions in Eqs. (4.30) and (4.31), the expressions for B_r, C_r and D_r can be determined in function of A_r as follows:

$$B_r = \left(\frac{EI\beta_r^3(1 - k_{cr})}{2k_o} - \frac{r_o(1 + k_{cr})}{2EI\beta_r}\right)A_r \tag{A-7}$$

$$C_r = k_{cr} A_r \tag{A-8}$$

$$D_r \left(\frac{EI\beta_r^3(1 - k_{cr})}{2k_o} + \frac{r_o(1 + k_{cr})}{2EI\beta_r}\right)A_r \tag{A-9}$$

where k_{cr} can be represented as follows:

$$k_{cr} = -\frac{n_1 + n_2}{m_1 + m_2} \tag{A-10}$$

where

$$n_1 = -EI\beta_r^3 \cos\beta_r l_u + \frac{(EI\beta_r^3)^2}{2k_o}\sin\beta_r l_u - \frac{r_o\beta_r^2}{2}\sin\beta_r l_u + \frac{(EI\beta_r^3)^2}{2k_o}\sinh\beta_r l_u + \frac{r_o\beta_r^2}{2}\sinh\beta_r l_u \tag{A-11}$$

$$n_2 = -k_l \sin\beta_r l_u - \frac{k_l EI\beta_r^3}{2k_o}\cos\beta_r l_u + \frac{k_l r_o}{2EI\beta_r}\cos\beta_r l_u - \frac{k_l EI\beta_r^3}{2k_o}\cosh\beta_r l_u - \frac{k_l r_o}{2EI\beta_r}\cosh\beta_r l_u \tag{A-12}$$

$$m_1 = -\frac{(EI\beta_r^3)^2}{2k_o}\sin\beta_r l_u - \frac{r_o\beta_r^2}{2}\sin\beta_r l_u + EI\beta_r^3\cosh\beta_r l_u - \frac{(EI\beta_r^3)^2}{2k_o}\sinh\beta_r l_u + \frac{r_o\beta_r^2}{2}\sinh\beta_r l_u \tag{A-13}$$

$$m_2 = \frac{k_l EI\beta_r^3}{2k_o}\cos\beta_r l_u + \frac{k_l r_o}{2EI\beta_r}\cos\beta_r l_u - k_l\sinh\beta_r l_u + \frac{k_l EI\beta_r^3}{2k_o}\cosh\beta_r l_u - \frac{k_l r_o}{2EI\beta_r}\cosh\beta_r l_u \tag{A-14}$$

Appendix B

Characteristic Equations for the Multi-Span Beam Models

In the following sections, the derivation of the characteristic equations for three models of multi-span beams will be presented. The first two models are for a four-span and five-span beam used to generate the trial functions in the x-direction for the multi-span plate with and without change of thickness, respectively. The third model is for a three-span clamped-free beam used to generate the trial functions in the y-direction for the multi-span plate with change of thickness. For a multi-span beam, the relation between β_u and β_{u+1} can be expressed as:

$$\frac{\beta_{u+1}}{\beta_u} = \left(\frac{h_u}{h_{u+1}}\right)^{\frac{1}{2}} = R_u^{\frac{1}{2}} \tag{B-1}$$

where u is the index of the span of the beam and β_u and β_{u+1} are the eigenvalue parameters for spans u and $u+1$, respectively. For simplification of the notation, the term $\beta_u l_u$ will be referred to as $\overline{\beta}_u$, where l_u designates the length of the u^{th} span.

B.1 Four-Span Beam

The mode shapes of the four-span beam can be expressed according to Eq. (4.61) where a is the index for the a^{th} span and s_x is the total number of spans. By substituting Eq. (4.61) in Eqs. (4.59a), (4.59c) and (4.59d) for the edge $x = x_a$, Eqs. (B-2) to (B-4) are obtained, respectively, as follows:

$$B_a = -D_a \tag{B-2}$$

$$A_{a+1} + C_{a+1} = \left(\frac{h_{a+1}}{h_a}\right)^{\frac{1}{2}} [A_a \cos\overline{\beta}_a - B_a G_a + C_a \cosh\overline{\beta}_a] \tag{B-3}$$

where $G_a = \sin\overline{\beta}_a + \sinh\overline{\beta}_a$

$$B_{a+1} = -\frac{1}{2}\left(\frac{h_a}{h_{a+1}}\right)^2 [-A_a \sin\overline{\beta}_a - B_a S_a + C_a \sinh\overline{\beta}_a] \tag{B-4}$$

where $S_a = \cos\overline{\beta}_a + \cosh\overline{\beta}_a$

By inserting Eq. (4.61) in Eq. (4.59b) for the edge $x = x_{a+1}$, Eq. (B-5) is obtained by

$$A_{a+1} \sin\overline{\beta}_{a+1} + C_{a+1} \sinh\overline{\beta}_{a+1} = -B_{a+1} M_{a+1} \tag{B-5}$$

where $M_{a+1} = \cos\overline{\beta}_{a+1} - \cosh\overline{\beta}_{a+1}$.

Substituting B_{a+1} from Eq. (B-4) into Eq. (B-5), the following equation is obtained:

$$A_{a+1} \sin\overline{\beta}_{a+1} + C_{a+1} \sinh\overline{\beta}_{a+1} = \frac{1}{2} M_{a+1}\left(\frac{h_a}{h_{a+1}}\right)^2 [-A_a \sin\overline{\beta}_a - B_a S_a + C_a \sinh\overline{\beta}_a] \tag{B-6}$$

By writing Eqs. (B-3), (B-4), and (B-6) in a matrix form, Eq. (B-7) is obtained:

$$\begin{bmatrix} A_{a+1} \\ B_{a+1} \\ C_{a+1} \end{bmatrix} = \boldsymbol{\Phi_x}^{(a)} \begin{bmatrix} A_a \\ B_a \\ C_a \end{bmatrix} \tag{B-7}$$

where the transfer matrix $\boldsymbol{\Phi_x}$ can be expressed as:

$$\boldsymbol{\Phi_x}^{(a)} = \tfrac{1}{2} \begin{bmatrix} 1 & 0 & 1 \\ 0 & 1 & 0 \\ \sin\overline{\beta}_{a+1} & 0 & \sinh\overline{\beta}_{a+1} \end{bmatrix}^{-1}$$

$$\begin{bmatrix} 2R_a^{-\frac{1}{2}} \cos\overline{\beta}_a & -2R_i^{-\frac{1}{2}} G_a & 2R_a^{-\frac{1}{2}} \cosh\overline{\beta}_a \\ R_a^2 \sin\overline{\beta}_a & R_i^2 S_a & -R_a^2 \sinh\overline{\beta}_a \\ -M_{a+1} R_a^2 \sin\overline{\beta}_a & -M_{a+1} R_i^2 S_a & M_{a+1} R_a^2 \sinh\overline{\beta}_a \end{bmatrix} \tag{B-8}$$

Eq. (B-7) is the same as Eq. (4.63). Using the transformation in Eq. (4.63) or Eq. (B-7), the following equation can be obtained:

$$\begin{bmatrix} A_4 \\ B_4 \\ C_4 \end{bmatrix} = \prod_{a=3}^{a=1} \boldsymbol{\Phi_x}^{(a)} \begin{bmatrix} A_a \\ B_a \\ C_a \end{bmatrix} \tag{B-9}$$

Taking into account that the beam is continuous from span 4 to span 1, thus the coefficients of span 1 can be expressed in terms of the coefficients of span 4 as follows:

$$\begin{bmatrix} A_1 \\ B_1 \\ C_1 \end{bmatrix} = \prod_{a=3}^{a=1} \boldsymbol{\Phi}_{\boldsymbol{x}}^{\mathbf{(4)}} \begin{bmatrix} A_4 \\ B_4 \\ C_4 \end{bmatrix} \tag{B-10}$$

Substituting Eq. (B-10) in (B-9), the characteristic equation of the four-span beam, presented in Eq. (4.64), is obtained. The eigenvalues of the four-span beam and the coefficients of Eq. (4.61) can be determined by finding the non-trivial solutions of Eq. (4.64)

B.2 Five-Span Beam

The development of the mode shapes of the five span beam, shown in Fig. (4.4), can be also obtained by using the transfer matrix method. The coefficients of spans 4 and 5 are expressed in terms of the coefficients of spans 3 and 4, respectively, using Eqs. (B-7) and (B-8). The coefficients of span 3 are determined in terms of the coefficients of span 2 by substituting Eq. (4.61) in (4.59). In this case, $B_2 \neq -D_2$, and thus the following 3×4 transfer matrix is obtained:

$$\begin{bmatrix} A_3 \\ B_3 \\ C_3 \end{bmatrix} = \boldsymbol{\Phi_x}^{(2)} \begin{bmatrix} A_2 \\ B_2 \\ C_2 \\ D_2 \end{bmatrix} \tag{B-11}$$

such that,

$$\mathbf{\Phi_{x}}^{(2)} = \tfrac{1}{2}\begin{bmatrix} 1 & 0 & 1 \\ 0 & 1 & 0 \\ \sin\overline{\beta}_3 & 0 & \sinh\overline{\beta}_3 \end{bmatrix}^{-1}$$

$$\begin{bmatrix} 2R_2^{-\frac{1}{2}}\cos\overline{\beta}_2 & -2R_2^{-\frac{1}{2}}\sin\overline{\beta}_2 & 2R_2^{-\frac{1}{2}}\cosh\overline{\beta}_2 & 2R_2^{-\frac{1}{2}}\sinh\overline{\beta}_2 \\ R_2^2\sin\overline{\beta}_2 & R_2^2\cos\overline{\beta}_2 & -R_2^2\sinh\overline{\beta}_2 & -R_2^2\cosh\overline{\beta}_2 \\ -M_3R_2^2\sin\overline{\beta}_2 & -M_3R_2^2\cos\overline{\beta}_2 & M_3R_2^2\sinh\overline{\beta}_2 & M_3R_2^2\cosh\overline{\beta}_2 \end{bmatrix} \tag{B-12}$$

By satisfying the boundary conditions at $x = x_1$ according to Eq. (4.78), the coefficients of span 2 can be expressed in terms of the coefficient of span 1 according to the following set of equations:

$$\begin{bmatrix} A_2 \\ B_2 \\ C_2 \\ D_2 \end{bmatrix} = \mathbf{\Phi_{x}}^{(1)} \begin{bmatrix} A_1 \\ B_1 \\ C_1 \end{bmatrix} \tag{B-13}$$

such that,

$$\mathbf{\Phi_{x}}^{(1)} = \frac{1}{2}\begin{bmatrix} 1 & 0 & 1 & 0 \\ 0 & 1 & 0 & 1 \\ 1 & 0 & -1 & 0 \\ 0 & 1 & 0 & -1 \end{bmatrix}\begin{bmatrix} R_1^{-\frac{1}{2}}\cos\overline{\beta}_1 & -R_1^{-\frac{1}{2}}G_1 & R_1^{-\frac{1}{2}}\cosh\overline{\beta}_1 \\ \sin\overline{\beta}_1 & M_1 & \sinh\overline{\beta}_1 \\ R_1^{\frac{3}{2}}\cos\overline{\beta}_1 & -R_1^{\frac{3}{2}}N_1 & -R_1^{\frac{3}{2}}\cosh\overline{\beta}_1 \\ R_1^2\sin\overline{\beta}_1 & R_1^2S_1 & -R_1^2\sinh\overline{\beta}_1 \end{bmatrix} \tag{B-14}$$

where $N_{a+1} = \sin\overline{\beta}_{a+1} - \sinh\overline{\beta}_{a+1}$. In order to determine the transfer matrix to express the coefficients of span 1 in terms of the coefficients of span 5, the following four boundary condition equations will be used:

$$X^{(1)}(x_0) = 0 \tag{B-15a}$$

$$\left.\frac{dX^{(1)}}{dx}\right|_{x=x_0} = \left.\frac{dX^{(5)}}{dx}\right|_{x=x_5} \tag{B-15b}$$

$$h_1^3 \left. \frac{d^2X^{(1)}}{dx^2} \right|_{x=x_0} = h_5^3 \left. \frac{d^2X^{(5)}}{dx^2} \right|_{x=x_5} \tag{B-15c}$$

$$X^{(2)}(x_2) = 0 \tag{B-15d}$$

Using the mode shape expression in Eq. (4.61) and substituting Eq. (B-13) in Eq. (B-15d) gives:

$$[\ \sin\overline{\beta}_2\ \ \cos\overline{\beta}_2\ \ \sinh\overline{\beta}_2\ \ \cosh\overline{\beta}_2\ ]\boldsymbol{\Phi_x}^{(1)} \begin{bmatrix} A_1 \\ B_1 \\ C_1 \end{bmatrix} = 0 = [\tau_1\ \tau_2\ \tau_3\ ] \begin{bmatrix} A_1 \\ B_1 \\ C_1 \end{bmatrix} \tag{B-16}$$

According to Eq. (B-16), A_1 and C_1 can be expressed in terms of B_1. Consequently, by substituting Eq. (4.61) in Eqs. (B-15a) to (B-15c) and putting them in a matrix form gives the following relation between the coefficients of span 1 and span 5:

$$\begin{bmatrix} 1 & 0 & 1 \\ 0 & 1 & 0 \\ \tau_1 & 0 & \tau_3 \end{bmatrix} \begin{bmatrix} A_1 \\ B_1 \\ C_1 \end{bmatrix} = \frac{1}{2} \begin{bmatrix} 2R_5^{-\frac{1}{2}}\cos\overline{\beta}_5 & -2R_5^{-\frac{1}{2}}G_5 & 2R_5^{-\frac{1}{2}}\cosh\overline{\beta}_5 \\ R_5^2\sin\overline{\beta}_5 & R_5^2 S_5 & -R_5^2\sinh\overline{\beta}_5 \\ -\tau_2 R_5^2\sin\overline{\beta}_5 & -\tau_2 R_5^2 S_5 & \tau_2 R_5^2\sinh\overline{\beta}_5 \end{bmatrix} \begin{bmatrix} A_5 \\ B_5 \\ C_5 \end{bmatrix} \tag{B-17}$$

The characteristic equation of the five-span beam can be written as:

$$\begin{bmatrix} A_5 \\ B_5 \\ C_5 \end{bmatrix} = \prod_{a=4}^{a=1} \boldsymbol{\Phi_x}^{(a)} \begin{bmatrix} A_a \\ B_a \\ C_a \end{bmatrix} = \prod_{a=4}^{a=1} \boldsymbol{\Phi_x}^{(a)} \boldsymbol{\Phi_x^{(5)}} \begin{bmatrix} A_5 \\ B_5 \\ C_5 \end{bmatrix} \tag{B-18}$$

As can be seen, Eq. (B-18) can be expressed using Eq. (4.64).

B.3 Three-Span Clamped-Free Beam

For the three-span clamped free beam, b is the index for the b^{th} span and s_y is the total number of spans. At $y = y_0$, the conditions of zero displacement and rotation have to be satisfied by substituting Eq. (4.82) in (4.79), which leads to the following equations:

$$B_1 = -D_1 \tag{B-19a}$$

$$A_1 = -C_1 \tag{B-19b}$$

At $y = y_b$, for $b = 1, .., s_y - 1$, the conditions for the continuity of the displacement, rotation, bending moment and shear force expressed in Eq. (4.80) have to be satisfied. By substituting Eq. (4.82) in (4.80), the relation between the coefficients of span $b+1$ and span b can be expressed as:

$$\begin{bmatrix} A_{b+1} \\ B_{b+1} \\ C_{b+1} \\ D_{b+1} \end{bmatrix} = \boldsymbol{\Phi_y}^{(b)} \begin{bmatrix} A_b \\ B_b \\ C_b \\ D_b \end{bmatrix} \tag{B-20}$$

where $\boldsymbol{\Phi_y}^{(b)}$ is expressed as follows:

$$\boldsymbol{\Phi_y}^{(b)} = \frac{1}{2} \begin{bmatrix} 1 & 0 & 1 & 0 \\ 0 & 1 & 0 & 1 \\ 1 & 0 & -1 & 0 \\ 0 & 1 & 0 & -1 \end{bmatrix} \begin{bmatrix} R_b^{-\frac{1}{2}} \cos\overline{\beta}_b & -R_b^{-\frac{1}{2}} \sin\overline{\beta}_b & R_b^{-\frac{1}{2}} \cosh\overline{\beta}_b & R_b^{-\frac{1}{2}} \sinh\overline{\beta}_b \\ \sin\overline{\beta}_b & \cos\overline{\beta}_b & \sinh\overline{\beta}_b & \cosh\overline{\beta}_b \\ R_b^{\frac{3}{2}} \cos\overline{\beta}_b & -R_b^{\frac{3}{2}} \sin\overline{\beta}_b & -R_b^{\frac{3}{2}} \cosh\overline{\beta}_b & -R_b^{\frac{3}{2}} \sinh\overline{\beta}_b \\ R_b^{2} \sin\overline{\beta}_b & R_b^{2} \cos\overline{\beta}_b & -R_b^{2} \sinh\overline{\beta}_b & -R_b^{2} \cosh\overline{\beta}_b \end{bmatrix} \tag{B-21}$$

By substituting Eq. (4.82) in Eqs.(4.81), which represent the conditions of the free edge at $y = y_{s_y}$, the following equations are obtained:

$$-A_3 \sin\overline{\beta}_3 - B_3 \cos\overline{\beta}_3 + C_3 \sinh\overline{\beta}_3 + D_3 \cosh\overline{\beta}_3 = 0 \tag{B-22a}$$

$$-A_3 \cos\overline{\beta}_3 + B_3 \sin\overline{\beta}_3 + C_3 \cosh\overline{\beta}_3 + D_3 \sinh\overline{\beta}_3 = 0 \tag{B-22b}$$

Substituting Eqs. (B-19) and (B-20) in Eqs.(B-22), the following characteristic equation of the clamped-free beam can be obtained :

$$\boldsymbol{\Phi_t} \begin{bmatrix} A_1 \\ B_1 \end{bmatrix} = 0 \tag{B-23}$$

where $\boldsymbol{\Phi_t}$ can be expressed as follows:

$$\boldsymbol{\Phi_t} = \begin{bmatrix} -\sin\overline{\beta}_3 & -\cos\overline{\beta}_3 & \sinh\overline{\beta}_3 & \cosh\overline{\beta}_3 \\ -\cos\overline{\beta}_3 & \sin\overline{\beta}_3 & \cosh\overline{\beta}_3 & \sinh\overline{\beta}_3 \end{bmatrix} \boldsymbol{\Phi_y}^{(2)} \boldsymbol{\Phi_y}^{(1)} \begin{bmatrix} 1 & 0 \\ 0 & 1 \\ -1 & 0 \\ 0 & -1 \end{bmatrix} \tag{B-24}$$

The eigenfrequencies and the mode shapes of the beam are obtained by determining the non-trivial solution of Eq.(B-23).

Appendix C

Formulation of the Transfer Function of the Force Measurement System

From the tap tests on the dynamometer, the following transfer functions were determined experimentally:

$$T_F = \frac{F_D}{F_{in}} \tag{C-1}$$

$$T_x = \frac{z_D}{F_{in}} \tag{C-2}$$

In the system in Fig 6.11, the equation for the forces applied on the top plate of the dynamometer from the spring and damper k_2 and c_2, respectively, is:

$$F_k = (c_2 s + k_2)[z_2 - z_D] \tag{C-3}$$

Using the identified transfer function in C-2 and substituting in C-3, the following equation is obtained:

$$z_2 = \kappa \cdot F_k \tag{C-4}$$

where

$$\kappa = \left[\frac{1 + (c_2 s + k_2)T_x}{c_2 s + k_2}\right]$$

The equations of motion for m_1 and m_2 are:

$$m_1 s^2 z_1 = (c_1 s + k_1)[z_2 - z_1] + F \tag{C-5}$$

$$m_2s^2z_2 = (c_1s + k_1)[z_1 - z_2] - F_k \tag{C-6}$$

Adding C-5 and C-6

$$m_2s^2z_2 + m_1s^2z_1 = F - F_k \tag{C-7}$$

Rearranging C-6 and substituting z_2 from C-4, the following equation is obtained:

$$z_1 = \phi \cdot F_k \tag{C-8}$$

where

$$\phi = \frac{(m_2s^2 + c_1s + k_1)\kappa + 1}{c_1s + k}$$

Substituting C-8 and C-4 in C-7:

$$\varphi = \frac{F}{F_k} = m_2s^2\kappa + m_1s^2\phi + 1 \tag{C-9}$$

Using the transfer function identified in C-1 and C-9, the transfer function of the system can be expressed as:

$$T_{sys} = \frac{F_D}{F} = \frac{T_F}{\varphi} \tag{C-10}$$